University of Liège

Faculty of Sciences
Department of Astrophysics,
Geophysics and Oceanography

Detection and Characterization of Sub-Neptunes and Giant Planets around Nearby Red Dwarfs

Author: Ms. TIMMERMANS Mathilde

Thesis supervisor: Prof. GILLON Michaël

Members of the jury:

Prof. DE BECKER Michaël
President, University of Liège

Assoc. Prof. VAN GROOTEL Valérie
Secretary, University of Liège

Prof. JEHIN Emmanuel
University of Liège

Prof. TRIAUD Amaury
University of Birmingham

Assoc. Prof. POZUELOS Francisco J.
Instituto de Astrofísica de Andalucía

Assoc. Prof. LENDL Monika
University of Geneva

A dissertation submitted in partial fulfillment
of the requirements for the degree of

Doctor of Philosophy

Academic year 2023-2024

Abstract

In the last two decades, the field of Exoplanetology has seen incredible developments. Since the discovery of the first exoplanet, we are now close to 6000 exoplanets detected, revealing a great diversity in planet populations. The newest generation observatories, such as the JWST, allow their in-depth study to answer fundamental questions on the formation and evolution of these alien worlds, to search for traces of extraterrestrial life, and eventually to help us understand how our own solar system formed. In particular, low-mass stars represent the best opportunity for the atmospheric characterization of exoplanets thanks to their small sizes. This thesis focuses on the detection and characterization of two sub-populations transiting sub-Neptunes and close-in giants orbiting these small and cool stars.

In Chapter 1, I introduce field of Exoplanetology from a historical point of view, going over the different detection methods including the important discoveries and their current status. I then introduce the theoretical concepts and notions needed to understand the context of thesis: (a) what is a transit? (b) Why are low-mass stars interesting? (c) How can we study transiting planets? Finally, I describe what we know of sub-Neptunes and close-in giants orbiting red dwarfs today, and what there is still to learn.

In Chapter 2, I give an overview of the TESS space mission and how it allowed astronomers to detect hundreds of new planets. I describe my personal contribution to this effort thanks to a privileged access to two networks of ground-based telescopes: TRAPPIST and SPECULOOS. I then outline the data analysis procedure, and the process of validating a planet candidate. Lastly, I briefly describe the Hubble Space Telescope and ESPRESSO on the Very Large Telescope, the two facilities for which observing time was obtained for the characterization of planets during this thesis.

Chapter 3 is dedicated to the discovery of TOI-4336 A b, a sub-Neptune planet orbiting a M-type star part of a hierarchical triple system of M dwarfs. It has a radius of 2.1 ± 0.1 $R_\oplus$ and orbits its star every 16.3 days, which puts it at the inner edge of the habitable zone. This system is particularly interesting for atmospheric characterization. In Chapter 4, I describe the ongoing exploratory program with the Hubble Space Telescope to investigate whether chemical species can be detected in the upper atmosphere of TOI-4336 A b.

A second planet was found in the TOI-4336 A and TOI-237 systems, and I present their discovery in Chapter 5 in the context of the Hidden Gems project. This project aims to find additional planet candidates in the TESS data for known transiting systems orbiting low-mass stars.

In Chapter 6, I introduce the MANGOs program I led during this thesis. It is a joint TRAPPIST and SPECULOOS observing program targeting giant orbiters of red dwarf stars (giant planets, brown dwarfs, and M dwarfs).

I conclude this PhD thesis by summarizing the main results, highlighting my contribution to the discovery of new exoplanets, and evaluating the impact of this thesis work in the broader context of Exoplanet research. Finally, I discuss some prospects to further delve into the characterization of the systems studied during this PhD thesis.

Acknowledgements

There are so many people I wish to thank with all my heart for their support throughout this PhD. This thesis is as much yours as it is mine. Without you, it would not exist.

In four years, I have been so lucky to have worked with the best people ever.

First of all, I want to greatly thank Michaël, my supervisor. Thank you for trusting me with this project, and thank you for all the amazing opportunities it led me to. Being a part of the TRAPPIST and SPECULOOS teams was the best PhD experience I could have hoped for. Thank you for your guidance, your availability to read and correct my work, and your kindness.

I am so grateful to have shared an office with Laeti. Thank you for always answering even my dumbest questions with so much patience, and thank you for our deep conversations. Thank you for the daily support you've given me.

Lionel, thank you for everything. You have taught me so much, and you have been so patient with me struggling to code anything. I miss our coffee breaks and our chats. After years of work together, I am so happy to be able to call you a friend.

Elsa, thank you for being the best colleague a person could hope for. Your enthusiasm is contagious, and I absolutely love working with you. Thank you for your support during this thesis, and thank you for making us the dream team.

I want to deeply thank Fran for everything he has taught me. Thank you for being so kind and being so available whenever I struggled with an analysis. I am truly grateful to have had you as mentor for the TESS follow-up and TRAPPIST.

I wish to thank the TRAPPIST team. In particular, Manu, thank you for your trust and all the support you've given me during these last difficult months. I am also grateful to have shared with you the most unexpected experiences of this PhD: meeting royalty (on two occasions)!

Many thanks to the SPECULOOS team too, it was such a pleasure working with you all. Especially Amaury, thank you for allowing me to do so much in the WG6. I am so excited for the postdoc position, it will be amazing to be in Birmingham, and work with you as a supervisor! Thank you Julien for your support, for being so kind, and the amazing opportunity of visiting MIT for a month. I enjoyed it so much, I wish I could go back. Maybe someday.

A special thank you to Valérie. Your support and supervision in the last few months have been so important to me, I am truly grateful to have you in my thesis committee.

George. I could write a hundred pages to say all the things I am grateful for. I'll keep it simple: thank you for being one of the best human beings on this planet. You have taught me so much about science and about life. I never would have imagined I would meet one of my bestest friends during this PhD. Thank you for always being there for me, thank you for believing in me, and thank you for your unconditional support. We have had SO MANY adventures together, I hope it never stops.

I want to thank the rest of my colleagues in Liège, it was such a pleasure to be in a great team like ours. Especially, thank you Khalid, Seba, and Mourad, for the talks and the laughs. Thank you also to the +1 floor for allowing me to drink your coffee and use your kitchen. I want to especially thank Martin for always making me laugh, showing

me beautiful drawings, and just being one of the kindest person I've ever met. Thank you also to the rest of the astro gang: Antoine, Guillaume, Loïc, Linus, Manu, Mathieu, Eli, Camila, Gaël, Marc-Antoine, Michaël, Dominique, Maxime, ..., there are so many of you. Thank you for all the fun lunch breaks and the stimulating chats. I will stay in the WhatsApp group to get the daily fun fact, I could not eat lunch without it. I also want to thank the ones that have left already but are dearly missed, especially Clementine, Lyne, Charly, and Lorenzo.

I would never have made it through this thesis without the amazing support of my family. Thank you for giving me the opportunity to study and fail, study some more, and fail some more until it worked out. It was worth it. I love you so much.

To my friends, thank you for always being there to support me through the good and the bad times. I love you all.

Especially, the biggest thank you goes to Pauline. You have been the best supporter ever and I am so grateful to have you in my life. Thank you for making me laugh so hard I cry, thank you for all our adventures, thank you for being there in the darkest times. I truly don't know how I'll survive without seeing you every week. For that, I am thankful smartphones exist.

I wish to deeply thank Juliette L. too. I am so happy we reconnected in the past year and we got to spend more time together. Thank you for your unconditional support. Thank you for listening to me talk for hours, and thank you for always looking out for me.

Kelly, thank you for being there for me, always. Thank you for all the love and support. I love you to the moon and back.

Greg, thank you for being my first and best friend in Liège. Thank you so much for all our chats, all the pep talks you have given me, all the support in everything I do. I am truly so grateful to have you in my life.

Juliette S., thank you so much for our talks and your support in the last couple of years. They really meant the world to me.

A huge thanks to all the other important people that have been supporting me for years: Lucie, Sven, Sofia, Julie, Céline, Charlotte, the physicists, Miguel and Xavier. To all my new friends too, a huge thank you for making my time in Liège so fun and memorable: Manon, William, Dina, Amélie, the Guillaumes, Adri, Manu, and Vlad.

List of Abbreviations and Acronyms

2MASS Two Micron All-Sky Survey

ADU Analog Digital Unit

BD Brown Dwarf

BEB Blended Eclipsing Binary

BLS Box-Least Squares

BMA Bayesian Model Averaging

CARMENES Calar Alto high-Resolution search for M dwarfs with Exoearths with Near-infrared and optical Echelle Spectrographs

CCD Charged-Coupled Device

CoRoT Convection, Rotation and planetary Transits

CHEOPS CHaracterising ExOPlanets Satellite

CTIO Cerro Tololo Interamerican Observatory

CVZ Continuous Viewing Zone

DV Data Validation

EB Eclipsing Binary

ELODIE Echelle spectrograph for Low Dispersion and high resolution Optics with Infrared array detector and Echelle spectrometer

ELT Extremely Large Telescope

ESPRESSO Echelle Spectrograph for Rocky Exoplanet and Stable Spectroscopic Observations

ESO European Southern Observatory

ExTrA Exoplanets in Transit and their Atmospheres

FFI Full Frame Image

FPP False-Positive Probability

FORS2 FOcal Reducer and low dispersion Spectrograph 2

FWHM Full Width at Half Maximum

GP Gaussian Process

HARPS High Accuracy Radial velocity Planet Searcher

HATNet Hungarian Automated Telescope Network

HST Hubble Space Telescope

JWST James Webb Space Telescope

KMTNet Korea Microlensing Telescope Network

KPIC Keck Planet Imager and Characterizer

LCO Las Cumbres Observatory

LDSS-3 Low Dispersion Survey Spectrograph

MANGOs M dwarfs Accompanied by close-iN Giant Orbiters

MAROON-X Magellan AO Radial velocity Observations of Nearby eXoplanets

MCMC Markov Chain Monte Carlo

MD M Dwarf

MOA Microlensing Observations in Astrophysics

MuSCAT Multicolor Simultaneous Camera for studying Atmospheres of Transiting exoplanets

NACO Nasmyth Adaptive Optics System Near-Infrared Imager and Spectrograph

NEB Nearby Eclipsing Binary

NFPP Nearby False-Positive Probability

NGTS Next-Generation Transit Survey

NIRC2 Near InfraRed Camera 2

NIRPS Near InfraRed Planet Searcher

NPC Nearby Planet Candidate

OGLE Optical Gravitational Lensing Experiment

PDF Probability Distribution Function

PDC-SAP Pre-search Data Conditioning Simple Aperture

PSF Point Spread Function

QLP Quick Look Pipeline

RV Radial Velocity

RMS Root-Mean Square

SED Spectral Energy Distribution

SHERLOCK Searching for Hints of Exoplanets fRom Light curves Of spaCe-based seeKers

SPECULOOS Search for habitable Planets EClipsing ULtra-cOOl Stars

SAINT-Ex Search And characterIsatioN of Transiting EXoplanets

SDE Signal Detection Efficiency

S/N Signal-to-noise ratio

SPHERE Spectro-Polarimetic High contrast imager for Exoplanets REsearch

SPIRou SPectropolarimètre InfraROUge

SPOC Science Processing Operation Center

SNO SPECULOOS Northern Observatory

SSO SPECULOOS Southern Observatory

TFOP WG TESS Follow-up Observing Program Working Group

TCE Threshold Crossing Event

TIC TESS Input Catalog

TLS Transit Least Squares

TOI TESS Object of Interest

TESS Transiting Exoplanet Survey Satellite

TSM Transmission Spectroscopy Metric

TRAPPIST TRAnsiting Planets and PlanetesImals Small Telescope

TN TRAPPIST-North

TS TRAPPIST-South

TTV Transit Timing Variation

UCD UltraCool Dwarf

VLT Very Large Telescope

WASP Wide Angle Search for Planets

WFC3 Wide Field Camera 3

WISE Wide-field Infrared Survey Explorer

Contents

Chapter 1

Introduction

It is a humbling feeling to look up at a night sky full of stars. Our entire existence is placed in the context of a seemingly infinite universe: we are just tiny human beings on a tiny planet, orbiting around a not-so-tiny star along with seven other planets, in a kind-of-big spiral galaxy with a funny name: the Milky Way. It forms our immediate neighborhood and is made up of hundreds of billions of stars of all sizes. In fact, to get a sense of distance, our solar system lives in a region called the Orion Arm located about 27 000 light-years away from its center. Then, scaling our galaxy to the hundreds of billions of galaxies that populate the visible Universe makes us that much more insignificant. This perspective shifts our point of view and raises fundamental questions about our place in the Cosmos, the origin of life on Earth, and our behavior as an intelligent civilization: *how unique is our solar system? What were the conditions that led to the emergence of life? Could life develop on other planets too?*

The scientific implications are immense and span a wide range of fields. The most direct are addressed by geologists and biologists, who seek to understand how terrestrial life originated, how it evolved, and what conditions are necessary to sustain it. Astronomers approach the problem by finding new planetary systems and comparing their properties to those of the solar system. Finding new potentially *habitable* worlds is now a priority, as current technological capabilities make it possible to probe the atmospheres of terrestrial exoplanets. More generally, understanding how other worlds form and evolve gives us insights into the history of our own planetary system. This is precisely the goal of this thesis: to increase the sample of known exoplanets for which atmospheric characterization is possible. My work has focused on two flavors of planets, super-Earths and warm Jupiters orbiting low-mass stars. It involves the detection of such planets through the photometric follow-up of planetary candidates of NASA's Transiting Exoplanet Survey Satellite (TESS) space mission, and their characterization to infer their physical and atmospheric properties.

In this introductory chapter, I will first briefly describe the history of Exoplanetology, and the events that led to the development of the field. I will then focus on transiting exoplanets, explaining the fundamental equations and how transits are used as an indirect method of detection. I will discuss two ways to characterize a transiting planet: radial velocities and transmission spectroscopy. Finally, I will outline the rest of the thesis.

1.1 A brief history of exoplanets

In the 4th century B.C., the dominant theory for the structure of the Universe was the geocentric theory of the Greek philosopher Aristotle, according to which the Earth is a spherical body at the center of the universe around which all celestial bodies orbit. Because this meant that the Earth was unique, since there could not be multiple centers, the competing theory of multiple worlds developed by Epicurius and Democritus was severely criticized.

They believed that the universe consisted of infinite void and matter, with the consequence that there should be an infinite number of worlds. The geocentric outlook prevailed for centuries with the theory of Ptolemy which explained the orbits of celestial bodies around the Earth through a combination of two circular motions (deferent and epicycle).

In 1543, Nicolaus Copernicus triggered a paradigm shift with the publication of *De revolutionibus orbium coelestium*, that described the Sun as the center of the Universe around which the planets, including the Earth, revolved. Although controversial at the time, this heliocentric theory was the beginning of the Copernican revolution from which modern science emerged. In 1609, Galileo Galilei was the first to provide observational evidence in support of the heliocentric model. Equipped with one of the first telescopes, he made two important discoveries that discredited Ptolemy's geocentric model. The first was the four "Galilean" moons of Jupiter, now known to be the largest of just under a hundred. Their existence directly contradicted the fundamental principle of the geocentric theory that all celestial bodies should orbit the Earth. Second, he realized that Venus had a complete cycle of phases, similar to the Moon. This could only be explained if Venus revolved around the Sun, and on a shorter orbit than the Earth. The early 17th century was also marked by the publication of Johannes Kepler's three laws of planetary motion. These described the orbits of the planets as ellipses around the Sun and were based on the unprecedentedly accurate measurements of the orbit of Mars made by Tycho Brahe, an influential Danish astronomer. Similarly, the laws of motion and theory of Universal Gravitation established by Sir Isaac Newton in his book *Philosophiæ Naturalis Principia Mathematica* in 1687 are rightly regarded as the foundations of modern Physics. Building upon Kepler's insights, Newton unified the physical laws describing the motion of celestial bodies and motion on Earth.

As it became accepted that planets orbit the Sun, the idea that our system was unique began to be challenged. The Italian philosopher Giordano Bruno, in his book *De L'infinito Universo E Mondi*, published in 1584, proposed that fixed stars were actually other suns, producing their own light and heat, and having planets revolving around them. These "earths" are similar in nature to the Earth, but could not be seen because of their great distance and their small size compared to their sun. With the advancement of technology, observational claims of exoplanet detections started to be made in the late 1800s, but by the late 1900s, all were refuted.

The first proven detection of planets outside the solar system dates back to 1992 (Wolszczan & Frail, 1992). Aleksander Wolszczan and Dale Frail published the detection of anomalies in the timing of radio pulses from the millisecond pulsar PSR1257+12, and attributed them to two planetary-mass bodies. While the evidence was clear, the discovery was met with caution by the scientific community. Given the extreme environment of a neutron star, the formation and survival of a planet was not expected. The most likely hypothesis is that the planets formed in a disk of material in the supernova remnant that created the pulsar. Three years later, the discovery of a giant exoplanet orbiting a Sun-like star by the Swiss astronomers Michel Mayor and Didier Queloz was received with much more excitement (Mayor & Queloz, 1995). While observing the star 51 Pegasi with a spectrograph named ELODIE and located at the Haute-Provence Observatory, they measured a shift in the spectral lines of the star that could only be explained by the presence of a second body. This wobbling of the star around the system's center of mass induces Doppler shifts in the star's spectral lines that are sensitive to the companion's mass and distance from the star. This is known as the radial velocity (RV) technique, and it is now a very popular method for detecting exoplanets. Mayor and Queloz discovered the first of a new flavor of exoplanets, the *hot Jupiters*, with 51 Pegasi b, a Jupiter-sized planet orbiting its host star in just 4.2 days. It was a complete surprise given what we knew about giant planets from our solar system, so much so that this discovery revolutionized our understanding of exoplanets and launched

the field of Exoplanetology. For this groundbreaking work, Michel Mayor and Didier Queloz were awarded the 2019 Nobel Prize in Physics.

Since then, more than 5600 exoplanets[1] have been found, revealing a much broader panel of exoplanet types than we have as examples in our own system. In Figure 1.1 is shown the distribution of exoplanets according to the four main detection methods, with over 74% and 19% of exoplanet discoveries attributed to the transit method and the RV method, respectively. Both of these techniques will be described thoroughly in Section 1.2 and Section 1.3.1. Although the radial velocity method is a detection method, I will describe it in the context of characterizing transiting planets.

Like RV measurements, the transit method is indirect. When a planet passes in front of the star, it blocks some of the light emitted in our direction fading the apparent brightness of the star. This is called a *transit*, and it can be measured as a characteristic dip when the brightness of the star is monitored (see Section 1.2.2). This dip is proportional to the ratio of the surface area of the planetary disk to that of the star, making this method sensitive to the radius of the planet. Since the first detection of a transiting planet by Charbonneau et al. (2000) and Henry et al. (2000), a hot Jupiter orbiting a Sun-like star, this method has been the most productive for detecting extrasolar worlds. Essentially, this method allows the detection of planets down to sub-Earth sizes and it is biased towards the detection of planets with relatively short orbital periods, as will be discussed in Section 1.2.3. The RV method is also biased towards the detection of short-period planets, but less than the transit method. Furthermore, it is limited by stellar noise and instrument stability for the smaller Earth-like planets.

Direct imaging is the only method that provides images of the planets themselves, provided the contrast is high enough (for a full review of the method, see Traub & Oppenheimer, 2010). Capturing the light of an object so faint relative to its host star presents many challenges. Although technological advances in direct imaging are growing rapidly, the capabilities of this technique are still limited. As shown in the lower left panel of Figure 1.1, this method is currently most successful in detecting planets with large orbital periods.

Finally, microlensing has been used to discover more and more planets in recent years (e.g. Han et al., 2024; Rektsini et al., 2024). The principle is the same as that of gravitational lensing: when the alignment between a foreground star and a background star is favorable, the background object is magnified (see Gaudi, 2010, for a review of the technique). This is because the foreground star's gravitational field bends space-time, creating a gravitational lens that bends the light rays from the background star. Since it is not possible to distinguish the contribution of both sources, it appears as a large increase in brightness of the lens (foreground) star. If a planet is present around the lens star and it is positioned close enough to cross the light of the background star, it can act as a second lens and produce a third image of the background source. This results in a deviation from the regular magnification pattern with a short spike in brightness.

Figure 1.2 shows how each detection method has contributed to the total population of known exoplanets as a function of the year. For the first decade, early radial velocity surveys with high-resolution spectrographs such as the Lick Observatory Planet Search, the ELODIE or Keck Observatory surveys did pioneering work with the detection of the first extrasolar giant planets. The number of RV planets steadily grows thanks to the numerous new ultra-high-stabilization spectrographs such as HARPS (Mayor et al., 2003), or ESPRESSO (Pepe et al., 2014) located on the Very Large Telescope, providing exquisite precision in the visible spectral range. Other surveys target specifically M-dwarf stars which allow to reach into the rocky parameter space such as CARMENES (Reiners et al., 2018), MAROON-X (Seifahrt

[1]Data from NASA Exoplanet Archive, https://exoplanetarchive.ipac.caltech.edu/, accessed on June 17, 2024.

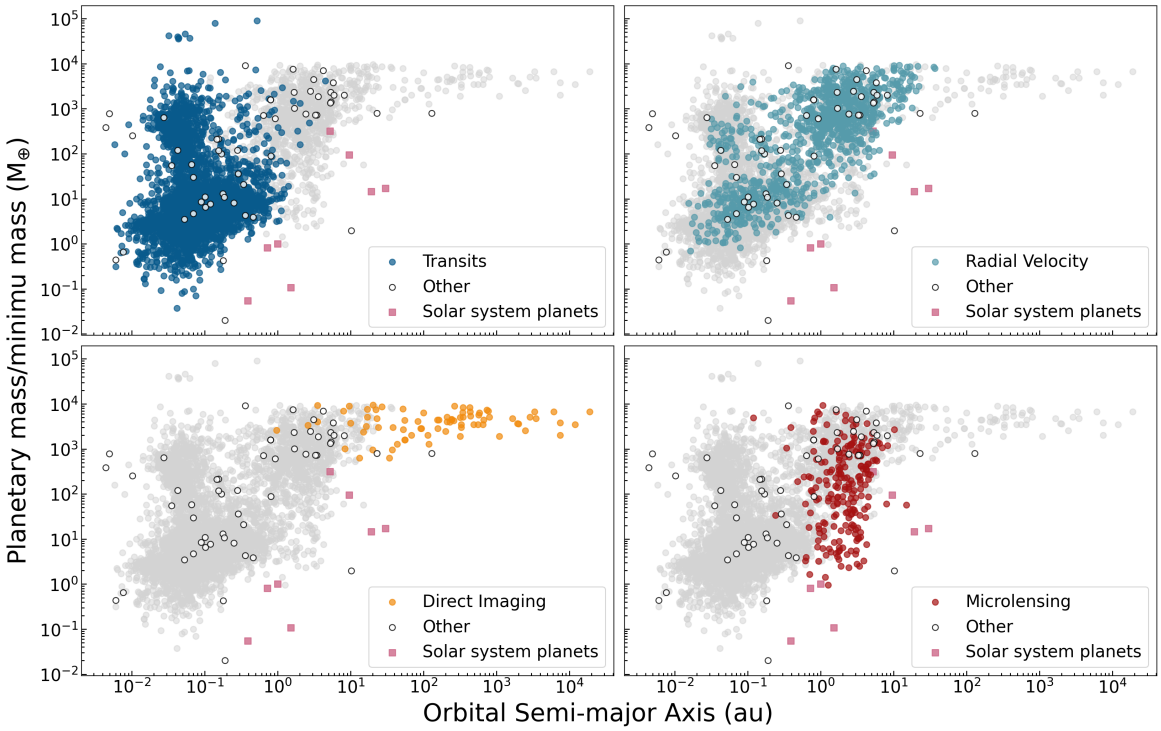

Figure 1.1: Distribution of the known exoplanets as a function of their mass or minimum mass (in Earth masses, $M_\oplus$) and orbital semi-major axis (in astronomical units, au). Each panel highlights those detected by one of the four leading techniques: transits, radial velocity, direct imaging, and microlensing. The contribution of the other methods is also highlighted by white circles, including astrometric variations, eclipse timing variations, pulsar timing variations, pulsation timing variations, orbital brightness modulations, and disk kinematics. The eight planets of the solar system are also added for comparison and represented by pink squares. This plot was made using data from the NASA Exoplanet Archive, accessed on June 17, 2024.

et al., 2020), SPIRou (Donati et al., 2018), or the recently commissioned NIRPS instrument (Wildi et al., 2017) observing fully in the near-infrared (NIR). The transit discoveries were pushed by the space-based Kepler/K2 (Koch et al., 2010) and TESS (Ricker et al., 2014) missions launched in 2009 and 2018, respectively. Both were specifically designed to hunt for transiting planets by monitoring the brightness of thousands of stars, and identifying dips attributable to planetary transits. In total, the yield of Kepler/K2 exceeds 3300 planets with still over 2000 candidates still to be confirmed. So far, the yield of TESS is already nearing 500 planets, with over 4600 candidates. Many ground-based transit surveys were also very successful, such as WASP (Pollacco et al., 2006) which allowed the discovery of many well-studies hot Jupiters, and HATNet (Bakos et al., 2004). Other high-precision photometry projects also focus on transiting planets around M dwarfs, like MEarth (Nutzman & Charbonneau, 2008) or NGTS (Wheatley et al., 2018). In particular, the SPECULOOS project searches for habitable zone terrestrial planets around the smallest red dwarfs, called ultracool dwarf stars (Delrez et al., 2018; Sebastian et al., 2021; Gillon, 2018; Jehin et al., 2018).

The first directly imaged exoplanet-mass object was 2M1207 b in 2005 with the NACO instrument on the VLT (Chauvin et al., 2005). Since then, more than 80 exoplanet-mass objects have been studied with various instruments such as the Gemini Planet Imager, NIRC2 and KPIC at Keck Observatory, or SPHERE also on the VLT (e.g. Marois et al., 2008;

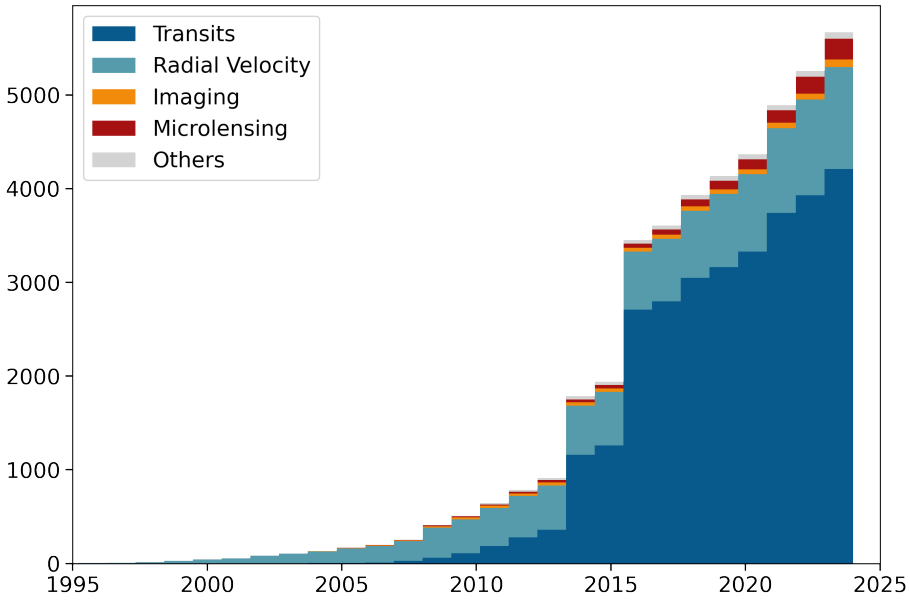

Figure 1.2: Cumulative distribution of exoplanets according to the discovery year. The color code indicates the discovery method. The transit and radial velocity methods are the ones which contributed most to the current population of known exoplanets. The data is obtained from the NASA Exoplanet Archive, accessed on June 17, 2024.

Currie et al., 2012; Keppler et al., 2018). The upcoming Extremely Large Telescope will also potentially allow for the imaging of habitable zone planets (Brandl et al., 2016).

The microlensing technique has yielded over 200 detections. This method allows to reach far into the Galaxy, probing a specific parameter space, though the prospects for atmospheric characterization of such distant planets are limited (Rektsini & Batista, 2024). Indeed, microlensing events are difficult to re-observe as they require a very specific alignment, and the apparent faintness of the host stars make it unlikely to allow the use of another detection or characterization method. The three main projects focusing on this method are OGLE (Udalski et al., 1992), MOA (Bennett et al., 2012) and KMTNet (Kim et al., 2016). The ESA Euclid mission (Laureijs et al., 2011) and the upcoming Nancy Grace Roman Space Telescope (Johnson et al., 2020) include microlensing surveys which should allow for the detection of many new planets (e.g. Johnson et al., 2020; Bachelet et al., 2022).

Having access to such a large pool of confirmed exoplanets allows us to delve into the fundamental scientific questions that drive exoplanet research, such as the search for traces of life outside the solar system. In 2002, Charbonneau et al. (2002) used the Hubble Space Telescope (HST) to observe a planetary transit of HD 209458 b simultaneously in twelve bands spanning the UV to the near-infrared. They obtained variations of the transit depths corresponding to the absorption feature of sodium. This was the first detection of an exoplanet atmosphere with transmission spectroscopy (see Section 1.3.2), which is now the most widely used method to characterize atmospheres. Water vapor, one of the most searched atmospheric components, was detected for the first time on the Neptune-sized planet HAT-P-11 b in 2014 (Fraine et al., 2014). A few years later, its detection on the habitable zone sub-Neptune K2-18 b was particularly intriguing (Benneke et al., 2019), as it was the first detection of this kind for such a small and temperate planet. Previous attempts had led to featureless spectra attributed to the presence of clouds (e.g. Kreidberg et al., 2014). With the launch of the James Webb Space Telescope (JWST Gardner et al., 2006) in December 2021, we have entered a new era of atmospheric characterization. Its incredible precision and

its wide spectral coverage extending from the visible to the mid-infrared now allows to search for atmospheres around temperate Earth-sized planets, such as the TRAPPIST-1 planets (Gillon et al., 2016, 2017).

1.2 Transiting planets

1.2.1 Geometry of transiting systems

The motion of a planet around a star can be described by the two-body problem, each exerting a gravitational force on the other. Following Newton's universal law of gravitation, it can be shown that the motion resulting from such a system, if closed, is an ellipse (see Murray & Correia, 2010, for the derivation). All planetary systems obey Kepler's three laws of motion: both the star and planet orbit a common center of mass located at one of the foci following an elliptical motion. In the heliocentric system, the star is at one of the foci and the planet orbits around it following an elliptical motion. This section is based on Winn (2010), and Perryman (2018).

The geometry of the orbital plane is shown in Figure 1.3 as viewed from above. The trajectory of the planet along the orbit is described by Equation 1.1 in polar coordinates, centered on the star at one of the focus points F, with a the semi-major axis, and e the eccentricity of the system:

$$r = \frac{a(1-e^2)}{1+e\cos f}, \tag{1.1}$$

with the distance between the star and the planet given by r, and f the angle between the periastron (also called the periapsis, the point of minimum distance) and the planet's position, also called the *true anomaly*. Contrary to the semi-major axis a and the eccentricity e, the distance r and true anomaly f are functions of time and vary as the planet moves along its orbit.

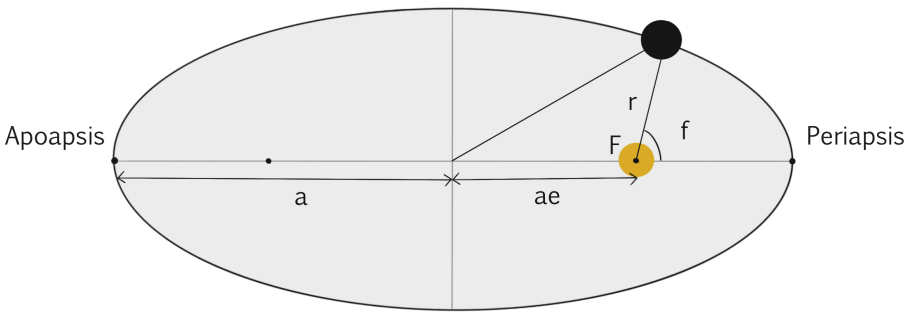

Figure 1.3: Two-dimensional view of the elliptical orbit of a planetary system. The planet is represented by the full black circle, and the star by the yellow one. The star is placed at the focus F of the ellipse, the star-planet distance is noted r, and the semi-major axis a. The eccentricity is e, and f is the true anomaly.

Considering the problem in three dimensions, the orbital motion of the planet is fully described by seven parameters:

- a, the semi-major axis.

- e, the eccentricity ($0 < e < 1$).
- P, the orbital period of the planet given by Kepler's third law:

$$P^2 = \frac{4\pi^2}{GM} a^3, \tag{1.2}$$

  with G the universal gravitational constant and M the mass of the star.
- t_p, the pericenter crossing time.
- i, the orbital inclination with respect to the reference frame ($0 < i < 180°$), with $i = 0$ corresponding to a face-on orbit.
- Ω, the longitude of the ascending node, where the planet crosses the reference frame moving towards the observer.
- ω, the argument of periastron, which is the angle between the periastron and the ascending node, measured in the orbital plane.

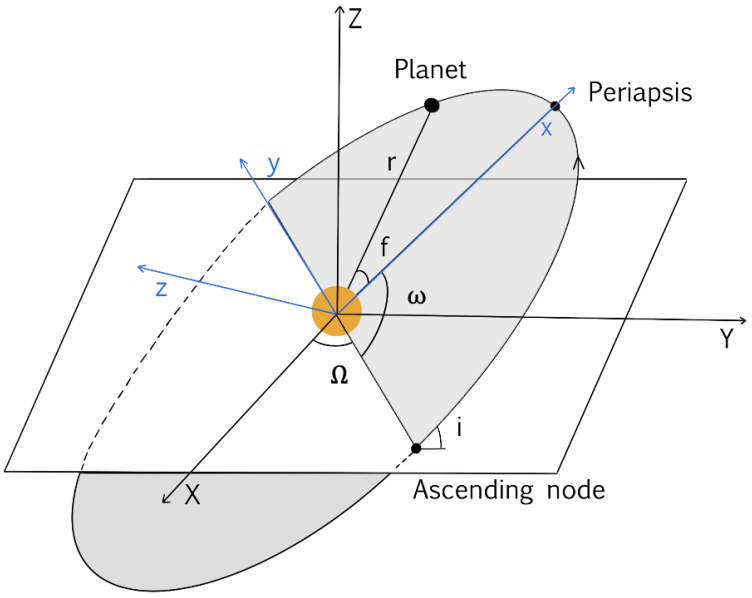

Figure 1.4: Three-dimensional view of the elliptical orbit. The orientation of the orbital plane is described by the orbital inclination i, the angle between the reference plane and the orbital plane, and the longitude of the ascending node Ω, the angle between the reference direction and the ascending node. The latter is the point where the planet crossed the reference plane along the reference direction. The argument of periastron ω is the angle between the periastron and the ascending node. Figure adapted from Figure 4 of Murray & Correia (2010) and Figure 2.2 from Perryman (2018).

The shape and size of the elliptical orbit are described by a and e, and the angles i, Ω, and ω are the three angles used to describe the orientation of the orbital plane. To resolve the position of the planet from any coordinate system centered on the star, we evaluate the transformation from the orbit coordinate system to a reference one. As illustrated in Figure 1.4, let us consider a coordinate system for the orbit (x,y,z) with the semi-major axis along the x-axis, the y-axis being perpendicular and including the orbit, and the z-axis

forming a right-handed orthonormal system. The ellipsoidal motion of the planet is then confined to the $x-y$ plane. We choose the reference system (X,Y,Z) depicted in Figure 1.4 with the reference direction set along the X-axis, and also an orthonormal right-handed system such that all directions are perpendicular to each other. In the (X,Y,Z) coordinate system, one can express the position of the planet (x,y,z) by a series of three rotations:

- a rotation of angle ω about the z-axis so that the x-axis coincides with the line joining the ascending node to the star,
- a rotation of angle i about the x-axis so that the planes $x-y$ and $X-Y$ are matching,
- a rotation of angle Ω to finally make the axes correspond.

These can be represented by two 3×3 rotation matrices, noted $\boldsymbol{P}_x(\phi)$ and $\boldsymbol{P}_z(\phi)$ for an angle ϕ along the x- and z-axes:

$$\boldsymbol{P}_x(\phi)=\begin{pmatrix}1&0&0\\0&\cos\phi&-\sin\phi\\0&\sin\phi&\cos\phi\end{pmatrix}\quad\text{and}\quad\boldsymbol{P}_z(\phi)=\begin{pmatrix}\cos\phi&-\sin\phi&0\\\sin\phi&\cos\phi&0\\0&0&1\end{pmatrix}. \tag{1.3}$$

The transformations are then:

$$\begin{pmatrix}x\\y\\z\end{pmatrix}=\boldsymbol{P}_z(\Omega)\boldsymbol{P}_x(i)\boldsymbol{P}_z(\omega)\begin{pmatrix}X\\Y\\Z\end{pmatrix}\quad\text{and}\quad\begin{pmatrix}X\\Y\\Z\end{pmatrix}=\boldsymbol{P}_z^{-1}(\omega)\boldsymbol{P}_x^{-1}(i)\boldsymbol{P}_z^{-1}(\Omega)\begin{pmatrix}x\\y\\z\end{pmatrix}, \tag{1.4}$$

with the inverse matrices $\boldsymbol{P}_x^{-1}(\phi)=\boldsymbol{P}_x(-\phi)$ and $\boldsymbol{P}_z^{-1}(\phi)=\boldsymbol{P}_z(-\phi)$.

For coordinates within the orbital plane, $x=r\cos f$, $y=r\sin f$, $z=0$. In the reference plane (X,Y,Z), the coordinates then become:

$$\begin{aligned}X&=r(\cos\Omega\cos(\omega+f)-\sin\Omega\sin(\omega+f)\cos i),\\Y&=r(\sin\Omega\cos(\omega+f)+\cos\Omega\sin(\omega+f)\cos i),\\Z&=r\sin(\omega+f)\sin i.\end{aligned} \tag{1.5}$$

Because we do not know the absolute orientation of the orbit in the case of a transiting system, Ω is unknown. We can then choose to align the node line with the X-axis, $\Omega=\pi$, Equation 1.5 simplifies as:

$$\begin{aligned}X&=-r\cos(\omega+f),\\Y&=-r\sin(\omega+f)\cos i,\\Z&=r\sin(\omega+f)\sin i.\end{aligned} \tag{1.6}$$

For an observer placed along the Z-axis, the sky corresponds to the $X-Y$ plane. For an eclipse to occur, the planet should pass in front of the star as seen by the observer, i.e. the projected distance on the plane of the sky should be minimal. We define the sky projected distance as $r_{sky}\equiv\sqrt{X^2+Y^2}$, and using Equation 1.6 with Equation 1.1:

$$\begin{aligned}r_{sky}=&\sqrt{r^2\cos^2(\omega+f)+r^2\sin^2(\omega+f)\cos^2 i},\\=&\frac{a(1-e^2)}{1+e\cos f}\sqrt{1-\sin^2(\omega+f)\sin^2 i}.\end{aligned} \tag{1.7}$$

We define the conjunction points at $X = 0$. If the planet is in front of the star from the observer's point of view with $Z > 0$, we call it *inferior*, if $Z < 0$ and the planet passes behind the star, we call it *superior*. In the case of a transit, $f = \pi/2 - \omega$. We define the transit impact parameter b as the sky-projected distance between the centers of the planet and the star at inferior conjunction:

$$\begin{aligned} b =& \frac{a(1-e^2)}{R_\star(1+e\sin\omega)}\sqrt{1-\sin^2 i}, \\ =& \left(\frac{a\cos i}{R_\star}\right)\left(\frac{1-e^2}{1+e\sin\omega}\right). \end{aligned} \tag{1.8}$$

It is illustrated in Figure 1.5 in the case of a circular orbit.

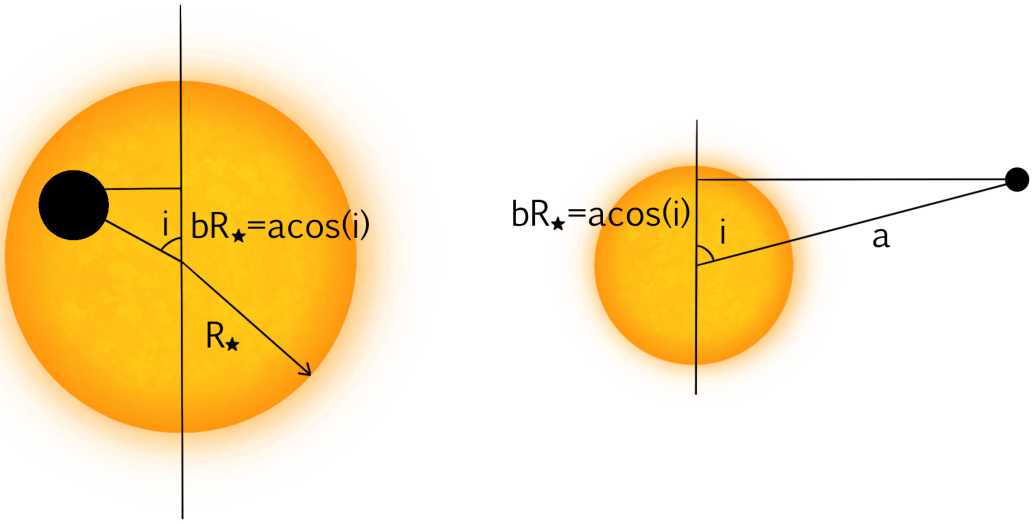

Figure 1.5: Illustration of the geometry of the transit from an observer's point of view (left) and side view (right). The transit occurs when the planet disk crosses the stellar disk. The parameters shown are: a the semi-major axis of the orbit, i the inclination of the orbital plane, $R_\star$ the stellar radius and b the impact parameter. Figure adapted from Figures 3.2 and 3.3 of Haswell (2010).

From this, we can define a geometric condition for a transit to happen from the point of view of an observer:

$$\begin{aligned} & a\cos i < R_p + R_\star, \\ \Leftrightarrow\ & |b| < 1 + \frac{R_p}{R_\star}. \end{aligned} \tag{1.9}$$

The transit is in a grazing configuration if $1 - R_p/R_\star < |b| < 1 + R_p/R_\star$ and full, i.e. the full disk of the planet is inscribed in the stellar disk, if $|b| \leq 1 - R_p/R_\star$. Using Equation 1.8, we can write Equation 1.9 like:

$$|\cos i| < \frac{R_p + R_\star}{a}\left(\frac{1+e\sin\omega}{1-e^2}\right). \tag{1.10}$$

Integrating Equation 1.10 along the full parameter range of possible values of cos$i$ (0 to 1) to consider a randomly placed observer, we define the transit probability, for full or grazing

configurations, as:

$$p_{tra} = \left(\frac{R_p + R_\star}{a}\right)\left(\frac{1 + e\sin\omega}{1 - e^2}\right). \tag{1.11}$$

In the case of a circular orbit and assuming $R_p << R_\star$, this expression simplifies to $p_{tra} \simeq \frac{R_\star}{a}$.

1.2.2 Transit light curves

Time-series photometry is the technique used to monitor the flux of a star as a function of time, graphically represented by a light curve. As a transit occurs, the apparent flux from the host star of the system drops following a U-shape in the case of non-grazing transits, and V-shape in the case of grazing transits. It is characterized by four observable quantities as described in Seager & Mallén-Ornelas (2003): the transit depth ΔF, the total transit duration t_T, the full transit duration t_F, and the orbital period P. These parameters are illustrated in Figure 1.6.

If we assume we have two consecutive transits and no significant perturbations from other bodies, the orbital period P is simply the time elapsed between the two. As the planet passes in front of the star, four contact points can be defined: t_1 occurs when the planetary disk comes into contact with the stellar disk, t_2 when the planet has fully entered the stellar disk, t_3 when it starts to leave it, and t_4 when the edge of the planetary disk loses contact with the stellar disk. The ingress and egress times are defined by the duration between t_1 and t_2, and t_3 and t_4, respectively. In the case of a grazing transit, the second and third contact points do not exist. The full transit duration is the duration of the flat part of the transit, between the ingress and egress: $t_F = t_3 - t_2$, and the total duration is $t_T = t_4 - t_1$.

Geometrically, we can set the sky projected distance to $R_\star \pm R_p$ in Equation 1.7 and retrieve the true anomaly f at the four contact points (the derivation can be found in Winn, 2010). Integrating over the range of true anomalies, and using Kepler's second law of planetary motion, we get:

$$t_T = \frac{P}{\pi}\sin^{-1}\left(\frac{R_\star}{a}\frac{\sqrt{(1+\frac{R_p}{R_\star})^2 - b^2}}{\sin i}\right)\frac{\sqrt{1-e^2}}{1+e\sin\omega}, \tag{1.12}$$

$$t_F = \frac{P}{\pi}\sin^{-1}\left(\frac{R_\star}{a}\frac{\sqrt{(1-\frac{R_p}{R_\star})^2 - b^2}}{\sin i}\right)\frac{\sqrt{1-e^2}}{1+e\sin\omega}. \tag{1.13}$$

The transit depth corresponds to the decrease of the flux of the host star as the planet blocks a fraction of the light. It can be written as $\Delta F = \frac{F_{oot} - F_t}{F_{oot}}$ with F_{oot} the out-of-transit flux of the host star and F_t the flux as the planet is transiting. This can be expressed in terms of surface brightness F_s:

$$\begin{aligned} F_{oot} &= F_{s,\star}\pi R_\star^2 + F_{s,p}\pi R_p^2, \\ F_t &= F_{s,\star}(\pi R_\star^2 - \pi R_p^2) + F_{s,p}\pi R_p^2, \\ \Rightarrow \Delta F &= \frac{F_{s,\star}\pi R_p^2}{F_{s,\star}\pi R_\star^2 + F_{s,p}\pi R_p^2}. \end{aligned} \tag{1.14}$$

where $F_{s,\star}$ and $F_{s,p}$ are the surface fluxes of the star and planet, respectively. Assuming $F_{s,p}\pi R_p^2$ is negligible compared to $F_{s,\star}\pi R_\star^2$, which is a reasonable assumption given the temperature and size differences between the planet and its host star, we can simplify the expression to:

$$\Delta F \simeq \left(\frac{R_p}{R_\star}\right)^2. \tag{1.15}$$

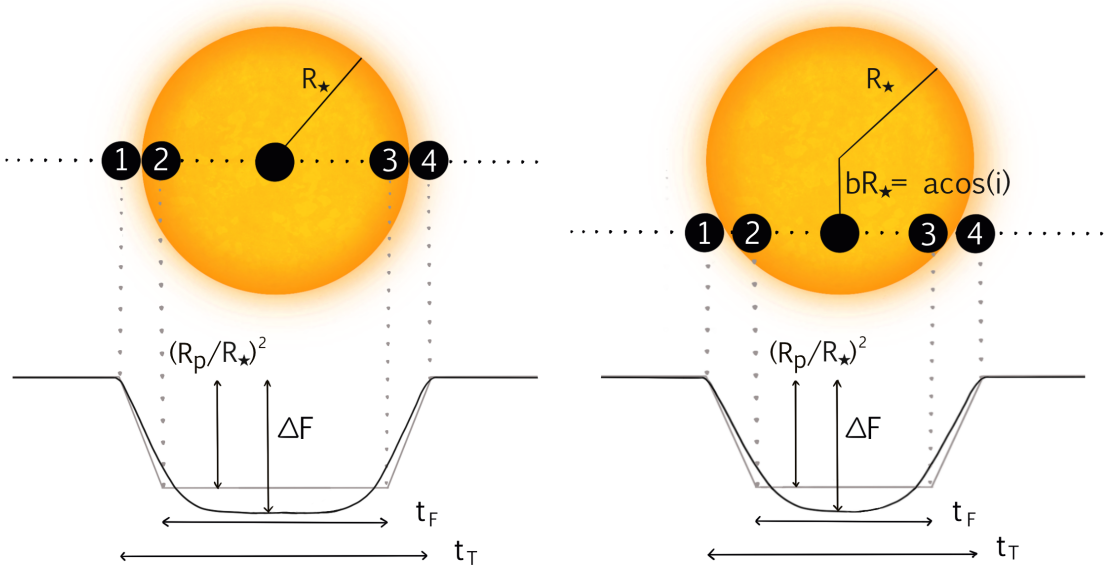

Figure 1.6: Illustration of a planetary transit with an orbital inclination $i = 90°$ on the left, and $i \neq 90°$ on the right. The bottom parts of the figures represent the flux as a function of time. The gray line shows the transit light curve in the case of a uniform stellar disk and the solid black line shows the transit with a limb darkening of the star. The dotted lines give the four contact points, the ingress is the drop of flux between t_1 and t_2 as the planet disk enters the stellar disk and begins to occult part of its light, and the egress is the increase of flux as the planetary disk exits the stellar disk. Figure adapted from Seager & Mallén-Ornelas (2003).

We should note this expression is valid only when the limb darkening effect of the star is neglected (see below).

From the four observable quantities ΔF, t_T, t_F, and P, five physical quantities can be derived: the stellar mass $M_\star$, the stellar radius $R_\star$, the semi-major axis of the orbit a, the orbital inclination i, and the radius of the planet R_p. The full derivation is presented in Seager & Mallén-Ornelas (2003). Here, I only give the resulting simplified equations relating the observables to the physical parameters under the assumptions of a circular orbit and that $R_\star << a$:

$$\frac{R_p}{R_\star} = \sqrt{\Delta F}, \tag{1.16}$$

$$b = \sqrt{\frac{(1-\Delta F)^2 - (t_F/t_T)^2(1+\Delta F)^2}{1-(t_F/t_T)^2}}, \tag{1.17}$$

$$\frac{a}{R_\star} = \frac{2P}{\pi}\frac{\Delta F^{1/4}}{\sqrt{t_T^2 - t_F^2}}, \tag{1.18}$$

with Equation 1.16 resulting directly from Equation 1.15, and Equation 1.17 being the combination of Equation 1.13 and Equation 1.12. The ratio $\frac{a}{R_\star}$ of Equation 1.18 comes from Equation 1.12 under the approximation $t_T\pi/P \ll 1$. The inclination i can be determined from $b = \frac{a}{R_\star}\cos i$. If we consider that $M_p << M_\star$, we can get access to the stellar density $\rho_\star \equiv \frac{M_\star}{R_\star^3}$ through Kepler's third law. From Equation 1.2, we can write:

$$\begin{aligned} a &= \left(\frac{P^2 G M_\star}{4\pi^2}\right)^{1/3}, \\ \Rightarrow \frac{a^3}{R_\star^3} &= \left(\frac{P^2 G}{4\pi^2}\right)\frac{M_\star}{R_\star^3}, \\ \Leftrightarrow \rho_\star &= \frac{4\pi^2}{P^2 G}\left(\frac{a}{R_\star}\right)^3. \end{aligned} \tag{1.19}$$

Injecting Equation 1.18 in this result gives:

$$\rho_\star = \frac{32}{G\pi}P\frac{\Delta F^{3/4}}{(t_T^2 - t_F^2)^3/2}. \tag{1.20}$$

So far, we have considered the star as a homogeneous and uniform disk. This is useful to grasp how the geometry of transiting systems can be linked to physical parameters. However, this neglects the effect of limb darkening which induces a gradual decrease in brightness from the center to the edges of the stellar disk. The light is propagated radially from the center of the star to the stellar atmosphere, and an observer sees the light emerging from the star at an angle θ with respect to the radial direction (see Figure 1.7). At a frequency ν, the light mostly originates from the atmospheric layers corresponding to an optical depth of $\tau_\nu = 1$, defined as:

$$\tau_\nu(x) = \int_x^\infty \kappa_\nu(s)\rho(s)ds. \tag{1.21}$$

with $\tau_\nu(x)$ the optical depth integrated over a column from the stellar surface down to the deepest layers, κ_ν the absorption coefficient of the column of material considered at the wavelength ν and ρ its density. Figure 1.7 illustrates how an optical depth of $\tau_\nu = 1$ corresponds to higher altitude layers of the atmosphere as θ increases. At the center, the light is emitted by the layer A which is deep in the star. The primary emitting layers corresponding to $\tau_\nu = 1$ get cooler, and thus dimmer, as we increase θ and as we move towards the limb of the star, creating this gradual decrease in flux.

The effect of limb darkening on a transit light curve is two-fold: (1) it changes the shape of the transit by making the ingress and egress rounder, (2) it increases or decreases the apparent transit depth ΔF as a function of the impact parameter, as illustrated in Figure 1.8. The limb darkening effect is wavelength dependent and appears more and more pronounced at wavelengths shorter than 1 μm. This dependence is directly related to the wavelength-dependent contrast between the emission of two atmospheric layers of different temperatures. Assuming a Planck function as the source function for the two layers, this contrast is proportional to $1/\lambda^4$, which is why we see a larger effect at shorter wavelengths.

The stellar limb darkening can be modeled analytically by a function linking the surface intensity at the center of the disk of the star and the surface intensity at any given angle θ. The most widely used expression is the quadratic limb darkening law, expressed as:

$$\frac{I(\mu)}{I(1)} = 1 - u_1(1-\mu) - u_2(1-\mu)^2. \tag{1.22}$$

where $I(1)$ is the surface intensity at the center of the disk, u_1 and u_2 are the quadratic limb darkening coefficients, and $\mu = \cos\theta$. They are computed using stellar atmospheric models

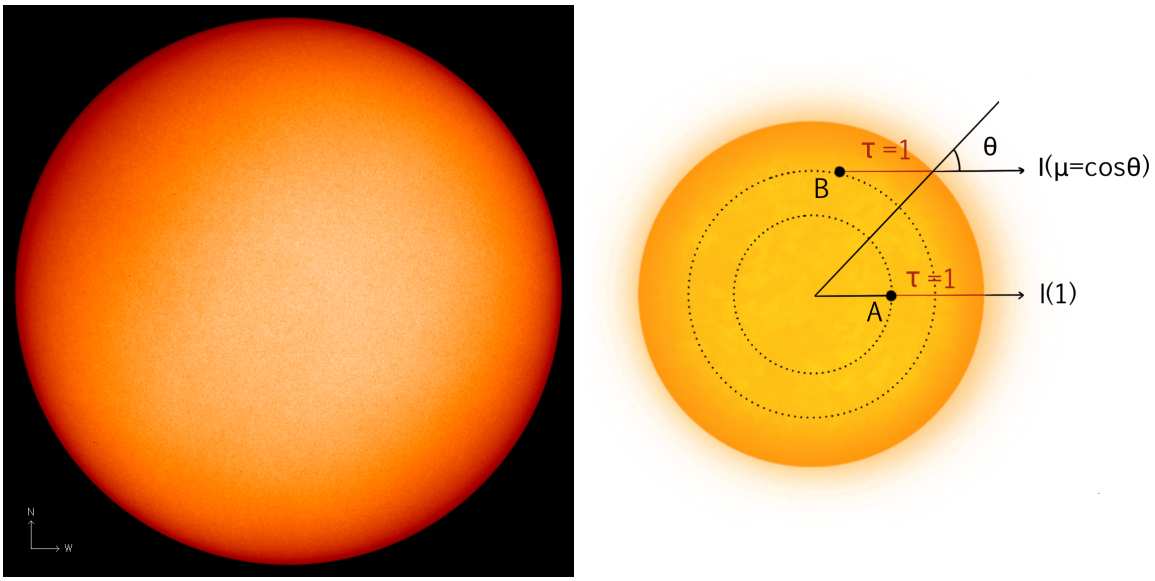

Figure 1.7: On the left: image of the Sun obtained with SOHO (ESA/NASA) taken during a minimum of the solar cycle on March 18 2009. On the right: illustration of the limb darkening effect. The dotted lines represent atmospheric layers at different altitudes. θ is the angle between the direction to the observer and the normal to the stellar surface, and μ is $\cos(\theta)$. In all cases, light emitted towards the observer originates mostly from a layer corresponding to an optical depth $\tau = 1$. For $\mu = 1$ and $\mu < 1$, light emitted towards the observer originates thus mostly from layers A and B, respectively. As the outer layers are cooler than the deeper ones, the light of the star appears darker for increasing θ and $I(1) > I(\mu)$, with I being the light's intensity at the surface of the star. Figure adapted from Haswell (2010).

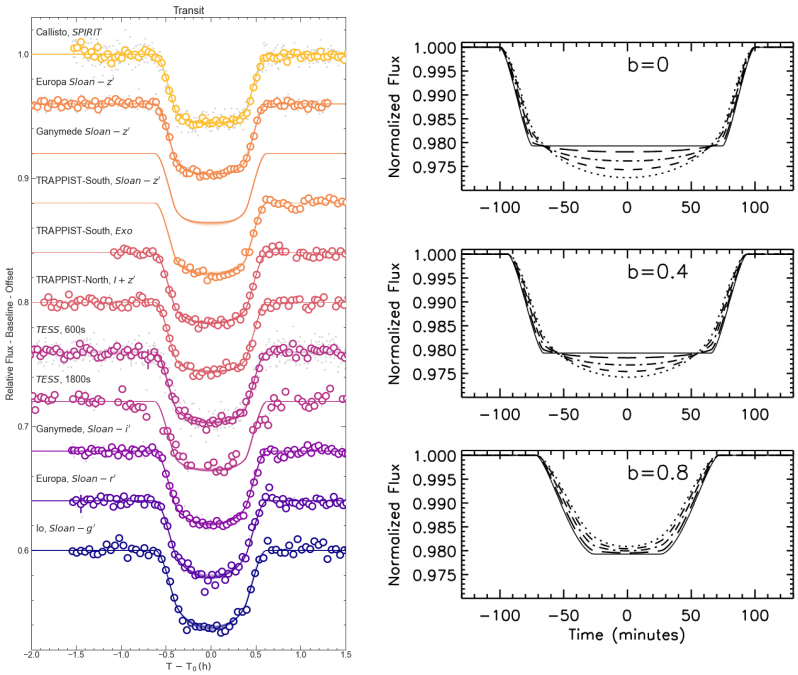

Figure 1.8: On the left: effect of wavelength-dependent limb darkening on the transit of TOI-4860 b (Figure 1 of Triaud et al., 2023). The filters used in this study cover the range 0.4-1.1μm. As the filters go towards the blue, with the bluest being *Sloan-g'*, the bottom of the transit gets a rounder shape due to the stellar limb darkening effect. On the right: effect of stellar limb darkening for a range of impact parameters (Figure 11 of Seager & Mallén-Ornelas, 2003). The solid line corresponds to the transit model neglecting the limb darkening, and the various dashed lines correspond to limb-darkened transit models at 3, 0.8, 0.55, and 0.45 μm with fixed limb darkening coefficients.

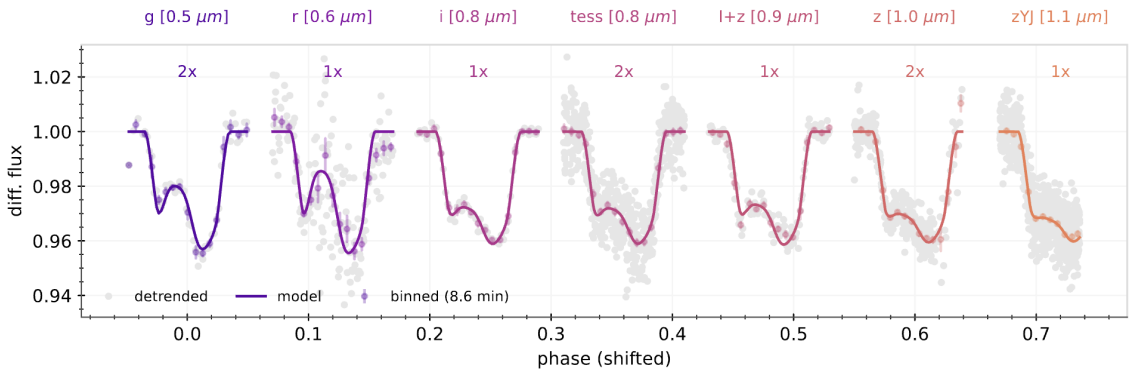

Figure 1.9: Photometry of the transit of TOI-3884 b obtained in various filters with SSO. With a wavelength range from 0.4 to 1.1 μm, the spot crossing is clearly chromatic, with amplitudes going from $\sim$ 30 ppt in the *Sloan-r'* band to $\sim$ 10 ppt in the zYJ band. Figure provided by Lionel Garcia.

(e.g. Claret et al., 2012). Taking into account this effect increases the complexity of the transit light-curve equations, yet it is critical to avoid biases in the observed parameters t_T, t_F, and ΔF. Especially, the impact parameter b is the most sensitive to limb darkening because of the apparent decrease of t_F which causes its overestimation (Seager & Mallén-Ornelas, 2003). In turn, this causes an underestimation of the stellar density and an overestimation of the planetary radius. Mandel & Agol (2002) derived the equations in the case of a limb-darkened stellar disk, and these are generally the ones used in transit fitting models.

In addition to the stellar limb darkening, the stellar surface may also exhibit active regions. These heterogeneities of the stellar photosphere can appear as spots or faculae. Spots are observed when the star's magnetic field is inhibiting convection of the plasma, it causes the region to become cooler and appear darker (Parker, 1955). Faculae are produced by an enhancement of the magnetic field which increases convection, they appear as brighter and hotter spots (Spruit, 1976). For a transiting planet, crossing an active region produces a signature on the light curve which can deform the transit and make the determination of the physical parameters difficult (Oshagh et al., 2013). One example is TOI-3884 b, a super-Neptune planet orbiting a low-mass star with a likely giant polar spot (Almenara et al., 2022; Libby-Roberts et al., 2023). Figure 1.9 shows the photometry gathered with the SPECULOOS-Southern Observatory to characterize the spot. By its nature, the spot has a different spectrum than the rest of the photosphere and it is then possible to estimate its temperature from multi-band observations. It is important to note that TOI-3884 b represents an extreme case, and most spot crossings are less noticeable. Still, if the signal-to-noise ratio is high enough, spots can perturb a chromatic analysis if they are present in the transit by biasing the measurement of the observable quantities t_T, t_F, and ΔF.

Finally, we have considered until now a transiting system as a two-body system with a planet orbiting a host star. In this configuration, the dynamics of the system are ruled by Kepler's laws. However, in the case of multi-planetary systems, dynamical interactions between the planets can lead to a deviation of the Keplerian orbits (Agol & Fabrycky, 2018). It implies a loss of periodicity of the orbit and thus a shift in the transit timings compared to the linear predictions, called Transit Timing Variations (TTVs). As TTVs are a result of dynamical interactions, they are sensitive to the masses involved. In particular, planets near or in mean motion resonance where their orbital periods are commensurate, i.e. they are related by a ratio of integer numbers, produce the largest TTVs by exchanging angular momentum at conjunction. TTV fitting is now a popular method of characterizing transiting

systems as they give access to the dynamical masses, which can be out of reach of radial velocities in some cases. It can also be used as a detection method for additional non-transiting planets (e.g. Almenara et al., 2024; Greklek-McKeon et al., 2023; Agol et al., 2021).

1.2.3 The M dwarf opportunity

M-dwarf stars occupy the lower end of the main sequence in the Hertzsprung-Russel diagram, down to the hydrogen-burning limit. With masses between 0.08 and 0.6 $M_{\odot}$ and radii between 0.1 and 0.6 $R_{\odot}$, they are the smallest and faintest main sequence stars, as shown in Figure 1.10.

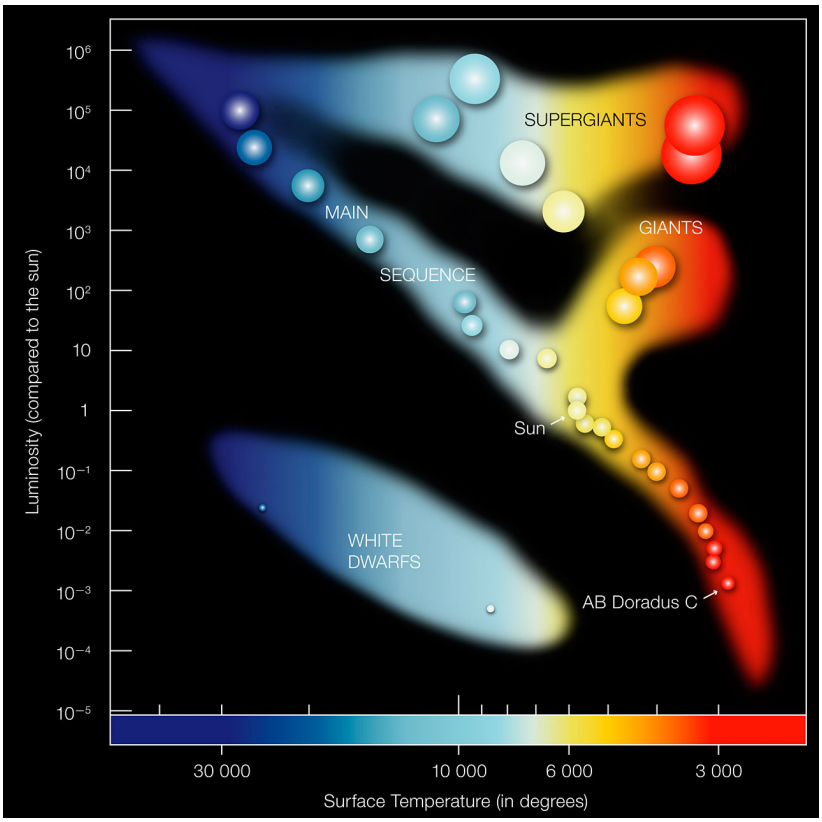

Figure 1.10: Hertzsprung-Russel diagram showing the stellar effective temperature as a function of the luminosity. It highlights the different categories of stars. M dwarfs occupy the bottom of the main sequence, i.e. the faint and cool corner on the right of the diagram. Image credit: ESO.

Also called red dwarfs, or low-mass stars, they are ubiquitous in the solar neighborhood as they make up over 70% of the galactic population (Winters et al., 2015). Because of their small masses and sizes, M-dwarf stars have a low hydrogen burning rate which grants them a long lifetime that can reach thousands of billions of years for the lowest-mass specimens. These facts explain why M-dwarf stars present the best opportunity for exoplanet detection and characterization. Indeed, the small sizes mean that for a given planet size, a transit signal is 100 times larger for a 0.1 $R_{\odot}$ star than for a solar-like star, and its atmospheric features in transmission are also enhanced (see Section 1.3.2). Additionally, the orbital period of a planet receiving a given amount of flux is also much smaller for a red dwarf because of their low luminosity. This increases the number of transits that can be obtained, thus increasing the signal-to-noise ratio and the efficiency of the detection. Since the transit probability scales

with $\frac{R_\star}{a}$, as given in Equation 1.11, a habitable zone planet orbiting an M dwarf is also more likely to transit. Similarly, the semi-amplitude of the radial velocity of the star is inversely proportional to the mass of the star and the period of the planet (see Section 1.3.1). Given the current technological capabilities for the stabilization of spectrographs, bright M dwarfs represent the best possibility for finding and accurately characterizing Earth-mass planets (e.g. Pepe et al., 2021; Reiners et al., 2018).

Finally, from the Kepler sample, Mulders et al. (2015a) has shown that the occurrence rate of small planets with radii between 1 and 4 $R_\oplus$ for orbital periods under 50 days is twice as high for M dwarfs (with $T_{\text{eff}} < 3865K$) than G stars, and thrice for F stars. Many space-based and ground-based surveys such as the MEarth project (Nutzman & Charbonneau, 2008), the SPECULOOS project (Delrez et al., 2018; Sebastian et al., 2021), CARMENES (Reiners et al., 2018), SPIRou (Donati et al., 2018), NIRPS (Wildi et al., 2017), and TESS (Ricker et al., 2014) are now focusing on M dwarfs.

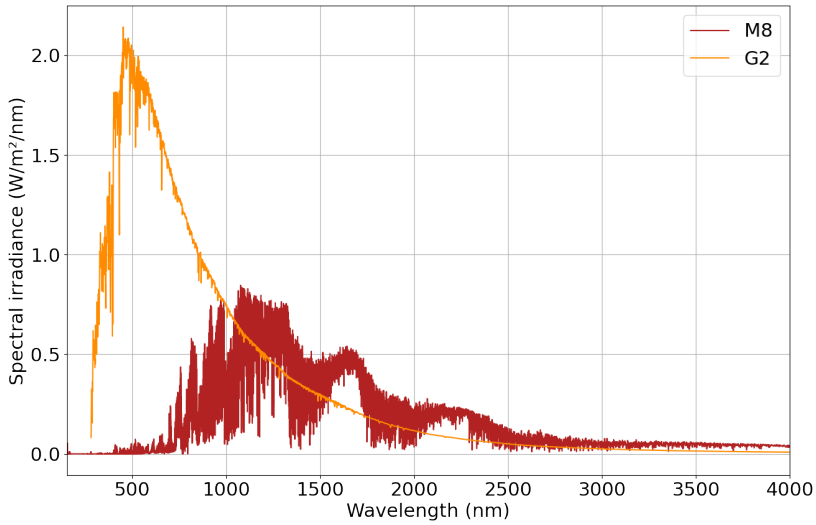

Figure 1.11: Comparison of the stellar spectrum of a G2-type star and a M8-type star, with the wavelength plotted against the spectral irradiance.

One of the challenges with M-dwarf planets comes from the spectra of the host stars. As red dwarfs are cool objects with effective temperatures T_{eff} in the range of 2300-4000 K, they emit the bulk of their light in the infrared. Figure 1.11 shows the spectrum of a G2-type star compared to the one of a M8-type star. The peak of the spectrum for a solar-type star is in the visible, around 0.5 μm, while the one for a very low-mass star is located in the near-infrared at around 1.2 μm. The spectrum complexity increases with later-type stars, including more and more weak absorption lines (Rajpurohit et al., 2018). Very low-mass stars often also exhibit signs of stellar activity which can distort the spectral lines, and as the amount of flux received is less than for a solar-type star, estimating the physical parameters for these stars proves to be a challenge. Though for the lowest mass M dwarfs, the main difficulty arises from the current inaccuracy of the atmospheric models available. Currently, the fundamental parameters that can be retrieved from the spectroscopic study of a star are: the metallicity $[Fe/H]$, the surface gravity log g, and the effective temperature T_{eff}. The radius of the star can then be obtained from the distance, the T_{eff}, and the bolometric luminosity. Estimating the mass of the star requires the use of stellar structure models, empirical relationships, or a density measurement from transit light curves. An accurate

stellar characterization is crucial for transit fitting as uncertainties on the stellar parameters directly propagate to the planetary parameters through the measurement of the observables (Mann et al., 2015).

1.3 Characterization of transiting planets

In this section, I will review the two methods I used in this thesis to characterize exoplanets: the radial velocity method to get access to the relative mass of transiting planets, and transit spectroscopy for atmospheric exploration. I will then go over phase curve analysis and emission spectroscopy which are techniques that evaluate the direct contribution of the planet to the total observed brightness of the system.

1.3.1 Radial velocities

We can now consider the movement of the two bodies around the common center of mass as a planet orbits a star. We can show that the star and the planet exhibit elliptical motions (see Murray & Correia, 2010, for the full derivation), with the same eccentricity but the semi-major axes are scaled to the reduced mass:

$$\begin{aligned} a_\star =& a\frac{m_p}{M_\star + m_p}, \\ a_p =& a\frac{M_\star}{m_p + M_\star}. \end{aligned} \tag{1.23}$$

From Kepler's third law, the two bodies should have the same orbital periods. If we define the mean motion n as $n = \frac{2\pi}{P}$, then we can write:

$$n^2 = \frac{G(m_p + M_\star)}{a^3}. \tag{1.24}$$

The two mean motions of the star and the planet should then be equal as well, but the semi-major axes are not. Each body revolves around the center of mass, and the periapses of their elliptical orbits differ by π. If the observer lies in the positive direction of the $Z-$axis on Figure 1.4, the radial velocity projected along the line of sight is given by:

$$v_r = v_Z + K(\cos(\omega + f) + e\cos\omega), \tag{1.25}$$

where v_Z is the proper motion of the center of mass due to the fact that we are considering a system in motion with respect to the observer, and

$$\begin{aligned} K =& \frac{m_p}{m_p + M_\star}\frac{na\sin i}{\sqrt{1-e^2}}, \\ =& \left(\frac{2\pi G}{P}\right)^{1/3}\frac{m_p}{(m_p + M_\star)^{2/3}}\frac{\sin i}{\sqrt{1-e^2}}, \end{aligned} \tag{1.26}$$

where K is the semi-amplitude of the radial velocity. As the planet moves along the orbit, the value of the radial velocity is modulated in a sinusoidal shape, as shown in Figure 1.12. The shape and orientation of the orbit are affected by the eccentricity e and argument of periastron ω, respectively; a non-zero eccentricity will cause the RV variation to deviate from a simple sinusoid. To sample effectively the RV variations, the full phase should be sampled and multiple periods should be covered.

The radial velocity shift due to the existence of a planet orbiting a star is translated into a Doppler shift of the star's spectral lines (Lovis & Fischer, 2010). Because of the reflex

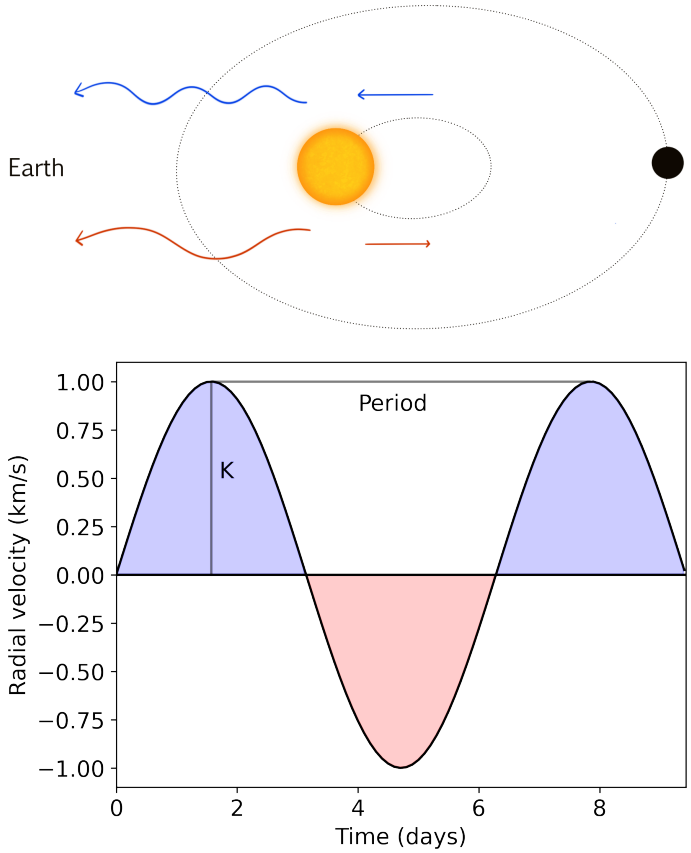

Figure 1.12: Top figure: illustration of the elliptical motions of a star and a planet around their common center of mass. The reflex motion of the star with respect to the observer causes a blue and red shift of the star's spectral lines as the star moves towards and away from them, respectively. Figure adapted from Tenefifi, CC0, via Wikimedia Commons. Bottom figure: induced radial velocity as a function of time in the case of a circular orbit. The semi-amplitude K is the maximum variation of radial velocity. The blue and red shaded regions correspond to the blue and red-shifted zones.

motion of the star, the photons emitted will undergo a blue or red shift towards the shorter or longer wavelengths, respectively. The frequencies are modified, much like in the famous case of the ambulance pitch changing as it moves towards or away from an observer. The radial velocity can then be measured by:

$$v_{r,planet} = c\frac{\lambda_{obs} - \lambda_{em}}{\lambda_{em}}, \tag{1.27}$$

with c the speed of light, λ_{obs} the observed wavelength, and λ_{em} the wavelength at which the light was emitted.

In practice, the radial velocity is extracted from spectroscopic observations with a high-resolution spectrograph. The most commonly used method is the one of the cross-correlation function (CCF) first introduced in the case of redshifted galaxies (Tonry & Davis, 1979). It is based on the comparison of the observed spectrum with a calibrated template of the stellar spectrum. By computing the correlation of the two spectra for a set of wavelength shifts, the resulting CCF gives an idea of an average spectral line as seen in the observed spectrum. The width of the CCF is related to the rotational velocity of the star, $v_{rot} \sin i$, where the orbital inclination i is the inclination of the rotation axis of the star relative to the plane of the sky.

Assuming $i = 0°$, half of the star moves towards the observer and its light is blue-shifted, and inversely for the other half. This averages out, not inducing an actual wavelength shift, but instead creating a symmetric broadening of the spectral lines. The CCF's minimum value (or maximum value, depending on how it is computed) is at the wavelength corresponding to the Doppler shift of the radial velocity.

This method allows to observe systems with orbital inclinations significantly departing from $i \sim 90°$, which is a much looser constraint than the case of transiting planets. It is sensitive to the minimum mass of the planet $m_p \sin i$, since i cannot be determined from RVs. However, this parameter can be obtained from transits for a favorable orbital configuration, so combining the two methods gives access to m_p and R_p, which in turn gives access to the bulk density of the planet. This density is critical to evaluate the extent of the atmosphere (if any) and to constrain the composition of the interior. By the definition of the semi-amplitude of the RV signal given in Equation 1.26, it is easier to detect massive planets with short orbital periods, or planets around low-mass stars.

The main limitation for the detection of planets comes from stellar noise, as explained in Lovis & Fischer (2010). Magnetic activity creating inhomogeneities in the photosphere of stars can translate into RV variations of 10-100 m/s. Mitigating stellar activity is one of the biggest challenges tackled today, with many new data processing techniques being developed (Gomes da Silva et al., 2022; Dumusque, 2018; Collier Cameron et al., 2021; de Beurs et al., 2022, for instance). Such stellar activity corrections allow to reach precisions down to 20 cm/s for bright, nearby, and quiet stars observed with new generation high-precision spectrographs such as ESPRESSO (Pepe et al., 2021). Moreover, low-mass planets orbiting nearby M dwarfs are now within reach thanks to the recently commissioned SPIRou (Donati et al., 2018) and NIRPS (Artigau et al., 2024) infrared high-resolution spectrographs.

1.3.2 Transmission spectroscopy

If a transiting planet possesses an atmosphere, part of the stellar light emitted in the direction of the observer is filtered by the atmospheric annulus surrounding the planet as it is transiting its host star. The photons passing through the atmosphere interact with the chemical constituents and are either absorbed by atoms and molecules or scattered by aerosols. At specific wavelengths, the atmosphere of the planet can thus be more opaque, resulting in a larger measured radius. This translates to a chromatic behavior for the transit depth ΔF. The spectroscopic observation of a transit can thus reveal the existence and the composition of the planet's atmosphere. This method is called transmission spectroscopy and is illustrated in Figure 1.13. Given the grazing geometry of the light rays, the deeper layers of the atmosphere remain opaque due to the stronger interactions. This method then only allows to probe the upper part of the atmosphere that is clear enough to let photons go through with mild interactions.

A transmission spectrum can be modeled using extensive radiative transfer calculations such as in Seager & Sasselov (2000). However, it is possible to get a rough estimate of the amplitude of the spectral features by considering the scale height H of the atmosphere, as given in Kreidberg (2018), assuming hydrostatic equilibrium:

$$H = \frac{k_b T_{eq}}{\mu_m g_p}, \tag{1.28}$$

with H the atmospheric scale height, i.e. the altitude at which the pressure drops by a factor of the neperian number e, k_b the Boltzmann constant, T_{eq} the planet's equilibrium temperature, μ_m the mean molecular weight, and g_p the surface gravity of the planet. In that case, the variation of transit depth expected from spectral features is:

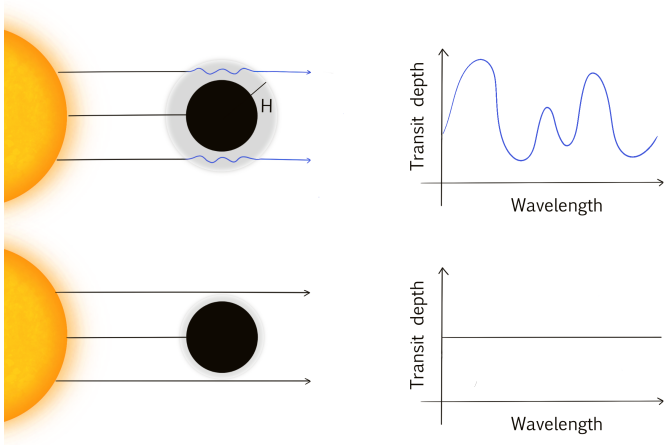

Figure 1.13: Comparison of the transit of a planet with an extended atmosphere (top figure) and one with a thin layer of atmosphere (bottom figure). A variation of transit depth is produced as the starlight interacts with the atmosphere at certain wavelengths due to the presence of chemical species.

$$\begin{aligned} d\Delta F_\lambda =& \frac{(R_p + nH)^2}{R_\star^2} - \frac{R_p^2}{R_\star^2}, \\ \simeq& 2nH\frac{R_p}{R_\star^2}, \end{aligned} \tag{1.29}$$

where n is the number of scale heights crossed at wavelengths with high opacity. From Equation 1.29, the detection of atmospheric signals is favored for small stars orbited by large planets with extended atmospheres. Typically, in the ideal case of a hot Jupiter, the amplitudes of the features are of the order of 0.1% which is out of reach of most ground-based facilities.

The challenge of this method resides in the interpretation of the data. Because the absorption features of many chemical compounds cover fully or partially a common wavelength range, it is tricky to disentangle them. In order to draw the most accurate conclusions, a large panel of models is explored and a marginalization over the models consistent with the data allows to derive sound statistical constraints on atmospheric parameters such as the abundances of the various species. Furthermore, Fairman et al. (2024) has shown that combining data in various wavelength ranges is the best approach to have a complete picture of the atmospheric properties of an exoplanet.

The first detection of an atmosphere using this technique was on the hot Jupiter HD 209458 b by Charbonneau et al. (2002) with the HST. Since then, atmospheric characterization has become a central topic in Exoplanetology. Some of the biggest telescopes on Earth can reach the precision required to measure the transit transmission spectrum of relatively large exoplanets, such as FORS2 on the Very Large Telescope (e.g. Nikolov et al., 2016). Space-based observatories are not subject to atmospheric variability, and can then reach the precision needed to measure the transmission spectrum of smaller planets. For instance Spitzer, now decommissioned, was one of the first to measure exoplanets' transmission spectra, together with HST (e.g. Charbonneau et al., 2002; Knutson et al., 2011). Now, JWST is the most coveted facility thanks to its broad coverage in the NIR and mid-IR. An example of the exquisite precision of the order of 0.01% achievable with JWST is given in Figure 1.14, enabling the clear detection of the signatures of gases such as H_2O and CO_2. In addition,

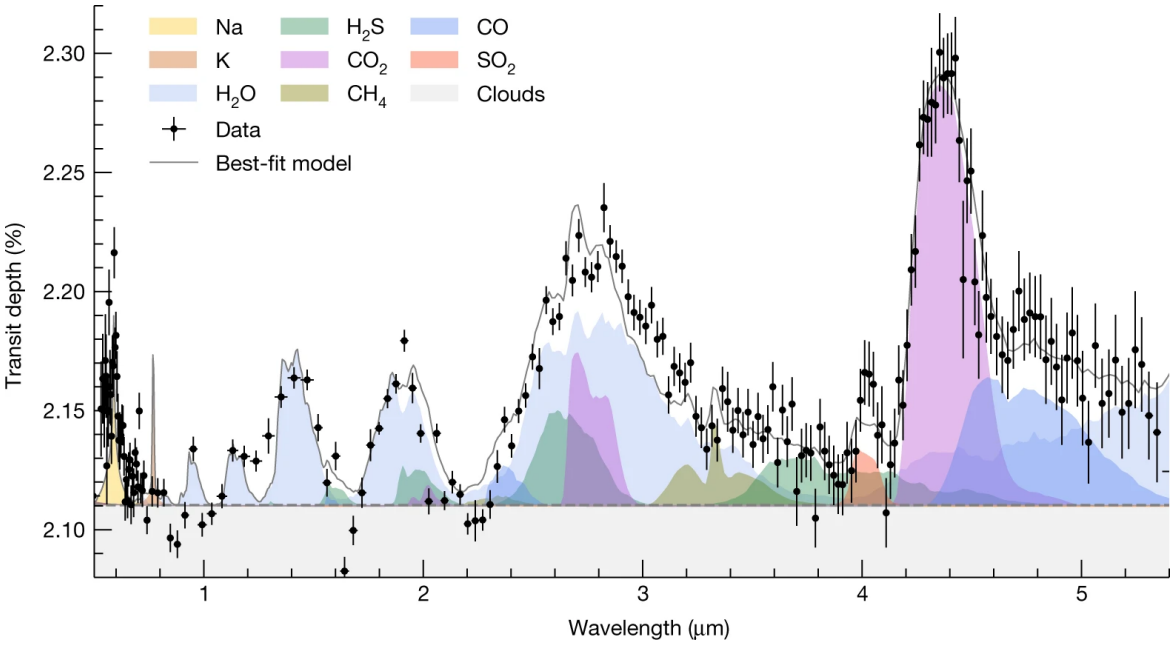

Figure 1.14: Transmission spectrum of WASP-39 b obtained with JWST NIRSpec PRISM. The contribution of the various atomic and molecular species are highlighted in color, the data points are in black and the solid black line is the fitted model. Figure from Rustamkulov et al. (2023).

Ariel (Tinetti et al., 2016) is an upcoming ESA mission that will be entirely dedicated to the study of exoplanet atmospheres with transmission spectroscopy in the NIR, as well as emission and phase curve spectroscopy (see Section 1.3.3).

To aid in the selection of the best candidates for atmospheric characterization through transmission spectroscopy, Kempton et al. (2018) devised a metric: the Transmission Spectroscopy Metric (TSM).

$$TSM = (scalefactor)\frac{R_p^3 T_{eq}}{m_p R_\star^2} 10^{-m_J/5}, \tag{1.30}$$

where the scale factor is a constant, R_p and m_p are the radius and mass of the planet, respectively, and m_J is the magnitude in the J-band. The equilibrium temperature T_{eq} represents the temperature of the planet in radiative equilibrium. For a zero albedo and a full day-night heat redistribution, it is given by:

$$T_{eq} = T_{eff}\sqrt{\frac{R_\star}{a}}\left(\frac{1}{4}\right)^{1/4}, \tag{1.31}$$

with $T_\star$ the effective temperature of the star, a the semi-major axis, and $R_\star$ the radius of the star.

Equation 1.30 is based on the theoretical JWST/NIRISS signal-to-noise ratio in the case of a 10 hour observing campaign as calculated by Louie et al. (2018), and applied to a statistical sample of planets with various sizes. A threshold value above which the planet is recommended for transmission was found by selecting the best targets in the sample split into planet categories. This metric is meant to be used as a selection tool by comparing systems with similar properties. It is now widely used in the community and has motivated the atmospheric exploration of dozens of systems since its publication. However, this metric should be interpreted with caution: it does not take into account the noise floor of the

instrument. If a star is very bright, the TSM can be very high, but JWST won't detect signals of a few ppm, whatever the brightness of the source.

1.3.3 Phase curves and emission spectroscopy

While phase curve analysis and emission spectroscopy constitute powerful techniques to probe the atmosphere of transiting exoplanets, I have not had the opportunity to use them in this thesis. Nevertheless, the following paragraphs are intended to give the reader a brief description of the basic principle.

So far, we have considered the star to be the only source of the observed flux. In reality, the planet contributes as well with its thermal emission and reflected starlight. As the planet travels along the orbit, the hotter day side is gradually exposed until it is hidden by the star at superior conjunction and gradually decreases again. This results in a flux modulation along the planet's orbit, its *phase curve*, combined with a secondary eclipse, also called *occultation*, as illustrated in Figure 1.15.

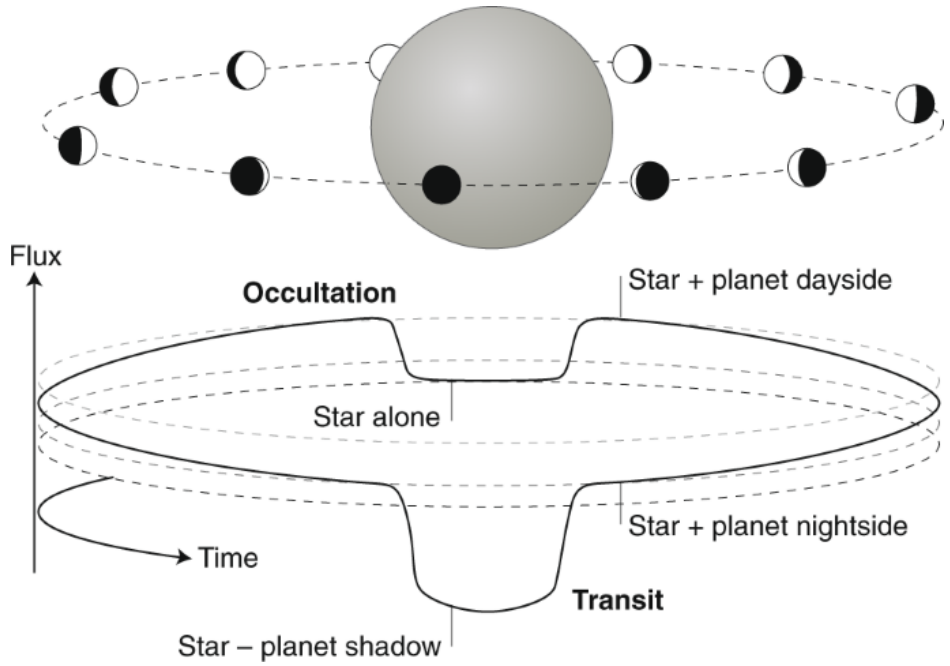

Figure 1.15: Illustration of the variation of the flux during a full phase of a planet orbiting a star. Figure from Winn (2010).

Calculating the drop of flux during an occultation, we can write $\Delta F_{occ} = \frac{F_{ooo} - F_{occ}}{F_{ooo}}$, with F_{ooo} the out-of-occultation flux, and F_{occ} the in-occultation flux. Then, with $F_{s,p}$ and $F_{s,\star}$ the planet's and star's surface fluxes, respectively, if we assume $F_{s,p}\pi R_p^2 << F_{s,\star}\pi R_\star^2$:

$$\begin{aligned} F_{ooo} &= F_{s,\star}\pi R_\star^2 + F_{s,p}\pi R_p^2, \\ F_{occ} &= F_{s,\star}\pi R_\star^2, \\ \Rightarrow \Delta F_{occ} &= \frac{F_{s,p}\pi R_p^2}{F_{s,\star}\pi R_\star^2 + F_{s,p}\pi R_p^2}, \\ &\simeq (R_p/R_\star)^2 \frac{F_{s,p}}{F_{s,\star}}. \end{aligned} \tag{1.32}$$

The occultation depth is a function of the ratio of the surface brightness of the planet to that of the star. Typically, the planet is a lot cooler than the star, and its thermal emission peaks

in the infrared. If we consider an occultation at wavelengths where the reflected starlight is negligible compared to the thermal emission, we can write:

$$\Delta F_{occ} = \left(\frac{R_p}{R_\star}\right)^2 \frac{B_\lambda(T_{p,day})}{B_\lambda(T_{eff})}, \tag{1.33}$$

where $B_\lambda(T)$ is the Planck function at a given temperature T, $T_{p,day}$ the temperature of the dayside of the planet and T_{eff} the effective temperature of the star.

Emission spectroscopy informs on the composition and thermal structure of the atmosphere of exoplanets (e.g. Stevenson et al., 2014; Haynes et al., 2015; Line et al., 2016). In addition, it can also be used to study atmospheric dynamics (Zhang et al., 2017). Particularly, the spectroscopic observation of the phase curve of the planet (including transit and occultation) proves to be the best atmospheric probe thanks to its sensitivity to the day/night side contrast. This method has been mostly used to study tidally locked hot Jupiters because of the large difference between the day and night side temperatures which implies large phase curve amplitudes (e.g. Demory et al., 2016; Kreidberg et al., 2018; Mikal-Evans et al., 2022). Indeed, for such systems, tidal forces have caused the planet's rotation to slow down over time and ultimately synchronize with its orbital period. This means only one side of the planet is continuously irradiated, creating a perpetual hot day side and cold night side. With JWST, phase curves of smaller planets are also within reach, as was done for GJ 1214 b (Kempton et al., 2023). In that particular case, the transmission spectrum is featureless due to the presence of aerosols in the upper atmosphere (Kreidberg et al., 2014), preventing any insights into the atmospheric composition. However, the phase curve provided valuable information into the atmospheric properties of the planet, such as a high metallicity, a possible high water abundance, and a high Bond albedo.

1.3.4 A word on habitability and biosignatures

As I mentioned in the introduction of this chapter, one of the main motivations behind Exoplanet research is to search for potentially habitable worlds. Schwieterman et al. (2018) describes the three fundamental requirements for life on Earth as having: (1) an energy source to drive metabolic reactions, (2) a liquid solvent to perform these reactions, and (3) the necessary nutrients to sustain them. Thanks to its physicochemical properties, liquid water is the solvent required for biochemical reactions to occur. Although the notion of *habitability* is intricate given the complex atmospheric and surface conditions involved (see Cockell et al., 2016, for a comprehensive review), astronomers use the concept of *habitable zone* (HZ) to identify exoplanetary systems fulfilling two out of the three requirements to sustain life. The HZ is defined as the range of orbital distances where a terrestrial-mass planet with a CO_2-H_2O-N_2 atmosphere could maintain liquid water on its surface (Kopparapu et al., 2013). The location and width of the HZ depend mainly on two parameters: the incident stellar flux and the planetary atmospheric composition (Kaltenegger, 2017). In fact, the incident stellar flux is dependent on the stellar type and varies as the star evolves, meaning the HZ boundaries are not fixed for the lifetime of a given system. Intuitively, the HZ sits at larger orbital distances for a hotter and more massive star than for a cooler and smaller star. On the other hand, the planet's atmospheric makeup and energy distribution plays a crucial role on the possible existence of surface liquid water through the greenhouse effect. This leads to diverging definitions of the HZ boundaries depending on the type of atmosphere considered (e.g. Abe et al., 2011; Kaltenegger & Sasselov, 2011; Kopparapu et al., 2013; Kasting et al., 2014; Ramirez & Kaltenegger, 2017; Kopparapu et al., 2017).

By investigating the atmospheres of terrestrial habitable zone planets, we hope to find traces of biological life by identifying *biosignatures*, i.e. gases possibly resulting from metabolic

activity. Biosignature gases may always be the product of abiotic chemistry, that is why all biosignatures are considered potential indicators of life and are open to a range of interpretations (Schwieterman et al., 2018). Meadows (2008) groups biosignatures into three broad categories: (1) gaseous biosignatures, indicating a change in the atmosphere's composition; (2) surface biosignatures, indicating a change in the reflected or scattered light by organisms on the surface of the planet; (3) temporal biosignatures, which are changes of the characteristics of the planets over time that can be attributed to biological processes. The typical biomarker gases searched for with transmission or emission spectroscopy in an Earth-like atmosphere are: O_2, O_3, CH_4, N_2O, and sulfur gases (dimethyl sulfide, dimethyl disulphide, and CH_3SH) (Meadows, 2008; Schwieterman et al., 2018). Chemical disequilibrium is also regarded as a robust potential biosignature (e.g. Lovelock, 1965; Margulis & Lovelock, 1974). As such, having an indication of the oxidization state of the atmosphere can also aid in the interpretation of the detection of biosignatures gases.

In practice, many of the absorption features of biomarker gases overlap and interpreting spectra is difficult if the observations only span one absorption band. One example is the case of the habitable zone sub-Neptune K2-18 b, where a detection of water vapor was first claimed by Benneke et al. (2019) and Tsiaras et al. (2019). This was later refuted by Bézard et al. (2022) who showed that the data could also be explained by the presence of methane in the atmosphere of K2-18 b. Based on JWST observations covering a much larger wavelength range in the NIR, Madhusudhan et al. (2023) and Wogan et al. (2024) showed the dominant features are in fact CH_4 and CO_2. Statistical methods allow to infer the properties of atmospheres with a certain degree of confidence. However, gathering a broad range of data accross multiple bands is crucial to paint a complete picture of the system's characteristics and reduce degeneracies.

1.4 Sub-Neptunes

Historically, the terms "super-Earth" and "sub-Neptune" pointed to the same category of planets: the ones larger than the Earth but smaller than Neptune, i.e. with radii between 1 and 4 $R_\oplus$. From the first months of data, Kepler revealed these planets to be very frequent in short orbits around Sun-like stars (Borucki et al., 2011), though radial velocity surveys had already previously found these planets to be very frequent (Mayor et al., 2011). Subsequent studies have shown that small planets are more frequent around M dwarfs than FGK stars, and that on average low-mass stars host more than two sub-Neptune-sized planets per star (e.g. Mulders et al., 2015b; Dressing & Charbonneau, 2015; Cloutier & Menou, 2020; Ment & Charbonneau, 2023).

Surprisingly, Fulton et al. (2017) showed that the planetary radius distribution for FGK stars was not homogeneous, but rather bimodal with two peaks around 1.3 $R_\oplus$ and 2.4 $R_\oplus$, as shown in Figure 1.16. This scarcity of planets between 1.5 and 2.0 $R_\oplus$ is known as the *radius valley* or *Fulton gap*. From investigations into the density of small planets (e.g. Marcy et al., 2014), it was clear that the sub-Neptunes are actually split into two distinct populations: the small super-Earths which should be mostly solid objects, possibly with a compact atmosphere, and the larger mini- or sub-Neptunes which possess an extended atmosphere. A third possible origin for these planets was first proposed by Kuchner (2003) and Léger et al. (2004): water worlds. They correspond to small planets with masses below 10 $M_\oplus$ with a significant water mass fraction $\gtrsim 10\%$. Many subsequent studies have investigated the possible existence of water worlds (e.g. Zeng et al., 2019; Luque & Pallé, 2022; Rogers et al., 2023; Madhusudhan et al., 2021; Rigby & Madhusudhan, 2024). Because these planets populate a region of the mass-radius parameter space prone to degeneracies for interior structure models and atmospheric compositions (Rogers & Seager, 2010), determining the exact nature of a super-

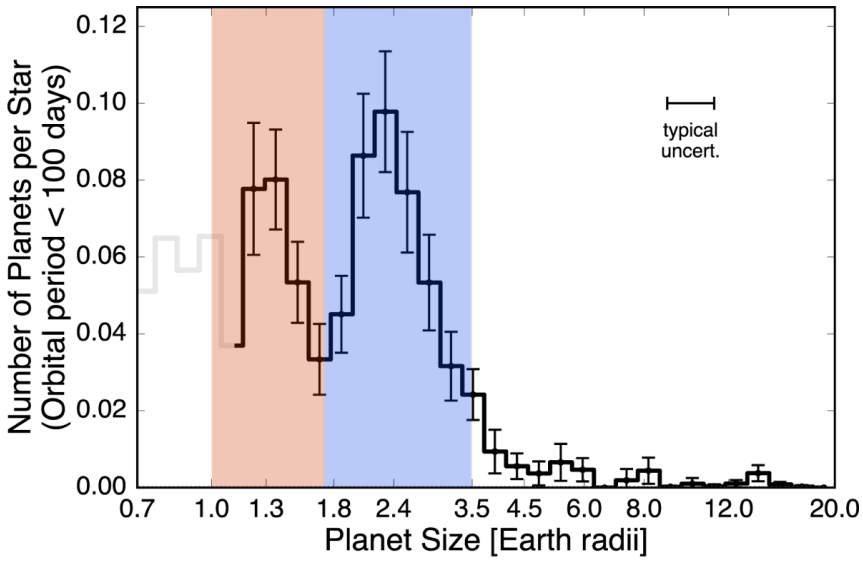

Figure 1.16: Histogram of the radius of a sample of Kepler planets with orbital periods shorter than 100 days. The red and blue regions correspond to the super-Earths and mini-Neptunes, respectively. Figure adapted from Figure 7 of Fulton et al. (2017).

Earth and a sub-Neptune is a difficult task (e.g. Nettelmann et al., 2011; Rogers et al., 2023; Cadieux et al., 2024).

The dependence on the incident stellar flux represents strong evidence in favor of thermally-driven mass-loss processes as the cause for the radius valley (Fulton et al., 2017; Cloutier & Menou, 2020; Van Eylen et al., 2021). The two main competing models that reproduce naturally the observed bimodal distribution are: (a) photoevaporation, where the UV flux coming from the star ionizes the upper atmosphere and heats it, creating hydrodynamic outflows (Owen & Wu, 2013); (b) core-powered mass loss, where the outer layers of the atmosphere are ejected as the planet cools down in the first few million years after dissipation of the protoplanetary disk (Ginzburg et al., 2018). In both these evolution models, the planets that lose part of their atmospheres become super-Earths while the ones retaining them are classified as sub-Neptunes. These models assume a hydrogen and helium-rich (H/He) atmosphere and require ice-poor core compositions to reproduce the observed distribution of planetary radii. This indicates that the planets have formed inside the water ice line where there was no supply of volatile ices available during the formation process (Owen & Wu, 2017; Gupta & Schlichting, 2019). However, the combination of formation models and evolution models allow for the existence of volatile-rich worlds. Notably, Venturini et al. (2020) and Venturini et al. (2024) found that water-rich planets are typically formed by pebble accretion outside the snowline before migrating inwards. They included photoevaporation mass-loss after formation in their study to reproduce the radius gap. While they found super-Earths to be rocky cores, Sub-Neptunes could then harbor water in the form of ice in their interiors. As such, they blur the separation in mass and radius between rocky and water worlds. Burn et al. (2024) also proposed a hybrid theory between formation and evolution models where the super-Earths are composed of evaporated rocky cores formed in-situ and sub-Neptunes are migrated icy cores formed ex-situ. This reproduces the radius valley as well as the *radius cliff* corresponding to the occurrence drop at $\sim 3R_{\oplus}$ (see Figure 1.16). Overall, it is accepted that thermally-driven mass-loss processes play a central role in shaping the radius valley. Although, volatile-rich cores and atmospheres can only exist by considering migration

effects for short period planets.

The existence of the radius valley for low-mass stars was evaluated in multiple publications, and conflicting results were found: Cloutier & Menou (2020) found a positive slope for the radius valley around M dwarfs, while Van Eylen et al. (2021) found a negative one similar to the slope measured for FGK stars. This is illustrated in Figure 1.17 where Ref. (22) corresponds to Cloutier & Menou (2020), and Ref. (30) to Van Eylen et al. (2021). Such a discrepancy is explained in Van Eylen et al. (2021) by the different approaches used for the determination of the radius valley, and the fact that they used a smaller sample but for which planets are better characterized. As new observational constraints came into play, Luque & Pallé (2022) found that the demographics of small planets for low-mass stars can be better seen as a density valley, and that the radius valley was partially filled. The comparison found between the radius gap and the density gap is given in Figure 1.17. In addition, they argue that small transiting planets around M dwarfs can be categorized in three populations with distinct compositions: the small rocky super-Earths, the intermediate water-ice-rich worlds, and the large puffy sub-Neptunes. The fading of the radius valley for M dwarfs was further confirmed by Bonfanti et al. (2024) and Venturini et al. (2024) who also found results in line with the ones of Luque & Pallé (2022) regarding the density valley. However, the latest study on the matter presented in Parc et al. (2024) showed that there is no clear radius or density gap between super-Earths and sub-Neptunes, and that super-Earths are more common than sub-Neptunes. The latter is in agreement with the occurrence rates calculated by Ment & Charbonneau (2023) for mid- to late-M dwarfs. Parc et al. (2024) argued that a measured bulk density can correspond to a range of internal compositions and structures, creating a continuity in the volatile content of super-Earths and sub-Neptunes. They also observed that the transition between the two types of planet appears to occur at different masses and radii depending on the spectral type of the host star. Importantly, they highlighted that the biggest limitation to the comprehensive interpretation of the distributions examined in such studies is the size of the sample of well-characterized planets. It is crucial to increase the number of planets in the considered parameter space to reduce biases and ensure the robustness of future demographic studies. In particular, this can be achieved by combining RV measurements and the radius measurement of transiting planets by providing a value for the planetary mass. Atmospheric studies can also relieve degeneracies of internal compositions by the detection of an extended H/He atmosphere, and by giving access to the abundances of H_2O, CO_2, and CH_4, for instance.

1.5 Hot Jupiters

The discovery in 1995 of the first extrasolar planet orbiting a main sequence star completely challenged our understanding of giant planets (Mayor & Queloz, 1995). Indeed, until then it was thought giant planets could only form far away from their host star based on the only example of planetary system at hand. 51 Pegasi b is a Jupiter-sized planet with a mass of 0.46 M_{Jup}, orbiting a solar-like star in 4.2 days. This corresponds to an orbit well inside the one of Mercury, and as a result, its equilibrium temperature is over 1200 K. Radial velocity surveys quickly unearthed the existence of more close-in giants orbiting bright stars (e.g. Butler et al., 1997, 1998; Udry et al., 2000). The lack of a radius measurement for RV planet candidates motivated the search for transiting planets, which led to the first detection of a planetary transit on the star HD 209458 in 2000 by Charbonneau et al. (2000) and Henry et al. (2000). For the first time, a gas giant was actually confirmed with a mass of 0.62±0.05 M_{Jup} and a radius of 1.42±0.10 R_{Jup}, orbiting its host star every 3.5 days (Henry et al., 2000).

Today, the term "hot Jupiter" refers to a gas giant with a mass $> 0.25 M_{Jup}$ with a period

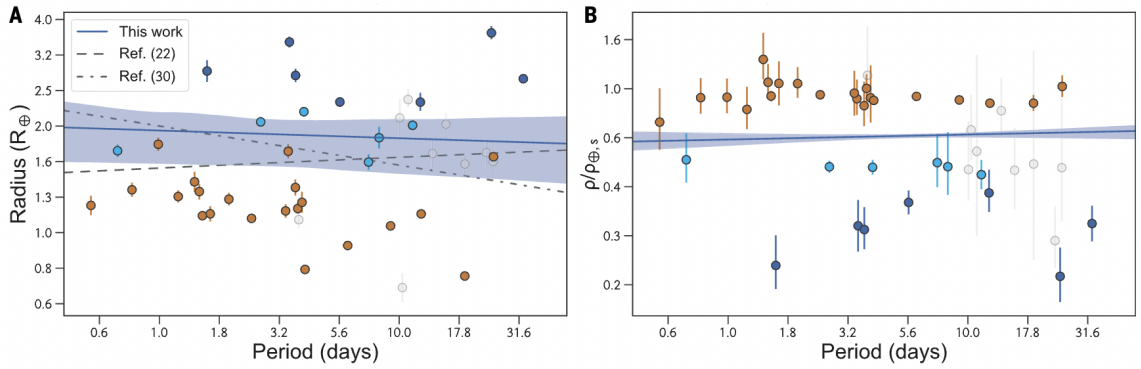

Figure 1.17: Radius (panel A) and density (panel B) as a function of the orbital period for a sample of planets with determined masses orbiting low-mass stars. Planets are color-coded according to their bulk density, the orange corresponding to rocky planets, the light blue water worlds, and dark blue puffy sub-Neptunes. On the left, the dashed lines correspond to the radius valleys found in Cloutier & Menou (2020), labeled Ref. (22), and Van Eylen et al. (2021), labeled Ref. (30). In both panels, the blue solid line and shaded region correspond to the best-fit model and the $1-\sigma$ uncertainty, which are consistent with a zero slope. This Figure is Figure 4 from Luque & Pallé (2022) with an adapted caption.

under 10 days, granting them an equilibrium temperature larger than 1000 K. About 20% of the confirmed exoplanets fit into this category[2] and the vast majority orbit solar-type stars. RV surveys revealed the occurrence rates of hot Jupiters around FGK-type stars to be of the order of ∼1% (e.g. Wright et al., 2012; Mayor et al., 2011; Marcy et al., 2005). This appeared at odds with results from the Kepler sample of planets where an occurrence rate of the order of ~ 0.5 % is found (Howard et al., 2012; Fressin et al., 2013). This discrepancy is attributed to stellar metallicity, age and population. In particular, higher metallicity stars are more likely to host hot Jupiters (e.g. Fischer & Valenti, 2005).

The very few detections of giants orbiting M dwarfs prevented for a long time the construction of an unbiased statistical sample. Thanks to the Transiting Exoplanet Survey Satellite (TESS, Ricker et al., 2014), the number of confirmed close-in giants around M dwarfs more than doubled in the last few years (e.g. Hobson et al., 2023; Triaud et al., 2023; Hartman et al., 2023). Gan et al. (2023) showed the occurrence rates of such hot Jupiters orbiting early M stars with masses between 0.45 and 0.65 $M_\odot$ is 0.27 ± 0.09 %. This was further confirmed by Bryant et al. (2023) who investigated a sample of low-mass stars down to 0.08 $M_\odot$. They reported a similar result with 0.29 ± 0.15 % for early M stars (0.42-0.71 $M_\odot$) and provided for the first time estimates of 0.14 ± 0.10 and 0.11 ± 0.09 % for late-type and mid-type M dwarfs (0.09-0.26 $M_\odot$ and 0.26-0.42 $M_\odot$, respectively).

Three main theories were put forward to explain the existence of hot Jupiters around FGK stars (Dawson & Johnson, 2018): core accretion, where the planets are formed at their current orbital distance; gas-disk migration, where the planets are formed further out in the disk but migrate inwards by exchange of angular momentum with the disk; and high-eccentricity tidal migration, where the planet migrates due to an exchange of angular momentum with another planet or a second star, putting it on a highly elliptical orbit before the dissipation of energy causes circularization of the orbit. Studies have focused on whether these formation theories valid for FGK stars are also applicable to M dwarfs, and the core accretion model is currently the least favored by the community. For instance, Ida & Lin (2005) and Laughlin et al. (2004)

[2]Data from NASA exoplanet archive https://exoplanetarchive.ipac.caltech.edu/, accessed on the 1st of July 2024.

showed that forming giant planets by core accretion is impossible for M dwarfs due to the depletion of material in the protoplanetary disk compared to solar-type stars. In addition, protoplanetary disks evaporate faster than the timescale needed to produce a giant planet in the case of M dwarfs. Additionally, the efficiency of giant planet formation increases as the stellar mass increases. A study on theoretical population synthesis led by Burn et al. (2021) agrees with these general conclusions, but reports that increasing the concentration of planetesimals toward the star and reducing migration are sufficient to allow the formation of giants around low-mass stars. Further, they note that gravitational instability, where part of the disk contracts to create a protoplanet, could also be a formation pathway for such planets (e.g. Boss, 1997). Schlecker et al. (2022) goes on to say that this particular formation pathway would tend to create planets with masses of the order of $10 M_{Jup}$, which has not been observed so far around M dwarfs. In short, the various formation mechanisms of close-in giants orbiting low-mass stars are still actively discussed. Testing these theories is possible by confronting the observed population of giants with the expected outcomes. Evaluating occurrence rates offers one avenue, but formation tracers are mostly found in the atmosphere of giant planets.

The composition of the protoplanetary disk changes as snow lines of chemical species are crossed, and determining the atmospheric content can then be indicative of the formation and migration history of a planet. Öberg et al. (2011) shows C/O ratio is strongly affected by the position at which the planet formed with respect to the H_2O and CO ice lines. In this intermediate region, most of the oxygen is present in the form of icy grains and most of the carbon is in the gas phase. Planets forming outside the water ice line have a C/O$\sim$1, while sub-stellar and stellar C/O ratios are expected when most of the material is mixed in the gas phase. Many studies have investigated the C/O ratio as primary formation tracer (e.g. Mordasini et al., 2016; Madhusudhan et al., 2017; Cridland et al., 2019). However, Turrini et al. (2021) showed that the C/O ratio alone provided limited insight into the formation pathways of giants that undergo orbital migration. They advocated that jointly using multiple elemental ratios such as C/N, N/O, and C/O ratios breaks the degeneracies between formation models. Characterizing the abundance of refractory materials such as silicon and iron has also recently been recognized as a tracer for the location of the formation of giant planets (Chachan et al., 2023). More chemical species (TiO, CH_4, CO_2, HCN, NH_3, etc.) have been linked to formation processes in recent works (e.g. Hobbs et al., 2022; Ramírez et al., 2020; Edwards & Changeat, 2024).

The sample of confirmed close-in giants orbiting M dwarfs is currently at 20 planets. Their formation pathways is uncertain, and a thorough characterization of the atmosphere is able to break degeneracies between formation models by identifying and measuring formation tracers. Increasing this sample is critical to study this population as a whole. The identification of trends in atmospheric composition and stellar environment will allow to improve our knowledge of how these systems form and evolve.

1.6 Dissertation outline

In this first introductory Chapter, I have talked about two categories of planets that are absent from our solar system: the sub-Neptunes and the close-in giants. On the one hand, the supposed common nature of super-Earths and sub-Neptunes is still an open debate. The lack of a radius valley for M dwarfs is now demonstrated, but confirming the density gap requires a larger sample of sub-Neptunes with measured radii and masses. Alleviating the high degree of degeneracy between interior structure and composition for a given density would also require a large sample of planets not only with precise mass and radius measurements, but also with a thorough atmospheric characterization. On the other hand, the existence of

close-in giants orbiting low-mass stars still baffles formation theories. As the core accretion model does not allow the formation of such large planets in M-dwarf disks, a migration mechanism seems more likely. Detecting more warm Jupiters around M dwarfs is the only way to confirm whether migration dominates or if the current core accretion model needs to be adapted. During my thesis, I aimed at confirming new planets with a focus on these two flavors. In Chapter 2, I describe how I used the TRAPPIST and SPECULOOS facilities to validate planetary candidates from the TESS mission. I present the methods adopted to analyze the photometric data, and how they are used to discard false positives. I then describe the Bayesian framework used to retrieve the system parameters. Finally, I focus on the facilities used to characterize some validated planets: HST for the atmospheres, and ESPRESSO on ESO's Very Large Telescope for the mass measurements of giant planets. In Chapter 3, I present the discovery of TOI-4336 A b, a sub-Neptune planet in a nearby triple M-dwarf system. The results of its atmospheric exploration are given in Chapter 4. Chapter 5 is dedicated to the first planets confirmed of the Hidden Gems project: two new super-Earths found in the TOI-4336 A and TOI-237 systems. The project aims to find additional planet candidates in systems known to host at least one transiting planet by making use of the capabilities of the `SHERLOCK` pipeline. I present the MANGOs program I am co-leading in Chapter 6, a large-scale program on TRAPPIST and SPECULOOS aiming at the validation of close-in giants orbiting M dwarfs. I present its current status, and the efforts made towards the characterization of the validated planets. In the final Chapter 7, I conclude this manuscript by providing a brief summary of this thesis work and discussing possible prospects.

Chapter 2

Follow-up of TESS candidates

In this Chapter, I will describe my work as part of the TESS Follow-up Observing Program Working Group (TFOP WG) and how it led to the discovery of dozens of planets. Firstly, I will present the TESS mission and the organization of TFOP WG, and how my PhD fits into this large international collaboration. I will detail the process of validating a TESS planetary candidate, as well as describe the TRAPPIST and SPECULOOS facilities used for this purpose. I will then go over the data analysis process that takes us from astronomical images to transit light curves. I will go over the Bayesian analysis framework in which the system parameters are inferred. Finally, I will describe how I searched the TESS light curves for additional planet candidates. The last part of this Chapter is dedicated to the facilities I used to characterize TESS planets.

2.1 Detection of planets from space

Space-based observatories have the great advantages of not being subject to the day/night cycle, and being free of atmospheric turbulence reducing the photometric precision. This makes them ideal for transit surveys as they can stare at one portion of the sky for an extended period of time. The first space mission to find transiting planets was CoRoT, which stands for Convection, Rotation and planetary Transits (Auvergne et al., 2009). Launched in 2006, its primary goal was to study the internal structure of stars by observing their oscillations. This is done by monitoring the small changes in the flux of the stars over a period of time. As the first planetary transit was observed in 2000 (Charbonneau et al., 2000; Henry et al., 2000), a search for transiting planets was added as a secondary goal of the mission because it also required time series photometry. In total, it yielded the discovery of 37 planets. Then, NASA's Kepler mission (Koch et al., 2010) observed continuously a single field of view of 115 square degrees, which included over 100 000 stars, for over 4 years to search for terrestrial planets around solar-type stars. The loss of two reactions wheels in 2013 meant that the precise pointing of the original field of view was no longer possible. Still, the telescope was re-purposed, and the extended mission K2 (Howell et al., 2014) observed different fields along the ecliptic in the remaining years of operation (2014 to 2018). It took advantage of the spacecraft's two remaining reaction wheels and the solar pressure to stabilize its pointing. The impressive combined yield of Kepler and K2 is over 3300 confirmed planets. Needless to say, Kepler/K2 revolutionized the field of exoplanets. But, unfortunately, most of those planets are orbiting stars too faint to allow detailed follow-up observations. This motivated the concept of NASA's TESS mission to find small planets orbiting stars that are bright and nearby enough to allow the use of spectroscopy to measure the mass and the atmospheric composition of the detected planets.

2.1.1 TESS

The Transiting Exoplanet Survey Satellite concept was first submitted to NASA as Mission of Opportunity in early 2006, but was initially rejected. After years of refining the mission concept, and several attempts, the proposal was finally accepted in 2011 as an Explorer mission (Ricker et al., 2014). The mission was successfully launched in April 2018, and is currently in its second extension which will conclude in October 2024. It was placed on an elliptical orbit around the Earth with a period of 13.7 days in 2:1 resonance with the Moon's orbit. This configuration proved to be the best to limit perturbations by the Moon and provide a low-radiation environment, while also eliminating eclipses by the Earth and Moon.

TESS is a nearly all-sky survey. Its primary objective is to find hundreds of planets with $R_p < 4R_\oplus$, and determine the masses of 50 of them thanks to spectroscopic follow-up (Barclay et al., 2018; Guerrero et al., 2021). In fact, the total exoplanet yield obtained from simulations reaches the thousands for orbital periods below 50 days (Barclay et al., 2018). The observing strategy is illustrated in Figure 2.1: the sky is divided into 26 sectors, 13 per hemisphere, each being observed for a period of 27 days at a time. The time coverage extends to up to 351 days in regions where sectors overlap. In particular, the regions centered on the ecliptic poles benefit from a continuous coverage during the observation of the full hemisphere. They also correspond to the Continuous Viewing Zone (CVZ) of JWST which facilitates the follow-up of TESS planets in that portion of the sky. With this strategy, TESS is sensitive to planets with a maximum period of 10 days, or larger than 40 days in the CVZ taking into account the mission duration and the transit detection efficiency. This allows to reach habitable zone planets with periods between 25 and 75 days for an average M0 star with a T_{eff} of 3800 K (Ricker et al., 2014).

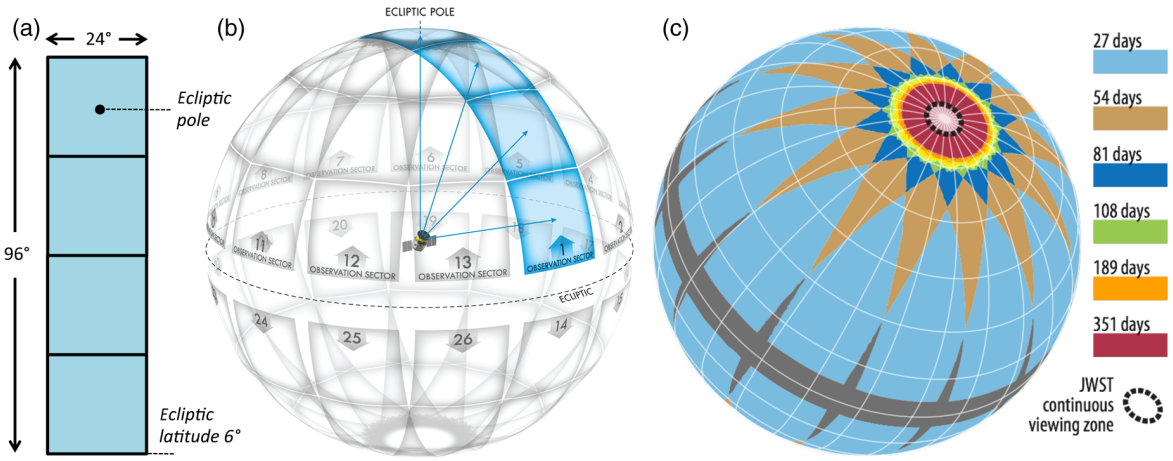

Figure 2.1: (a) Combined field of view of all four cameras. Each camera has a field of view of 24° × 24 °. (b) Global view of the celestial sphere divided into the 26 sectors of TESS. (c) Combined sky coverage. Each sector observes a portion of the sky for 27 days, some regions benefit from overlap between sectors and are indicated by the color code. The ecliptic poles are in the continuous viewing zone, and the dashed black line represent where JWST can point at any time. Figure 7 from Ricker et al. (2014).

TESS targets main sequence stars with spectral types between F5 and M5. Especially, M-dwarf stars represent the best opportunity to find small transiting planets, as explained in Section 1.2.3. Their small size facilitates the detection of small planets, and the expected periods, for a given equilibrium temperature, are smaller which produces more frequent transits. TESS is equipped with four stacked CCD cameras with fields of view of 26 ° × 26 ° each and a pixel scale of 21″ per pixel. They observe within a bandpass ranging from 600 to 1000

nm in order to be most sensitive to red dwarfs (see Figure 2.2). Assuming the photometric noise to be dominated by the camera read noise and zodiacal light, TESS is sensitive to small planets around Sun-like stars within 1000 pc, and 200 pc for a typical M dwarf star (Sullivan et al., 2015).

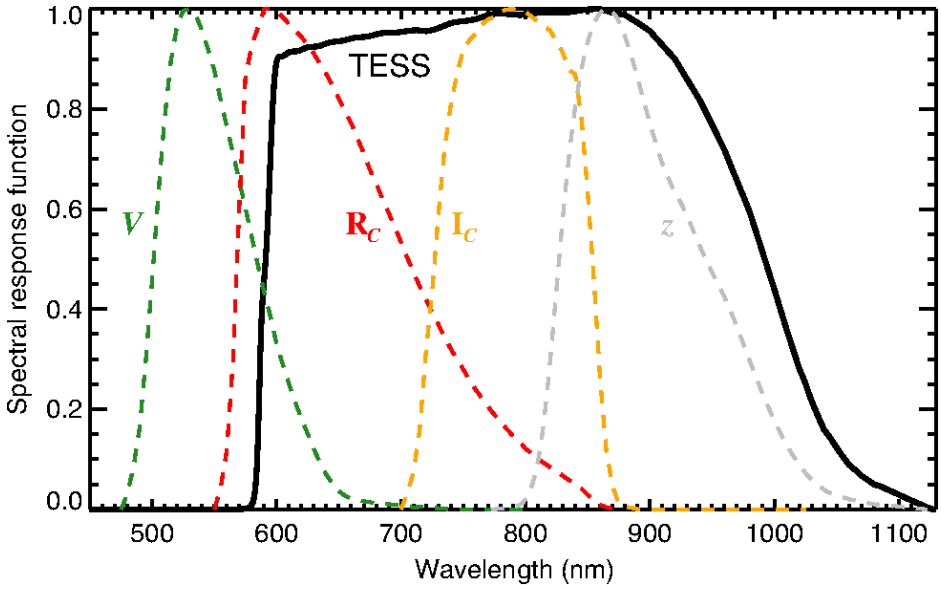

Figure 2.2: Spectral response function as a function of wavelength. The TESS spectral band is given by the solid black line, and compared to other usual bands shown with colored dashed lines. Figure 1 from Ricker et al. (2014).

Over 200 000 FGKM-type stars were initially selected for short-cadence observations with a sampling of two minutes (see Stassun et al., 2019, for a full review of the TESS Input Catalog). By the first extended mission, there was a 6 times increase of this number, and thousands more were included in the second extended mission[1]. Similarly, with the first extended mission, data with a cadence of 20 seconds were made available to the community for a select number of stars. In addition to short-cadence data, TESS provides Full Frame Images (FFIs) with a cadence of 30 minutes for the full field of view. This was reduced to 10 minutes in the first extended mission and 200 seconds in the second one.

2.1.2 Planet candidates

The TESS cameras continuously take images every two seconds. Postage stamps are created by making cutouts around the target stars and by stacking the images to create two-minute exposures. In the case of FFIs, the images are not cut out, and the exposures are grouped by 900 to create 30-minutes exposures. The TESS data are processed by two pipelines: the Science Processing Operations Center (SPOC, Jenkins et al., 2016; Jenkins, 2020) pipeline handles the postage stamps, and the Quick Look Pipeline (QLP, Huang et al., 2020a,b) takes care of the FFIs. Both pipelines are built upon the ones used for the Kepler mission. The SPOC pipeline is made of several modules with the following functions: (1) data calibration; (2) computation of the optimal apertures by maximizing the signal-to-noise ratio (S/N) of the light curves and estimation of the contamination of nearby sources; (3) extraction of the photometry with background correction and centroid measurements; (4) correction of the data to remove systematic trends. The QLP follows the same procedure but uses different methods, as explained in Guerrero et al. (2021). For instance, it always combines all the

[1] https://heasarc.gsfc.nasa.gov/docs/tess/

available sectors for a given target. It also uses a series of five fixed circular apertures to extract the photometric measurements instead of exploring a grid of pixels centered on the target.

The final light curves then go through a module dedicated to searching for periodic transit signals. In the case of the SPOC pipeline, a signal is elected as a Threshold Crossing Event (TCE) if: it has a significance of $> 7.1\sigma$, there are two or more transit events, and it passes a series of initial vetting tests to remove unrealistic transits (Twicken et al., 2018; Guerrero et al., 2021). This threshold value was selected on the basis of a statistical study to minimize the false positive rate (Twicken et al., 2016). A Data Validation (DV) module then fits a limb-darkened transit model to the periodic signal and performs a suite of robust diagnostic tests in order to identify instrumental signals or astrophysical false positives. For instance, the transit depth is evaluated between odd and even transits to identify any discrepancy, a difference image centroid offset is calculated to identify the source of the transit-like feature, a statistical bootstrap analysis is made to determine a false alarm probability, and a ghost diagnostic test is done to check if the transit feature is due to scattered light or some other contamination source (Twicken et al., 2018; Guerrero et al., 2021). In the case of the QLP, the light curves of all sectors are stitched together and a box-least squares (BLS, Kovács et al., 2002) algorithm is used to search for transit signals. A TCE is elected when the signal-to-pink-noise ratio (combining white and red noise, defined in Hartman & Bakos, 2016) is above 9, and the BLS peak significance is also above 9 (Guerrero et al., 2021). The DV diagnostic tests are similar to the ones of the SPOC pipeline. TCEs from both pipelines then go through a triage process to separate transit-like events from stellar variability or instrument systematics. Finally, the remaining TCEs are manually vetted by the TESS Science Office who award the TESS Object of Interest (TOI) label to the most promising signals in order to trigger follow-up observations. TOIs are made available to the community periodically, after each sector has been processed. Up until now, 7203 TOIs have been issued, 470 are now confirmed planets, 1554 have been discarded, and 5179 are yet to be confirmed[2].

2.1.3 TESS Follow-up Observing Program

In order to support the TESS mission and exploit at best its scientific output, the TESS Follow-up Observing Program (TFOP) Working Group (WG) was set up. It is a global collaboration between research teams that enables a large scale coordinated effort to follow-up on possible planet candidates. TFOP WG is divided into five sub-groups (SG): SG1 Seeing-limited Photometry, SG2 Recon Spectroscopy, SG3 High-resolution Imaging, SG4 Precise Radial Velocity, SG5 Space-based Photometry.

During my PhD I was involved in SG1, led by Karen Collins at MIT, with the TRAPPIST and SPECULOOS facilities. Because of the large pixel scale of $21''$, the TESS apertures are subject to crowding. As shown in Figure 2.3, there are frequently multiple stars in a single pixel which can lead to false positives. Although TOIs go through vigorous vetting, the spatial resolution is a limiting factor. The most likely remaining false positives scenarios are: the transit is not due to a planet but rather a star (eclipsing binary, EB), a nearby eclipsing binary (NEB) that can be spatially resolved, a blended eclipsing binary (BEB) that cannot be resolved but shows chromatic behavior, or a nearby planet candidate (NPC) where the transit could still be due to a planet but is on a neighboring star.

SG1 has several objectives:

- Checking if the event is on target with a red filter similar to the TESS band. This removes the possibility of NEBs or NPCs. It also confirms the existence of the transit

[2] https://exofop.ipac.caltech.edu/tess/view_toi.php, accessed on July 8, 2024.

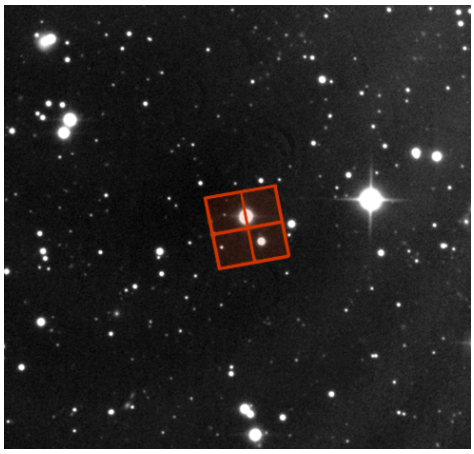

Figure 2.3: Field of view around TOI-3288 taken with Europa (SPECULOOS-South) in the $I+z$ band on August 12, 2022. The red square represents the TESS pixels selected in the pipeline aperture for sector 67. The TESS aperture includes multiple stars in addition to the target which can potentially be sources of false positives.

to remove the unlikely case of a false alarm due to detrending of the TESS light curves or stellar variability.

- Refining the ephemerides by providing updates on the transit timing and/or measure transit timing variations.
- Confirming there is no difference in the odd and even transit depths to remove the possibility of an EB.
- Measuring the depth of the transit in bluer filters to check if there is a chromatic behavior. If a transit shows strong chromaticity between the blue and red filters, it implies there is another source of light in the system. Indeed, planets are considered opaque at all wavelengths, except for their upper atmosphere, but TESS and ground-based photometry are not precise enough to detect such low-amplitude atmospheric transmission signatures.

On a weekly basis, I selected candidates to observe with TRAPPIST-South, and my colleague Mourad Ghachoui did the same for TRAPPIST-North. The candidates were then discussed with the rest of the team members (Francisco J. Pozuelos and Khalid Barkaoui), and, once agreed upon, we scheduled them on the telescopes. Once the data analysis was finalized, a report was sent to SG1 with the findings for each observation. In parallel, I did a similar job with George Dransfield and Elsa Ducrot to schedule TOI observations of planets candidates around red dwarfs with the SPECULOOS telescopes. The observation reports are shared to the SG1 members by Karen Collins and Christilyn Watkins who are coordinating this effort, and the status of the TOIs are updated accordingly. This allows an efficient large collaboration between all the observatories to avoid duplicating unnecessary observations, and a quick validation of the very numerous TOIs. The observations dedicated to SG1 of the TRAPPIST and SPECULOOS teams are illustrated in Figure 2.4.

2.2 Validation of planets from the ground

As explained in Section 2.1, planet candidates obtained from TESS are still subject to false positives. Confirming their planetary nature requires follow-up observations from ground-based facilities. In fact, we speak of a *statistical validation* when all false positive scenarios

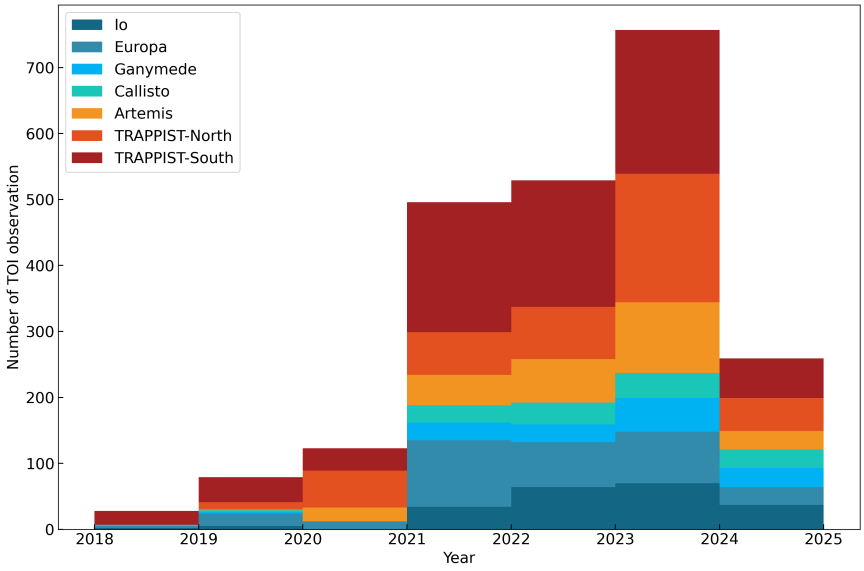

Figure 2.4: Distribution of the number of TOIs observed with the SPECULOOS and TRAPPIST networks since the beginning of the TESS mission.

have been ruled out, i.e. the transit is achromatic, on target, and possible blends have been dismissed by high-angular resolution and archival imaging. We then speak of a *confirmation* when an unequivocal measurement of the mass of the planet is obtained either from RV measurements or from TTV analyses. In the following sections, I give an overview of the methods used in this thesis to validate, confirm, and characterize planets. This includes a technical description of the observatories used for follow-up observations of TESS candidates. I also present the methods used to analyze the data and infer the properties of the planetary systems.

2.2.1 TRAPPIST

The project

The TRAPPIST (TRAnsiting Planets and PlanetesImals Small Telescope) project started in 2010 with the TRAPPIST-South telescope set up in La Silla Observatory (Chile), part of the European Southern Observatory (ESO) (Jehin et al., 2011; Gillon et al., 2011). It was installed by the University of Liège in collaboration with Geneva Observatory (Switzerland). The second telescope of the network was installed in 2016 at Oukaïmeden Observatory in Morocco by the University of Liège and in collaboration with Cadi Ayyad University of Marrakesh (Morocco) (Barkaoui et al., 2019). It is a twin of TRAPPIST-South and extends the TRAPPIST project to the northern hemisphere. The project shares equally the observing time between two main focuses: the detection of transiting exoplanets and the study of the small bodies of the solar system.

The exoplanet program is divided into three main parts: (1) the follow-up of planetary candidates of large-scale transit surveys such as CoRoT (e.g. Guenther et al., 2012), WASP (e.g. Delrez et al., 2016; Triaud et al., 2017), K2 (e.g. Sanchis-Ojeda et al., 2015), or currently TESS (e.g. Ghachoui et al., 2023; Hobson et al., 2023). The main goals of these observations are to identify false positives, provide chromaticity checks of the transit depth, and provide a refinement of the ephemerides. (2) The characterization of known transiting planets thanks to the high-precision photometry it enables. In particular, TRAPPIST has been used to monitor the transit timing variations of the planets of the TRAPPIST-1 system (Grimm

et al., 2018; Agol et al., 2021). (3) The follow-up of SPECULOOS candidates: between 2011 and 2020, the TRAPPIST network was used for a prototype survey of the SPECULOOS project (Gillon, 2018; Delrez et al., 2018; Sebastian et al., 2021), which will be described in Section 2.2.2. In short, the goal is to search over a thousand nearby ultracool dwarf stars to find habitable zone terrestrial planets. In 2017, it led to the discovery of seven temperate Earth-sized planets orbiting an M8 star (Gillon et al., 2016, 2017). TRAPPIST is no longer part of the survey as the SPECULOOS telescopes are now in operation, but it is still used to follow-up the SPECULOOS planetary candidates (e.g. the SPECULOOS-3 system, Gillon et al., 2024).

Instrumentation

Because my thesis relied mostly on observations with TRAPPIST-South, and the fact that its northern counterpart is a twin, I focus the technical description on the TRAPPIST-South telescope. It is a 0.6-m Ritchey-Chrétien light weight telescope with a focal ratio of f/8 built by the German company ASTELCO (Jehin et al., 2011). It is equipped with a NTM-500 German equatorial mount manufactured by the same company and powered by direct drive motor systems. This allows a pointing accuracy under 1″ with a pointing model, a tracking accuracy of 1″ per 4 minutes, and a slewing speed up to 50° per second. Each image is plate solved, and the software guiding system allows to keep the target centered in the same few pixels during a sequence of observations.

Figure 2.5: Images of the TRAPPIST-South telescope at ESO's La Silla Observatory in Chile.

TRAPPIST-South is equipped with a thermoelectrically-cooled FLI ProLine camera with a back-illuminated CCD chip 2048 × 2048 pixels. The pixel scale of 0.64 ″ per pixel results in a total field of view of 22′ ×22 ′. The sensitivity of the camera is shown in Figure 2.6. It peaks at 98% at 750 nm, then drops gradually to 80% at 550 nm and 60% at 300 nm in the bluer end, and 40% at 950 nm in the redder end. The gain of the camera is set to 1.1 e^-/ADU. It is the conversion factor from a number of photo-electrons to one Analog Digital Unit (ADU). The digital counts in ADUs in each pixel then represent effective measurements of the number of photons that are actually detected. The cooling system usually brings the CCD temperature down to -30°C which corresponds to a dark current of $\sim$ 0.1 e^-/s/pixel.

Three readout modes are available: a slow mode used for observations of asteroids and comets (readout noise = 9.5 e^- in 6 seconds), a fast mode used for observations of exoplanets (readout noise = 14 e^- in 4 seconds), and a very fast mode (readout noise = 14 e^- in 2 seconds). The latter has proven to be less stable, hence it is not usually selected. A double filter wheel specifically designed is placed ahead of the camera, each holding up to twelve filters. One is loaded with the broad-band filters used for exoplanets: the Johnson-Cousins *B*, *V*, *Rc*, *Ic*, the Sloan *z'* filter, as well as the custom *I+z*, and *Exo* filters. The transmission curves are shown in Figure 2.6. The second one is loaded with narrow-band filters used for the study of comets.

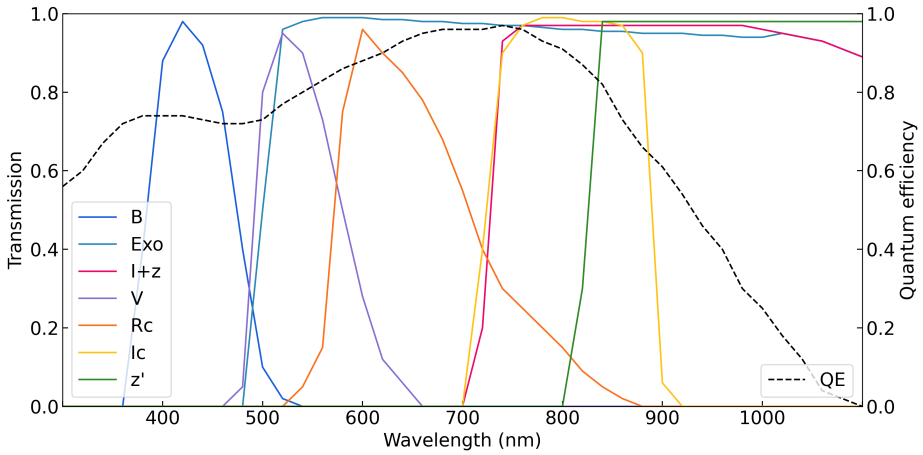

Figure 2.6: Transmission curves of the broad-band filters used for photometric observations of planetary transits with the TRAPPIST telescopes. The quantum efficiency curve of the TRAPPIST-South CCD chip is overplotted as the black dashed line.

2.2.2 SPECULOOS

The project

The smallest and latest red dwarf stars represent the best opportunity to study the atmosphere of transiting terrestrial planets with potentially habitable surface conditions. Particularly, the expected S/N on spectroscopic biosignatures with JWST is the highest for *ultracool dwarfs* (UCDs, e.g. Seager et al., 2009; Kaltenegger & Traub, 2009). They inhabit the lower end of the mass-radius parameter space, and encompass the very low-mass main sequence stars and brown dwarfs of spectral type later than M6, including L, Y, and T dwarfs, i.e. masses below $0.1M_\odot$, and radii $\sim 0.1R_\odot$ (Delrez et al., 2018). Because these targets are intrinsically faint and active, the TRAPPIST-South telescope was first used to demonstrate the feasibility of a transit survey to search for terrestrial planets (Gillon et al., 2013). This prototype survey launched in 2011 aimed to monitor the brightness of 50 of the nearest ultracool stars, and it led to the discovery of the first planetary system orbiting a UCD in 2016 (Gillon et al., 2016, 2017). TRAPPIST-1 is an M8 star hosting a compact system of seven Earth-sized planets, including three in the habitable zone. Thanks to this groundbreaking proof of concept, the SPECULOOS (Search for Planets EClipsing ULtra-cOOl Stars) project was specifically designed to extend the transit survey to over a thousand of UCDs (Burdanov et al., 2018; Delrez et al., 2018; Sebastian et al., 2021). The SPECULOOS Southern Observatory (SSO) is located at ESO's Paranal Observatory in Chile (Jehin et al., 2018), and consists of four identical 1-m class telescopes named after the Galilean moons (Io, Europa, Ganymede, and Callisto, Figure 2.7). Similarly, the SPECULOOS Northern Observatory

(SNO) located in Teide Observatory in Tenerife, Spain, currently hosts a twin of the southern telescopes named Artemis. A second telescope named Orion is under construction and should be installed in Tenerife, next to Artemis, in 2025. To complete this network, the SAINT-Ex telescope is installed at the National Astronomical Observatory of Mexico, in San Pedro Mártir. The SPECULOOS project is led by the University of Liège, in collaboration with the University of Birmingham, the University of Cambridge, the Massachusetts Institute of Technology, the University of Bern, and the ETH Zurich[3].

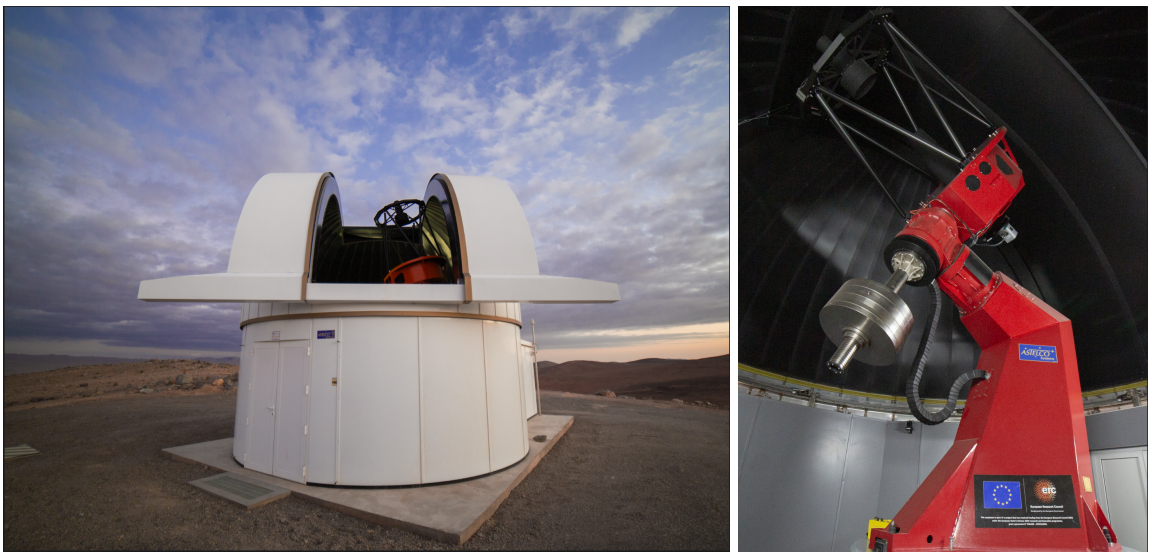

Figure 2.7: Images of the Ganymede (left) and Io (right) telescopes of the SPECULOOS Southern Observatory at ESO's Paranal Observatory in Chile.

The SPECULOOS target list is made of 1657 stars within 40 pc from the Sun, which includes mid-type M-dwarfs (M4-M6) and UCDs, as well as over 100 L-type brown dwarfs (Sebastian et al., 2021). This volume limited sample allows to fulfill the two main objectives of the survey: detecting terrestial planets well-suited for atmospheric characterization with JWST, and provide occurrence rate for planets orbiting UCDs. In order to optimise the scientific return of the survey, it is divided into three programs: Program 1 includes 365 targets for which an 'Earth-like' planet with an irradiation of 1 $S_{\oplus}$, similar to the Earth's, would allow transmission spectroscopy with JWST. Program 2 includes 171 targets where an Earth-sized planet with an irradiation of 4 $S_{\oplus}$ could be detected by the TESS mission. The goals of Program 2 include investigating the TESS data to search for potentially missed low S/N inner planet candidates in TOI systems, and using the improved precision of SPECULOOS to search for outer planet candidates as was succesfully done for the SPECULOOS-2 system (Delrez et al., 2022). Program 3 contains the remaining targets of the full volume limited sample. The observing strategy relies on the observation of each target for a total time between 100 and 200 hours depending on the program. This allows to reach an effective phase coverage of up to 80% for planets in the habitable zone in the case of Program 1 targets, and planets with $4S_{\oplus}$ in the case of targets in Programs 2 and 3. So far, the SPECULOOS survey has yielded the discovery of two new planetary systems around late-type M-dwarfs (Delrez et al., 2022; Gillon et al., 2024). In addition to the core program, 20% of the observing time is dedicated to annex programs, such as the follow-up of TESS candidates or special observation requests for specific projects. This has already led to the discovery of dozens of planets (e.g. Wells et al., 2021; Schanche et al., 2022; Triaud et al., 2023; Hobson et al., 2023; Pozuelos et al., 2023; Ghachoui et al., 2023; Dransfield et al., 2024; Barkaoui et al.,

[3] https://www.speculoos.uliege.be/cms/c_4259452/en/speculoos?id=c_4259452

2023), including the discoveries of the two planets of the TOI-4336 A system, and TOI-237 c, described in Chapters 3 and 5.

Instrumentation

All the SPECULOOS telescopes are fully robotic 1-m class telescopes built by the German company ASTELCO. They are Ritchey-Chrétien telescopes with f/8, equipped with a NTM-1000 mount powered by direct drive torque motors (Jehin et al., 2018). This allows very fast slewing (8°/second, up to 20°/second), a pointing accuracy better than 5″, and a tracking accuracy better than 1″ over 10 minutes without periodic errors (Delrez et al., 2018). The guiding system enabling the targets to remain on the same few pixels for a whole exposure sequence is an updated version of the DONUTS autoguiding system (McCormac et al., 2013).

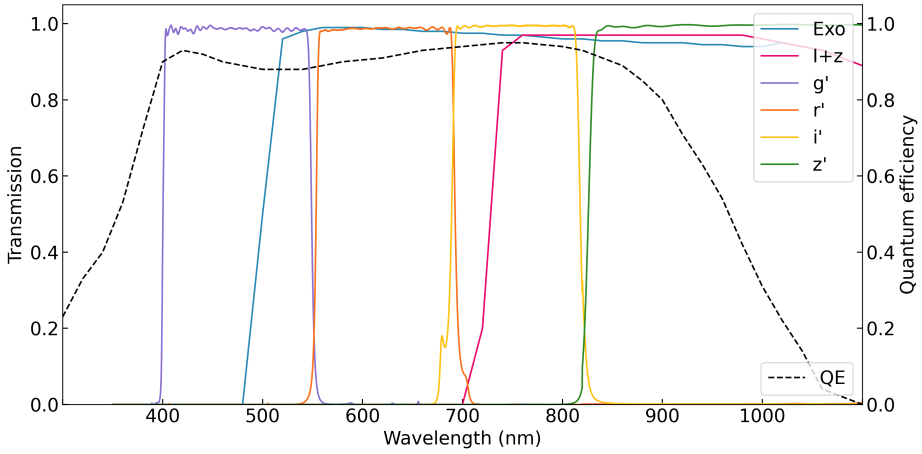

Figure 2.8: Transmission curves of the broad-band filters used for photometric observations of planetary transits with the SPECULOOS telescopes. The quantum efficiency of the SPECULOOS CCD chip is overplotted as the black dashed line.

On each of the SPECULOOS telescopes are installed a thermoelectrically-cooled Andor iKon-L camera with a deep-depletion CCD chip of 2K×2K pixels. The total field of view is $12' \times 12'$, resulting in a pixel scale of 0.35″ per pixel. The camera sensitivity peaks at 420 and 740 nm with a quantum efficiency of 94%, although it provides a good sensitivity between 350 and 950 nm (see Figure 2.8). The camera is operated at -60°C, which corresponds to a dark current of $\sim 0.1 e^-/s/pixel$. The SPECULOOS observations are performed using a 1MHz readout mode, providing a readout noise of 6.2 e^-. The resulting gain of the camera is 1.04 e^-/ADU. The filter wheel is attached to all cameras, each allowing up to ten filters. For the broad-band filters chosen for the SPECULOOS projects are the Sloan-g', -r', -i', -z', as well as the custom $I + z$ and *Exo* filters. The transmission curves are given in Figure 2.8. Only the SAINT-Ex telescope is operated with slightly different settings than the other telescopes: the camera is cooled at -70°C, and the gain is set to 3.6 e^-/ADU. This is optimized for the ground-based support SAINT-Ex brings to the CHEOPS mission (Benz et al., 2021).

2.2.3 Data reduction and photometry with `prose`

The process of transforming a sequence of raw astronomical images into a light curve gives the scientific product required to extract the physical parameters of a transiting system. To do so, astronomers use so-called processing "pipelines", referring to softwares that ingest the raw data and generate specific end products by combining individual algorithms and sub-routines (i.e. pipes in the analogy).

During the most of my thesis, I assisted Lionel Garcia in the development of `prose`[4], a Python package to build personalized image processing pipelines (Garcia et al., 2021, 2022). Such a modular concept is made possible thanks to the software architecture utilizing three key objects: an *Image* that contains the data and metadata of an exposure frame, a *Block* that is a single processing unit performing a specific action on an image, and a *Sequence* that is composed of blocks assembled to process images. This is illustrated in Figure 2.9.

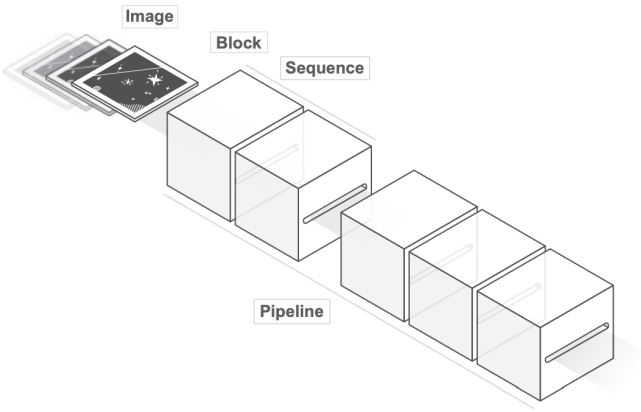

Figure 2.9: Illustration of the `prose` key objects. Figure 1 from Garcia et al. (2022).

My involvement resided in testing, in the context of follow-up observations of TESS candidates, newly developed blocks and fix and/or report any bugs. Describing in detail each block is beyond the scope of this thesis, I refer to the paper presenting the package (Garcia et al., 2022) and the online documentation[5] for a thorough description. In this context, I led the development of annex package to `prose`, named `verse`[6], specifically designed to deal with TESS follow-up observations. The package allows the user to reduce raw images, build a transit light curve, model the transit, and create automatic reports that follow the TFOP SG1 guidelines. In the following sections, I describe the main processing steps included in the pipeline built with `prose` and `verse` that I used to reduce follow-up photometric data, extract light curves, and produce reports for TFOP SG1.

Image processing pipeline

Let us consider the time-series photometric observation of a transit where the data is made up of a suite of raw images. First, an image is selected as a reference for the observation. Because raw astronomical images are subject to systematic sources of noise of instrumental origin, they need to be calibrated prior to any scientific use. The calibration, also called *reduction*, is a multi-step correction process:

- **Bias images** are taken at the beginning and end of each night, with an exposure time of zero, and the camera shutter closed. The CCD is simply read out to measure the offset voltage applied to each pixels of the CCD chip, called *bias*. This is required to ensure there are no negative counts during readout. A master bias image is created by taking the median of a set of bias images. An example of all master calibration frames is shown in Figure 2.10.

[4] Available at https://github.com/lgrcia/prose/
[5] https://prose.readthedocs.io/en/latest/index.html
[6] Available at https://github.com/mathtimm/verse

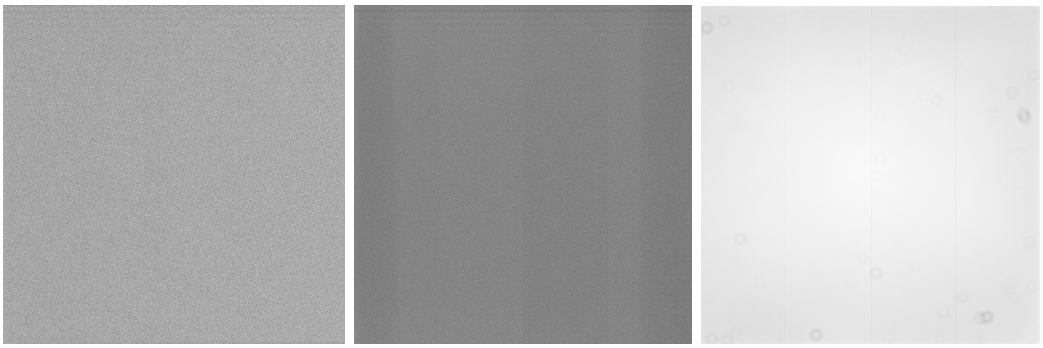

Figure 2.10: Example of calibration frames for the observation of TOI-3288.01 with SSO/Europa on August 22, 2022. From the left to right: master bias, master dark, master flat.

- **Dark images** are also taken at the beginning or end of each night, with the shutter closed and varying exposure times. Dark current is produced by thermally excited electrons in the CCD. The dark images allow to measure the amount of dark current for a given exposure time. They are usually taken with the same exposure time as the science images. As the dark current scales linearly with time, it is also standard to use dark frames of various exposure times and produce the master dark by taking the median of the scaled images.
- **Flat images** are taken around nautical twilight and dawn as the sky presents a uniform field. The goal of flat-fielding is to correct for the pixel-to-pixel sensitivity, any vignetting effect, and the presence of dust particles on the camera window or filters. As these effects are chromatic, flat images are taken with the same filter as the observation. The exposure time is selected depending on the sky brightness to reach around 30 000 ADUs in each frame. Similarly to the other calibration frames, a master flat is created by taking the median, and normalized.
- Before calibrating the science images, the master dark is corrected for the bias by subtracting the master bias. Likewise, the master flat needs to be corrected for the dark current and the bias, then divided by the mean of the individual flat fields.
- Calibrated science images are obtained by subtracting the master bias and the master dark, and dividing by the master flat.

Once the reference image is calibrated, a detection algorithm based on image segmentation implemented by `PhotUtils`[7] finds the n brightest stars, and the effective point-spread function (PSF) is characterized. This gives access to the typical value of the full-width at half-maximum (FWHM) for the stars in the field during the observation. The positions of the stars on the detector are stored in the reference Image object to be used for the whole observation.

A second sequence is used to process the full set of images, starting with the calibration step. Although the guiding software keeps the target within the same few pixels during a full observation sequence, the stars in the field of view are not perfectly aligned in all the images. The `twirl`[8] package allows to compute the transformation matrix between each image and the reference. The star coordinates are then aligned using the calculated transformation for each image, and the `ballet`[9] algorithm is used to refine the star position on the centroid.

[7] https://photutils.readthedocs.io/en/stable/segmentation.html
[8] Available at https://github.com/lgrcia/twirl
[9] Available at https://github.com/lgrcia/ballet

Aperture photometry is then performed: for each image, the total flux of the detected stars is measured in a set of forty circular apertures. They are automatically scaled to the FWHM of the effective PSF, ranging from 0.1 to 10 times the FWHM, but a set of radii can also be provided as input. Finally, external parameters able to impact the measured fluxes are also recorded for each image. These include the airmass, the mean of the FWHM of the effective PSF, an estimation of the background flux levels, and the displacement of the target along the x and y axes of the detector.

Differential photometry

Because we are only interested in relative flux variations for follow-up observations, we use the standard technique of differential photometry. It relies on the assumption that stars in the field of view are affected by the same systematic effects, whether atmospheric or instrumental in origin. Differential photometry aims to reduce these non-astrophysical patterns in the target star by dividing its absolute flux by the combination of the absolute fluxes of a set of comparison stars. `prose` uses a Python implementation of the algorithm presented in Broeg et al. (2005) for the automatic selection of comparison stars and optimal aperture. It is done by building an artificial comparison star by combining the weighted sum of all the detected stars. The weights are obtained in iteratively by minimizing the variance over all the differential light curves. This entails that higher S/N comparison stars are given higher weights compared to stars displaying large variability. The optimal aperture is then selected by minimizing the white noise in the differential light curve of the target. `prose` also allows to manually select comparison stars and apertures if needed. The final product of `prose` is a differential light curve, hopefully showing a clear transit.

Reporting with `verse`

As explained in Section 2.1.3, the follow-up observations of TESS candidates can have multiple purposes. If a transit appears clearly in the data, we want to compare it to the transit parameters obtained with the TESS pipelines and report any deviation. A modeling function is implemented in `verse` using the `exoplanet`[10] (Foreman-Mackey et al., 2021) and `PyMC3` (Salvatier et al., 2016) packages that implement a Markov Chain Monte Carlo-based (MCMC) sampler. The MCMC technique is briefly discussed in Section 2.2.5. The `verse` function automatically searches the ExoFOP[11] database to access the system parameters obtained from TESS and use them as prior probability distribution function (PDFs) in the statistical modeling of the transit.

In the case no clear transit is visible, it is possible one of the nearby stars is the source of the TESS alert. In `verse` is implemented a Python version of the near-eclipsing binary check of `AstroImageJ` (Collins et al., 2017). It searches all detected stars within a $2.5'$ radius for a possible transit-like signal. A score is attributed to each star by comparing the expected depth, taking into account the dilution of the transit per star, and the root-mean square (RMS) scatter of the data. The stars are then categorized: (a) *likely cleared* if the score is between 3 and 5; (b) *cleared* is the score is over 5; (c) if the expected depth exceeds 100% the star, is deemed *too faint* to be the source of the event; (d) if the mean flux per aperture pixel is < 2, the *flux is deemed too low* to conclude; (e) if none of these conditions are met, the star is *not cleared*.

The reports are constructed by creating LaTeX pages assembled into a single pdf file. The first page contains a summary of the observation processed with `prose`, an example is given in Figure 2.11. It includes the results of the characterization of the PSF and the

[10] Available at https://github.com/exoplanet-dev/exoplanet
[11] https://exofop.ipac.caltech.edu/tess/

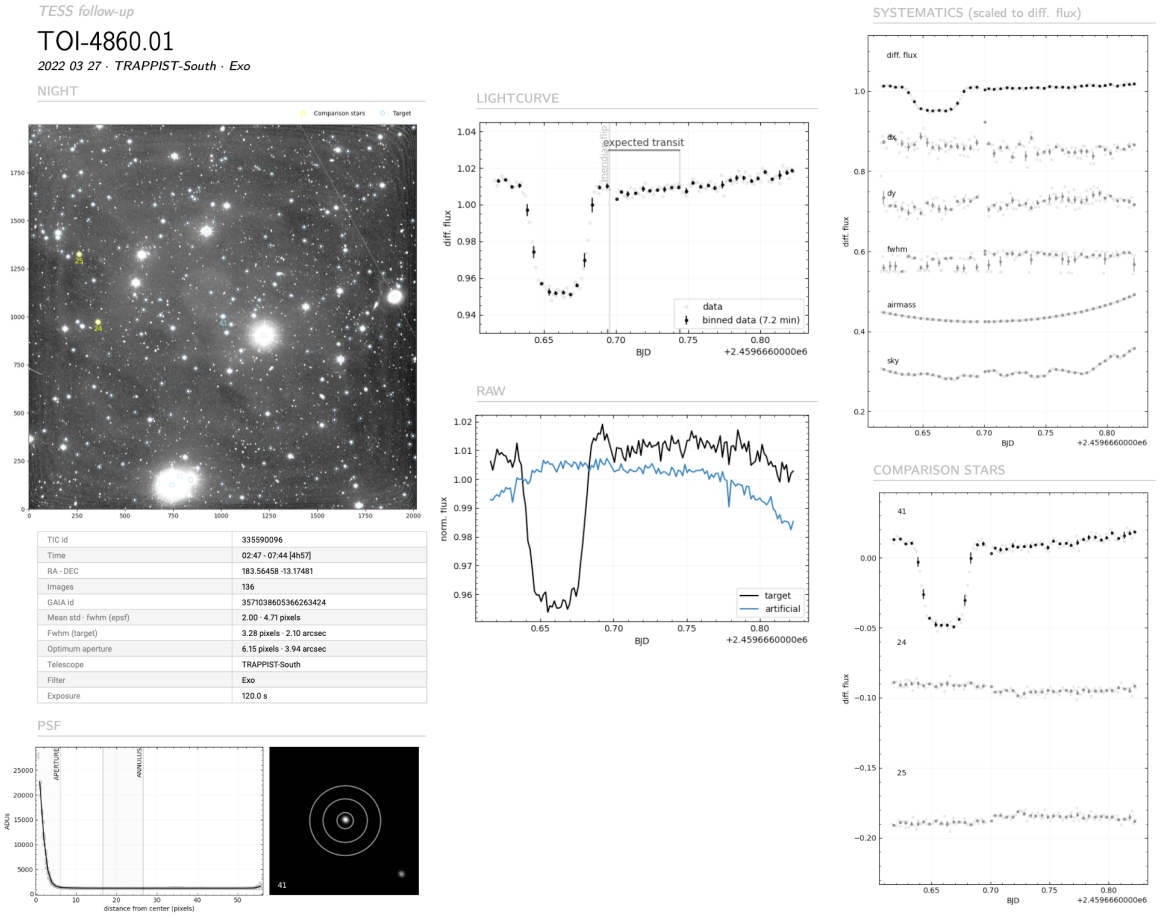

Figure 2.11: Summary page produced by `verse` for the observation of TOI-4860 b with TRAPPIST-South in the *Exo* filter obtained on March 27, 2022. It includes a field image with the detected stars, a summary of the important quantities to characterize the observation such as the FWHM of the PSF, the size of the optimum aperture, etc. It also shows a plot of a radial cut of the PSF of the target and the background annulus. The final light curve is plotted against the expected transit, and the artificial comparison light curve produced during the differential photometry is also shown. In the upper right, a plot shows the evolution of the external parameters during the observation. It is used to help identifying any possible correlation between the measured fluxes and one or several of these external parameters. Finally, in the lower right, the target light curve is confronted to the ones of the comparison stars.

differential photometry. A second page can be added with the results of the transit modeling with `verse` and the comparison with the transit parameters obtained from TESS, as shown in Figure 2.12. In the case a NEB diagnostic needs to be established, a summary page showing the results and the suspicious stars can also be added. An example is given in Figure 2.13. Finally, `verse` produces a page with the observing notes based on the results of the full analysis. The two reports used to illustrate this section are given in full in section A.1.

2.2.4 Statistical validation of the planet

Because many of the Kepler planet candidates were too faint to be confirmed by precise radial velocities, the process of *statistical validation* was developed. It relies on statistical methods to rule out all astrophysical false positive scenarios to a confidence degree similar

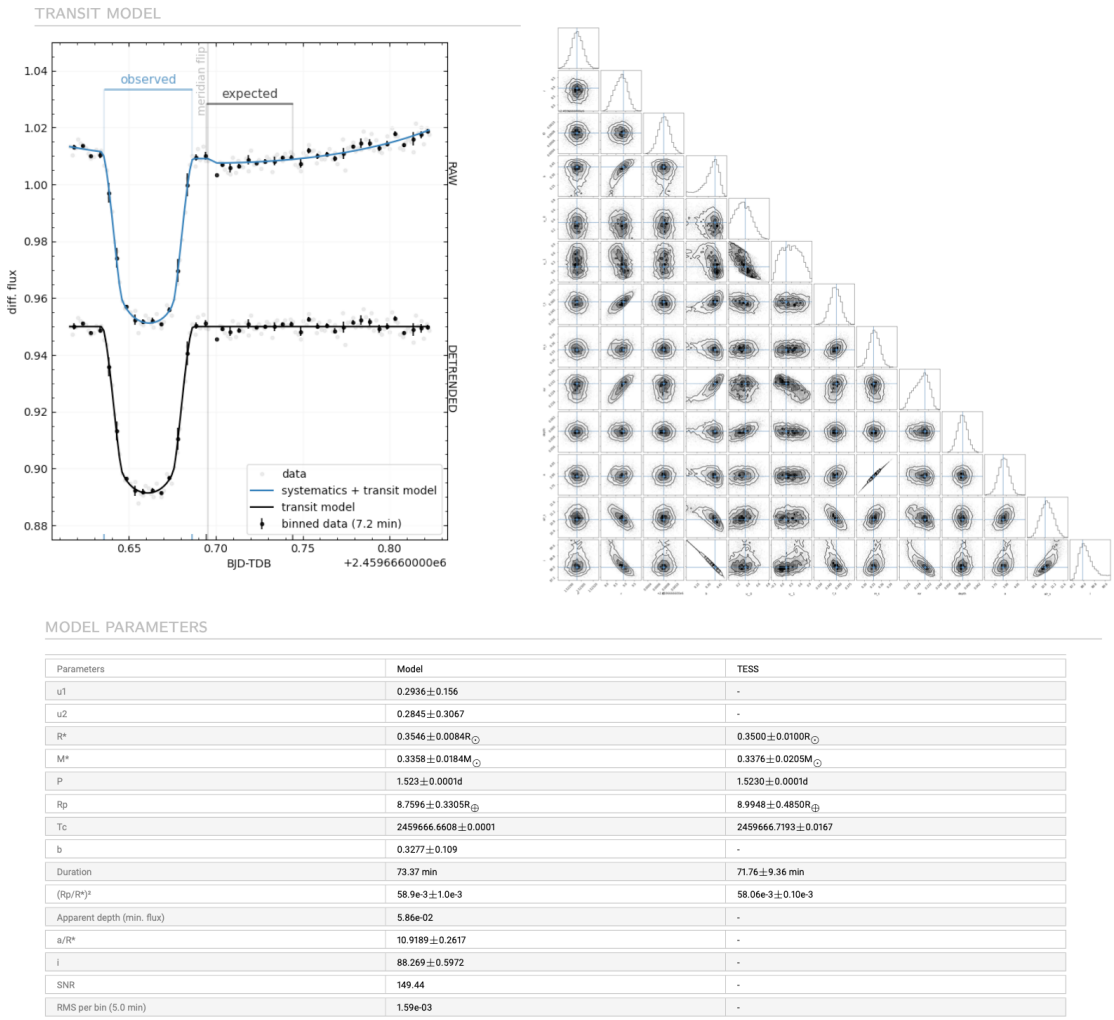

Parameters	Model	TESS
u1	0.2936±0.156	-
u2	0.2845±0.3067	-
R*	0.3546±0.0084$R_\odot$	0.3500±0.0100$R_\odot$
M*	0.3358±0.0184$M_\odot$	0.3376±0.0205$M_\odot$
P	1.523±0.0001d	1.5230±0.0001d
Rp	8.7596±0.3305$R_\oplus$	8.9948±0.4850$R_\oplus$
Tc	2459666.6608±0.0001	2459666.7193±0.0167
b	0.3277±0.109	-
Duration	73.37 min	71.76±9.36 min
(Rp/R*)²	58.9e-3±1.0e-3	58.06e-3±0.10e-3
Apparent depth (min. flux)	5.86e-02	-
a/R*	10.9189±0.2617	-
i	88.269±0.5972	-
SNR	149.44	-
RMS per bin (5.0 min)	1.59e-03	-

Figure 2.12: Transit model page produced by `verse` for the observation of TOI-4860 b with TRAPPIST-South in the *Exo* filter obtained on March 27, 2022. On the top left the transit and systematics model is shown as the solid blue line, and the black line is the transit model with the systematics removed. On the top right is a `corner` plot of the posterior PDFs of the transit parameters (Foreman-Mackey, 2016). They are given in the table, with their associated uncertainties, and compared to the values given in the ExoFOP database.

to the one of a mass measurement. Several statistical validation algorithms were used for the Kepler sample of candidates, such as `Blender` (Torres et al., 2011) , `Vespa` (Morton, 2012), or `pastis` (Díaz et al., 2014). With varying probabilistic frameworks, they each relied on the generation of synthetic light curves of transiting planets and EB scenarios, identified statistically viable scenarios compared to the planetary one, and used follow-up observations to obtain tighter constraints on the overall false-positive probability (FPP). Since the pixel scale of TESS is much larger than Kepler's, the basic assumption of these algorithms that only one external source could be the origin of false positives is no longer likely. `Triceratops`[12] (Giacalone et al., 2021) was then formulated specifically to include multistar analyses using the TIC catalog (Stassun et al., 2019). This algorithm considers in total fifteen different scenarios involving the target star, including a transiting planet, EB scenarios, BEB scenarios, and three for each bright nearby star. It then calculates the

[12] Available at https://github.com/stevengiacalone/triceratops

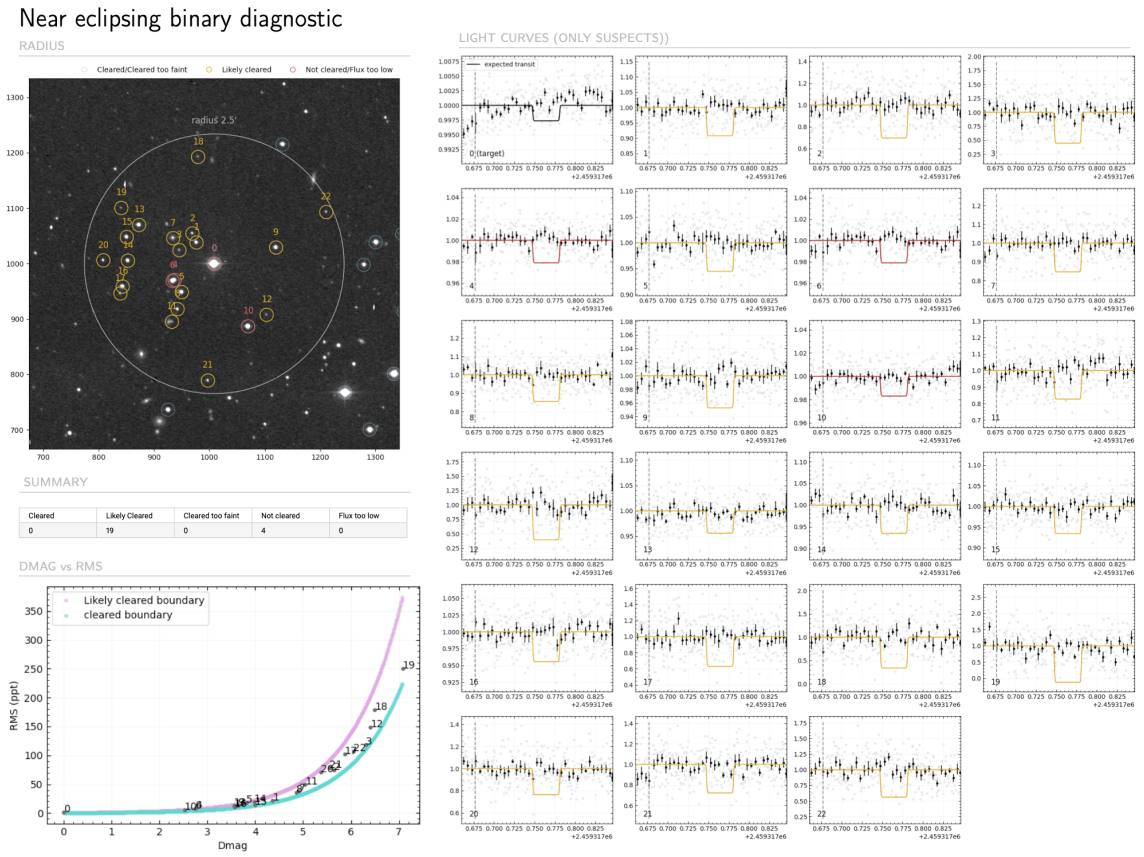

Figure 2.13: NEB diagnostic page produced by `verse` for TOI-2354.01 observed on April 12, 2021 with TRAPPIST-South in the $I+z$ filter. The top left panel shows the zoomed-in field of view, including the target and all the detected stars within a 2.5′ radius. The plot on the lower left shows the mean difference in magnitude with respect to the target as a function of the RMS for each star to highlight the likely cleared stars. The likely cleared and the cleared boundaries are defined for scores 3 and 5, respectively, and are plotted in pink and cyan. The light curves of the non-cleared stars are plotted on the right with the expected transit to visualize any possible transit-like feature.

FPP and nearby false positive probability (NFPP) by fitting models for each scenario on the phase folded TESS light curves. If the FFP<0.015 and the NFPP$<10^{-3}$, a candidate is classified as validated planet. `Triceratops` also allows to include follow-up observations such as contrast curves obtained from high-resolution imaging, or ground-based photometry to lower the FPP and NFPP values.

2.2.5 Light curve analysis in a Bayesian framework

A transit light curve corresponds to observational data describing a true physical system. In Section 1.2.2, we reviewed how the transit parameters are linked to observable quantities of the light curve. The framework of Bayesian inference allows to construct a probabilistic transit model incorporating the new information (i.e. the observed data) with any prior knowledge on the system. This approach also allows to consistently: combine different types of observational data (photometric time series, radial velocity, etc.), give access to a comprehensive quantification of the uncertainties, produce a self-consistent estimation of the parameters, and perform model comparison (Parviainen, 2018). Bayes' theorem is the key

concept of Bayesian statistics:

$$\Pr(H \mid D) = \frac{\Pr(H)\Pr(D \mid H)}{\Pr(D)}, \tag{2.1}$$

where:

- $\Pr(H \mid D)$ is the *posterior probability* for a hypothesis H given the data D.
- $\Pr(H)$ is the *prior probability* for the hypothesis.
- $\Pr(D \mid H)$ is the *likelihood*, the probability of the data D given the hypothesis H.
- $\Pr(D)$ is the *evidence*, it is the probability of the data D.

Considering Bayes' theorem in terms of parameter estimation, we can write:

$$P(\theta \mid y) = \frac{P(\theta)P(y \mid \theta)}{P(y)} = \frac{P(\theta)P(y \mid \theta)}{\int P(\theta)P(y \mid \theta)d\theta}, \tag{2.2}$$

where the hypothesis H is a model parameter vector θ, y represents the observed data, and all probabilities are continuous probability distributions. The prior distributions $P(\theta)$ encapsulate the current information about the model parameters. They are updated by the likelihood as new data is obtained to produce posterior distributions that can be used as prior in a subsequent analysis. Importantly, priors can put tight constraints on the posterior distributions, in that case we speak of *informative* priors, or inversely priors can produce weaker constraints, they are then said *uninformative*. In practice, the priors take the form of normal or uniform distributions in the respective cases of informative and uninformative priors. The likelihood $P(y \mid \theta)$ represents the probability that the observed data follows the model for a given point in the associated parameter space. It is usually made up of a deterministic part that can be described by a parametric model, and a stochastic part due to the noise which can be correlated (red noise) or uncorrelated (white noise). The denominator $\int P(\theta)P(y)d\theta$ is the model evidence, also called *marginal likelihood*. This important quantity is the one used in Bayesian model comparison.

In the case of parameter estimation, the model evidence is a normalizing term that can be ignored. Doing so, the joint posterior distribution is given by $P(\theta \mid y) = P(\theta)P(y \mid \theta)$. We can marginalize for each parameter over the parameter space to get *marginal posterior distributions* by $P(\theta_i \mid y) = \int P(\theta \mid y)d\theta_{j\neq i}$. In many practical cases, the joint posterior distribution is not analytically accessible due to its complex nature. Sampling methods are then used to explore it and construct the marginal posterior distributions for each parameter, which are in turn used to find the best-fit values and their associated uncertainties. In the following sections I describe the Markov Chain Monte Carlo (MCMC) and nested sampling algorithms, two of the standard methods used to sample from the posterior in transit modeling that have been used in this thesis.

MCMC samplers

One of the most widely used algorithm class to sample from the posterior distribution is Markov Chain Monte Carlo (MCMC) (e.g. Gregory, 2005; Gelman et al., 2013; Parviainen, 2018). There are many implementations of MCMC methods used in the context of the modeling of photometric time series data. In the following paragraphs, I describe briefly the concepts of the methods implemented in the codes used throughout this thesis: (1) the adaptive MCMC sampler `Trafit` presented in Gillon et al. (2012) (and references therein), which I used for the validation of TOI-4336 A b (see Chapter 3); (2) the NUTS sampler

(Hoffman & Gelman, 2014) of `PyMC3` (Salvatier et al., 2016) associated with the `exoplanet` package (Foreman-Mackey et al., 2021), which I used for the `verse` reports described in Chapter 2.2.3.

MCMC methods leverage the concept of a Markov chain to perform Monte Carlo sampling: a *Markov chain* is a series of samples where the state of each new sample is only dependent with some probability on the state of the current sample; *Monte Carlo* methods rely on the repeated random sampling of a distribution to approximate solutions. In short, MCMC methods construct a Markov chain that has the posterior distribution as its equilibrium distribution, and as the chain is run for a long time and the stationary state is reached, the samples drawn approximate samples from the posterior distribution.

One way to construct a Markov chain is the Metropolis Hastings algorithm (Hastings, 1970). It describes how the transitions are made from one sample to the other through a series of steps that can be summarized by:

- We start with an initial state corresponding to a set of parameters θ_0.
- We generate a candidate state θ_{t+1} by drawing a sample in a distribution dependent on the current state $g(\theta_{t+1} \mid \theta_t)$. This distribution is usually centered on θ_t and can be symmetric or not.
- We calculate a model with the proposed parameters θ_{t+1} and compute the χ^2_{t+1} to measure the goodness of the fit. A merit function M_{t+1} is then computed by combining the χ^2_{t+1} with any prior knowledge on the system parameters which acts as penalties. The likelihood ratio $r = e^{-(M^2_{t+1} - M^2_t)/2}$ is computed to evaluate the probability of the transition between θ_t and θ_{t+1}.
- If $r \geq 1$ (i.e. $M^2_{t+1} \leq M^2_t$), the new state is accepted. If not, we draw a random sample u in a uniform distribution between 0 and 1, and:
  - if $u \geq r$ the candidate is accepted,
  - if $u < r$ the candidate is rejected, and a new one is generated from the same distribution $g(\theta_{t+1} \mid \theta_t)$.

The Metropolis-Hastings algorithm is iterative, once the equilibrium distribution is reached, the sampling acts as a Monte Carlo process randomly drawing from the target distribution. The more this distribution is sampled, the best is the approximation to the posterior density. Because the first iterations are not representative of the target distribution, we define a *burn-in* phase after which we assume equilibrium is reached, usually it is the first 20% of the chain. To test the convergence towards the posterior distribution, one can use the Gelman-Rubin diagnostic (Gelman & Rubin, 1992). It compares the estimate for the marginal posterior variance V for the parameter θ to the mean within-chain variance W. These two quantities should be approximately equal for a converged chain and the estimated scale reduction for M chains with N steps,

$$\begin{aligned} \sqrt{\hat{R}} &= \sqrt{\frac{\hat{V}}{W}}, \\ &= \sqrt{\frac{N-1}{N} + \frac{M+1}{MN}\frac{B}{W}}, \end{aligned} \tag{2.3}$$

should be close to 1 (Parviainen, 2018). B is the between-chain variance, and W the within-

chain variance given by:

$$
\begin{aligned}
B =& \frac{N}{M-1} \sum_{m=1}^{M} (\hat{\theta}_m - \hat{\theta})^2, \\
M =& \frac{1}{M} \sum_{m=1}^{M} \hat{\theta}_m^2,
\end{aligned}
\tag{2.4}
$$

where $\hat{\theta}$ is the parameter mean estimated using all samples, and $\hat{\theta}_m$ and $\hat{\sigma}_m^2$ are the mean and the parameter variance estimated from a single chain m. The Gelman-Rubin diagnostic has to be computed for all parameters.

`Trafit` also allows to use the `EMCEE`[13] sampler presented in Foreman-Mackey et al. (2013) through a `Fortran` implementation. It is a Python implementation of the affine-invariant ensemble sampler for MCMC presented in Goodman & Weare (2010). `EMCEE` uses parallel chains made of affine invariant ensemble samplers called *walkers*. Each walker represents a position in the full parameter space. A proposal is done for a new position of a walker k by considering the current position of all other walkers. The new position is either accepted or rejected based on the detailed balance condition, similarly to Metropolis-Hastings. The operation is repeated a number of iterations to reach the stationary state. The affine-invariant ensemble sampler is particularly well-suited for high-dimensional models, and the convergence can also be tested by the Gelman-Rubin diagnostic.

Finally, the `exoplanet` package used to model single transits for SG1 reports allows to manually build a transit model. The posterior distribution is then sampled by an implementation of The No-U-Turn Sampler (NUTS) in `PyMC3`. It is a self-tuning variant of Hamiltonian Monte Carlo (Duane et al., 1987), an advanced MCMC method. It makes use of the concept of Hamiltonian mechanics to propose new states in the Markov chain. NUTS takes advantage of gradient information from the likelihood and achieves much faster convergence than traditional sampling methods, especially for larger models.

Nested Sampling

When there are several possible models to explain the observed data, Bayesian model comparison provides a formal way of evaluating their probabilities given any prior information on the system (e.g. Gregory, 2005; Trotta, 2008; Parviainen, 2018). Naturally, a model with more free parameters will fit the data as well as a simpler model, if not better. However, increased model complexity is not necessarily required to explain the data. The guiding principle of model comparison is known as Occam's razor: the simplest theory compatible with the observed data should be favored. In practice, this effect is governed by the number of free parameters and the range of prior values. Indeed, models that can access a large range of values in the parameter space that are not supported by the data and prior knowledge are penalized for their unwarranted complexity.

In Equation 2.2, the denominator is the Bayesian evidence, also called marginal likelihood, as described in Parviainen (2018):

$$
Z = \int P(\theta) P(y \mid \theta) d\theta. \tag{2.5}
$$

This quantity represents the probability of the data given a model with a set of parameters θ, it can also be recognized as the integrated posterior density, i.e. the likelihood multiplied by the prior for a given parameter. The likelihood measures how well the parameters θ explain

[13] Available at https://github.com/dfm/emcee

the data, increasing the number of parameters increases the likelihood because it will give a better fit. In that case, each parameter is associated with a prior which overall occupies a larger parameter space than for a simpler model. Because it is more spread out, it dilutes the likelihood, lowering the evidence. For a model with a higher complexity to be favored, the likelihood must increase more than the prior penalizes the posterior.

Given two competing models M_0 and M_1, we look at the ratio of the posterior probabilities, or *posterior odds*:

$$O_{01} = \frac{\Pr(M_0 \mid y)}{\Pr(M_1 \mid y)} = \frac{Z_0}{Z_1}\frac{P(M_0)}{P(M_1)} = B_{01}\frac{P(M_0)}{P(M_1)}, \tag{2.6}$$

where B_{01} is the *Bayes factor*, the ratio of the model evidences, and $P(M_0)$ and $P(M_1)$ are the prior probabilities. If $B_{01} > 0$, M_0 is favored, and inversely if $B_{01} < 0$, M_1 is favored. The Bayes factor represents how the relative odds between two models have changed after the data is considered, regardless of what we believed prior to the data (represented by the ratio of the priors). Kass & Raftery (1995) proposed guidelines to evaluate the strength of a model compared to another: if $B_{01} > 150$, the evidence against M_1 is very strong, if $150 > B_{01} > 20$ is it strong, if $20 > B_{01} > 3$ it is positive, and if $3 > B_{01} > 1$ it is worth mentioning but not significant enough to conclude.

One of the challenges to compute the evidence is that it involves a multi-dimensional integration over the full parameter space. In 2004, John Skilling proposed a new algorithm that solves this issue focused on the computation of the evidence rather than the posterior (Skilling, 2004): nested sampling transforms the multi-dimensional integral into a one-dimensional integral over the likelihood levels. It does so by introducing the concept of *prior mass* X which represents the cumulative probability of the prior distribution enclosed by a certain likelihood level:

$$\begin{aligned} X(L) &= \int_{L(\theta)>L} P(\theta)d\theta, \\ \Rightarrow Z &= \int_0^1 L(X)dX, \end{aligned} \tag{2.7}$$

where $L(\theta)$ is the likelihood of the parameters θ, and L is a certain value in the likelihood space. I describe briefly the algorithm below, for a full description I refer to Skilling (2004):

- N points are drawn from the prior distribution of the parameters θ: θ_1, ..., θ_N. The evidence Z is initalized at $Z = 0$, and the prior volume $X_0 = 1$.
- The lowest likelihood associated with the points of the sample is L_i. We set $X_i = exp(-i/N)$ where i is an iteration, and $w_i = X_{i-1} - X_i$. We increment Z by $L_i w_i$.
- The point corresponding to L_i is replaced by a new point drawn from the prior distribution, with the condition $L(\theta) > L_i$ to sample increasing likelihoods.
- The evidence is then approximated by $Z_i \approx \sum_i (L_i w_i)$. We iterate this process until a convergence criterion is met. For example, the algorithm can track $\Delta logZ = logZ_i - logZ_{i-1}$ and if this quantity is below a threshold of typically 0.01, the evidence is considered converged.
- The sampling of the posterior is a direct byproduct of nested sampling. The parameters θ_i are in fact already samples of the posterior distribution, they only need to be weighted by $W_{\theta_i} = \frac{L_i w_i}{Z}$.

During this thesis, I used the `Allesfitter`[14] (Günther & Daylan, 2019, 2021) package to perform model comparison (see Chapter 5). It is a flexible Python package that allows to combine photometric and radial velocity data and produce a global model. It uses `dynesty`[15] (Speagle, 2020) for nested sampling to compute the evidence and sample the posterior distribution.

2.3 Finding new candidates with `SHERLOCK`

The process of identifying TCEs in the TESS data and electing them to TOIs was reviewed in Section 2.1.2. The choice of 7.1σ in significance for the transit events was made to minimize the false positives. Although, this leaves room for true positives to be missed by the TESS pipelines. For this reason, the `SHERLOCK`[16] (Searching for Hints of Exoplanets fRom Light curves Of spaCe-based seeKers) pipeline was developed. It was first introduced in Pozuelos et al. (2020) and Demory et al. (2020), and the most advanced version is presented in Dévora-Pajares et al. (2024). This user-friendly package allows to carefully scrutinize the TESS data following a multi-detrend and iterative transit search approach. It is organized into seven modules briefly described as:

- Light curve acquisition and preparation: the light curves for a given TIC number are automatically downloaded from the NASA Mikulski Archive for Space Telescope using the `lightkurve` package (Lightkurve Collaboration et al., 2018). The user can choose to specify the cadence, and, by default, the detrended Pre-search Data Conditioning Simple Aperture (PDC-SAP) flux is selected. Noisy regions can be masked by specifying an RMS limit. The light curves are then detrended by a bi-weight filter implemented by the `wōtan` package (Hippke et al., 2019) with varying window sizes.

- Search for planetary candidates: the transit search is performed on the nominal light curve as well as the detrended ones using a modified version of the `Transit Least Square` (TLS, Hippke & Heller, 2019) algorithm. If a signal has a S/N above a threshold value I typically set at 5, the results are stored, the transit is masked, and a new search is performed. The operation is repeated until the algorithm no longer finds signals above the threshold or reaches a number of repeats specified by the user. In the case of low S/N detections, it is also possible to smooth the light curve using a Savitsky-Golay digital filter to improve the results (Savitzky & Golay, 1964).

- Semi-automatic vetting: the `WATSON`[17] package was developed to inspect the candidates found by `SHERLOCK` and vet them, similarly to the DV module of the TESS pipelines. The vetting tests include: single transit inspection, cadence-based curves signal reliability, odd-even and secondary tests, transit source offset using difference imaging, optical ghost diagnostic.

- Planetary stability (*optional module*): `SHERLOCK` also includes the possibility to test the stability of the system in case of orbital periods very close to each other using the `REBOUND` package (Rein & Liu, 2012).

- Statistical validation: `SHERLOCK` makes use of `Triceratops` to statistically validate the planetary candidates (see Section 2.2.4).

[14] Available at https://github.com/MNGuenther/allesfitter
[15] Available at https://pypi.org/project/dynesty/
[16] Available at https://github.com/franpoz/SHERLOCK
[17] Available at https://github.com/PlanetHunters/watson

- Bayesian modeling: once a candidate is vetted and validated, a model can be done to refine the ephemeris of the candidate using the nested sampling algorithm of `Allesfitter` (see Section 2.2.5).
- Ground-based observational windows: based on the results of the fit, `SHERLOCK` allows to plan follow-up observation from ground-based facilities. The user provides the list of facilities and observational constraints, and this module produces upcoming observation windows thanks to the `Astropy` package (Astropy Collaboration et al., 2013) to confirm the candidate.

The search for extra planet candidates with `SHERLOCK` is now widely adopted as a necessary analysis in papers presenting the validation of planets including TESS data (e.g. Wells et al., 2021; Schanche et al., 2022; Delrez et al., 2022; Ghachoui et al., 2023; Pozuelos et al., 2023; Dransfield et al., 2024). It is also the case in the validation paper of TOI-4336 A b I present in Chapter 3. Finally, `SHERLOCK` is used in the Hidden Gems Project dedicated to finding new planets in known transiting systems. In Chapter 5, I present the confirmation of the two first candidates produced by the Hidden Gems project: TOI-4336 A c and TOI-237 c.

2.4 Characterization of TESS planets

Detecting new planets is the first step towards a broader understanding of how exoplanets form and evolve. In Sections 1.2 and 1.3, I explained how the transit technique only gives access to one key parameter (i.e. the radius of the transiting planet) and other methods are needed to complete its ID card. Combining radial velocity measurements with transit photometry for systems without TTVs allows to obtain the mass, which in turn allows to compute the bulk density. This parameter is critical to constrain the presence of volatile species in the atmosphere of the planet, as well as investigate the planet's interior composition and structure. Then, it opens up the possibility to study, for example, the surface conditions, possible habitability, or mass loss mechanisms to reveal the formation history of the planet. Finding and characterizing planets for which this is possible is currently the main focus of the field. In addition to numerous ground-based projects, many current and upcoming large-scale space missions are either fully or partially dedicated to this. In particular, the primary science goal of TESS is to find at least 50 planets amenable for spectroscopic observations (see Section 2.1.1). The goal of this thesis is to participate in this effort by focusing on the validation and characterization of TESS candidates orbiting red dwarfs. Thanks to a privileged access to the TRAPPIST and SPECULOOS facilities, the bulk of my work resided in the validation of a large number of candidates. For the most interesting ones, in collaboration with my SPECULOOS colleagues, I attempted to obtain observing time on high-resolution spectrographs to measure their masses, and space-based spectro-photometric facilities to explore their atmospheres. Proposals on two of those facilities were successful: the preliminary exploration of the atmosphere of TOI-4336 A b with HST (Program 16875 led by George Dransfield, co-led by myself), and the mass measurements of MANGOs targets with ESPRESSO (ESO P112.25ZF.001 led by George Dranfield, co-led by myself; ESO P114.27JF.001 led by myself, co-led by Khalid Barkaoui). I give the full description of these observing programs in Chapters 4 and 6, respectively. Below, I give a brief description of the facilities and the data analysis process in the context of these programs.

2.4.1 Hubble Space Telescope (HST)

HST is a space-based observatory launched by NASA in 1990. The science goals of HST are varied, and it has revolutionized our understanding of the Universe over the course of its 34 years of operations, notably with deep field images (e.g. Clampin et al., 2002).

The spacecraft is placed in a low-Earth orbit with an orbital period of 95 minutes. The primary mirror is 2.4 meters in diameter in a Ritchey-Chrétien configuration with a focal length of 57.6 meters. It is currently equipped with four instruments: the Wide Field Camera 3 (WFC3), Cosmic Origins Spectrograph (COS), Advanced Camera for Surveys (ACS), Space Telescope Imaging Spectrograph (STIS). Combining the spectral range of all four instruments, HST covers the mid IR to the UV with both imaging and spectroscopy.

In the context of exoplanet atmospheres, the most prized instrument is WFC3. The complete technical description can be found in Dressel (2022). It possesses two channels: UVIS (Ultraviolet and Visible, 200-1000 nm) and IR (Infrared, 800-1700 nm). The detectors are backside illuminated UV optimised 2K×4K CCDs, and a Teledyne 1K×1K HgCdTe detector, respectively for the UVIS and IR channels, with pixel scales of 0.04 and 0.13″/pixel.

Focusing on WFC3/IR, the focal plane of the camera is tilted by 24 ° with respect to the incoming light, causing the rectangular field of view of 123″ ×136″. The detector operates at a temperature of 145K thanks to a thermoeclectric cooler, and has a peak sensitivity between 1.0 and 1.7 μm. This type of IR detector allows to sample non-destructively the signal as it accumulates in each pixel, this constitutes the default observing mode of the camera. Such non-destructive readouts allow to reduce the dark current and readout noise which are typically higher than for CCD detectors. It is also useful in the case of cosmic ray corrections as cosmic rays are only caught in a single readout. The detector is made up of four quadrants of 512×512 pixels, each read out independently. By default, the entire detector is read out, but it is possible to do so for subarrays as well with an equal number of pixels in each quadrant. When specifying an IR observation, an aperture must be selected with four possible subarrays: 512 × 512, 256 × 256, 128 × 128, and 64 × 64. The list of apertures can be found in Section 7.4.5 of Dressel (2022).

The exposure time of a WFC3/IR observation is determined by a timing sequence and a total number of reads. There are twelve possible pre-defined timing sequences: one rapid sequence where the detector is sampled with the shortest possible time interval between reads; six linear sequences where the detector is sampled with uniform time intervals between reads (called SPARS with 5, 10, 25, 50, 100, and 200 second intervals); and five rapid-log-linear sequences where the detector is initially sampled with the shortest possible time interval between reads, then increases logarithmically until a specific time interval then transitions to a sequence of uniform samples (called STEP with 25, 50, 100, 200, and 400 second intervals reached). The total number of reads is a parameter called NSAMP and must be under 15.

For bright sources with a risk of saturation, a spatial scanning mode is available. This implies the movement of the instrument as the exposures are taken in order to spread the light onto the detector. Usually, the scan is performed perpendicularly to the dispersion direction.

WFC3/IR is equipped with a single filter wheel containing 15 narrow-band and broad-band filters, two grisms, and an opaque element used for dark current measurements (Dressel, 2022). Of particular interest is the G141 grism which is sensitive to water vapor. It allows for detailed high resolution spectral analysis in the 1.1-1.7μm range with slitless spectroscopy.

The data analysis is performed with the `Iraclis`[18] pipeline presented in Tsiaras et al. (2016b). It is a Python-based package fully dedicated to the analysis of single-object spatially scanned spectroscopic observations of exoplanets obtained with WFC3. `Iraclis` is user-friendly as the only inputs needed are a "parameters file" where all the requirements for the analysis are set, and a "bins file" with the desired spectral bins and limb darkening coefficients per bin.

The three major tasks performed by the package are: reduction and calibration of the data, extraction of the white and spectral light curves, and light curve fitting. The reduction

[18] Available at https://github.com/ucl-exoplanets/Iraclis

steps include bias and zero-read corrections, nonlinearity corrections following the behavior of the IR detector, dark current subtraction, gain variation corrections, sky background subtraction, and bad pixels and cosmic rays corrections. Because of the tilt of the focal plane of WFC3/IR, the light is not dispersed uniformly across the detector. This variation of dispersion can reach ∼4.5 nm/pixel, which is sufficient to cause significant changes in the extracted spectrum if not taken into account. Similarly, the tilt affects the wavelength calibration. These challenges are tackled by `Iraclis` by following a specific calibration process that monitors the position of the dispersed photons during a scan, and defines the wavelength-dependent photon trajectories. A 1D spectrum is then extracted using apertures with quadrangular shapes, and taking into account the geometric distortions and position shifts along the detector. For bright sources, the accumulation of signal in the IR detector introduces two time-dependent systematic signals called *ramps*: a short-term one with an exponential behavior visible in each orbit, and a long-term one with a linear behavior in the case of multiple orbits. `Iraclis` accounts for these effects as it fits the light curves with a custom Python code and including normalization factor. For more information on the individual steps, I refer to Tsiaras et al. (2016b,a, 2018).

2.4.2 ESPRESSO on the Very Large Telescope

ESPRESSO (Echelle SPectrograph for Rocky Exoplanet and Stable Spectroscopic Observations) is a high-resolution spectrograph installed on the Very Large Telescope at ESO Paranal Observatory, in the Atacama desert in Chile (Pepe et al., 2014, 2021). ESPRESSO was designed specifically to hunt for small rocky exoplanets in the habitable zone of stars ranging from G to M dwarfs, but also to measure the variation of physical constants, and to analyse the chemical compositions of stars in nearby galaxies. The instrument can be operated in single-UT mode or 4-UT mode making use of all four 8.2-m telescopes of the VLT. The wavelength range of the spectrograph is 380 to 788 nm, with a median resolving power of 140 000 in the high-resolution 1-UT mode, up to 190 000 in the ultra-high precision 1-UT mode. This allows to reach a precision down to 10 cm/s thanks to its advanced stability. The apertures are then $1''$ and $0.5''$, respectively. For faint targets, it is possible to observe with a 2×1 (spatial × spectral) binning.

An automated pipeline processes the data at Paranal, providing observers with preliminary results. This quick-look pipeline performs data reduction and provides the basic properties of the data and operational status of the instrument. However, the quality of the analysis may not be science-grade, and a more detailed analysis of the data is recommended. A data reduction software and a data analysis software is available to the community for that purpose (Pepe et al., 2021).

Chapter 3

Discovery of TOI-4336 A b

3.1 Introduction

Most of my PhD work resided in the follow-up of TESS candidates with the TRAPPIST and SPECULOOS facilities. As explained in Section 2.1.3, my weekly job included carefully selecting candidates to observe. In the context of this thesis project, interesting candidates were chosen on the basis of their host star properties and initial planetary parameters obtained from the TESS pipelines. I targeted in priority bright nearby mid- to late-M dwarfs ($T_{eff} \lesssim$ 3600K) with Jmag $\lesssim$ 12 hosting a potential planet with a radius below 4$R_\oplus$.

One particular target stood out: a mid-M star with a radius of $\sim 0.3 R_\odot$, a Jmag of $\sim$ 9.6, harboring a 2.2 $R_\oplus$ planet candidate. TESS identified the likely source of the signal to be TOI-1955 (TIC 166184426), and the TOI was issued in June 2020. I observed the transit with TRAPPIST-South (TS) as soon as the new observing season allowed it, on April 30, 2021. I quickly identified the star TOI-1955 as part of a hierarchical triple system of M dwarfs, including an almost equal mass close neighbor 6.2″ away, and a later-type M star 98.4″ away. Because of the spatial resolution of TS, the PSFs of the closer pair were blended, making difficult the identification of the exact source of the event. Elsa Ducrot and George Dransfield, two of my closest collaborators in the SPECULOOS team, scheduled the observations with the SPECULOOS Southern Observatory (SSO) that allowed to separate the flux from the two stars and determine that the transit event was on the brighter star of the system, TIC 166184428. After notifying Karen Collins who leads TFOP SG1 dedicated to seeing-limited photometry, a new TOI number was issued (TOI-4336.01) and TOI-1955.01 was retired as nearby planet candidate.

Following TESS's policy, I submitted an abstract on the TESS Wiki to secure the validation paper on behalf of the SPECULOOS and TRAPPIST teams. We continued to observe TOI-4336.01 with the TS and SSO facilities to increase the S/N of the detection. Doing so we collected observations in various filters accross the visible wavelength range to perform a robust chromaticity check. I also coordinated with Karen Collins and Khalid Barkaoui to gather transit observations from the Las Cumbres Observatory (LCO) network. Marion Cointepas and Xavier Bonfils agreed to share their transits obtained with the Exoplanets in Transit and their Atmospheres (ExTrA) facility, which gave access a NIR band. I performed the reduction and photometric extraction for all the TS and SSO data, as well as the photometric extraction for the reduced LCO images that were provided to me by Karen Collins and Khalid Barkaoui. As the PDC-SAP flux of TESS is corrected for the dilution of the flux by the nearby stars included in the aperture, I performed a custom extraction of the photometry, and added the dilution as a free parameter in the global analysis. The ExTrA light curves were sent to me already reduced. I carried out the global analysis of all the photometric data under the supervision of Michaël Gillon and Laetitia Delrez.

I liaised with Benjamin Rakham and Adam Burgasser who collected spectra with the SpeX and Low Dispersion Survey Spectrograph (LDSS-3) instruments to perform a spectroscopic reconnaissance of all three stars of the system. Keivan Stassun provided a Spectral Energy Distribution (SED) analysis and an estimate of the stellar parameters. High-resolution spectroscopic observations were also obtained and analyzed by Sam Quinn and Emily Pass with the CHIRON spectrograph. An estimation of the age of the system by analyzing its kinematics was done by Christian Aganze. Finally, Sebastian Zùñiga Fernandez provided a characterization of the orbits of the triple system.

High-angular resolution imaging were provided by Carl Ziegler and Steve Howell. The statistical vetting of the system using `Triceratops` was carried out by George Dransfield. Martín Devora Pajares performed the search for additional candidates in the TESS data using `SHERLOCK`, which produced a second candidate at 7.5 days. This search fit into the context of the Hidden Gems project we devised together with Francisco J. Pozuelos to find additional candidates in systems with confirmed transiting planets. We later confirmed this candidate to be a planet, and this constitutes the second paper I am leading for my PhD work (see Chapter 5). In addition, Catriona Murray performed injection and recovery tests on the TESS data and a suite of out-of-transit observations obtained with SSO to assess the detection limits of both instruments.

Because TOI-4336 A b sits near the inner boundary of the empirical HZ, Lisa Kaltenegger proposed a discussion on the potential habitability of the planet. Sean Raymond provided a discussion on the formation of the planet given the peculiar architecture of the system. Lastly, the prospects for a mass characterization was done by Daniel Sebastian, and for atmospheric characterization by George Dransfield.

This paper was published in Astronomy and Astrophysics (Timmermans et al., 2024).

3.2 Paper: Validation of TOI-4336 A b

A&A, 687, A48 (2024)
https://doi.org/10.1051/0004-6361/202347981

Astronomy & Astrophysics

TOI-4336 A b: A temperate sub-Neptune ripe for atmospheric characterization in a nearby triple M-dwarf system

M. Timmermans[1], G. Dransfield[2], M. Gillon[1], A. H. M. J. Triaud[2], B. V. Rackham[3,4], C. Aganze[5,6], K. Barkaoui[1,3,7], C. Briceño[8], A. J. Burgasser[9], K. A. Collins[10], M. Cointepas[11,12], M. Dévora-Pajares[13], E. Ducrot[14,15], S. Zúñiga-Fernández[1], S. B. Howell[17], L. Kaltenegger[18], C. A. Murray[19], E. K. Pass[10], S. N. Quinn[10], S. N. Raymond[20], D. Sebastian[2], K. G. Stassun[16], C. Ziegler[17], J. M. Almenara[11], Z. Benkhaldoun[21], X. Bonfils[11], J. L. Christiansen[22], F. Davoudi[1], J. de Wit[3], L. Delrez[1,23], B.-O. Demory[24], W. Fong[4], G. Fűrész[4], M. Ghachoui[1,21], L. J. Garcia[25], Y. Gómez Maqueo Chew[26], M. J. Hooton[27], K. Horne[28], M. N. Günther[29], E. Jehin[23], J. M. Jenkins[30], N. Law[31], A. W. Mann[31], F. Murgas[7,32], F. J. Pozuelos[33], P. P. Pedersen[34], D. Queloz[27,34], G. Ricker[4], P. Rowden[35], R. P. Schwarz[10], S. Seager[4,32,36], R. L. Smart[37], G. Srdoc[38], S. Striegel[39], S. Thompson[27], R. Vanderspek[4], and J. N. Winn[40]

(Affiliations can be found after the references)

Received 15 September 2023 / Accepted 18 April 2024

ABSTRACT

Context. Small planets transiting bright nearby stars are essential to our understanding of the formation and evolution of exoplanetary systems. However, few constitute prime targets for atmospheric characterization, and even fewer are part of multiple star systems.
Aims. This work aims to validate TOI-4336 A b, a sub-Neptune-sized exoplanet candidate identified by the TESS space-based transit survey around a nearby M dwarf.
Methods. We validated the planetary nature of TOI-4336 A b through the global analysis of TESS and follow-up multi-band high-precision photometric data from ground-based telescopes, medium- and high-resolution spectroscopy of the host star, high-resolution speckle imaging, and archival images.
Results. The newly discovered exoplanet TOI-4336 A b has a radius of 2.1 ± 0.1 $R_\oplus$. Its host star is an M3.5-dwarf star with a mass of 0.33 ± 0.01 $M_\odot$ and a radius of 0.33 ± 0.02 $R_\odot$, and is a member of a hierarchical triple M-dwarf system 22 pc away from the Sun. The planet's orbital period of 16.3 days places it at the inner edge of the habitable zone of its host star, which is the brightest of the inner binary pair. The parameters of the system make TOI-4336 A b an extremely promising target for the detailed atmospheric characterization of a temperate sub-Neptune by transit transmission spectroscopy with JWST.

Key words. techniques: photometric – planets and satellites: detection – planets and satellites: individual: TOI-4336 A b – stars: low-mass – planetary systems

1. Introduction

The Transiting Exoplanet Survey Satellite (TESS, Ricker et al. 2015) has already added about 400 confirmed planets to the known sample[1]. More than half of these new objects are smaller than Neptune, and transit stars that are bright enough for a detailed characterization with high-precision spectroscopy. Additionally, about 70 of these planets are hosted by M dwarfs. While the *Kepler* mission revealed a large abundance of such planets with no equivalent in the Solar System (Borucki et al. 2011; Dressing & Charbonneau 2013), most of the *Kepler* planets are currently out of reach for a detailed characterization due to the faintness of their host star.

The study of the bulk composition of these small planets shows two distinct populations with radii smaller than that of Neptune and bigger than that of the Earth. First, "super-Earths" are thought to be rocky planets with either thin or no atmosphere, while the other "mini-Neptunes" show smaller densities consistent with an extended atmosphere or a significant water fraction (e.g., Rogers 2015; Adams et al. 2008). The formation pathways of these planets are not fully understood (for a comprehensive review, see Bean et al. 2021), especially the paucity of planets found between ∼1.5 and ∼2.5 $R_\oplus$ (Fulton et al. 2017) for FGK stars. Several theories such as gas-poor formation (Lee et al. 2014), and atmospheric loss either by photoevaporation (Owen & Wu 2013) or core-powered mass loss (Gupta & Schlichting 2019) could explain this so-called radius valley, which may drift toward smaller radii for low-mass stars (Berger et al. 2020; Cloutier & Menou 2020), depending on the model. Another approach considers a density valley rather than a radius valley for M-type stars (Luque & Pallé 2022). The study distinguishes between three populations: rocky planets, water worlds, and puffy mini-Neptunes, with a common formation history for these last two. To illuminate these different formation theories, an increase in the sample of thoroughly characterized sub-Neptune-sized planets is critical. Small and cool M dwarfs are particularly interesting targets for transmission spectroscopy as they present high signal-to-noise ratios (S/Ns)

[1] NASA Exoplanet Archive, Jun 2023, https://exoplanetarchive.ipac.caltech.edu/

even for smaller transiting planets. Extended atmospheres, such as those expected for mini-Neptunes, should further increase the S/N for transmission spectroscopy.

TOI-4336 A is part of a hierarchical triple M-dwarf system (M3.5-, M3.5-, and M4-type stars) located at 22 pc from the Sun. The host star is the brightest component of the inner binary pair that has a minimum orbital separation of over a hundred au, and is at a projected angular separation of 6.25″. We adopted them as TOI-4336 A and B (TIC 166184428 and TIC 166184426, respectively) according to their brightness. The third star, which we refer to as TOI-4336 C (TIC 166184390), is the latest of the system and is on a wider orbit at a distance of over 2900 au, and at an angular separation of 98.44″. Here we report the detection of TOI-4336 A b, a planet that lies at the inner edge of the empirical habitable zone (HZ) (Kopparapu et al. 2013, 2017; Kaltenegger 2017; Zsom et al. 2013) of the system. It receives less irradiation than a young Venus; however, since M-dwarf irradiation warms planets more effectively than Sun-like stars (see, e.g., Kasting et al. 1993), that flux moves TOI-4336 A b just closer to the star than the inner edge of the empirical HZ, making the planet an intriguing example of a planet near a boundary of the HZ.

We describe in Sect. 2 the observations and methods used to characterize the triple star system. The TESS and ground-based observations used to validate the planetary nature of TOI-4336 A b are detailed in Sect. 3, and the statistical validation is reported in Sect. 4. The joint analysis of all the photometric data is presented in Sect. 5 and the results are discussed in Sect. 6. Finally, we present our conclusions in Sect. 7.

2. Stellar characterization

2.1. Spectroscopic reconnaissance

We gathered near-infrared spectra of TOI-4336 A and the two resolved, co-moving stars (TOI-4336 B and TOI-4336 C) with the SpeX spectrograph (Rayner et al. 2003) on the 3.2-m NASA Infrared Telescope Facility (IRTF) on 2021 Jun 27 (UT) and again on 2021 Jun 28 (UT). We used the short-wavelength cross-dispersed (SXD) mode of SpeX and the 0.″5 × 15″ slit aligned to the parallactic angle, which yielded spectra covering 0.75–2.42 µm at R∼1200 (Fig. 1). We collected 6 exposures of each target, nodding in an ABBA pattern. Our total exposure times were 360 s each for TOI-4336 A and TOI-4336 B, and 540 s for TIC 166184390 TOI-4336 C. We collected the standard set of SXD flat-field and arc-lamp exposures immediately after the science frames, followed by the A0 V standard HD 130163. We reduced the data with SPEXTOOL v4.1 (Cushing et al. 2004). We used SPLAT to compare the spectra to standards in the IRTF Spectral Library (Cushing et al. 2005; Rayner et al. 2009), focusing on the 0.9–1.4 µm region for the spectral classification (Kirkpatrick et al. 2010), and to estimate metallicity [Fe/H] via the Mann et al. (2013) relation (see Delrez et al. 2022, for details). Between nights, the spectral-type determinations of each target are identical and their metallicity estimates are consistent at $<1\sigma$. We estimate spectral types of M3.5 ± 0.5 for TOI-4336 A and TOI-4336 B and M4.0 ± 0.5 for TOI-4336 C. Combining measurements from both nights, we obtain final [Fe/H] estimates of -0.20 ± 0.12, -0.21 ± 0.12, and -0.17 ± 0.12 for TOI-4336 A, B, and C, respectively (see Table 1).

We acquired an optical spectrum of TOI-4336 A on 2022 Jan 07 (UT) using the Low Dispersion Survey Spectrograph (LDSS3-C, Stevenson et al. 2016) on the 6.5-m *Magellan* II (*Clay*) Telescope under clear and stable conditions. We used LDSS-3C in long-slit mode with the standard setup (fast readout speed, low gain, 1 × 1 binning) and the VPH-Red grism, OG-590 blocking filter, and the 0.″75 × 4′ center slit, which provides spectra covering 6000–10 000 Å at $R \sim 1810$. We collected eight, 60-s exposures of the target, followed by a 1-s arc-lamp exposure and three 10-s flat field exposures with the quartz high lamp and reduced the data with a custom Python-based pipeline (Dransfield et al. 2024). We used the ratio of the spectrum of the G2 V star HR 5325, observed at a similar airmass, to a G2 V template from Pickles (1998) to compute a relative flux calibration of the TOI-4336 spectrum. No correction was made to address telluric absorption. The reduced spectrum is shown in Fig. 2. It was then analyzed using tools in the `kastredux` package[2]. Comparison with the Sloan Digital Sky Survey templates from Kesseli et al. (2017) shows an excellent match to an M4 dwarf template. This is confirmed by analysis of spectral classification indices from Reid et al. (1995); Lépine et al. (2003); and Riddick et al. (2007). We also computed the ζ metallicity index (Lépine et al. 2007, 2013), determining a value of 1.026 ± 0.002, corresponding to a metallicity of [Fe/H] = +0.04±0.20 based on the empirical calibration of Mann et al. (2013).

We obtained high-resolution spectroscopic observations with the CHIRON spectrograph, located on the SMARTS 1.5-meter telescope at Cerro Tololo Inter-American Observatory, (Tokovinin et al. 2013) for both TOI-4336 A and the co-moving companion TOI-4336 B. We used CHIRON's 'slicer' mode, which employs an image slicer to achieve a resolving power of $R \sim 80\,000$ from 4100 to 8700 Å. Our observations yield per-pixel S/Ns that range from 10–12 in the TiO bands around 7100 Å. Spectra were extracted using the official CHIRON pipeline (Paredes et al. 2021), and we derived radial velocities (RVs) and spectral line profiles as described by Pass et al. (2023)[3]. This reduction is specifically optimized for mid-to-late M dwarfs and produces carefully calibrated relative RVs. For our relative RVs, the error budget is dominated by spectrograph stability. For our absolute RVs, the dominant uncertainty is a 0.5 km s^{-1} error in the RV scale; this error stems from the absolute RV uncertainty in a comparison spectrum of Barnard's Star, derived using 17 yr of measurements from the CfA Digital Speedometer. The RV measurements are given in Table 1. TOI-4336 A was observed on 2021 Feb. 06 and 2021 Jul. 12, and TOI-4336 B was observed on 2021 Feb. 06.

We find no evidence for significant velocity variation in TOI-4336 A, and the difference in absolute radial velocity between the two stars is consistent with orbital motion in a wide binary given their separation. We detect no significant rotational broadening for either star, setting upper limits of $v \sin i_\star < 1.9$ km s^{-1}. This limit corresponds to half a resolution element of the CHIRON spectrograph. Hα is seen in absorption for both stars, and following Newton et al. (2017), we measure $\mathrm{EW}_{\mathrm{H}\alpha} = 0.1644 \pm 0.0025$Å for TOI-4336 A, which places it among the sequence of quiescent M dwarfs. Taken together, we interpret the lack of detectable activity and rotational broadening as an indication that the star is not young, which is in agreement with the results of the LDSS3 spectral analysis, this is discussed in Sect. 2.3.

2.2. Spectral energy distribution

As an independent determination of the basic stellar parameters, we performed an analysis of the broadband spectral energy distribution (SED) of the star together with the *Gaia* DR3 parallax

[2] https://github.com/aburgasser/kastredux.
[3] This analysis builds upon the `tres-tools` package: https://github.com/mdwarfgeek/tres-tools.

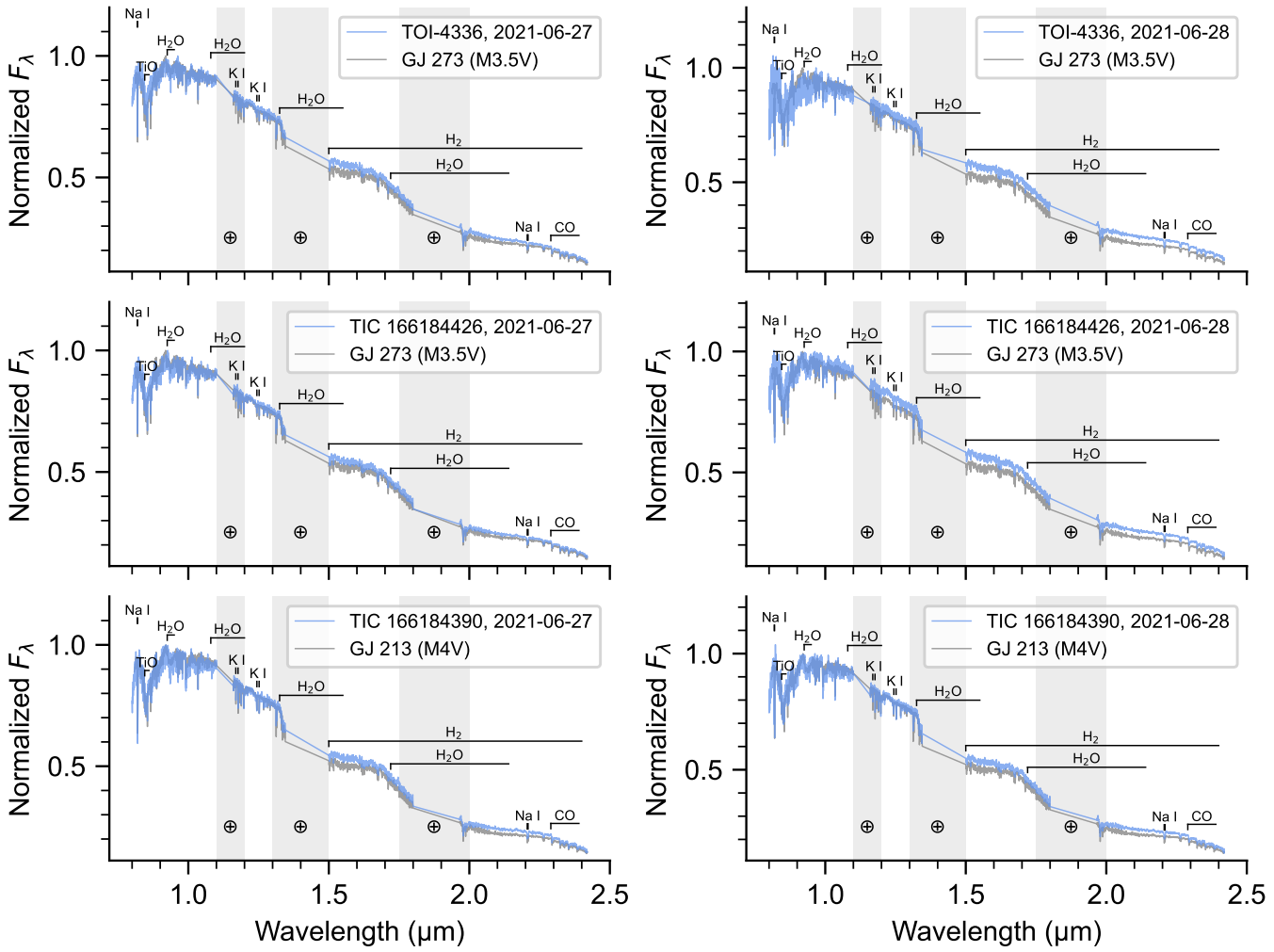

Fig. 1. SpeX spectra of TOI-4336 (TOI-4336 A, top row), TIC 166184426 (TOI-4336 B, middle row), and TIC 166184390 (TOI-4336 C, bottom row) from 2021 Jun. 27 (left column) and 2021 Jun. 28 (right column). The target spectrum (blue) is shown alongside the best-fit spectral template from the IRTF Spectral Library (gray). All spectra are normalized to their flux in the 0.9–1.4 μm region. Wavelengths with strong telluric absorption are shaded (and largely masked from the spectra), and prominent M-dwarf absorption features are highlighted.

(with no systematic offset applied; see, e.g., Stassun & Torres 2021), following the procedures described in Stassun & Torres (2016); Stassun et al. (2017, 2018). We pulled the JHK_S magnitudes from 2MASS (Cutri et al. 2003), the W1–W4 magnitudes from WISE (Cutri et al. 2021), the G_{BP} and G_{RP} magnitudes from *Gaia* (Gaia Collaboration 2022), and the NUV flux from GALEX (Bianchi et al. 2017). We also used the *Gaia* spectrophotometry spanning 0.4–1.0 μm, providing an especially strong constraint on the overall absolute flux calibration. Together, the available photometry spans the stellar SED over the wavelength range 0.2–22 μm (see Fig. 3).

We performed a fit using PHOENIX stellar atmosphere models (Husser et al. 2013), with the effective temperature ($T_{\rm eff}$) and metallicity ([Fe/H]) as free parameters (the surface gravity, $\log g$, has very little influence on the broadband SED). We set the extinction, A_V, to zero given the close proximity of the system. The resulting fit (Fig. 3) has a reduced χ^2 of 1.3 (excluding the NUV measurement, which suggests some chromospheric activity), with best-fit $T_{\rm eff} = 3300 \pm 75$ K and [Fe/H] $= 0.0 \pm 0.2$. The derived parameters are shown in Table 1.

Integrating the model SED gives the bolometric flux at Earth, $F_{\rm bol} = 7.40 \pm 0.17 \times 10^{-10}$ erg s^{-1} cm^{-2}. Taking the $F_{\rm bol}$ together with the *Gaia* parallax directly gives the luminosity, $L_{\rm bol} = 0.01163 \pm 0.00027\ L_\odot$. Similarly, the $F_{\rm bol}$ together with the $T_{\rm eff}$ and the parallax gives the stellar radius, $R_\star = 0.330 \pm 0.015\ R_\odot$. The stellar mass can also be estimated via the empirical M_K based relations of Mann et al. (2019), giving $M_\star = 0.331 \pm 0.010\ M_\odot$. All uncertainties are propagated in the usual manner, except for the M_K-based mass estimate for which we adopt the systematic uncertainties quoted for the Mann et al. (2019) relations as the dominant source of error. These parameters are summarized in Table 2.

For completeness, we applied the same SED-fitting procedures to the other two stars in the system, with the results shown in Fig. 3 and summarized in Table 1. We placed the three stars of the TOI-4336 system in a color-magnitude diagram to compare their properties to nearby M dwarfs (see Fig. A.1). TOI-4336 C appears less luminous than the other two, which is consistent with their spectral types.

2.3. Age estimation

To estimate the age of the system, we compared its kinematics and metallicity to a large sample of stars from GALAH survey DR3 (Buder et al. 2018). Ages for stars in the GALAH survey are estimated based on the Bayesian method by

Table 1. Properties of the TOI-4336 system.

Parameters	Values			Refs.
Designation				
This work	TOI-4336 A	TOI-4336 B	TOI-4336 C	
TIC	166184428	166184426	166184390	[1]
2MASS	J13442546-4020155	J13442500-4020122	J13442755-4018400	[2]
Gaia (DR3)	6113245033656232448	6113245033659187200	6113271494953274752	[3]
UCAC4	249-060094	249-060092	249-060096	[4]
WISE	J134425.61-402014.8	J134425.16-402011.4	J134427.70-401839.2	[5]
WDS	J13444-4020A	J13444-4020C	J13444-4020B	[6]
Photometric magnitudes				
TESS (mag)	11.0196 ± 0.0074	11.1825 ± 0.0074	11.9501 ± 0.0073	[1]
B (mag)	14.489 ± 0.001	14.510 ± 0.037	16.369 ± 0.012	[1,4,7]
V (mag)	12.893 ± 0.006	12.911 ± 0.052	14.732 ± 0.001	[1,4,7]
G (mag)	12.245831 ± 0.002774	12.434232 ± 0.002785	13.2893 ± 0.000731	[3]
J (mag)	9.453 ± 0.024	9.589 ± 0.024	10.249 ± 0.022	[2]
H (mag)	8.867 ± 0.046	9.038 ± 0.025	9.723 ± 0.023	[2]
K (mag)	8.632 ± 0.024	8.756 ± 0.021	9.426 ± 0.021	[2]
$W1$ (mag)	8.479 ± 0.029	8.588 ± 0.03	9.243 ± 0.023	[5]
$W2$ (mag)	8.333 ± 0.025	8.411 ± 0.026	9.063 ± 0.02	[5]
$W3$ (mag)	8.218 ± 0.025	8.311 ± 0.027	8.887 ± 0.025	[5]
$W4$ (mag)	7.865 ± 0.2	8.345 ± 0.303	8.579001 ± 0.255	[5]
Astrometric properties				
Distance (pc)	22.45 ± 0.02	22.44 ± 0.03	22.45 ± 0.08	[8]
Parallax (mas)	44.53 ± 0.03	44.55 ± 0.04	44.50 ± 0.02	[3]
RA (J2000)	13 : 44 : 25.4773	13 : 44 : 25.0160	13 : 44 : 27.5674	[3]
Dec (J2000)	−40 : 20 : 15.5222	−40 : 20 : 12.1623	−40 : 18 : 40.0242	[3]
$\mu_{\rm RA}$ (mas yr^{-1})	151.813 ± 0.033	150.407 ± 0.039	151.991 ± 0.016	[3]
$\mu_{\rm Dec}$ (mas yr^{-1})	68.402 ± 0.025	71.661 ± 0.028	71.798 ± 0.014	[3]
RUWE	1.86	1.80	1.21	[3]
U (km s^{-1})	23.5 ± 0.3	23.3 ± 0.3	24.0 ± 0.9	[3]
V (km s^{-1})	0.6 ± 0.3	0.6 ± 0.4	0.2 ± 0.9	[3]
W (km s^{-1})	10.0 ± 0.2	10.4 ± 0.2	10.6 ± 0.5	[3]
Radial velocity (km s^{-1})	18.37 ± 0.36	18.36 ± 0.51	19.23 ± 1.33	[3]
This work				
SpT	M3.5 ± 0.5	M3.5 ± 0.5	M4.0 ± 0.5	SpeX
$T_{\rm eff}$ (K)	3300 ± 75	3255 ± 75	3150 ± 75	SED
[Fe/H] (dex)	−0.20 ± 0.12	−0.21 ± 0.12	−0.17 ± 0.12	SpeX
	+0.04 ± 0.20	–	–	LDSS3
$L_{\rm bol,\star}$ ($L_\odot$)	0.0116 ± 0.0003	0.0102 ± 0.0002	0.0053 ± 0.0002	$F_{\rm bol,\star}$ + parallax
$F_{\rm bol}$ (10^{-10} erg cm^{-2} s^{-1})	7.40 ± 0.17	6.50 ± 0.15	3.35 ± 0.12	SED
$R_\star$ ($R_\odot$)	0.330 ± 0.015	0.318 ± 0.015	0.224 ± 0.012	$F_{\rm bol}$+ $T_{\rm eff}$ + parallax
$M_\star$ ($M_\odot$)	0.331 ± 0.010	0.314 ± 0.015	0.236 ± 0.007	M_K [(a)]
$\rho_\star$ ($\rho_\odot$)	$12.97^{+2.03}_{-1.66}$	$13.72^{+2.20}_{-1.79}$	$22.89^{+3.91}_{-3.16}$	$R_\star$ + $M_\star$
log $g_\star$ (cgs)	4.92 ± 0.04	4.93 ± 0.04	$5.04^{+0.05}_{-0.04}$	$R_\star$ + $M_\star$
Radial velocity (km s^{-1})	18.0 ± 0.5	18.7 ± 0.5	–	CHIRON
Age (Gyr)	$6.7^{+2.7}_{-3.1}$	$6.7^{+2.7}_{-3.1}$	$6.7^{+2.7}_{-3.1}$	Kinematics

Notes. [(a)]The stellar mass is estimated via the empirical M_K based relations of Mann et al. (2019).

References. [1] Stassun et al. (2019), [2] Cutri et al. (2003), [3] Gaia Collaboration (2022), [4] Zacharias et al. (2013), [5] Cutri et al. (2021), [6] Mason et al. (2001), [7] Henden et al. (2015), [8] Bailer-Jones et al. (2021).

Sharma et al. (2018), which is designed to fit the measured distribution of stellar parameters (sky positions, $T_{\rm eff}$, log g, [Fe/H], magnitudes) with a combination of model isochrones and a Galactic population synthesis model. We used the same reference frame as the GALAH DR3 catalog and the *Gaia* radial velocities to compute the UVW velocities of the system, given in Table 1. We selected objects with distances < 300 pc, and total 3D-velocity $|V - V_{\rm system}| < 10$ km s^{-1} and metallicities within 1-standard deviation of the system, our sample is shown in Fig. B.1. These constraints yield an age of $6.7^{+2.7}_{-3.1}$ Gyr. Additionally, the lack of Hα (6563 Å) and Li I (6708 Å) emission in any of the optical spectra further confirms that the system is likely old

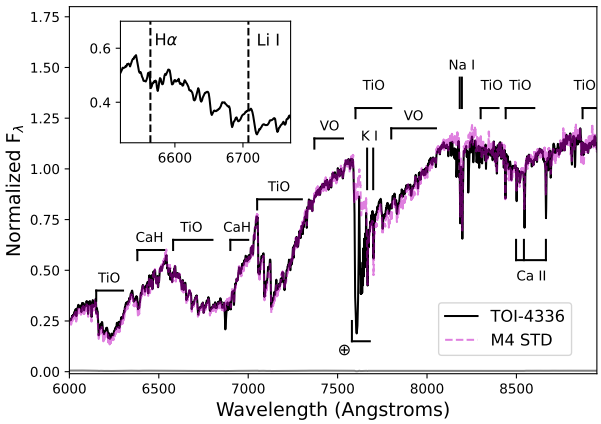

Fig. 2. LDSS3 red optical spectrum of TOI-4336 A (black line), compared to its best-fit M4 template (Kesseli et al. 2017, magenta line). Spectra are normalized in the 7400–7500 Å region, and major absorption features are labeled, including regions of strong telluric absorption (⊕). The inset box shows a close-up of the region encompassing Hα (6563 Å) and Li I (6708 Å) features, neither of which is detected.

(Newton et al. 2017; Kiman et al. 2021). In particular, examining the LDSS3 spectra, we find no evidence of significant Hα emission with a 3σ equivalent width limit of 0.12 Å, suggesting an age $\gtrsim$4.5 Gyr according to the age–activity relation of West et al. (2008). However, TOI-4336 A has a mass placing it near the fully convective boundary, and more recent studies have found the average age of transition to the inactive mode is 2.4 ± 0.3 Gyr for fully convective M dwarfs (Medina et al. 2022) with some of them transitioning as early as 600 Myr (Pass et al. 2022).

Finally, using the latest version of the BANYAN tool (Gagné et al. 2018)[4], we find that the system has a 99.9 percent probability of being a field object, with no association with nearby young moving groups. This further confirms that the triple system is likely old.

2.4. Triple M-dwarf system

TOI-4336 A is the primary star of a resolved triple system, with angular separations of 6.25″and 98.44″ from the B and C components respectively, identified as WDS J13444-4020 in the Washington Double Stars Catalog (WDS, Mason et al. 2001). We used the astrometric measurements from WDS, the stellar masses from SED analysis and the *Gaia* astrometry, distances and proper motions to get a first-order estimation of the orbital elements of the system with `LOFTI-Gaia` package[5] (Pearce et al. 2020). We obtained a posterior sample of 10 000 accepted orbits for each system (see Appendix C). The posterior parameters are given in Table C.2. The results show that the close binary has a median semi-major axis of 133 au with a 68% confidence interval from 72 to 175 au. This results correspond to a median periastron separation of 34.7 au. with a 68% confidence interval from 5 to 118 au. Although the short phase coverage does not allow a detailed orbital characterization of the system, these results are used as a point of reference to evaluate the effect of the triple system configuration on the formation of TOI-4336 A b (see Sect. 6.2).

[4] https://www.exoplanetes.umontreal.ca/banyan/banyansigma.php
[5] https://github.com/logan-pearce/lofti_gaia

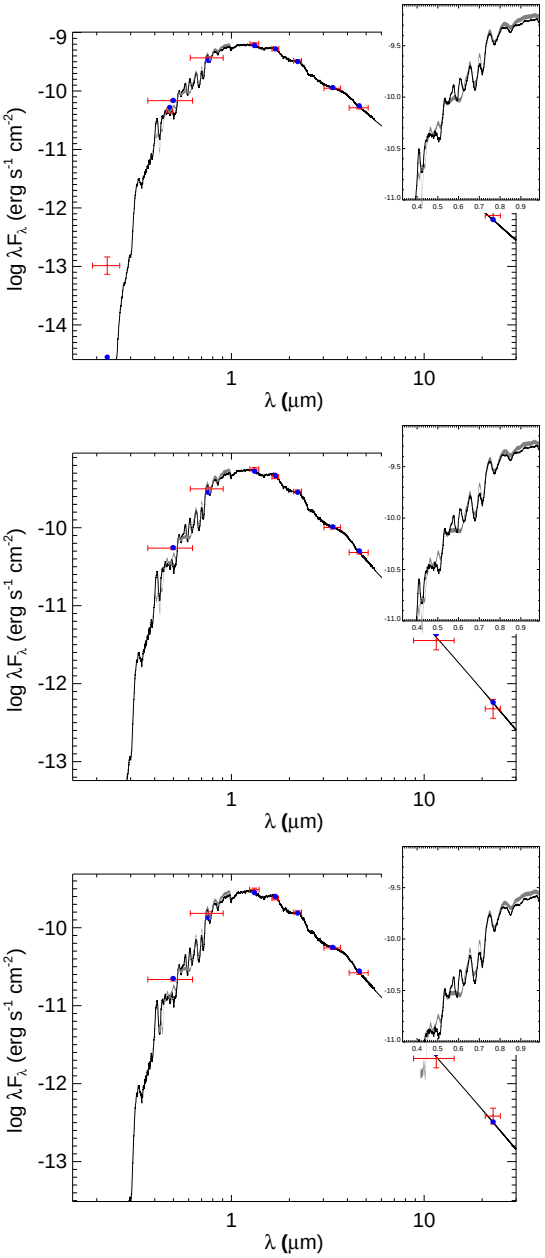

Fig. 3. Spectral energy distribution of TOI-4336 A (top panel) and its companion stars TOI-4336 B (middle panel) and TOI-4336 C (bottom panel). Red symbols represent the observed photometric measurements, the horizontal bars represent the effective width of the passband. Blue symbols are the model fluxes from the best-fit PHOENIX atmosphere model (black). The *Gaia* spectrophotometry is represented as a grey swathe; a closeup view is shown in the inset.

3. Photometric observations

3.1. TESS

The two close components of the system, TOI-4336 A and B, have an angular separation of 6″and thus are located in the same TESS pixel, given the pixel size of 21″. The tertiary component is, however, resolved in TESS. They were observed in Sector 11 (2019 Apr. 26 to 2019 May 20), Sector 38 (2021 Apr. 29 to 2021 May 26) and Sector 64 (2023 Apr. 06 to 2023 May 04), with both short- and long- cadence modes. The 2-min cadence image data were reduced and analyzed using the Science processing Operations Center (SPOC, Jenkins et al. 2016) pipeline at NASA

Table 2. Properties of TOI-4336 A and TOI-4336 A b based on our global transit model (see Sect. 5).

Parameters	Values	Priors
Luminosity, $L_\star$ ($L_\odot$)	$0.0114^{+0.0013}_{-0.0012}$	–
Metallicity, [Fe/H] (dex)	$-0.209^{+0.012}_{-0.013}$	$\mathcal{N}$ (–0.20, 0.12^2)
Effective temperature, $T_{\rm eff}$ (K)	3298^{+75}_{-73}	$\mathcal{N}$ (3300, 75^2)
Mass, $M_\star$ ($M_\odot$)	0.331 ± 0.015	$\mathcal{N}(0.330, 0.015^2)$
Radius, $R_\star$ ($R_\odot$)	$0.328^{+0.010}_{-0.010}$	$\mathcal{N}(0.331, 0.010^2)$
Density, $\rho_\star$ ($\rho_\odot$)	$9.4^{+1.06}_{-0.9}$	–
Log surface gravity, log $g_\star$ (cgs)	$4.927^{+0.034}_{-0.033}$	–
Quadratic limb-darkening coefficient $u_{1,\,g'}$	$0.475^{+0.048}_{-0.050}$	$\mathcal{N}(0.479, 0.050^2)$
Quadratic limb-darkening coefficient $u_{2,\,g'}$	$0.354^{+0.049}_{-0.048}$	$\mathcal{N}(0.349, 0.05^2)$
Quadratic limb-darkening coefficient $u_{1,\,r'}$	$0.551^{+0.044}_{-0.048}$	$\mathcal{N}(0.532, 0.050^2)$
Quadratic limb-darkening coefficient $u_{2,\,r'}$	$0.303^{+0.049}_{-0.048}$	$\mathcal{N}(0.278, 0.050^2)$
Quadratic limb-darkening coefficient $u_{1,\,z'}$	$0.149^{+0.051}_{-0.050}$	$\mathcal{N}(0.163, 0.050^2)$
Quadratic limb-darkening coefficient $u_{2,\,z'}$	0.360 ± 0.053	$\mathcal{N}(0.368, 0.050^2)$
Quadratic limb-darkening coefficient $u_{1,\,zs}$	$0.284^{+0.050}_{-0.047}$	$\mathcal{N}(0.276, 0.050^2)$
Quadratic limb-darkening coefficient $u_{2,\,zs}$	$0.237^{+0.048}_{-0.047}$	$\mathcal{N}(0.221, 0.050^2)$
Quadratic limb-darkening coefficient $u_{1,\,\rm TESS}$	$0.165^{+0.049}_{-0.050}$	$\mathcal{N}(0.157, 0.050^2)$
Quadratic limb-darkening coefficient $u_{2,\,\rm TESS}$	$0.455^{+0.051}_{-0.050}$	$\mathcal{N}(0.454, 0.050^2)$
Quadratic limb-darkening coefficient $u_{1,\,\rm ExTrA1.2\ \mu m}$	$0.180^{+0.048}_{-0.053}$	$\mathcal{N}(0.186, 0.050^2)$
Quadratic limb-darkening coefficient $u_{2,\,\rm ExTrA1.2\ \mu m}$	$0.138^{+0.050}_{-0.054}$	$\mathcal{N}(0.146, 0.050^2)$
Dilution TESS (%)	86.3 ± 2.9	$\mathcal{N}(86, 3^2)$
Dilution TRAPPIST-South (%)	$86.2^{+2.7}_{-2.9}$	$\mathcal{N}(86, 3^2)$
Transit depth, dF (ppm)	3487^{+126}_{-125}	–
Transit impact parameter, b ($R_\star$)	$0.453^{+0.056}_{-0.075}$	–
Orbital period, P (days)	$16.336334^{+0.000024}_{-0.000023}$	–
Mid-transit time, T_0 ($\rm BJD_{TDB}$ − 2 450 000)	$9335.57319^{+0.00068}_{-0.00062}$	–
Transit duration, W (min)	$125.38^{+1.34}_{-1.18}$	–
Orbital inclination, $i_{\rm p}$ (deg)	$89.55^{+0.09}_{-0.07}$	–
Orbital semi-major axis, $a_{\rm p}$ (au)	$0.0872^{+0.0013}_{-0.0014}$	–
Scale parameter, $a_{\rm p}/R_\star$	$57.16^{+2.07}_{-1.84}$	–
Radius, $R_{\rm p}$ ($R_\oplus$)	$2.12^{+0.08}_{-0.09}$	–
Stellar irradiation, $S_{\rm p}$ ($S_\oplus$)	$1.50^{+0.18}_{-0.17}$	–
Equilibrium temperature, $T_{\rm eq}$ (K)	308± 9	–

Ames Research Center. 30-min cadence data were obtained by the TESS-SPOC pipeline (Caldwell et al. 2020) and 10-min cadence data were obtained by the Quick Look Pipeline (QLP, Huang et al. 2020).

We extracted the photometry for the global analysis from the TESS target pixel files (TPFs) for all three sectors. We retrieved the 2-min TESS TPFs from the Mikulski Archive for Space Telescopes using the `lightkurve`[6] package (Lightkurve Collaboration et al. 2018) using the hard quality bitmask to remove the images affected by scattered light or sub-optimal attitude control. At the beginning of each orbit of Sector 11, Camera 1 was subject to scattered light, and the attitude control was disabled for a short period. Using the hard-quality bitmask allows removing this affected bit of data (quality flag 7407). We extracted the photometry from the images using a set of custom apertures inscribed within a square of 4×4 pixels centered on the target, these are shown in Fig. 4. The TESS TPFs are obtained with `tpfplotter`[7] (Aller et al. 2020). After the removal of the 5σ outliers, we used the cotrending basis vectors (CBVs) obtained by the presearch and data conditioning (PDC) pipeline module of SPOC, a method initially developed to remove low and high-frequency systematic trends in *Kepler* data (Kinemuchi et al. 2012). We used the multi-scale correction method, which is preferred to preserve transit signals, combined with a correction of short spikes. The correction was calculated using a linear regression approach with an L2 regularization implemented in `lightkurve`. To prevent under- or over-fitting of the data, the value of the L2 penalty is optimized according to the PDC goodness metrics. We compared the corrected light curves using the combined differential photometric precision (CDPP) metric as implemented in `lightkurve` and selected the one for which the metric was minimal. The extracted light curves are shown in Fig. 5.

Data Validation Reports were produced by the TESS pipelines each time a new sector became available. The validation tests systematically performed for a planet candidate were passed, although in the first instance the period found was half the true period and the centroid shift analysis did

[6] https://github.com/lightkurve/lightkurve
[7] https://github.com/jlillo/tpfplotter

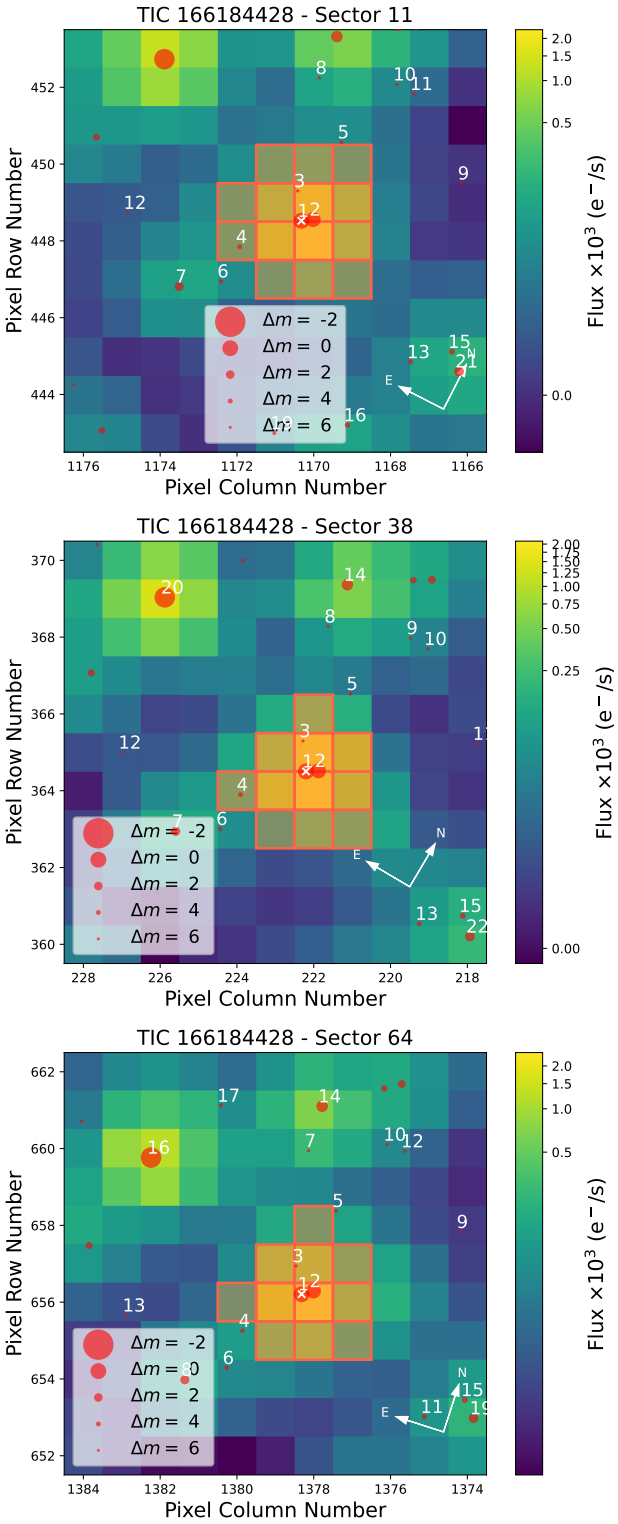

Fig. 4. TESS target pixel files showing the custom apertures used to extract the photometry of TOI-4336 A b in this work for Sectors 11, 38, and 64.

match to TOI-4336 A, TOI-1955.01 was in fact issued for TOI-4336 B. Our ground-based photometric follow-up confirmed the source to be TOI-4336 A. On the TESS side, the SPOC conducted a transit search of Sectors 38 and 64 on 2021 Jul. 2 and 2023 Jun. 20 respectively. The transit search was conducted with an adaptive, noise-compensating matched filter (Jenkins et al. 2002, 2010, 2020), producing a threshold crossing event for which an initial limb-darkened transit model was fitted (Li et al. 2019) and a suite of diagnostic tests were conducted to help make or break the planetary nature of the signal (Twicken et al. 2018). The TESS Science Office reviewed the vetting information and issued an alert for TOI-4336.01 on 2021 Jul. 28 (Guerrero et al. 2021). According to the difference image centroiding tests, the host star is located within 4.0 ± 2.7″ of the transit signal source of TOI-4336 A.

3.2. Ground-based photometry

We collected photometric data using four sets of facilities as part of the TESS follow-up observing program (TFOP) sub-group 1 (SG1) for seeing-limited photometry: SPECULOOS-Southern Observatory (SSO; Delrez et al. 2018; Sebastian et al. 2021), TRAPPIST-South (Gillon et al. 2011; Jehin et al. 2011), Las Cumbres Observatory Global Telescope (LCOGT; Brown et al. 2013), and ExTrA (Bonfils et al. 2015). The observations are summarized in Table D.1, and the quality of the light curves is quantified by their RMS value, it is given in Table E.1.

All but the ExTrA data reduction and analysis was done using a custom pipeline for image processing and photometric extraction built with the `prose`[8] package (Garcia et al. 2022, 2021). First, the image calibration was performed, and the images aligned using `twirl`[9]. We detected the stars using an implementation of DAOPhot from Photutils (Bradley et al. 2023), and used `ballet`[10] as centroiding algorithm. The photometric extraction was done on a set of 30 circular apertures ranging between 0.5 and twice the value of the full width at half maximum (FWHM) of the target's point-spread function (PSF), and the position of the background annulus was selected on the basis of the lack of contaminant in the vicinity of the target. We performed differential photometry on all data sets to retrieve our light curves. In doing so we selected comparison stars in the field as well as apertures minimizing the white and red noise in the target light curve as calculated by Pont et al. (2006). We treated each observation separately, and the number of comparison stars varied between 3 and 9. Given the proximity of stars A and B, the flux in the aperture of the TRAPPIST-South observations is contaminated as it contains fully the PSFs of the two stars. This is taken into account in the global analysis where we fit the dilution factor (see Sect. 5). For the observations with the 1-m class telescopes (SSO and LCO), the stars are completely resolved with a negligible overlap of the PSFs. In that case, we systematically selected TOI-4336 B as a comparison star.

3.2.1. TRAPPIST-South

TRAPPIST-South is a 0.6m Ritchey-Chrétien telescope located at La Silla Observatory in Chile (Gillon et al. 2011; Jehin et al. 2011). It is equipped with an FLI ProLine CCD camera with a pixel scale of 0.64″, providing a field of view of 22′ × 22′. We observed four transits of TOI-4336 A b with this facility in the *Sloan-z'* filter with 15 s exposures on 2021 Apr. 30, 2021 Jun. 18, 2021 Aug. 6, and 2023 May 27.

3.2.2. SPECULOOS-South

The SPECULOOS Southern Observatory, located at ESO Paranal Observatory in Chile, is composed of four 1.0m F/8 Ritchey-Chrétien telescopes (Delrez et al. 2018; Sebastian et al.

[8] https://github.com/lgrcia/prose
[9] https://github.com/lgrcia/twirl
[10] https://github.com/lgrcia/ballet

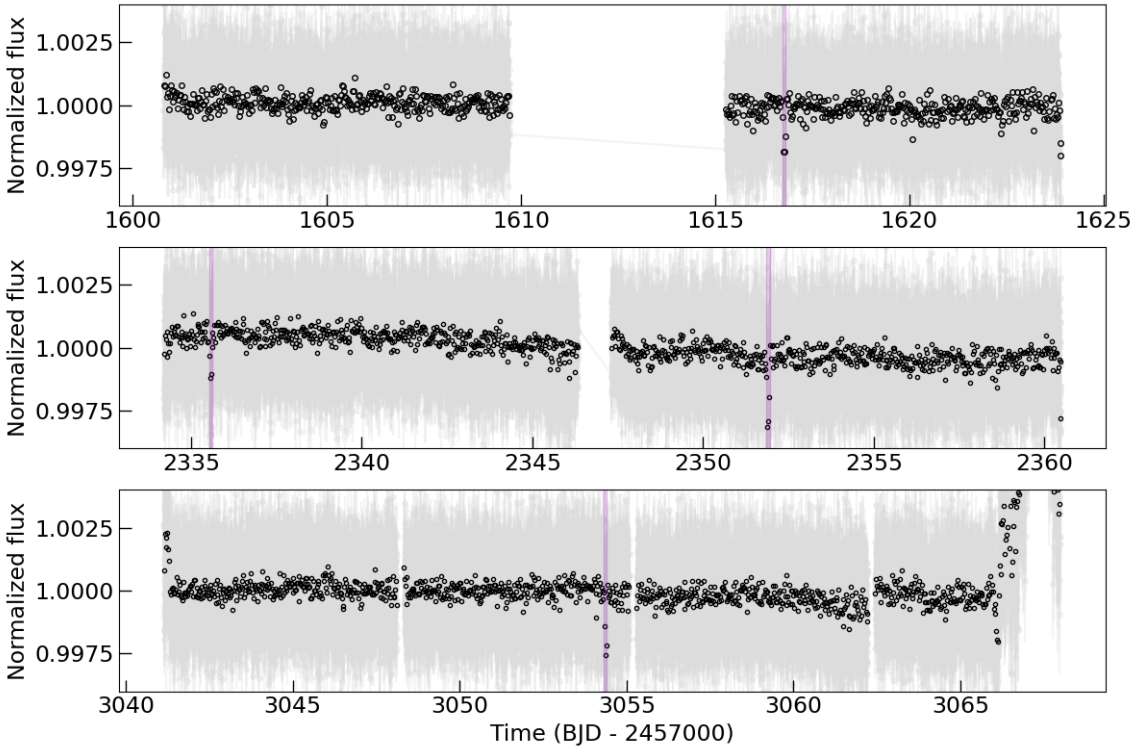

Fig. 5. TESS 2-min cadence photometry obtained using custom apertures for Sectors 11, 38, and 64. The transits are highlighted in purple.

2021), named after the Galilean moons Io, Europa, Ganymede, and Callisto. All telescopes are equipped with a deep-depletion Andor iKon-L 2k × 2k CCD camera with a total field of view of 12′ for a pixel scale of 0.35″ (Burdanov et al. 2018). We collected data on the nights of 2021 Jun. 18, 2022 Apr. 8, 2022 May 27, and 2023 Mar. 17 with SSO in the *Sloan-r'* filter with 10s exposures and the *Sloan-g'* filter with 24s exposures.

3.2.3. LCOGT

A total of six transits were obtained with LCOGT in the *Sloan-g'* with 150s exposures and Pan-STARRS *zs* with 45s exposures on the nights of 2021 Jun. 18, 2022 Feb. 18, 2022 Apr. 8, and 2023 Mar. 17. The telescopes are equipped with 4096 × 4096 SINISTRO Cameras, having an image scale of 0.389″ per pixel, resulting a field of view of 26′ × 26′. The raw data were calibrated by the standard LCOGT `BANZAI` pipeline (McCully et al. 2018) and photometric measurements were extracted using the `prose` package, similarly to the TRAPPIST and SPECULOOS data.

3.2.4. ExTrA

The ExTrA facility, located at ESO's La Silla Observatory, is composed of three 0.6m telescopes feeding a near-infrared multi-object spectrograph. We simultaneously obtained one transit with two ExTrA telescopes (Bonfils et al. 2015) on 2022 May 27 in a bandpass centered on 1.21 µm with 60 s exposures and the spectrograph's low resolution mode ($R \sim 20$) and 8″diameter aperture fibers. The resulting ExTrA data were analyzed with custom data reduction software, detailed in Cointepas et al. (2021).

4. Validation of the planet

4.1. Archival imaging

Investigating archival imaging of the field of view of the considered target is common practice to look for a possible blend with a background object in the current images. The large proper motion of the TOI-4336 system (166 mas yr^{-1}; Gaia Collaboration 2022) makes this possible. We inspected DSS/POSS II images in blue and IR (Lasker et al. 1996; Reid et al. 1991) spanning 47 yr compared to the SSO observation, as shown in Fig. 6. We conclude there is no background star with a limiting magnitude of B∼22.5 at the current position of TOI-4336 A which could potentially be the source of the transit events or impact our conclusions.

4.2. High-angular resolution imaging

A search for proper motion blend candidates does not eliminate the possibility that the star itself is an unresolved binary. Close-bound stellar companions can confound exoplanet discovery and parameter derivation. If a close companion does exist, the detected transit signal will yield incorrect stellar and exoplanet parameters (Ciardi et al. 2015; Furlan & Howell 2017). Additionally, the presence of a close companion star could lead to the non-detection of small planets residing within the same exoplanetary system (Lester et al. 2021).

The renormalized unit weight error (RUWE) quantifies the possible presence of an unresolved companion or acceleration during the astrometric solution estimation from *Gaia* measurements (Gaia Collaboration 2022). As all components of the systems have values above the expected value of ∼1.0 for a single star (see Table 1), we use high-resolution imaging to constrain the presence of unresolved companions.

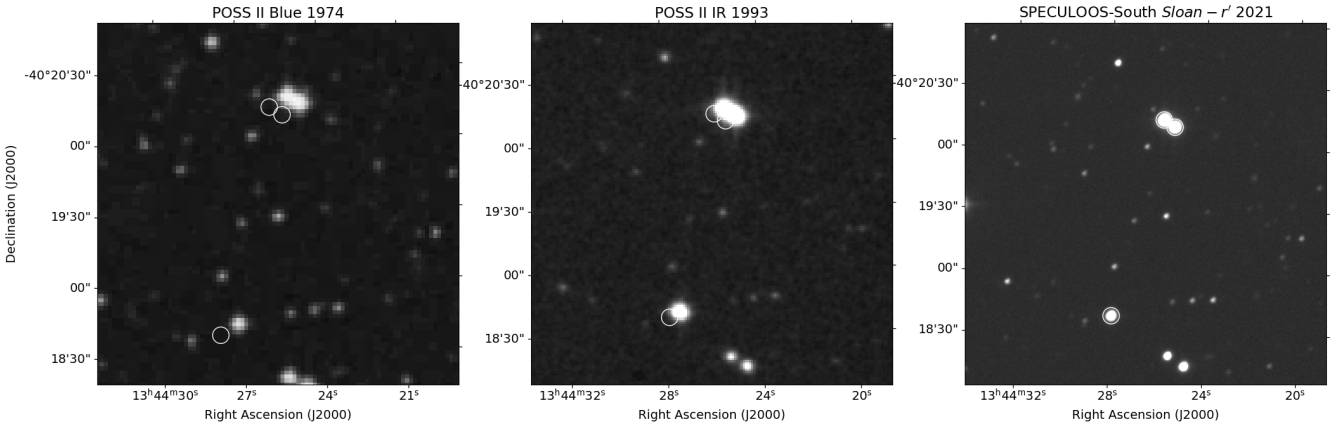

Fig. 6. Archival images of the field around the TOI-4336 system. From left to right: 1974 image taken with the blue plate of DSS/POSS-II, 1993 image taken with the InfraRed plate of DSS/POSS-II, and 2021 image taken with SSO in *Sloan-r'*. The white circles indicate the position of the stars on the 2021 images.

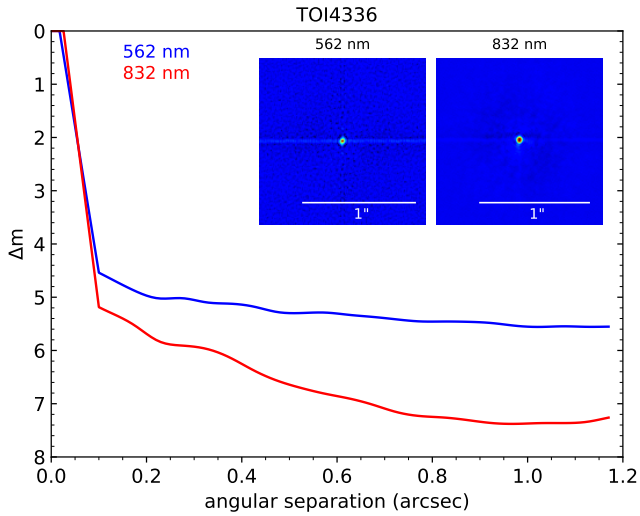

Fig. 7. Contrast curve obtained with Zorro for TOI-4336 A in two bands (562 nm and 832 nm) and the reconstructed speckle image of the observation from 2022 May 17.

TOI-4336 A was observed three times with the Zorro instrument on the Gemini-South 8-m telescope (Scott et al. 2021; Howell & Furlan 2022): 2022 Mar. 19, 2022 May 17, and 2023 May 27. Zorro provides simultaneous speckle imaging in two bands (562 nm and 832 nm) with output data products including a reconstructed image with robust contrast limits on companion detections (e.g., Howell et al. 2016). All three observations were processed with our standard reduction pipeline (Howell et al. 2011), Fig. 7 shows the final contrast curves and the reconstructed speckle images for the 2022 May 17 observation. TOI-4336 A is an isolated star with no companion brighter than 5–7 magnitudes below that of the target star from the 8-m telescope diffraction limit of 0.2″ out to 1.2″. This excludes the presence of companion stars with spectral types between M4 and early-L at these angular limits. At the distance of the TOI-4336 system (d = 22.5 pc), they correspond to spatial limits of 0.45 to 27 au.

We acquired a second set of speckle imaging for the A and B components of the TOI-4336 system with the HRCam instrument of the SOAR telescope (Tokovinin 2018), the data were analyzed following the method outlined in Ziegler et al. (2020). The observations were obtained on 2021 Jul. 14, and 2022 Mar. 20 for B and A respectively, both in the *Cousins-I* filter, and the contrast curves yielded no companions within 1″ with a contrast of 6.7 and 7 magnitudes. The 5σ sensitivity and speckle autocorrelation functions are shown in Fig. 8.

4.3. Statistical validation

We made use of the statistical validation package `TRICERATOPS`[11] (Giacalone et al. 2021; Giacalone & Dressing 2020) using the same procedures detailed in Dransfield et al. (2024); Pozuelos et al. (2023); Barkaoui et al. (2023), to validate the planetary nature of TOI-4336.01. The threshold for validation is set at 0.015, and initially we find the false positive probability (FPP) to be 0.444. However, upon inspection of the probability breakdown, we found that the nearby transiting planet (NTP) probability on TOI-4336 B is 0.444, while probabilities for all other false positive scenarios are of order 10^{-8} or smaller. The reason for the high FPP is therefore that the two stars are blended within the TESS aperture. While we do fold in ground-based observations to the light curve used for the statistical validation to improve the precision, `TRICERATOPS` only makes use of TESS apertures for the calculation of scenario probabilities. However, in our ground-based observations, the close binary components of the triple system are resolved and we were able to confirm that the transits are on TOI-4336 A. Therefore, by eliminating this scenario, the FPP for TOI-4336.01 falls to $\sim 10^{-8}$, placing it well below the threshold for validation.

5. Global analysis

5.1. Transit analysis

We performed a global analysis of the photometric data using a custom `Fortran` code described in Gillon et al. (2012); Delrez et al. (2022) in which we made use of `emcee` (Foreman-Mackey et al. 2013), a Markov Chain Monte Carlo affine invariant ensemble sampler proposed by Goodman & Weare (2010). We used a combination of quadratic limb-darkening transit model (Mandel & Agol 2002) and baseline model to fit the data. The baseline model represents the combination of systematic effects producing correlated (red) noise, such as atmospheric conditions

[11] https://github.com/stevengiacalone/triceratops

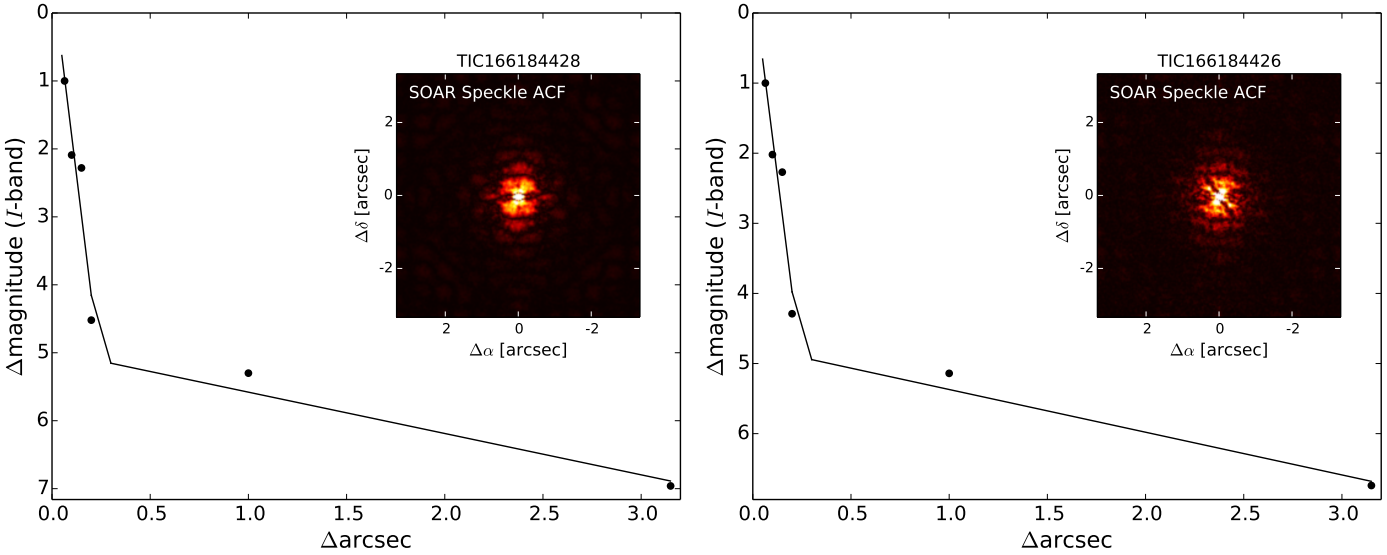

Fig. 8. Speckle autocorrelation functions (ACF) and 5σ sensitivity functions of the SOAR observations obtained for A (on the left) and B (on the right).

(airmass, FWHM of the PSF, sky background) or instrumental effects (the variation of the position of the star on the detector along the x and y directions). To remove these effects, we select a linear combination of low-order polynomials with respect to these five parameters, in addition to the time as a parameter, which minimizes the Bayesian information criterion (BIC, Schwarz 1978). Fitting simultaneously the transit signal and the correlated noise allows a good propagation of the uncertainties to the derived parameters. The TS light curves are also affected by an additional offset coming from a constraint of the German equatorial mount it is equipped with. As it crosses the meridian, the telescope mount rotates by 180° and the stars fall onto different pixels with varying sensitivity, affecting the flux measurements. The code also produces β_w and β_r, two scaling factors to apply to the photometric errors to account for an under- or over-estimation of white and red noise in each light curve. The baseline models and the error scaling factors are shown in Table E.1.

Given that the TRAPPIST-South and TESS photometric data sets are contaminated by the second fainter star of the system, we computed the dilution factor as the flux ratio in the TESS band following the definition used in the code: Dil = $\frac{F_{\rm blend}}{F_{\rm source}}$ with F_{blend} the flux of the contaminant and F_{source} the flux of the target star. We used a normal prior with a conservative 3% error to account for possible faint stars contaminating the apertures. The quadratic limb darkening coefficients u_1, u_2 are taken from Claret (2018) for TESS and the ground-based observations from Claret et al. (2012), except for the ExTrA 1.2 µm and *Sloan-zs* filters for which the priors were obtained with `PyLDTK` (Parviainen & Aigrain 2015) and the PHOENIX model atmospheres (Husser et al. 2013). We used a conservative value of 0.05 for the uncertainty in the normal prior distributions of these parameters. We also assumed a normal prior probability distribution function (PDF) for the effective temperature, and the stellar mass and radius based on the results described in Sect. 2.2 (see Table 1). The jump parameters sampled in our analysis are: the effective temperature, the metallicity, the transit epoch, the log of the orbital period, the transit depth as defined by $\mathrm{d}F = R_p^2/R_\star^2$, the cosine of the orbital inclination, the log of the stellar density, and the log of the stellar mass. The limb darkening coefficients are also taken as jump parameters following the parametrization of Kipping (2013) for triangular sampling with the quadratic limb darkening law: $q_1 = (u_1 + u_2)^2$ and $q_2 = 0.5u_1(u_1 + u_2)^{-1}$. Finally, we also fitted for the dilution parameters of the TRAPPIST-South and TESS data. We ran the `emcee` fit using two repeats of 100 walkers with 1000 steps per walker to explore efficiently the full parameter space. We monitored the convergence of the fit using the Gelman-Rubin statistic (Gelman & Rubin 1992) which allowed to check that the two independent `emcee` analyses had produced consistent posterior PDFs for the jump parameters. Table 2 shows the results of the fit for a fixed depth across all filters. This includes the jump parameters as well as the derived parameters, for each we give the median of the posterior distribution and the $1-\sigma$ interval. The posterior distributions of the jump parameters are given in the form of a `corner` plot (Foreman-Mackey 2016) in Fig. F.1.

We then performed a chromaticity check, using the same priors but allowing the depth to vary as a function of wavelength. All the depths found agree within 1-σ, they are shown in Fig. 9. We also performed an eccentric fit, adding $\sqrt{e_p}\cos\omega_p$ and $\sqrt{e_p}\sin\omega_p$ as jump parameters with e_p the eccentricity and ω_p the argument of periapsis, both of these quantities left as free parameters with no priors. We find a value of $0.12^{+0.18}_{-0.09}$ for the eccentricity. Following the Bayesian Information Criterion approximation to the Bayes Factor outlined in Wagenmakers (2007), we find a Bayes Factor of 10 654 which heavily favors the circular fit. Finally, we performed an analysis allowing the transit timings to vary to check for the existence of Transit Timing Variations (TTVs) which could be indicative of a third body in the system. We found the fitted timings to be consistent with no TTVs down to a few minutes, as shown on Fig. G.1. The lack of detected TTVs does not allow us to conclude on the presence of an additional planet orbiting TOI-4336 A.

5.2. Search for additional candidates

Given the high occurrence rates of small planets around M stars (Dressing & Charbonneau 2013; Hsu et al. 2020), a system hosting one confirmed planet is likely to host additional ones. As the threshold for a possible TOI detection is set at $S/N = 7$

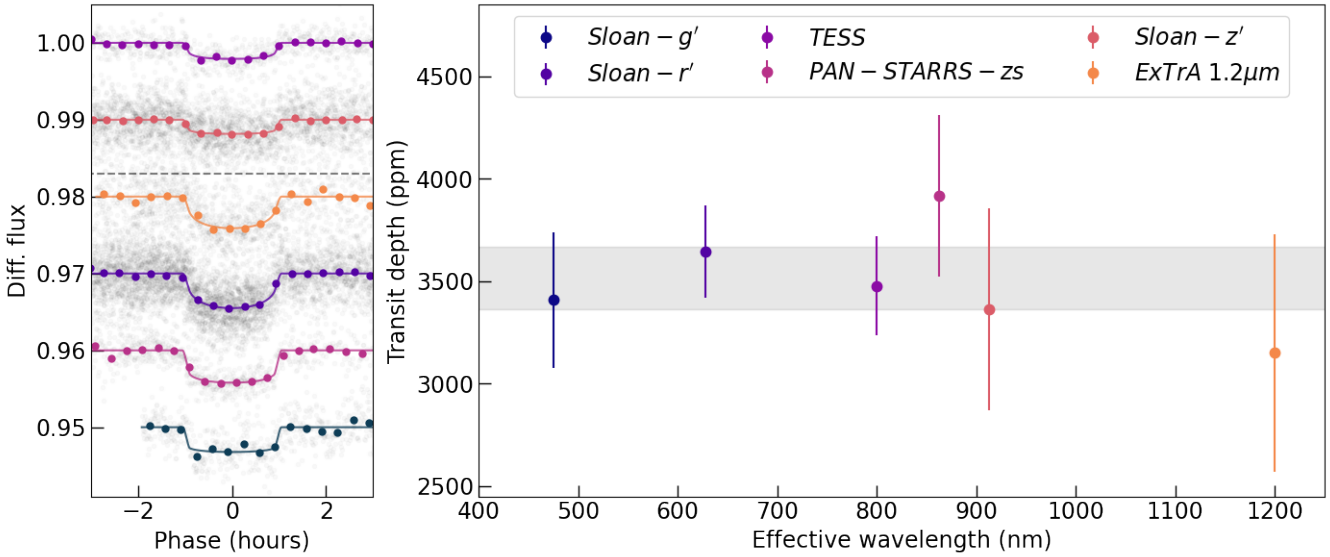

Fig. 9. Chromaticity check of TOI-4336 A b. On the left: phase folded transits from TESS and ground-based observations. The filters above the dashed line correspond to the TESS and TRAPPIST-South observations which are diluted by TOI-4336 B. On the right: comparison of the depths obtained for the chromatic fit. All the bands agree within 1-σ, and the shaded region corresponds to the depth obtained from the achromatic fit for comparison.

by the TESS pipelines, we then used the `SHERLOCK` [12] package to determine if there could be other candidates in the system that would have been missed (Pozuelos et al. 2020; Demory et al. 2020). `SHERLOCK` is a community pipeline built on robust and deeply tested astrophysical tools that performs an iterative search for signals on a given star for missions such as TESS. To carry on the task, `SHERLOCK` follows the next steps: (1) Downloading and preparing the light curves from online databases using the `lightkurve` package. (2) Computing a Lomb-Scargle periodogram (Lomb 1976; Scargle 1982; VanderPlas 2018) to identify stellar variability, and the field of view plots using `tpfplotter`. Other preprocessing steps include correction of stellar variability, and adding a high RMS mask to remove outliers. (3) Following a multi-detrend approach, a bi-weight filter provided by the `Wōtan`S [13] package (Hippke et al. 2019) is applied on the light curves using a range of window sizes. (4) The transit search is performed iteratively on the nominal light curve as well as all the detrended light curves using the `Transit Least Squares` [14] package (Hippke & Heller 2019). Once a signal is found above a certain threshold of S/N, it is masked for the next iterations, and this goes on until no more signals with sufficient S/N are found or the search reaches a certain number of iterations. (5) Vetting reports can be created for interesting signals in PDF format, where some metrics are computed and flagged in red when they are considered problematic. (6) A statistical validation can be performed using `TRICERATOPS`. (7) A Bayesian fit using the nested sampling algorithm of `Allesfitter` [15] (Günther & Daylan 2019, 2021), `Dynesty` [16] (Speagle 2020; Koposov et al. 2023), can be run for a set of selected signals to refine the system parameters. (8) An observation plan can be created based on the results of the fit for a chosen ground-based observatory.

For TOI-4336 A, we performed the transit search on the short-cadence data we extracted with custom apertures for Sectors 11, 38, and 64 of TESS, as described in Sect. 3.1. We first corrected the light curves for dilution using the value of 86.3% we obtained in the global analysis. We selected a range of ten window sizes between 0.2 and 1.3 days to generate the detrended light curves. We explored periods between 0.5 and 20 days, and selected a threshold signal of $S/N \geq 5$, with a maximum number of five runs. We ran the transit search algorithm considering all three sectors combined in addition to individual sectors. We found the signal of TOI-4336 A b to be recovered easily in the first run of all our analyses with an S/N of 18.70. We also found a second potential candidate in the combined search with a period of 7.59 days, a duration of 1.74 h, and a depth of 1.18 ppt. We denote it as TIC 166184428.02[17], assuming it corresponds to a transiting planet orbiting TOI-4336 A as well. The candidate is recovered in four out of the ten detrended light curves in the second transit search run with an S/N of 5.35. We performed the vetting stage and TIC 166184428.02 passed all the tests except for two: (1) The transit source offset computed from difference imaging, a method introduced in Bryson et al. (2017). (2) The per-pixel Box Least Squares (BLS, Kovács et al. 2002) search showed some deviation from the target. This method uses a fixed epoch and period for the BLS run on each pixels and computes the S/N of the detections. The S/N are then normalized and the centroid is found, then compared to the one found by difference imaging. These metrics are affected by the significant contamination from nearby sources which shifts the centroid on the TPFs. Given the presence of TOI-4336 B in the aperture, we do not consider these failed tests to be critical. Finally, we performed the fitting stage of `SHERLOCK` to recover the system parameters. The results of the nested sampling fit are found in Table H.1, the folded light curve and the posterior distributions of the fitted parameters can be found in Figs. H.1 and H.2. `Allesfitter` uses the parameters found in the transit search as uniform priors for the Nested Sampling fit and a GP with a Matern 3/2 kernel for detrending.

[12] https://github.com/franpoz/SHERLOCK
[13] https://github.com/hippke/wotan
[14] https://github.com/hippke/tls
[15] https://github.com/MNGuenther/allesfitter
[16] https://github.com/joshspeagle/dynesty

[17] The candidate has been submitted as a Community TESS Object of Interest https://exofop.ipac.caltech.edu/tess/target.php?id=166184428

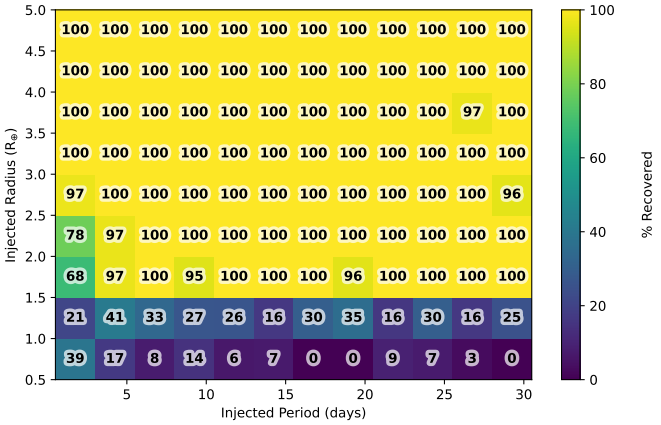

Fig. 10. Results of the injection-recovery tests on TESS light curves, described in Sect. 5.3. Almost all planets larger than 1.5 $R_\oplus$ were recovered successfully up to 30 d.

TIC 166184428.02 is at the limit of the detection threshold we set in our transit search with SHERLOCK. The shallow depth of the signal makes it challenging to check whether the single events look consistent in shape with the transit of a planet. We also performed an independent transit search on the TESS data to assess the detection limits of the data, and we did not recover the candidate (see Sect. 5.3).

5.3. Detection limits and injection-recovery tests

We used the SPECULOOS-Southern Observatory to collect ground-based data to check if monitoring of TOI-4336 A from 1-m class telescopes would allow the detection of smaller planets thanks to an improved precision compared to TESS, as it has been successfully done in Delrez et al. (2022). We gathered twelve nights of photometric observations without any transits, in the *Sloan-r'* filter, the details are shown in Table D.1. The photometric light curves for each night were extracted using the `prose` package, following the method described in Sect. 3.2 as for other ground-based data, and combined. We ran transit-search pipeline `occultence`[18] to search for additional transiting planets around TOI-4336 A with both SPECULOOS and TESS (Sect. 3.1). `occultence` consists of several steps: cleaning (cosmic ray and spurious data point removal), an initial search to mask transit structures (for detrending) using Box Least Squares (BLS, Kovács et al. 2002), a detrending method, followed by a final transit search on the detrended light curve using BLS. For SPECULOOS detrending, we chose ridge regression (Hoerl & Kennard 1970) to fit polynomials of airmass, FWHM, sky background, δx and δy (change in the position of the target on the CCD). For each night, we fit for all combinations of these parameters with different polynomial orders (up to cubic) and selected the combination with the lowest AIC (Akaike information criterion, Akaike et al. 1973), which assesses a model's likelihood of describing the data while penalizing larger numbers of parameters. For TESS's detrending step instead we performed GP-detrending to capture the remaining correlated noise. We did not detect any transit structures in either SPECULOOS or TESS detrended light curve with $S/N > 3$.

To assess the detection efficiency of our transit-search pipeline we ran injection-recovery tests on both the SPECULOOS and TESS light curves (with real transits masked). For each instrument, we generated transits for 3000 artificial planets using PyTransit (Parviainen 2015) and injected each in turn into TOI-4336 A's light curves. We used the *Sloan−r'* and TESS limb-darkening coefficients from Table 2 for SPECULOOS and TESS, respectively. Each planet's remaining parameters (radius R_p, period P, and inclination i) were drawn from the following uniform distributions: $R_p \sim U(0.5, 5.0)\,R_\oplus$, $\cos i \sim U(\cos i_{min}, \cos i_{max})$, $\log P \sim U(\log 0.5, \log 30.5)$ d, where $U(a, b)$ represents a value drawn from a uniform distribution between a and b. i_{min} and i_{max} are the minimum and maximum inclinations for a transiting planet. Due to the shorter baseline of SPECULOOS data, we limited the explored period range up to 10.5 d. The host mass and radius were taken from Table 1. However, the inclination limits depend on the orbital period; therefore, when drawing the planetary parameters, we drew each inclination from a range set by the period. Only circular orbits we considered. The time at which the first transit was injected was also drawn from a uniform distribution, $\phi \sim U(0, 1)$, where ϕ is the phase of the period, such that the first transit was injected at ϕP from the start of observations.

We used the transit-search method described at the start of this section to search for the injected planets. A planet was recovered if at least one epoch from the highest likelihood period from BLS was within 1 h of an injected transit and the S/N of that transit is >3. This recovery criterion allows us to detect even single transits. The results from our injection-recovery for TOI-4336 A with TESS are shown in Fig. 10. Due to the day-night cycle and the complications in dealing with ground-based systematics, the injection-recovery results for TESS exceed SPECULOOS for all periods > 1 d, though the results are comparable for small (<1.5 $R_\oplus$) planets and very short periods. From the TESS results it is unlikely that there exist additional planets orbiting TOI-4336 A with R>1.5 $R_\oplus$ and P<30 d, though we cannot rule out smaller, or longer period, planets.

6. Discussion

6.1. Habitability

The stellar irradiation from its host, $1.50^{+0.18}_{-0.17}$ $S_\oplus$, puts TOI-4336 A b very close at a distance consistent with the inner edge of the empirical HZ of the system (about 1.488 $S_\oplus$) (Kopparapu et al. 2013), as shown in Fig. 11. The limits of the HZ and the environments of planets orbiting close to these limits are not fully understood. Considering the error bars on the stellar irradiation, the planet could receive less or more irradiation than the irradiation at the empirical HZ limit. Probing the atmosphere of planets at the limit of the HZ will provide further insights into the environments at these stellar irradiations. A planetary radius of 2.12 $R_\oplus$ places the planet beyond the radius valley (e.g., Gupta et al. 2022), in the realm of mini-Neptunes where planets are likely to have an extended gaseous atmosphere. This expected atmosphere should allow for ease of atmospheric characterization. This makes TOI-4336 A b an interesting target to explore the environment at and around the empirical inner edge limit of the HZ and assess whether it is the likely case of a Mini-Neptune or the less likely case of a rocky planet at the inner edge of the HZ.

TOI-4336 A b orbits a host star in a triple system. While multiple host stars can influence the HZ boundaries (Kaltenegger & Haghighipour 2013; Haghighipour & Kaltenegger 2013; Kane & Hinkel 2013), the two other mid-M stars in the system orbit far enough apart to have no significant influence on the HZ limits. Using the bolometric luminosity from the SED fit (see Sect. 2.2)

[18] https://github.com/catrionamurray/occultence

and for a median semi-major axis of 133 au (see Sect. 2.4), the added flux from the second star would only add $5.76710^{-7}\ S_\oplus$ to the overall irradiation. Still, TOI-4336 A b provides a very interesting, as well as accessible, target to explore the region around the empirical HZ limits.

6.2. Formation in the triple system

Hundreds of planets have been discovered in binary systems (e.g., Raghavan et al. 2010; Matson et al. 2018). Yet binaries – especially on close or eccentric orbits – shrink the orbital real estate available for planets (Holman & Wiegert 1999). In addition, an inclined binary can trigger Kozai oscillations (Takeda et al. 2008), although this is impeded during the disk phase (Batygin et al. 2011) and in multiple-planet systems (Innanen et al. 1997; Kaib et al. 2011). In general, wider binaries have a progressively weaker influence. There is an observed deficit of exoplanets in systems with binaries closer than ∼50 au (Kraus et al. 2016). Yet, in some cases, binaries wider than ∼1000 au can reach very eccentric orbits due to external Galactic perturbations and destabilize the orbits of gas giants orbiting at Jupiter- to Saturn-like distances (Kaib et al. 2013). However, there is no evidence that the overall occurrence rate of exoplanets is strongly affected by wide binary companions (e.g., Kraus et al. 2016; Ziegler et al. 2020) .

For the case of TOI-4336 A b, we do not expect the triple stellar configuration to have played a strong role in the planet's formation or evolution. The maximum orbital radius that remains stable in the face of perturbations from a binary is a function of the companion's mass and the binary orbital parameters (Holman & Wiegert 1999; Pilat-Lohinger et al. 2003). The closer stellar companion of TOI-4336 A has a semi-major axis of 133 au (see Sect. 2.4). Assuming a binary orbital eccentricity of 0.7 (the median for a thermal distribution) and equal stellar masses, the outermost stable orbit around TOI-4336 A would be about 3% of the binary semi-major axis, or ∼4 au (assuming coplanarity between the stellar and planetary orbits; Holman & Wiegert 1999), more than an order of magnitude larger than the orbital radius of 0.09 au of TOI-4336 A b. If the binary's periastron distance were 5 au, which is the minimum value in the 1-σ contours from the analysis in Sect. 2.4, then the binary's eccentricity would have been so high that it could potentially have disrupted planet formation entirely. Given the existence of the planet, we expect that the binary's eccentricity is likely no higher than 0.7–0.8, to avoid any drastic consequences during planetary growth. The second companion, with a semi-major axis of 2915 au, would have a much smaller effect. It therefore seems unlikely that the companion stars played a direct role in the formation or evolution of the sub-Neptune TOI-4336 A b.

6.3. Prospects for detailed characterization

We explore the possibility to constrain the planet mass using high-resolution spectroscopy. Following the mass–radius relationship by Chen & Kipping (2017), we estimate the planet mass to be $5.4^{+4.1}_{-2.2}\ M_\oplus$. Measuring the implied semi-amplitude of the spectrocopic orbit, $2.9 \pm 1.6\,\mathrm{m\,s^{-1}}$, would require high-precision spectroscopy using stabilized spectrographs such as ESPRESSO (Pepe et al. 2010). Thanks to its apparent brightness (Vmag∼12.9), the star is within reach of ESPRESSO with a $3.2 \pm 1.8\,\sigma$ detection of the planet with 15 spectra. Because of its infrared brightness (Hmag=8.9), we expect detection to be also possible using NIRPS (Bouchy et al. 2017), which has been proven to show a long-term stability of 2–3 $\mathrm{m\,s^{-1}}$ for bright targets. There is already an ongoing radial velocity campaign with both these facilities to measure the mass of TOI-4336 A b.

Given the infrared brightness of the host (Kmag ∼ 8.6) and the favorable planet-to-star radius ratio due to the low-mass host star, we assess the suitability of TOI-4336 A b for the characterization of an atmosphere. We first calculated the transmission spectroscopy metric (TSM, Kempton et al. 2018) as it is a convenient metric to compare the amenability for characterization of different planets. We find that TOI-4336 A b has an exceptionally high TSM of 83^{+5}_{-4} in the temperate sub-Neptune category, making it even more favourable than some of the best-studied sub-Neptunes for a detailed atmospheric characterization by transit transmission spectroscopy with HST and JWST (e.g., LHS 1140 b, Edwards et al. 2021).

We then used `ExoTransmit` (Kempton et al. 2017) to calculate two simulated transmission spectra for TOI-4336 A b, assuming a typical H/He-rich atmosphere with an isothermal P-T profile at the planet's equilibrium temperature (∼300K). We also assume equilibrium chemistry and include all the opacities available in `ExoTransmit`. The spectra are shown in the bottom right panel of Fig. 11. The first spectrum assumes a mass equal to the estimate derived from empirical mass-radius relations presented in Chen & Kipping (2017), while the second allows for a case where the planet has a similar density to one of the densest known mini-Neptune (Kepler-231 b, Hadden & Lithwick 2014). A lower mass would simply increase the scale height making atmospheric investigations easier. We find that for the mass estimate of $\sim 5.4\ M_\oplus$, we could detect atmospheric features with $> 16\sigma$ significance in the case of a transparent atmosphere with just three transits of HST. Even in the higher mass limit of $\sim 10.1\ M_\oplus$, our simulations show that we could still detect a putative atmosphere to $> 5\sigma$ with the same observing setup. This makes TOI-4336 A b one of the most promising sub-Neptunes for atmospheric investigations. However, the presence of clouds and/or hazes could hinder the detection of atmospheric signals. Atmospheric exploration with HST is then crucial to determine whether this is the case or not. In fact, a proposal for these observations has already been accepted for HST and the campaign to measure the atmosphere of this exquisite sub-Neptune is underway. We expect this planet to become one of the best studied in its category in the coming years.

7. Conclusions

Our analyses show that TOI-4336 A b is a temperate sub-Neptune orbiting a nearby star part of a triple M-dwarf system. We tested the chromaticity of the transit with multicolor photometry and found the transit depths to be consistent within 1-σ in all the bands. We found no significant variations in the transit depth between odd and even transits, which could be an indicator of binarity or a blended source. In addition, we statistically validate the planetary nature using archival imaging spanning 47 yr of observations, and high angular resolution imaging, which excludes unresolved companions with spectral type between M4 and early-L between 0.2 and 1.2″ in separation. Our global model yields a planetary radius of $2.12^{+0.08}_{-0.09}\ R_\oplus$ and an orbital period of 16.33 days, resulting in an incident irradiation of $1.50^{+0.18}_{-0.17}\ S_\oplus$. This incident irradiation would lead to an equilibrium temperature estimate of 308 ± 9 K, assuming a Bond albedo of zero and perfect heat redistribution ($f = 1/4$). We find the host to be an M3.5 star ($T_{\rm eff} = 3298^{+75}_{-73}$ K, $M_\star = 0.33$

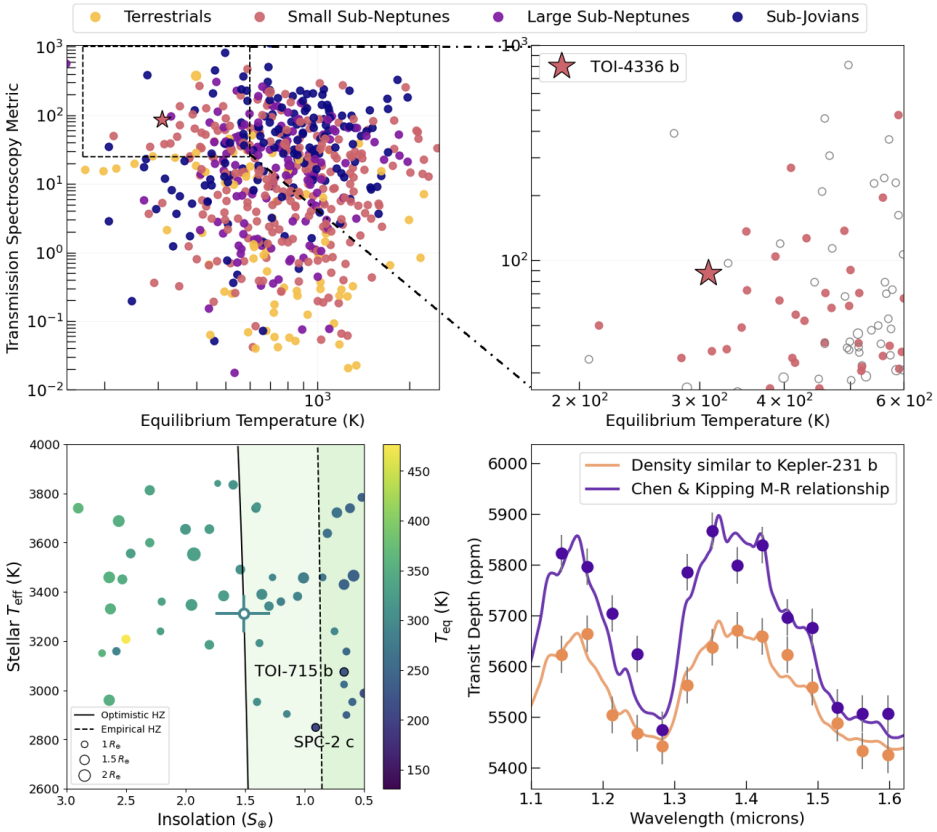

Fig. 11. Top left panel: complete sample of all known exoplanets with measured masses (Data from NASA Exoplanet Archive, Apr 2024, https://exoplanetarchive.ipac.caltech.edu/). Following Kempton et al. (2018), terrestrial planets correspond to planetary radii below 1.25 $R_\oplus$, small sub-Neptunes radii between 1.25 and 2.75 $R_\oplus$, large sub-Neptunes radii between 2.75 and 4 $R_\oplus$, and sub-Jovians are planets with radii between 4 and 10 $R_\oplus$. TOI-4336 A b is shown by the star symbol. Top right panel: zoomed in view that puts TOI-4336 A b in the context of small sub-Neptunes only. Bottom left panel: stellar effective temperature as a function of insolation of transiting exoplanets orbiting hosts cooler than 4000 K. The solid black line denotes the empirical HZ boundary and the dashed line the conservative one (Kopparapu et al. 2013). The size of points scales with the planetary radius. The points are colored according to their equilibrium temperature. TOI-4336 A b is highlighted with errorbars, and it is well placed at the inner edge of the HZ of its host star. Bottom right panel: synthetic transmission spectra for TOI-4336 A b, assuming a typical H/He-rich atmosphere with isothermal temperature profile at the planet's equilibrium temperature (~300 K). The simulated data points are for the Wide Field Camera 3 instrument of HST.

± 0.02 $M_\odot$), with estimated semi-major axes of 133 au and 2915 au with respect to the other two mid-M stars of the triple system.

The radius of this new planet puts it most likely in the mini-Neptune category, and is thus likely to have retained an extended atmosphere. The incident radiation places TOI-4336 A b at the inner edge of the empirical HZ, which makes it a good candidate to explore this region and its consequences on habitability. We investigated the implications of the triple star system on the formation of the planet and found that the eccentricity of the closer pair should be no higher than 0.8. In addition, the orbital configuration of the system implies TOI-4336 B did not have any effect on the formation of TOI-4336 A b. Indeed, the planet would need to be at more than 40 times the orbital distance from its host star for the companion to disrupt the formation of the planet.

TOI-4336 A b shows similar properties to the widely studied K2-18 b (e.g., Benneke et al. 2017, 2019; Cloutier et al. 2017; Tsiaras et al. 2019). We examined the suitability of this temperate sub-Neptune for detailed characterization and found it is a prime target for atmospheric studies with HST and JWST. The determination of its mass is a key ingredient for the interpretation of transmission spectra. We find both ESPRESSO and NIRPS are appropriate to measure the radial velocities of the planet and constrain its mass.

Acknowledgements. Funding for the TESS mission is provided by NASA's Science Mission Directorate. We acknowledge the use of public TESS data from pipelines at the TESS Science Office and at the TESS Science Processing Operations Center. This research has made use of the Exoplanet Follow-up Observation Program website, which is operated by the California Institute of Technology, under contract with the National Aeronautics and Space Administration under the Exoplanet Exploration Program. This paper includes data collected by the TESS mission that are publicly available from the Mikulski Archive for Space Telescopes (MAST). Based on data collected by the SPECULOOS-South Observatory at the ESO Paranal Observatory in Chile.The ULiege's contribution to SPECULOOS has received funding from the European Research Council under the European Union's Seventh Framework Programme (FP/2007–2013) (grant Agreement n° 336480/SPECULOOS), from the Balzan Prize and Francqui Foundations, from the Belgian Scientific Research Foundation (F.R.S.-FNRS; grant n° T.0109.20), from the University of Liege, and from the ARC grant for Concerted Research Actions financed by the Wallonia-Brussels Federation. This work is supported by a grant from the Simons Foundation (PI Queloz, grant number 327127). This research is in part funded by the European Union's Horizon 2020 research and innovation programme (grants agreements n° 803193/BEBOP), and from the Science and Technology Facilities Council (STFC; grant n° ST/S00193X/1, and ST/W000385/1). The material is based upon work supported by NASA under award number 80GSFC21M0002. Based on data collected by the TRAPPIST-South telescope at the ESO La Silla Observatory. TRAPPIST is funded by the Belgian Fund for Scientific Research (Fond National de la Recherche Scientifique, FNRS) under the grant PDR T.0120.21,

with the participation of the Swiss National Science Fundation (SNF). Based on data collected under the ExTrA project at the ESO La Silla Paranal Observatory. ExTrA is a project of Institut de Planétologie et d'Astrophysique de Grenoble (IPAG/CNRS/UGA), funded by the European Research Council under the ERC Grant Agreement n. 337591-ExTrA. This work has been supported by a grant from Labex OSUG@2020 (Investissements d'avenir – ANR10 LABX56). This work has been carried out within the framework of the NCCR PlanetS supported by the Swiss National Science Foundation. The Digitized Sky Surveys were produced at the Space Telescope Science Institute under U.S. Government grant NAG W-2166. The images of these surveys are based on photographic data obtained using the Oschin Schmidt Telescope on Palomar Mountain and the UK Schmidt Telescope. The plates were processed into the present compressed digital form with the permission of these institutions. This work makes use of observations from the LCOGT network. Part of the LCOGT telescope time was granted by NOIRLab through the Mid-Scale Innovations Program (MSIP). MSIP is funded by NSF. Based in part on observations obtained at the Southern Astrophysical Research (SOAR) telescope, which is a joint project of the Ministério da Ciência, Tecnologia e Inovações (MCTI/LNA) do Brasil, the US National Science Foundation NOIRLab, the University of North Carolina at Chapel Hill (UNC), and Michigan State University (MSU). IRAF was distributed by the National Optical Astronomy Observatory, which was managed by the Association of Universities for Research in Astronomy (AURA) under a cooperative agreement with the National Science Foundation. Some of the observations in the paper made use of the High-Resolution Imaging instrument Zorro obtained under Gemini LLP Proposal Number: GN/S-2021A-LP-105. Zorro was funded by the NASA Exoplanet Exploration Program and built at the NASA Ames Research Center by Steve B. Howell, Nic Scott, Elliott P. Horch, and Emmett Quigley. Zorro was mounted on the Gemini South telescope of the international Gemini Observatory, a program of NSF's OIR Lab, which is managed by the Association of Universities for Research in Astronomy (AURA) under a cooperative agreement with the National Science Foundation. on behalf of the Gemini partnership: the National Science Foundation (United States), National Research Council (Canada), Agencia Nacional de Investigación y Desarrollo (Chile), Ministerio de Ciencia, Tecnología e Innovación (Argentina), Ministério da Ciência, Tecnologia, Inovações e Comunicações (Brazil), and Korea Astronomy and Space Science Institute (Republic of Korea). The postdoctoral fellowship of K.B. is funded by F.R.S.-FNRS grant T.0109.20 and by the Francqui Foundation. This publication benefits from the support of the French Community of Belgium in the context of the FRIA Doctoral Grant awarded to M.T. E.D. acknowledges support from the innovation and research Horizon 2020 program in the context of the Marie Sklodowska-Curie subvention 945298. B.V.R. thanks the Heising-Simons Foundation for support. M.G. is F.R.S.-FBRS Research Director. F.J.P. acknowledges financial support from the grant CEX2021-001131-S funded by MCIN/AEI/10.13039/501100011033 and through projects PID2019-109522GB-C52 and PID2022-137241NB-C43. KAC and SNQ acknowledge support from the TESS mission via subaward s3449 from MIT. B.-O.D. acknowledges support from the Swiss State Secretariat for Education, Research and Innovation (SERI) under contract number MB22.00046. E.J. is a Belgian FNRS Senior Research Associate. YGMC acknowledges support from UNAM-PAPIIT-IG101321. L.D. is an F.R.S.-FNRS Postdoctoral Researcher. SNR acknowledges support from the French Programme National de Planétologie (PNP). This research made use of Lightkurve, a Python package for *Kepler* and TESS data analysis (Lightkurve Collaboration, 2018). This research has made use of the NASA Exoplanet Archive, which is operated by the California Institute of Technology, under contract with the National Aeronautics and Space Administration under the Exoplanet Exploration Program. Resources supporting this work were provided by the NASA High-End Computing (HEC) Program through the NASA Advanced Supercomputing (NAS) Division at Ames Research Center for the production of the SPOC data products. This work made use of `tpfplotter` by J. Lillo-Box (publicly available in `www.github.com/jlillo/tpfplotter`), which also made use of the python packages `astropy`, `lightkurve`, `matplotlib` and `numpy`. This work has made use of data from the European Space Agency (ESA) mission *Gaia* (`https://www.cosmos.esa.int/gaia`), processed by the *Gaia* Data Processing and Analysis Consortium (DPAC, `https://www.cosmos.esa.int/web/gaia/dpac/consortium`). Funding for the DPAC has been provided by national institutions, in particular the institutions participating in the *Gaia* Multilateral Agreement. This research has made use of the Washington Double Star Catalog maintained at the U.S. Naval Observatory. This publication makes use of data products from the Two Micron All Sky Survey, which is a joint project of the University of Massachusetts and the Infrared Processing and Analysis Center/California Institute of Technology, funded by the National Aeronautics and Space Administration and the National Science Foundation.

References

Adams, E. R., Seager, S., & Elkins-Tanton, L. 2008, ApJ, 673, 1160
Akaike, H., Petrov, B. N., & Csaki, F. 1973, Second International Symposium on Information Theory (Budapest: Akadémiai Kiadó)
Aller, A., Lillo-Box, J., Jones, D., Miranda, L. F., & Barceló Forteza, S. 2020, A&A, 635, A128
Bailer-Jones, C. A. L., Rybizki, J., Fouesneau, M., Demleitner, M., & Andrae, R. 2021, AJ, 161, 147
Barkaoui, K., Timmermans, M., Soubkiou, A., et al. 2023, A&A, 677, A38
Batygin, K., Morbidelli, A., & Tsiganis, K. 2011, A&A, 533, A7
Bean, J. L., Raymond, S. N., & Owen, J. E. 2021, J. Geophys. Res. (Planets), 126, e06639
Benneke, B., Werner, M., Petigura, E., et al. 2017, ApJ, 834, 187
Benneke, B., Wong, I., Piaulet, C., et al. 2019, ApJ, 887, L14
Berger, T. A., Huber, D., Gaidos, E., van Saders, J. L., & Weiss, L. M. 2020, AJ, 160, 108
Bianchi, L., Shiao, B., & Thilker, D. 2017, ApJS, 230, 24
Bonfils, X., Almenara, J. M., Jocou, L., et al. 2015, SPIE Conf. Ser., 9605, 96051L
Borucki, W. J., Koch, D. G., Basri, G., et al. 2011, ApJ, 736, 19
Bouchy, F., Doyon, R., Artigau, É., et al. 2017, The Messenger, 169, 21
Bradley, L., Sipőcz, B., Robitaille, T., et al. 2023, `https://doi.org/10.5281/zenodo.7946442`
Brown, T. M., Baliber, N., Bianco, F. B., et al. 2013, PASP, 125, 1031
Bryson, S. T., Jenkins, J. M., Klaus, T. C., et al. 2017, Kepler Data Processing Handbook: Target and Aperture Definitions: Selecting Pixels for Kepler Downlink, Kepler Science Document KSCI-19081-002, 3, ed. J. M. Jenkins
Buder, S., Asplund, M., Duong, L., et al. 2018, MNRAS, 478, 4513
Burdanov, A., Delrez, L., Gillon, M., & Jehin, E. 2018, in Handbook of Exoplanets, eds. H. J. Deeg, & J. A. Belmonte (Springer International Publishing AG), 130
Caldwell, D. A., Tenenbaum, P., Twicken, J. D., et al. 2020, RNAAS, 4, 201
Chen, J., & Kipping, D. 2017, ApJ, 834, 17
Ciardi, D. R., Beichman, C. A., Horch, E. P., & Howell, S. B. 2015, ApJ, 805, 16
Claret, A. 2018, A&A, 618, A20
Claret, A., Hauschildt, P. H., & Witte, S. 2012, A&A, 546, A14
Cloutier, R., & Menou, K. 2020, AJ, 159, 211
Cloutier, R., Astudillo-Defru, N., Doyon, R., et al. 2017, A&A, 608, A35
Cointepas, M., Almenara, J. M., Bonfils, X., et al. 2021, A&A, 650, A145
Cushing, M. C., Vacca, W. D., & Rayner, J. T. 2004, PASP, 116, 362
Cushing, M. C., Rayner, J. T., & Vacca, W. D. 2005, ApJ, 623, 1115
Cutri, R. M., Skrutskie, M. F., van Dyk, S., et al. 2003, VizieR Online Data Catalog II/246
Cutri, R. M., Wright, E. L., Conrow, T., et al. 2021, VizieR Online Data Catalog II/328
Delrez, L., Gillon, M., Queloz, D., et al. 2018, SPIE Conf. Ser., 10700, 107001I
Delrez, L., Murray, C. A., Pozuelos, F. J., et al. 2022, A&A, 667, A59
Demory, B. O., Pozuelos, F. J., Gómez Maqueo Chew, Y., et al. 2020, A&A, 642, A49
Dransfield, G., Timmermans, M., Triaud, A. H. M. J., et al. 2024, MNRAS, 527, 35
Dressing, C. D., & Charbonneau, D. 2013, ApJ, 767, 95
Edwards, B., Changeat, Q., Mori, M., et al. 2021, AJ, 161, 44
Foreman-Mackey, D. 2016, J. Open Source Softw., 1, 24
Foreman-Mackey, D., Hogg, D. W., Lang, D., & Goodman, J. 2013, PASP, 125, 306
Fulton, B. J., Petigura, E. A., Howard, A. W., et al. 2017, AJ, 154, 109
Furlan, E., & Howell, S. B. 2017, AJ, 154, 66
Gagné, J., Mamajek, E. E., Malo, L., et al. 2018, ApJ, 856, 23
Gaia Collaboration 2022, VizieR Online Data Catalog: I/355
Garcia, L. J., Timmermans, M., Pozuelos, F. J., et al. 2021, Astrophysics Source Code Library, [`record ascl:2111.006`]
Garcia, L. J., Timmermans, M., Pozuelos, F. J., et al. 2022, MNRAS, 509, 4817
Gelman, A., & Rubin, D. B. 1992, Statist. Sci., 7, 457
Giacalone, S., & Dressing, C. D. 2020, Astrophysics Source Code Library, [`record ascl:2002.004`]
Giacalone, S., Dressing, C. D., Jensen, E. L. N., et al. 2021, AJ, 161, 24
Gillon, M., Jehin, E., Magain, P., et al. 2011, EPJ Web Conf., 11, 06002
Gillon, M., Triaud, A. H. M. J., Fortney, J. J., et al. 2012, A&A, 542, A4
Goodman, J., & Weare, J. 2010, Commun. Appl. Math. Computat. Sci., 5, 65
Guerrero, N. M., Seager, S., Huang, C. X., et al. 2021, ApJS, 254, 39
Günther, M. N., & Daylan, T. 2019, Astrophysics Source Code Library [`record ascl:1903.003`]
Günther, M. N., & Daylan, T. 2021, ApJS, 254, 13
Gupta, A., & Schlichting, H. E. 2019, MNRAS, 487, 24
Gupta, A., Nicholson, L., & Schlichting, H. E. 2022, MNRAS, 516, 4585
Hadden, S., & Lithwick, Y. 2014, ApJ, 787, 80
Haghighipour, N., & Kaltenegger, L. 2013, ApJ, 777, 166

Henden, A. A., Levine, S., Terrell, D., & Welch, D. L. 2015, in Am. Astron. Soc. Meeting Abstracts, 225, 336.16
Hippke, M., & Heller, R. 2019, Astrophysics Source Code Library [record ascl:1910.007]
Hippke, M., David, T. J., Mulders, G. D., & Heller, R. 2019, AJ, 158, 143
Hoerl, A. E., & Kennard, R. W. 1970, Technometrics, 12, 55
Holman, M. J., & Wiegert, P. A. 1999, AJ, 117, 621
Howell, S. B., & Furlan, E. 2022, Front. Astron. Space Sci., 9, 871163
Howell, S. B., Everett, M. E., Sherry, W., Horch, E., & Ciardi, D. R. 2011, AJ, 142, 19
Howell, S. B., Everett, M. E., Horch, E. P., et al. 2016, ApJ, 829, L2
Hsu, D. C., Ford, E. B., & Terrien, R. 2020, MNRAS, 498, 2249
Huang, C. X., Vanderburg, A., Pál, A., et al. 2020, RNAAS, 4, 204
Husser, T. O., Wende-von Berg, S., Dreizler, S., et al. 2013, A&A, 553, A6
Innanen, K. A., Zheng, J. Q., Mikkola, S., & Valtonen, M. J. 1997, AJ, 113, 1915
Jehin, E., Gillon, M., Queloz, D., et al. 2011, The Messenger, 145, 2
Jenkins, J. M., Caldwell, D. A., & Borucki, W. J. 2002, ApJ, 564, 495
Jenkins, J. M., Caldwell, D. A., Chandrasekaran, H., et al. 2010, ApJ, 713, L87
Jenkins, J. M., Twicken, J. D., McCauliff, S., et al. 2016, SPIE Conf. Ser., 9913, 99133E
Jenkins, J. M., Tenenbaum, P., Seader, S., et al. 2020, Kepler Data Processing Handbook: Transiting Planet Search, Kepler Science Document KSCI-19081-003, 9, ed. J. M. Jenkins
Kaib, N. A., Raymond, S. N., & Duncan, M. J. 2011, ApJ, 742, L24
Kaib, N. A., Raymond, S. N., & Duncan, M. 2013, Nature, 493, 381
Kaltenegger, L. 2017, ARA&A, 55, 433
Kaltenegger, L., & Haghighipour, N. 2013, ApJ, 777, 165
Kane, S. R., & Hinkel, N. R. 2013, ApJ, 762, 7
Kasting, J. F., Whitmire, D. P., & Reynolds, R. T. 1993, Icarus, 101, 108
Kempton, E. M. R., Lupu, R., Owusu-Asare, A., Slough, P., & Cale, B. 2017, PASP, 129, 044402
Kempton, E. M. R., Bean, J. L., Louie, D. R., et al. 2018, PASP, 130, 114401
Kesseli, A. Y., West, A. A., Veyette, M., et al. 2017, ApJS, 230, 16
Kiman, R., Faherty, J. K., Cruz, K. L., et al. 2021, AJ, 161, 277
Kinemuchi, K., Barclay, T., Fanelli, M., et al. 2012, PASP, 124, 963
Kipping, D. M. 2013, MNRAS, 435, 2152
Kirkpatrick, J. D., Looper, D. L., Burgasser, A. J., et al. 2010, ApJS, 190, 100
Koposov, S., Speagle, J., Barbary, K., et al. 2023, https://doi.org/10.5281/zenodo.8408702
Kopparapu, R. K., Ramirez, R., Kasting, J. F., et al. 2013, ApJ, 765, 131
Kopparapu, R. K., Wolf, E. T., Arney, G., et al. 2017, ApJ, 845, 5
Kovács, G., Zucker, S., & Mazeh, T. 2002, A&A, 391, 369
Kraus, A. L., Ireland, M. J., Huber, D., Mann, A. W., & Dupuy, T. J. 2016, AJ, 152, 8
Lasker, B. M., Doggett, J., McLean, B., et al. 1996, in ASP Conf. Ser., 101, Astronomical Data Analysis Software and Systems V, eds. G. H. Jacoby, & J. Barnes, 88
Lee, E. J., Chiang, E., & Ormel, C. W. 2014, ApJ, 797, 95
Lépine, S., Rich, R. M., & Shara, M. M. 2003, AJ, 125, 1598
Lépine, S., Rich, R. M., & Shara, M. M. 2007, ApJ, 669, 1235
Lépine, S., Hilton, E. J., Mann, A. W., et al. 2013, AJ, 145, 102
Lester, K. V., Matson, R. A., Howell, S. B., et al. 2021, AJ, 162, 75
Li, J., Tenenbaum, P., Twicken, J. D., et al. 2019, PASP, 131, 024506
Lightkurve Collaboration (Cardoso, J. V. d. M., et al.) 2018, Astrophysics Source Code Library [record ascl:1812.013]
Lomb, N. R. 1976, Ap&SS, 39, 447
Luque, R., & Pallé, E. 2022, Science, 377, 6611
Mandel, K., & Agol, E. 2002, ApJ, 580, L171
Mann, A. W., Brewer, J. M., Gaidos, E., Lépine, S., & Hilton, E. J. 2013, AJ, 145, 52
Mann, A. W., Dupuy, T., Kraus, A. L., et al. 2019, ApJ, 871, 63
Mason, B. D., Wycoff, G. L., Hartkopf, W. I., Douglass, G. G., & Worley, C. E. 2001, AJ, 122, 3466
Matson, R. A., Howell, S. B., Horch, E. P., & Everett, M. E. 2018, AJ, 156, 31
McCully, C., Volgenau, N. H., Harbeck, D.-R., et al. 2018, SPIE Conf. Ser., 10707, 107070K
Medina, A. A., Winters, J. G., Irwin, J. M., & Charbonneau, D. 2022, ApJ, 935, 104
Newton, E. R., Irwin, J., Charbonneau, D., et al. 2017, ApJ, 834, 85
Owen, J. E., & Wu, Y. 2013, ApJ, 775, 105
Paredes, L. A., Henry, T. J., Quinn, S. N., et al. 2021, AJ, 162, 176
Parviainen, H. 2015, MNRAS, 450, 3233
Parviainen, H., & Aigrain, S. 2015, MNRAS, 453, 3821
Pass, E. K., Charbonneau, D., Irwin, J. M., & Winters, J. G. 2022, ApJ, 936, 109
Pass, E. K., Winters, J. G., Charbonneau, D., et al. 2023, AJ, 166, 11
Pearce, L. A., Kraus, A. L., Dupuy, T. J., et al. 2020, ApJ, 894, 115
Pepe, F. A., Cristiani, S., Rebolo Lopez, R., et al. 2010, SPIE Conf. Ser., 7735, 77350F
Pickles, A. J. 1998, PASP, 110, 863
Pilat-Lohinger, E., Funk, B., & Dvorak, R. 2003, A&A, 400, 1085
Pont, F., Zucker, S., & Queloz, D. 2006, MNRAS, 373, 231
Pozuelos, F. J., Suárez, J. C., de Elía, G. C., et al. 2020, A&A, 641, A23
Pozuelos, F. J., Timmermans, M., Rackham, B. V., et al. 2023, A&A, 672, A70
Raghavan, D., McAlister, H. A., Henry, T. J., et al. 2010, ApJS, 190, 1
Rayner, J. T., Toomey, D. W., Onaka, P. M., et al. 2003, PASP, 115, 362
Rayner, J. T., Cushing, M. C., & Vacca, W. D. 2009, ApJS, 185, 289
Reid, I. N., Brewer, C., Brucato, R. J., et al. 1991, PASP, 103, 661
Reid, I. N., Hawley, S. L., & Gizis, J. E. 1995, AJ, 110, 1838
Ricker, G. R., Winn, J. N., Vanderspek, R., et al. 2015, J. Astron. Telescopes Instrum. Syst., 1, 014003
Riddick, F. C., Roche, P. F., & Lucas, P. W. 2007, MNRAS, 381, 1067
Rogers, L. A. 2015, ApJ, 801, 41
Scargle, J. D. 1982, ApJ, 263, 835
Schwarz, G. 1978, Ann. Statist., 6, 461
Scott, N. J., Howell, S. B., Gnilka, C. L., et al. 2021, Front. Astron. Space Sci., 8, 138
Sebastian, D., Gillon, M., Ducrot, E., et al. 2021, A&A, 645, A100
Sharma, S., Stello, D., Buder, S., et al. 2018, MNRAS, 473, 2004
Speagle, J. S. 2020, MNRAS, 493, 3132
Stassun, K. G., & Torres, G. 2016, AJ, 152, 180
Stassun, K. G., & Torres, G. 2021, ApJ, 907, L33
Stassun, K. G., Collins, K. A., & Gaudi, B. S. 2017, AJ, 153, 136
Stassun, K. G., Corsaro, E., Pepper, J. A., & Gaudi, B. S. 2018, AJ, 155, 22
Stassun, K. G., Oelkers, R. J., Paegert, M., et al. 2019, AJ, 158, 138
Stevenson, K. B., Bean, J. L., Seifahrt, A., et al. 2016, ApJ, 817, 141
Takeda, G., Kita, R., & Rasio, F. A. 2008, ApJ, 683, 1063
Tokovinin, A. 2018, PASP, 130, 035002
Tokovinin, A., Fischer, D. A., Bonati, M., et al. 2013, PASP, 125, 1336
Tsiaras, A., Waldmann, I. P., Tinetti, G., Tennyson, J., & Yurchenko, S. N. 2019, Nat. Astron., 3, 1086
Twicken, J. D., Catanzarite, J. H., Clarke, B. D., et al. 2018, PASP, 130, 064502
VanderPlas, J. T. 2018, ApJS, 236, 16
Wagenmakers, E.-J. 2007, Psychon. Bull. Rev., 14, 779
West, A. A., Hawley, S. L., Bochanski, J. J., et al. 2008, AJ, 135, 785
Zacharias, N., Finch, C. T., Girard, T. M., et al. 2013, AJ, 145, 44
Ziegler, C., Tokovinin, A., Briceño, C., et al. 2020, AJ, 159, 19
Zsom, A., Seager, S., de Wit, J., & Stamenković, V. 2013, ApJ, 778, 109

[1] Astrobiology Research Unit, Université de Liège, 19C Allée du 6 Août, 4000 Liège, Belgium
e-mail: mathilde.timmermans@uliege.be
[2] School of Physics & Astronomy, University of Birmingham, Edgbaston, Birmingham B15 2TT, UK
[3] Department of Earth, Atmospheric and Planetary Science, Massachusetts Institute of Technology, 77 Massachusetts Avenue, Cambridge, MA 02139, USA
[4] Kavli Institute for Astrophysics and Space Research, Massachusetts Institute of Technology, Cambridge, MA 02139, USA
[5] Department of Physics, UC San Diego, 9500 Gilman Drive, La Jolla, CA 92093, USA
[6] Kavli Institute for Particle Astrophysics & Cosmology, Stanford University, Stanford, CA 94305, USA
[7] Instituto de Astrofísica de Canarias (IAC), 38205 La Laguna, Tenerife, Spain
[8] Cerro Tololo Inter-American Observatory/NSF's NOIRLab, Casilla 603, La Serena 1700000, Chile
[9] Department of Astronomy & Astrophysics, UC San Diego, 9500 Gilman Drive, La Jolla, CA 92093, USA
[10] Center for Astrophysics | Harvard & Smithsonian, 60 Garden Street, Cambridge, MA, 02138, USA
[11] Univ. Grenoble Alpes, CNRS, IPAG, 38000 Grenoble, France
[12] Observatoire de Genève, Département d'Astronomie, Université de Genève, Chemin Pegasi 51b, 1290 Versoix, Switzerland
[13] Dpto. Física Teórica y del Cosmos, Universidad de Granada, 18071 Granada, Spain

[14] LESIA, Observatoire de Paris, Université PSL, CNRS, Sorbonne Université, Université Paris Cité, 5 place Jules Janssen, 92195 Meudon, France
[15] AIM, CEA, CNRS, Université Paris-Saclay, Université de Paris, 91191 Gif-sur-Yvette, France
[16] Department of Physics & Astronomy, Vanderbilt University, 6301 Stevenson Center Ln., Nashville, TN 37235, USA
[17] Department of Physics, Engineering and Astronomy, Stephen F. Austin State University, 1936 North St, Nacogdoches, TX 75962, USA
[18] Carl Sagan Institute, Cornell University, 302 Space Science Building, 14850 Ithaca, NY, USA
[19] Department of Astrophysical and Planetary Sciences, University of Colorado Boulder, Boulder, CO 80309, USA
[20] Laboratoire d'Astrophysique de Bordeaux, CNRS and Université de Bordeaux, Allée Geoffroy St. Hilaire, 33165 Pessac, France
[21] Oukaimeden Observatory, High Energy Physics and Astrophysics Laboratory, Faculty of sciences Semlalia, Cadi Ayyad University, Marrakech, Morocco
[22] Caltech/IPAC-NASA Exoplanet Science Institute, 770 S. Wilson Avenue, Pasadena, CA 91106, USA
[23] Space Sciences, Technologies and Astrophysics Research (STAR) Institute, Université de Liège, Allée du 6 Août 19C, 4000 Liège, Belgium
[24] Center for Space and Habitability, University of Bern, Gesellschaftsstrasse 6, 3012, Bern, Switzerland
[25] Center for Computational Astrophysics, Flatiron Institute, New York, NY, USA
[26] Universidad Nacional Autónoma de México, Instituto de Astronomía, AP 70-264, Ciudad de México 04510, Mexico
[27] Cavendish Laboratory, JJ Thomson Avenue, Cambridge CB3 0HE, UK
[28] SUPA Physics and Astronomy, University of St. Andrews, Fife KY16 9SS, Scotland, UK
[29] European Space Agency (ESA), European Space Research and Technology Centre (ESTEC), Keplerlaan 1, 2201 AZ Noordwijk, The Netherlands
[30] NASA Ames Research Center, Moffett Field, CA 94035, USA
[31] Department of Physics and Astronomy, The University of North Carolina at Chapel Hill, Chapel Hill, NC 27599-3255, USA
[32] Departamento de Astrofísica, Universidad de La Laguna (ULL), 38206 La Laguna, Tenerife, Spain
[33] Instituto de Astrofísica de Andalucía (IAA-CSIC), Glorieta de la Astronomía s/n, 18008 Granada, Spain
[34] ETH Zurich, Department of Physics, Wolfgang-Pauli-Strasse 2, 8093 Zurich, Switzerland
[35] Royal Astronomical Society, Burlington House, Piccadilly, London W1J 0BQ, UK
[36] Department of Astronomy, University of Maryland, College Park, MD 20742, USA
[37] Istituto Nazionale di Astrofisica, Osservatorio Astrofisico di Torino, Strada Osservatorio 20, 10025 Pino Torinese, Italy
[38] Kotizarovci Observatory, Sarsoni 90, 51216 Viskovo, Croatia
[39] SETI Institute, Mountain View, CA 94043 USA/NASA Ames Research Center, Moffett Field, CA 94035, USA
[40] Department of Astrophysical Sciences, Princeton University, Princeton, NJ 08544, USA

Appendix A: Color-magnitude diagram

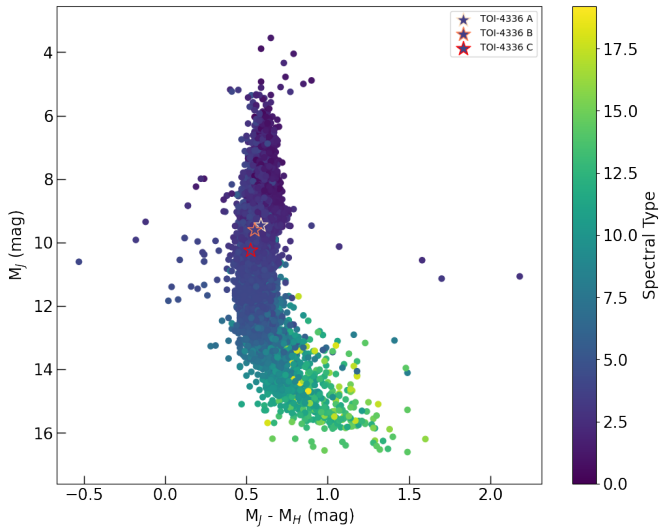

Fig. A.1. Color-magnitude diagram for nearby M dwarfs.The TOI-4336 system is marked with a star symbol and color-coded to distinguish the three stars. TOI-4336 C appear redder than A and B, which is consistent with a later spectral type (M4±0.5 compared to M3.5±0.5. We used the extended target list of the SPECULOOS survey which gathers over 14 000 M-dwarf stars within 40 parsecs to generate the diagram (Sebastian et al. 2021).

Appendix B: Age estimation

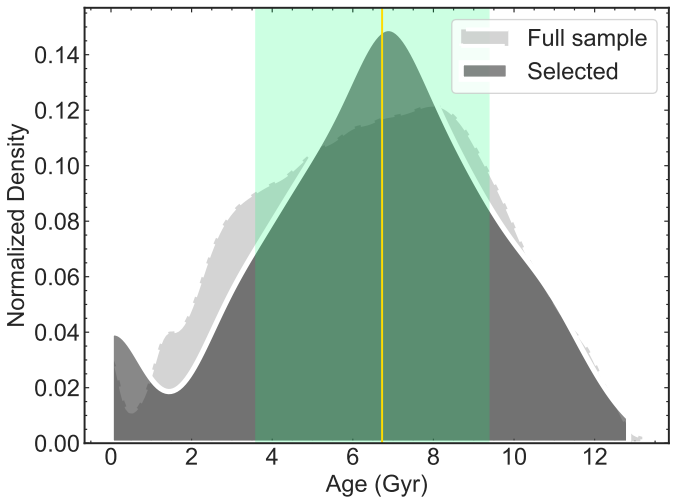

Fig. B.1. Age distribution of the *GALAH* survey (light grey) and the distribution of stars within our selection criteria (dark grey). The yellow line indicates the median age and the yellow bands are the 16 percentile and 84 percentile regions. We estimate an age of $6.7^{+2.7}_{-3.1}$ Gyr for the system.

Appendix C: Triple system orbital analysis

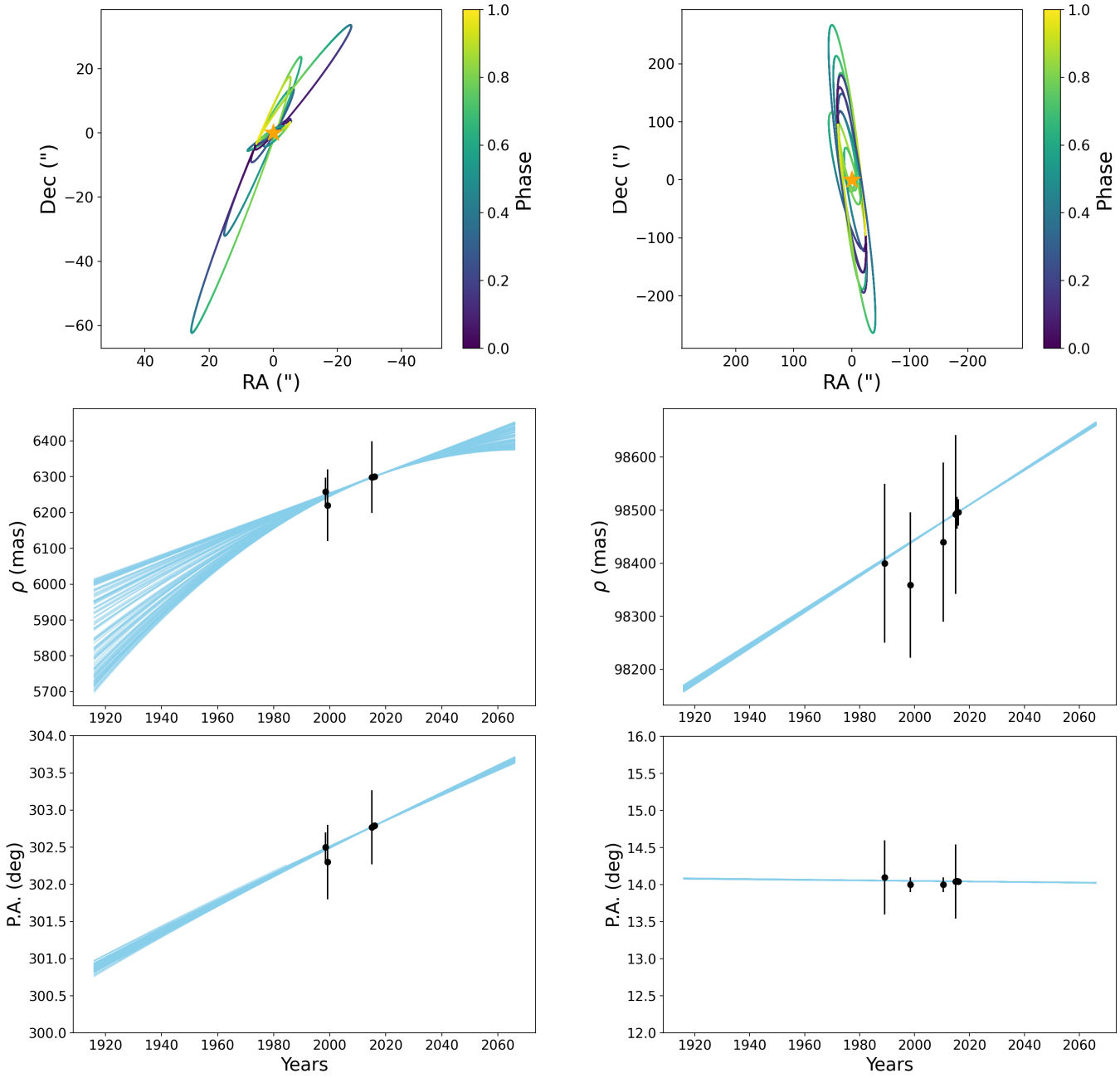

Fig. C.1. *Top row:* AB (left) and AC (right) orbits with ten random orbital solutions from posterior of the orbit fit. *Middle row:* separation with WDS astrometry for AB (left) and AC (right) orbits with a hundred random orbital solutions from posterior of the fit.*Bottom row:* the same for the position angle.

Table C.1. Astrometry measurements from WDS (Mason et al. 2001) for AC (left) and AB (right) systems used in the orbital fit.

Date	sep (″)	σ_{sep} (″)	P.A. (°)	σ_{PA} (°)
1989.17	98.40	0.15	14.10	0.50
1998.52	98.36	0.14	14.00	0.10
2010.50	98.44	0.15	14.00	0.10
2015.00	98.49	0.15	14.04	0.50
2015.50	98.50	0.03	14.05	0.01
2016.00	98.50	0.03	14.04	0.01

Date	sep (″)	σ_{sep} (″)	P.A. (°)	σ_{PA} (°)
1998.52	6.26	0.04	302.50	0.20
1999.29	6.22	0.10	302.30	0.50
2015.00	6.30	0.10	302.77	0.50
2015.50	6.30	$1.20\ 10^{-4}$	302.78	$1.00\ 10^{-3}$
2016.00	6.30	$3.30\ 10^{-5}$	302.79	$3.00\ 10^{-4}$

Table C.2. Summary of orbital parameters for the TOI-4336 system.

	AB system				AC system			
Parameter	**Median**	**Std Dev**	**68% CI**	**95% CI**	**Median**	**Std Dev**	**68% CI**	**95% CI**
a (″)	5.9	29.9	(3.2, 7.8)	(3.2, 44.4)	129.7	138.9	(60.2, 160.1)	(59.6, 325.4)
a (au)	133	605	(72, 177)	(72, 1005)	2915	3120	(1351, 3595)	(1340, 7309)
Periastron (au)	32.6	382.1	(5.1, 114.9)	(1.3, 434.1)	1705	1717	(169, 3765)	(25, 5493)
Period (years)	1908	33930	(752, 2886)	(746, 39282)	165150	418794	(52630, 227110)	(51972, 634155)
e	0.79	0.26	(0.65, 0.98)	(0.12, 0.99)	0.42	0.34	(0.00005, 0.71)	(0.01, 0.99)
i (deg)	80.5	12.8	(73.1, 85.5)	(45.8, 89.1)	96.6	12.9	(93.4, 100.1)	(92.3, 133.9)
ω (deg)	182.8	101.4	(82.5, 305.7)	(6.2, 342.9)	178.7	107.8	(146.3, 353.3)	(14.1, 359.9)
Ω (deg)	123.1	112.2	(-57.2, 137.9)	(-57.2, 299.8)	-165.5	104.9	(-174.8, 9.0)	(-331.3, 14.0)
Distance (pc)	22.44	0.02	(22.42, 22.47)	(22.40, 22.49)	22.46	0.02	(22.44, 22.48)	(22.42, 22.49)

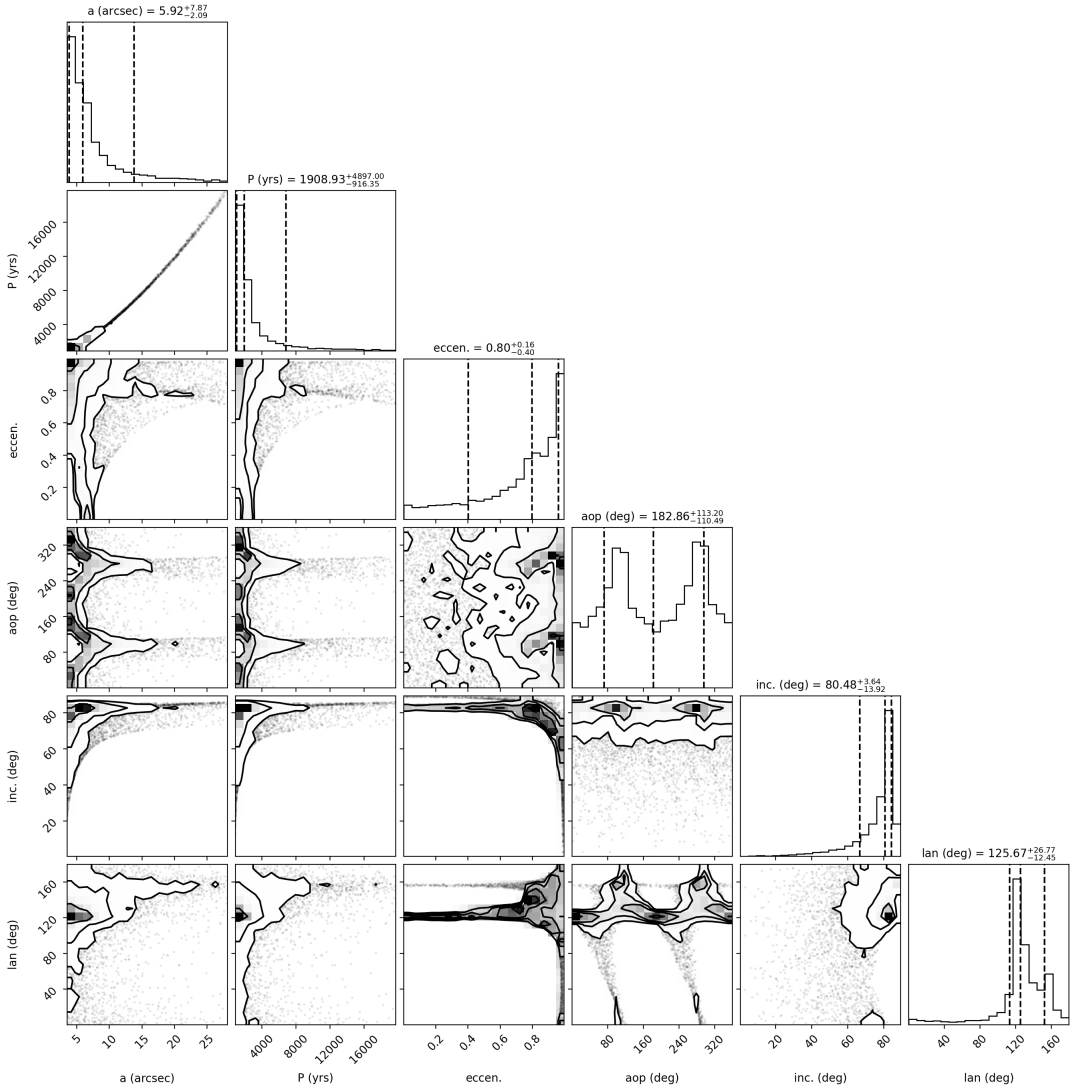

Fig. C.2. Posterior samples of the AB system. Histogram sub-panels show the posterior distribution, with the median and 68% confidence intervals marked by dashed lines, with titles quantifying those ranges.

Appendix D: Ground-based photometric observations

Table D.1. Summary of the ground-based follow-up observations obtained for the validation of TOI-4336 A b.

Observatory	Filter	Date	Coverage	Exp. time (s)	FWHM (″)	Aperture (″)	Measurements
TRAPPIST-South	*Sloan-z'*	2021 Apr 30	Full	15	2.62	11.11	1001
SSO/Europa	*Sloan-r'*	2021 Jun 18	Ingress	10	1.96	3.04	647
SSO/Ganymede	*Sloan-r'*	2021 Jun 18	Ingress	10	2.31	3.44	674
TRAPPIST-South	*Sloan-z'*	2021 Jun 18	Full	15	2.42	10.69	1029
LCO (CTIO)	*Pan-STARRS-zs*	2021 Jun 18	Full	45	1.64	2.35	308
TRAPPIST-South	*Sloan-z'*	2021 Aug 06	Ingress	15	2.99	10.59	443
LCO (SAAO)	*Sloan-g'*	2022 Feb 18	Ingress	150	1.76	2.54	54
SSO/Europa	*Sloan-g'*	2022 Apr 08	Full	24	1.19	2.38	473
LCO (CTIO)	*Sloan-g'*	2022 Apr 08	Ingress	150	1.76	3.00	60
LCO (CTIO)	*Pan-STARRS-zs*	2022 Apr 08	Ingress	45	1.53	2.30	144
SSO/Europa	*Sloan-r'*	2022 May 27	Full	10	1.11	2.60	1415
SSO/Io	*Sloan-g'*	2022 May 27	Full	24	1.70	1.88	685
TRAPPIST-South	*Sloan-z'*	2022 May 27	Full	15	1.82	11.91	857
ExTrA (Tel. 2)	1.2 µm	2022 May 27	Full	60	1.045	8.00	351
ExTrA (Tel. 3)	1.2 µm	2022 May 27	Full	60	1.367	8.00	351
SSO/Io	*Sloan-r'*	2023 Mar 17	Full	10	1.56	2.52	1323
SSO/Europa	*Sloan-r'*	2023 Mar 17	Full	10	1.11	2.52	1321
LCO (CTIO)	*Pan-STARRS-zs*	2023 Mar 17	Full	45	1.48	2.47	207
LCO (CTIO)	*Sloan-g'*	2023 Mar 17	Full	150	2.71	3.28	89
SSO/Callisto	*Sloan-r'*	2021 Jul 13	Monitoring	10	2.77	2.15	829
SSO/Callisto	*Sloan-r'*	2021 Jul 14	Monitoring	10	3.32	3.14	924
SSO/Callisto	*Sloan-r'*	2021 Jul 15	Monitoring	10	2.63	2.64	908
SSO/Callisto	*Sloan-r'*	2021 Jul 16	Monitoring	10	2.51	2.97	885
SSO/Callisto	*Sloan-r'*	2021 Jul 17	Monitoring	10	1.96	2.48	660
SSO/Callisto	*Sloan-r'*	2021 Jul 18	Monitoring	10	1.92	2.15	856
SSO/Io	*Sloan-r'*	2022 Mar 10	Monitoring	10	1.39	2.74	1404
SSO/Europa	*Sloan-r'*	2022 Mar 11	Monitoring	10	1.36	2.85	1411
SSO/Europa	*Sloan-r'*	2022 Mar 12	Monitoring	10	1.36	2.06	236
SSO/Io	*Sloan-r'*	2022 Mar 13	Monitoring	10	1.34	3.07	767
SSO/Europa	*Sloan-r'*	2022 Mar 14	Monitoring	10	1.21	2.62	783
SSO/Europa	*Sloan-r'*	2022 Mar 15	Monitoring	10	1.24	2.51	792

Appendix E: Global model errors and scaling factors

Table E.1. Global model errors and scaling factors for the MCMC analysis of the photometric data.

Observatory	Filter	T_0 (BJD-TDB-2 450 000)	Baseline model	Residual RMS (Exp. time)	β_w	β_r
TESS Sector 11	TESS	8616.7747	$p(t^2)$	1.21 10^{-3} (120s)	0.80	1.25
TESS Sector 38	TESS	9335.5733	$p(t^2)$	1.17 10^{-3} (120s)	0.99	1.01
TESS Sector 38	TESS	9351.9096	$p(t^2)$	1.26 10^{-3} (120s)	0.65	1.50
TRAPPIST-South	*Sloan-z'*	9335.5733	$p(t^2, a^2)$	2.59 10^{-3} (15s)	0.77	1.34
SSO/Europa	*Sloan-r'*	9368.2460	$p(t^2,f^2)$	2.39 10^{-3} (10s)	0.76	1.37
SSO/Ganymede	*Sloan-r'*	9368.2460	$p(t^2,f^2)$	2.63 10^{-3} (10s)	0.70	1.45
TRAPPIST-South	*Sloan-z'*	9368.2460	$p(t^2,a^2)$	2.77 10^{-3} (15s)	0.72	1.40
LCO (CTIO)	*Pan-STARRS-zs*	9368.2460	$p(t^4,a^2)$	1.41 10^{-3} (45s)	0.58	1.66
TRAPPIST-South	*Sloan-z'*	9433.5913	$p(t^2,a^2)$	2.47 10^{-4} (15s)	0.90	1.13
LCO (SAAO)	*Sloan-g'*	9629.9940	$p(t^2)$	2.38 10^{-3} (150s)	0.72	1.39
SSO/Europa	*Sloan-g'*	9678.6362	$p(t^2)$	3.49 10^{-4} (24s)	0.69	1.46
LCO (CTIO)	*Sloan-g'*	9678.6362	$p(t^2)$	1.70 10^{-3} (150s)	0.81	1.25
LCO (CTIO)	*Pan-STARRS-zs*	9678.6362	$p(t^2)$	1.33 10^{-3} (45s)	0.93	1.17
SSO/Europa	*Sloan-r'*	9727.6452	$p(t^2,f^2)$	2.40 10^{-3} (45s)	0.68	1.49
SSO/Io	*Sloan-g'*	9727.6452	$p(t^2)$	2.83 10^{-3} (24s)	0.77	1.35
TRAPPIST-South	*Sloan-z'*	9727.6452	$p(t^2)$	1.92 10^{-3} (15s)	0.67	1.45
ExTrA	1.2 µm	9727.6452	$p(t^4)$	2.29 10^{-3} (60s)	0.70	2.18
ExTrA	1.2 µm	9727.6452	$p(t^4)$	1.94 10^{-3} (60s)	0.62	1.73
SSO/Io	*Sloan-r'*	10021.6991	$p(t^2)$	3.32 10^{-3} (10s)	0.89	1.09
SSO/Europa	*Sloan-r'*	10021.6991	$p(t^2)$	3.24 10^{-3} (10s)	0.51	1.84
LCO (CTIO)	*Pan-STARRS-zs*	10021.6991	$p(t^4)$	1.35 10^{-3} (45s)	0.72	1.38
LCO (CTIO)	*Sloan-g'*	10021.6991	$p(t^2)$	1.93 10^{-3} (150s)	0.54	1.87
TESS Sector 64	TESS	8616.7747	$p(t^2)$	1.33 10^{-3} (120s)	0.89	1.12

For each transit observation, the chosen baseline model is denoted as $p(\alpha^n)$ with α a parameter such as t = time, a = airmass, f = FWHM of the PSF, x or y = position of the target on the detector along the $x-$ and $y-$ axes, and n the order of the considered polynomial. The residual RMS is also given with the corresponding exposure time and the error scaling factors β_w and β_r. The column T_0 represents the expected mid-transit times.

Appendix F: Posterior distributions of the transit model

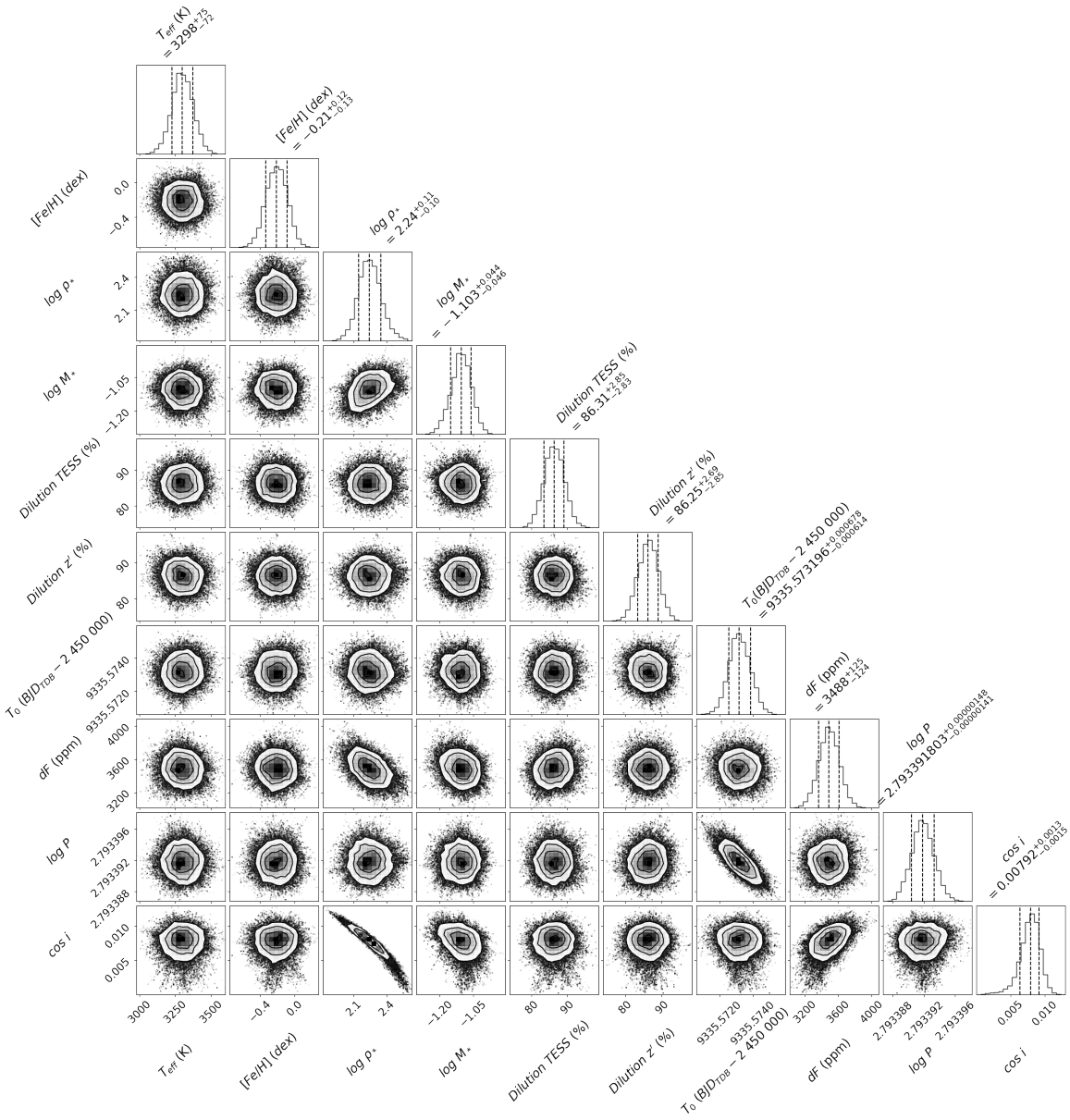

Fig. F.1. Posterior distributions for the main jump parameters used in the `emcee` fit (see Sect. 5): the effective temperature ($T_{\rm eff}$), the metallicity ([Fe/H]), the log of the stellar density (log $\rho_\star$), the log of the stellar mass (log $M_\star$), the dilution in the TESS and z' bands, the epoch (T_0), the transit depth (dF), the log of the orbital period (log P) and the cosine of the orbital inclination of the planet (cos i).

Appendix G: Transit timing variations

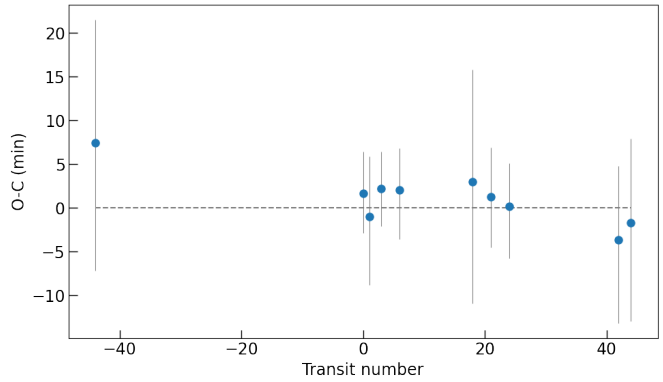

Fig. G.1. O-C diagram obtained from a global fit allowing transit timing variations. We used as reference the timing obtained in the global transit model of Table 2.

Appendix H: Search for additional candidates in the system

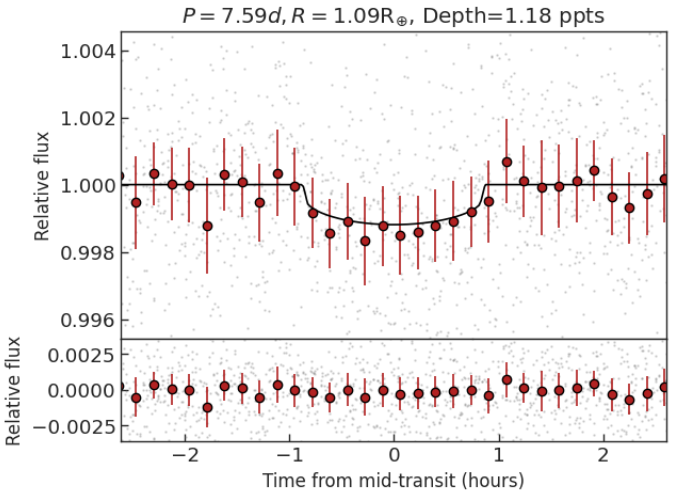

Fig. H.1. Transit model of TIC 166184428.02. Top panel: phase folded photometry of TIC 166184428.02. The best-fit model is shown in solid black. The grey points are the raw flux and the red points are the 15-minutes binned flux. Bottom panel: residuals of the best-fit model.

Table H.1. Properties of TIC 166184428.02 obtained from the fitting stage of SHERLOCK, see Sect. 5.2.

Parameter	Value	Unit	Source
Fitted parameters			
$R_b/R_\star$	$0.0306^{+0.0011}_{-0.0016}$		fit
$(R_\star + R_b)/a_b$	$0.0310^{+0.0012}_{-0.0010}$		fit
$\cos i_b$	$0.0069^{+0.0050}_{-0.0042}$		fit
$T_{0;b}$	2459333.2923 ± 0.0025	BJD	fit
P_b	$7.587329^{+0.000030}_{-0.000041}$	d	fit
$q_{1;\mathrm{lc}}$	$0.55^{+0.27}_{-0.30}$		fit
$q_{2;\mathrm{lc}}$	$0.55^{+0.27}_{-0.31}$		fit
$\log \sigma_{\mathrm{lc}}$	-6.062 ± 0.012		fit
gp : $\ln \sigma$(lc)	$-7.14^{+0.23}_{-0.21}$		fit
gp : $\ln \rho$(lc)	0.18 ± 0.47		fit
Derived parameters			
Host radius over semi-major axis; $R_\star/a$	$0.0301^{+0.0012}_{-0.0010}$		derived
Semi-major axis over host radius; $a/R_\star$	$33.2^{+1.2}_{-1.3}$		derived
Companion radius over semi-major axis; R_p/a	$0.000920^{+0.000047}_{-0.000052}$		derived
Companion radius; R_p	$1.088^{+0.051}_{-0.064}$	$R_\oplus$	derived
Semi-major axis; a	0.0504 ± 0.0024	au	derived
Inclination; i	$89.60^{+0.24}_{-0.29}$	deg	derived
Impact parameter; b	$0.23^{+0.16}_{-0.14}$		derived
Total transit duration; T_{tot}	$1.739^{+0.075}_{-0.083}$	h	derived
Full-transit duration; T_{full}	$1.631^{+0.074}_{-0.087}$	h	derived
Host density from orbit; $\rho_\star$	12.0 ± 1.3	cgs	derived
Equilibrium temperature; T_{eq}	378 ± 24	K	derived
Transit depth (undil.); $\delta_{\mathrm{tr;undil}}$	$1.18^{+0.14}_{-0.12}$	ppt	derived
Limb darkening; $u_{1;\mathrm{lc}}$	$0.73^{+0.47}_{-0.42}$		derived
Limb darkening; $u_{2;\mathrm{lc}}$	$-0.07^{+0.43}_{-0.37}$		derived

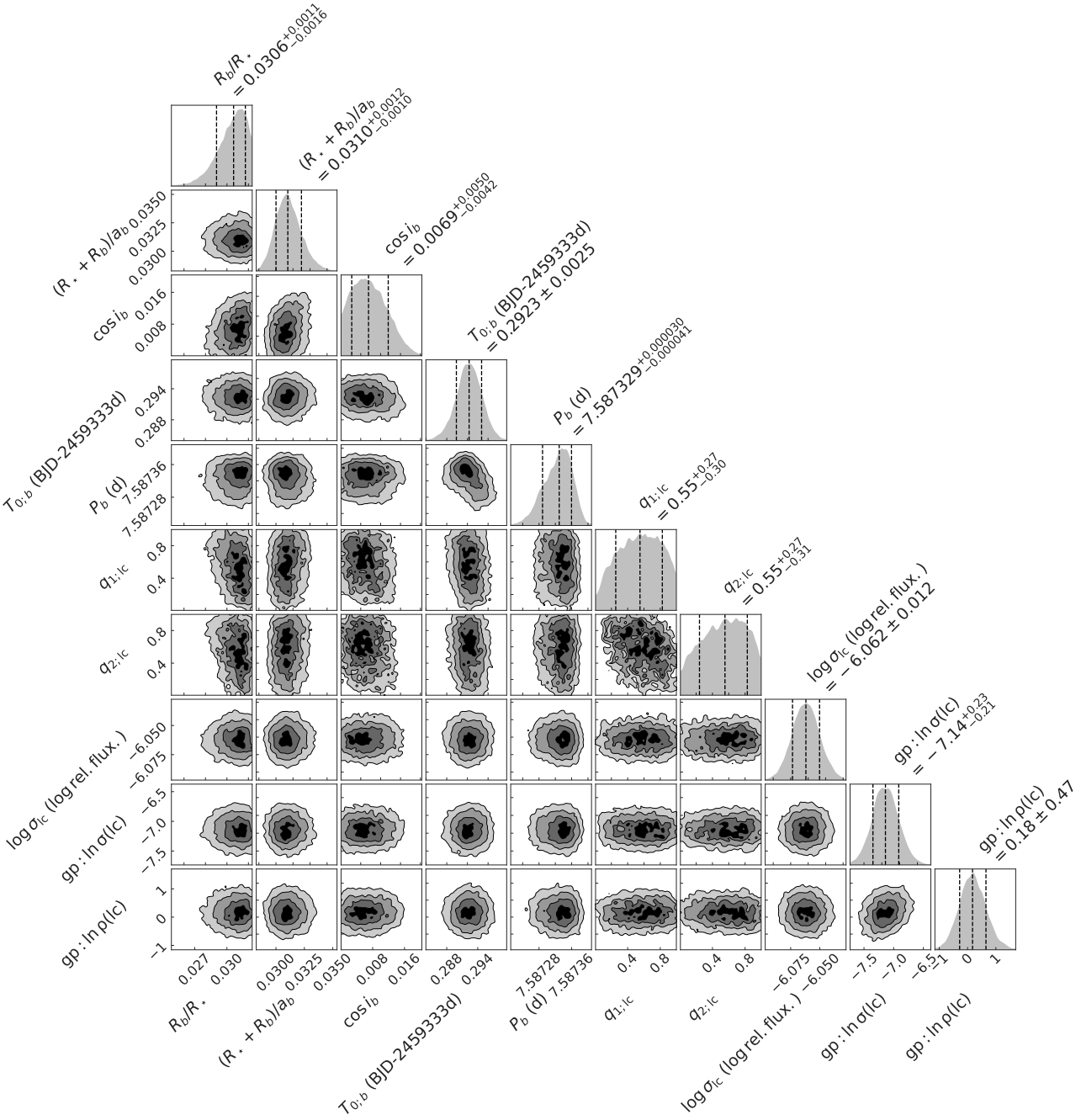

Fig. H.2. Posterior distributions for the main parameters fitted in the Nested Sampling fit for the second candidate found in the TOI-4336 system, TIC 166184428.02 (see Sect. 5.2), with R_b the candidate radius, $R_\star$ the stellar radius, i_b the inclination, $T_{0;b}$ the epoch, P_b the period, $q_{1;lc}$ and $q_{2;lc}$ the Kipping parametrisation (Kipping 2013) for the limb darkening coefficients, $log\sigma_1 c$ the error scaling parameter, and $ln\sigma(lc)$ and $ln\rho(lc)$ the two GP parameters related to the amplitude and length scale.

Chapter 4

Atmospheric reconnaissance of TOI-4336 A b

4.1 Introduction

TOI-4336 A b was firstly identified by TESS in 2020, as described in Chapter 3). Our follow-up efforts led to a quick validation of the planet. Given the very high TSM (Transmission Spectroscopy Metric, given by Equation 1.30) of the planet of over 80, George Dransfield (PI) and I (co-PI) opted to perform a first exploration of its atmosphere with HST (Hubble Space Telescope, described in Section 2.4.1). Our mid-cycle proposal was accepted (P16875) for the period 29 spanning November 15, 2021, to September 30, 2022. We obtained two transits during the allocated period. Unfortunately, due to pointing issues, part of the first transit and the full second transit were not usable. I was able to successfully request two new transits to make up for the lost data. The observations are summarized in Table 4.1. Given the constraints linked to our science case, we were only able to obtain one additional transit so far. HST has been put into Reduced Gyro Mode (RGM) since May 24, 2024, due to the loss of one gyroscope, it is now unlikely we will obtain the remaining transits of the program with the same observing setup. However, I am actively discussing with our program coordinator how to modify our initial requirements to comply with the new orientation constraints of HST.

I am leading the paper presenting the atmospheric reconnaissance of TOI-4336 A b with HST, although it is still in the early stages given that we are still acquiring data. I am also the contact point of our program coordinator to schedule the visits and check that each possible window fits our science goals requirements. Although our program is not complete at this time, this Chapter describes how the combination of the partial first observation and the third full transit still allows to conclude on the likely absence of clouds in the upper atmosphere of TOI-4336 A b. The data analysis was initially performed using a custom extraction method at the Massachusetts Institute of Technology by George Dransfield and myself during our month-long visit in August 2022 in the team of Julien de Wit. Given the difficulties encountered with the first two datasets, we enlisted the help of Billy Edwards, and decided to use the widely used `Iraclis` pipeline (Tsiaras et al., 2016b,a, 2018) instead. It is described in Section 2.4.1. The spectral extraction method described in Section 4.4 was initially developed by George Dransfield and Billy Edwards. Once a final spectrum is obtained, the fitting of synthetic spectra to the observed one (called a *retrieval*) will be performed to infer the physical and chemical properties of the planet. This is described in Section 4.5.

Table 4.1: Summary of the HST observations for the atmospheric reconnaissance of TOI-4336 A b (P16875).

Visit	**Orbit**	**Date**	**Status**
1	1	Jun. 13, 2022	Failed (Rescheduled)
	2	Jun. 13, 2022	Completed (Rescheduled)
	3	Jun. 13, 2022	Completed (Rescheduled)
	4	Jun. 13, 2022	Completed (Rescheduled)
2	1	Jun. 29, 2022	Failed (Rescheduled)
	2	Jun. 29, 2022	Failed (Rescheduled)
	3	Jun. 29, 2022	Failed (Rescheduled)
	4	Jun. 29, 2022	Failed (Rescheduled)
3	1	Sep. 25, 2023	Completed
	2	Sep. 25, 2023	Completed
	3	Sep. 25, 2023	Completed
	4	Sep. 25, 2023	Completed
4	1	-	Not scheduled yet
	2	-	Not scheduled yet
	3	-	Not scheduled yet
	4	-	Not scheduled yet
5	1	-	Not scheduled yet
	2	-	Not scheduled yet
	3	-	Not scheduled yet
	4	-	Not scheduled yet

4.2 Context

As mentioned in Chapter 1, studying the atmospheres of small planets is currently one of the main focus of the field of Exoplanetology. The favorable planet-to-star size ratio promises enhanced transmission features for planets orbiting M dwarfs. The WFC3/IR instrument of HST provides a window into the H_2O/CH_4 feature at 1.41μm with its G141 grism. In the last few years, it has notably been used to peer into the atmosphere of known terrestrial and sub-Neptune planets. There are two possible outcomes from such observations: (1) the spectrum appears flat and no molecular signatures are detected, (2) the spectrum is exhibiting the molecular signature of atmospheric constituents.

A flat transmission spectrum can be attributed either to a high mean molecular weight atmospheric composition, or high-altitude clouds or hazes. For example, GJ 1214 b was the first planet to be observed in transmission with WFC3/IR (Berta et al., 2012). The observations of this warm sub-Neptune yielded a flat spectrum, and the authors argued it was likely due to a large mean molecular weight outer envelope. However, high-altitude clouds were also discussed as a possible source of opacity. Kreidberg et al. (2014) later proved that molecular features should then have been detected thanks to the large number of new transits collected and the increased precision on the spectrum, yet this was not the case. They found that the presence of clouds in the atmosphere of GJ 1214 b is the only possibility to explain the data. This was later confirmed by Kempton et al. (2023) with a phase curve analysis obtained with JWST. Actually, flat spectra have also been observed for a variety of planet masses and temperatures, such as GJ 436 b (Knutson et al., 2014a), HD 97658 b (Knutson et al., 2014b), or Kepler 51 b and d (Libby-Roberts et al., 2020).

The first detection of water vapor in the atmosphere of a sub-Neptune was claimed for the planet K2-18 b (Tsiaras et al., 2019; Benneke et al., 2019). This detection was later challenged by Bézard et al. (2022) which supported that CH_4 is the dominant absorber. Recently, JWST observations confirmed the atmosphere is indeed dominated by CH_4 as well as CO_2 (Madhusudhan et al., 2023) thanks to its larger wavelength coverage and increased precision. Water absorption has since then been detected in several other sub-Neptunes (e.g. Roy et al., 2023; Mikal-Evans et al., 2023), as well as larger planets (e.g. Brande et al., 2022; Skaf et al., 2020).

HST WFC3/IR provides the opportunity to search for hints of molecular features or the presence of an aerosol layer in the upper atmosphere of small transiting planets. Given the very limited wavelength range, many degeneracies exist between atmospheric models in the case of a potential detection of features. Remediating this entails obtaining complementary observations with ground-based or space-based observatories. Because of the over-subscription of JWST, observers often request a first exploratory program with HST. However, it is likely that the WFC3/IR observations will be halted for next cycles based on redundancy with JWST[1]. Luckily, over 500 hours of Director's Discretionary Time on JWST will be allocated to a large scale exoplanet program investigating the atmosphere of rocky planets orbiting red dwarfs through emission spectroscopy during the upcoming Cycle 3 (Redfield et al., 2024).

4.3 WFC3/ IR observations

As explained in Section 2.4.1, HST is placed on a low-Earth orbit with an orbital period of approximately 95 minutes. This configuration allows an orbital visibility period of $\sim$ 50 minutes on target before the Earth blocks the field of view. This Earth occultation lasts

[1] https://www.stsci.edu/contents/newsletters/2024-volume-41-issue-02/the-space-telescope-users-committee-stuc-june-2024

between 40 to 50 minutes every orbit, and produces a discontinuity in the time-series data spanning multiple orbits. In the case of TOI-4336 A b, the transit has a total duration of 125 minutes. To cover the full transit and include a baseline orbit, four orbits per transit are needed. This is referred to as a *visit*. Each visit starts with a guide star acquisition image, then a target star acquisition image that is used for calibration purposes. Because of the brightness of TOI-4336 A in the NIR, we made use of the spatial scanning mode. We selected a 90° angle for the scanning direction to be perpendicular to the dispersion axis. We chose a scan length of 4.2 ″ using a scan rate of 0.14 ″/s to stay well under the saturation limit of 78 000e$^-$, with the brightest pixel counts being at $\sim$ 27000e$^-$[2]. We chose the GRISM256 aperture, resulting in 266 × 266 pixel images. Each image consists of five nondestructive reads with sampling time intervals of 10 seconds (i.e. the SPARS10 mode with NSAMP of 5), resulting in a total exposure time of 30 seconds. One visit included 18 measurements of forward and backward scans, resulting in 36 data points. Given the field of view of WFC3/IR of $\sim 33'' \times 33''$ with the selected observing setup, both TOI-4336 A and B are observed simultaneously. The geometry of the system is illustrated in Figure 4.1 in the ideal case of a scan perpendicular to the line joining the two stars.

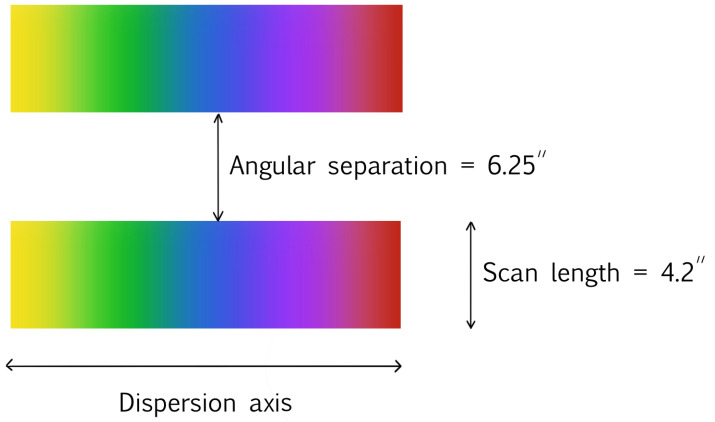

Figure 4.1: Illustration of the HST field of view for the WFC3/IR observation of TOI-4336 A b in spatial scanning mode. Both TOI-4336 A and B are visible on the detector.

In the case of an isolated star, all orientation angles (called *orients*) of the detector are convenient. In the peculiar configuration of the TOI-4336 system, this is not the case. We computed the limiting orient with respect to the scan direction to prevent any blending of the two stars, as shown in Figure 4.2. Given the scan length of 4.2″ and the angular separation of 6.25″ between the two stars, we find an angle of 47°. Our initial constraints were defined using the Astronomer's Proposal Tool software[3] dedicated to HST (and JWST) proposal Phases I and II. HST uses a specific coordinate system for WFC3/IR which takes into account the small distortion of the field of view due to the tilting of the detector. An overview of the initial orient range is given in Figure 4.3, we selected an orient of $\sim$ 75° as the ideal case corresponding to $\theta = 0°$, and added a conservative 3° margin. As HST entered RGM, the orient ranges allowed are now only 275 to 340°. Choosing a dispersion along the negative X-axis gives access to a possible orient range between 275 and 280°. This corresponds to an angle θ between 20 to 25° which still provides a separation of 1.4 and 1.6″, respectively, between the two spectra.

[2] https://etc.stsci.edu/etc/results/WFC3IR.ss.1935187/
[3] https://www.stsci.edu/scientific-community/software/astronomers-proposal-tool-apt

The dispersion length is over 16″ and is set by the use of the G141 grism. A nearby star at an angular separation of 14.9″ can be seen on Figure 4.3, which can potentially introduce some contamination. According to the HST Exposure Time Calculator[4], the contribution of this nearby star can be estimated by the brightest pixel per single exposure, which has a count of $\sim 90e^{-}$. This corresponds to a contribution of 0.3% of the total flux. Assuming a quiet star, this can be taken into account in the global fit of the transit light curve.

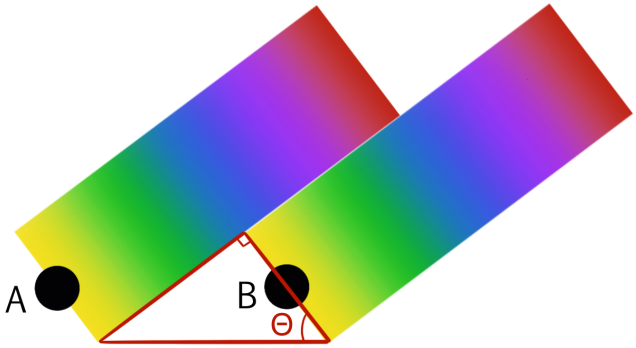

Figure 4.2: Illustration of the orientation constraints for the WFC3/IR observations of TOI-4336 A b. θ represents the angle between the scan axis and the system axis at which the two stellar spectra start to blend.

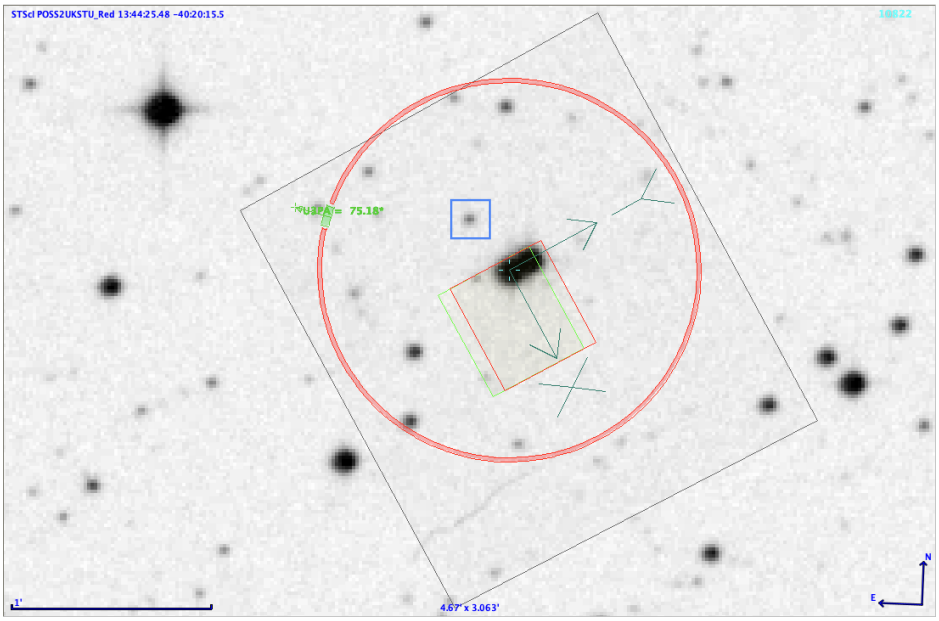

Figure 4.3: Initial orientation range chosen for the WFC3/IR observation of TOI-4336 A b. The field of view is represented by the black rectangle, the green arc indicates the orientation range selected for the observation, and the red one the forbidden angles. The green rectangle illustrates the beginning of the scan and the red one the end of it, the scan direction is then along the Y-axis and the dispersion along the X-axis. This figure is obtained using the Aladin Tool of the Astronomer's Proposal Tool software for HST. The star which could contaminate the spectrum for orients between 275 and 280° is highlighted by a blue rectangle.

[4] https://etc.stsci.edu/etc/results/WFC3IR.ss.1935186/

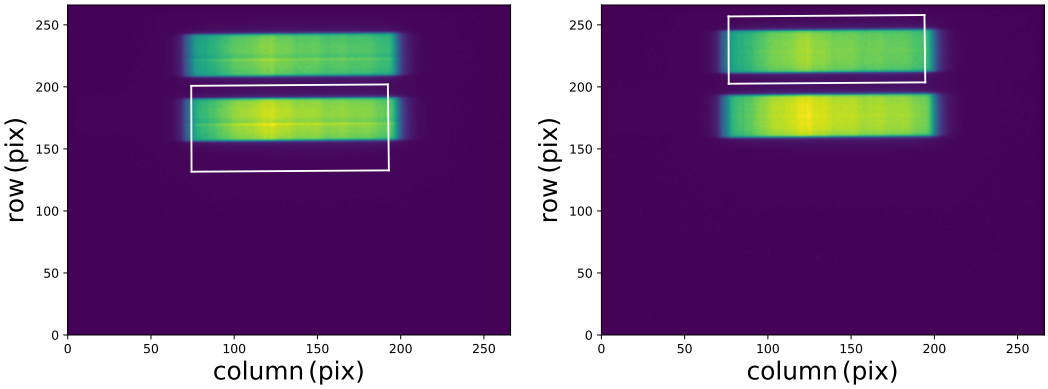

Figure 4.4: Apertures used for the reduction of the HST data of visit 1 with `Iraclis`. On the left, the aperture chosen for TOI-4336 A, and on the right, for TOI-4336 B.

4.4 Extraction of the transmission spectrum

The raw fits data from visits 1 and 3 were obtained from the Milkuski Archive for Space Telescopes. The data reduction was done using the `Iraclis` pipeline (Tsiaras et al., 2016b), a Python package specifically designed to deal with spatially scanned WFC3/IR data (see Section 2.4.1). Because `Iraclis` does not allow to combine visits, we engineered a new method specific to the TOI-4336 system which takes advantage of the presence of the two stars in the field of view.

Initially, we considered the dataset of the first visit. `Iraclis` uses a quadrangular aperture slightly larger than the scanned spectrum during the reduction process to allow the background subtraction. We expanded the aperture asymetrically by 15 pixels above and 20 pixels below in the $y-$axis direction to include sufficient background flux for TOI-4336 A and avoid any contamination. Similarly, we reduced the data selecting TOI-4336 B as the target star to extract the photometry. We then offset the aperture by 53 pixels along the $y-$axis, and used an expanded aperture by 10 pixels above and 10 pixels below the spectrum. The apertures are shown in Figure 4.4. The splitting function of `Iraclis` allows to separate the dataset into its individual up-the-ramp reads. Because our spectra are not overlapping with any background source, splitting the data is not needed.

The TOI-4336 system conveniently offers two spectra for the price of one: the two stars are nearly identical, and only one is hosting a planet. We extracted the white light curves (i.e. combining all spectral bins) for both stars. These are shown in Figure 4.5. Comparing the two light curves, we notice the short-term and long-term ramp trends are similar. We can then make use of the light curve of the star B to correct for the systematic effects in the light curve of star A. To do so, we divided the flux of A by the flux of B, and obtained a corrected white light curve. Given that both stars have slight differences in magnitudes, the corrected flux still needs to be normalized, as shown in Figure 4.6. We performed a similar analysis for the third visit, and obtained a second corrected white light curve.

We used `Allesfitter` (Günther & Daylan, 2021, 2019) to fit the corrected white light curves of TOI-4336 A. `Allesfitter` is a Python package used to to build light curve and transit models. Doing so, it utilizes the `ellc` package (Maxted, 2016), and has a variety of options to include correlated noise. From this fitting, we wished to obtain a tight constraint on any achromatic parameter, i.e. any parameter not related to the planetary radius: the orbital period P, the timing T_0, and the cosine of the orbital inclination $\cos i$. This allows us to fix these values in the subsequent spectral light curve analysis in order to only fit for the radius of the planet, and reduce any potential bias or source of uncertainty. For a precise

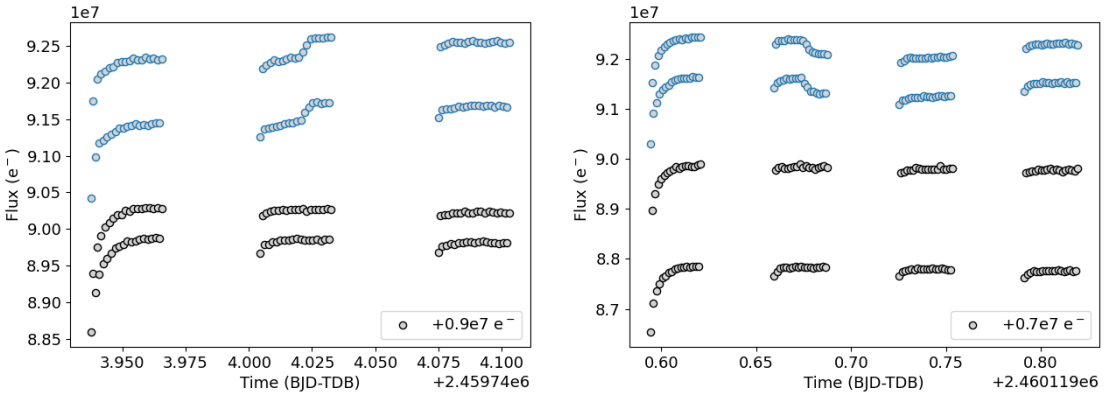

Figure 4.5: White light curves obtained from the photometric extraction. The left-hand plot shows the white light curves of TOI-4336 A in blue, including the transit of planet b, and TOI-4336 B in gray for visit 1. The right-hand plot corresponds to visit 3. Each light curve possesses offset data points which coincides to forward and backward scans. The light curves of TOI-4336 B are offset for clarity.

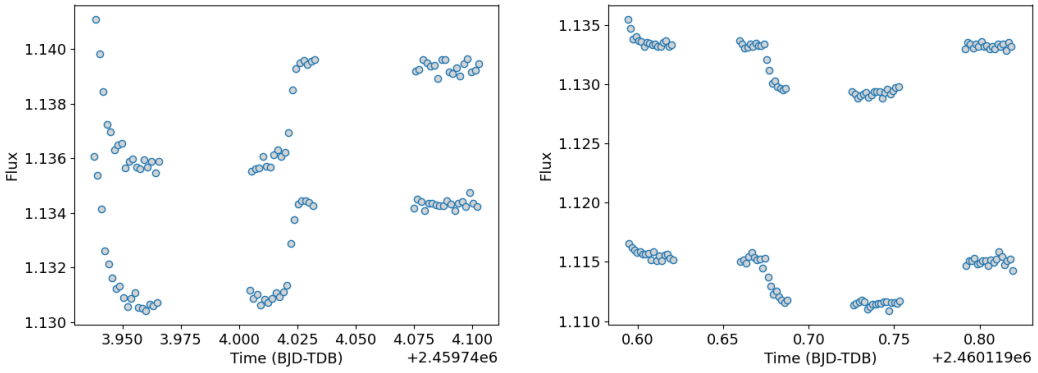

Figure 4.6: Corrected white light curves of TOI-4336 A for visits 1 and 3.

measurement of the period and timing, we jointly fitted the corrected white light curves with three high S/N ground-based transits (SSO/Europa in the $Sloan - r'$ filter on June 18, 2021, May 27, 2022, and March 17, 2023). We considered the orbit to be circular in accordance with the results of the discovery paper (Timmermans et al., 2024). We placed wide uniform priors on the radius ratio $\frac{R_p}{R_\star}$, the sum of the radii over the semi-major axis $\frac{R_p+R_\star}{a}$, the cosine of the inclination $\cos i$, the epoch T_0, and the period P. We included a hybrid spline detrending method for all light curves to correct any remaining noise source. The HST data includes periodic gaps that prevent the accurate modeling of the limb darkening coefficients because it is degenerated with other parameters (Tsiaras et al., 2018). We obtained the u_1,u_2 from `PyLDK` (Parviainen & Aigrain, 2015), and transformed them to q_1 and q_2 following the parametrization of Kipping (2013), as is required by `Allesfitter`. We fixed them for all light curves. We used the nested sampling algorithm of `Allesfitter` for this fit, and the resulting posterior distributions are given in Figure 4.7.

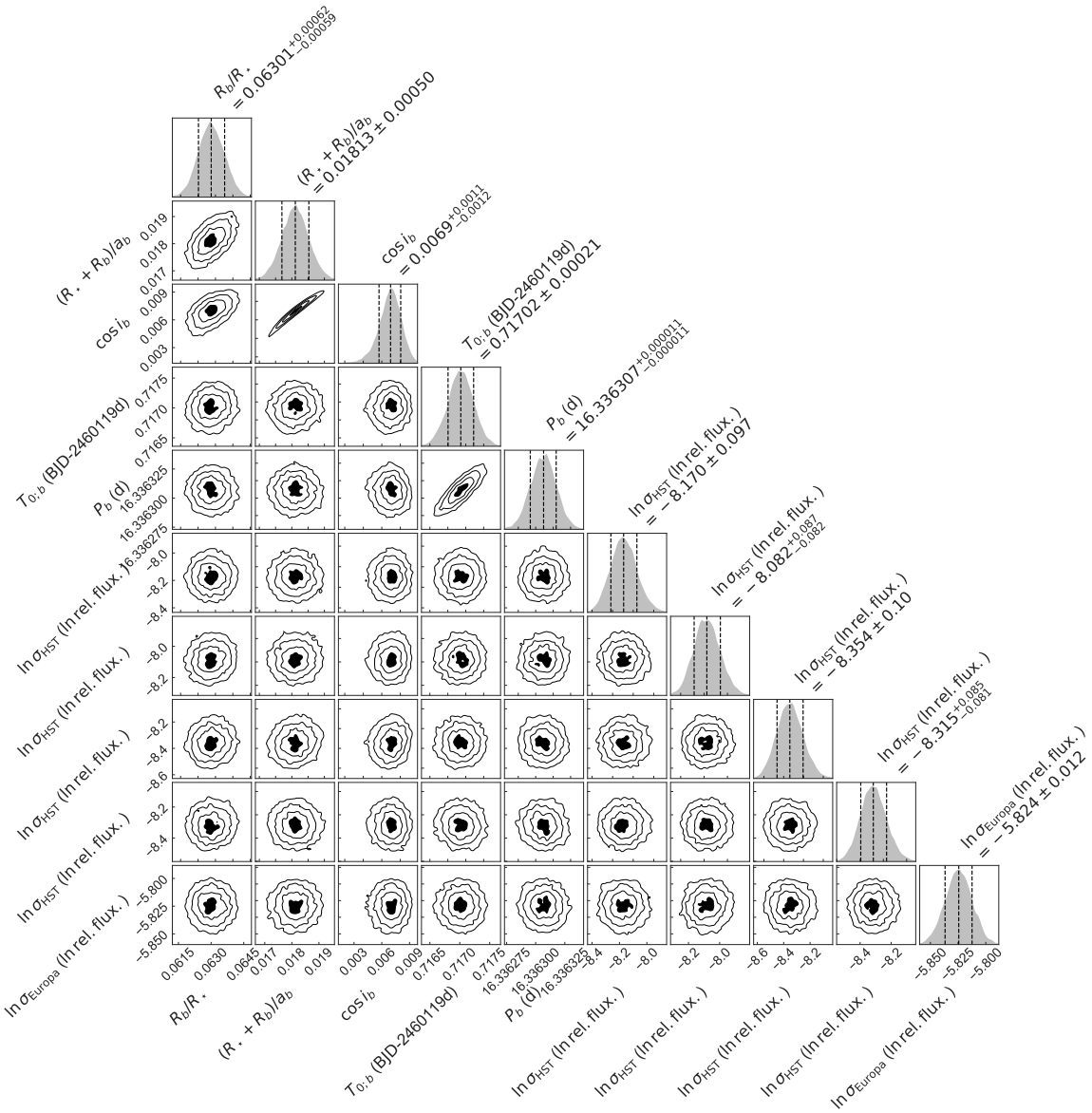

Figure 4.7: Posterior distributions of all the fitted parameters for the joint fit of the white light curves of TOI-4336 A and the SSO/Europa ground-based data. Figure obtained with the `corner` Python package.

Table 4.2: Limb darkening coefficients used in the spectral light curve fitting combining both visits 1 and 3.

Central wavelength (μm)	**Limb darkening coef. (q_1,q_2)**
1.126	(0.1111,0.2728)
1.148	(0.1055,0.2700)
1.169	(0.1014,0.2678)
1.189	(0.0975,0.2693)
1.208	(0.0991,0.2671)
1.228	(0.0951,0.2655)
1.246	(0.0957,0.2651)
1.266	(0.0936,0.2635)
1.285	(0.0916,0.2592)
1.304	(0.0885,0.2576)
1.322	(0.0876,0.2614)
1.341	(0.1040,0.2764)
1.361	(0.1102,0.2746)
1.380	(0.1061,0.2705)
1.400	(0.1190,0.2699)
1.420	(0.1307,0.2606)
1.441	(0.1211,0.2695)
1.462	(0.1324,0.2630)
1.483	(0.1223,0.2673)
1.505	(0.1346,0.2401)
1.528	(0.1362,0.2396)
1.552	(0.1314,0.2442)
1.576	(0.1236,0.2342)
1.602	(0.1128,0.2397)
1.629	(0.0937,0.2534)

We extracted the spectral light curves for 25 bins evenly spaced between 1.1 and 1.7μm for both visits. We attempted to divide by the spectral light curves of TOI-4336 B similarly to the white light curve, but this did not allow to significantly correct the trends in each dataset. Instead, we made use of the fitting function of `Iraclis` to provide detrended and normalized spectral light curves. We fitted the light curves of both visits per spectral bin with `Allesfitter`. We once again used the nested sampling algorithm and fixed the following parameters: the timing, the period, the cosine of the orbital inclination, and the eccentricity parameters f_s (given by $\sqrt{e}\cos\omega$) and f_c (given by $\sqrt{e}\sin\omega$). We obtained the limb darkening coefficients in the same way as for the white light curve fitting, and also fixed them in the spectral analysis. They are given in Table 4.2. The resulting transmission spectrum in shown in Figure 4.8.

4.5 Work in progress: atmospheric retrievals

The most common method used for the interpretation of a transmission spectrum is called *inverse atmospheric retrieval* modeling (e.g. Benneke & Seager, 2012; Rocchetto et al., 2016; Pinhas et al., 2018). While the implementations are numerous, the guiding principle is the same: a retrieval provides a Bayesian framework for the simultaneous inference of stellar, planetary, and atmospheric properties. It is done through the generation of *forward* atmo-

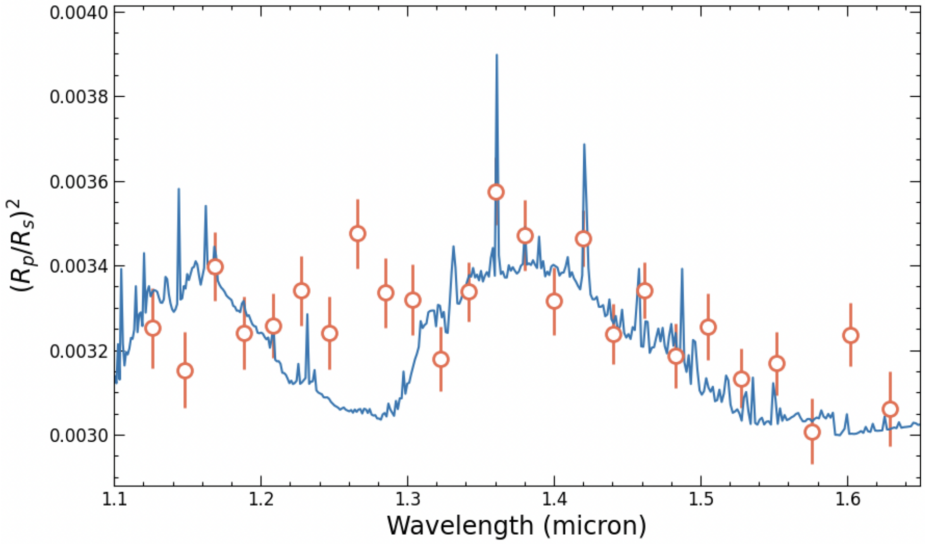

Figure 4.8: Transmission spectrum obtained from visits 1 and 3 of atmospheric exploration program of TOI-4336 A b. The data points are plotted against the predicted model from Timmermans et al. (2024), obtained for a typical H/He-rich atmosphere with an isothermal P-T profile at 300 K, assuming equilibrium chemistry and all the opacities available in `ExoTransmit` (Kempton et al., 2017).

spheric models, and a statistical sampling method allows to explore the parameter space obtain the posterior distributions. Forward models are generally constructed with specific temperature profiles, chemical compositions, opacities, the presence of clouds and hazes, and possibly include stellar contamination.

Performing a retrieval on the transmission spectrum of TOI-4336 A b represents the final task before the publication of this work. As the data acquisition is still ongoing, we are currently working on the data analysis. We anticipate to perform the retrieval with τ-`Rex` `3` (Al-Refaie et al., 2021) or `petitRadTrans` (Mollière et al., 2019), two widely used Python tools, in the coming months.

Chapter 5

Hidden Gems

5.1 Introduction

As explained in Section 2.1.2, searching the TESS data to identify potential planet candidates is done automatically. When the data is processed by the TESS pipelines, a periodic transit signal is elected to the TOI status if it passes a series of threshold values and statistical tests. Given the amount of data to comb through, a compromise was made between maximizing the number of true positives and minimizing the false positives. This opens the possibility of still finding new planet candidates by loosening the detection constraints with custom transit search pipelines.

Making use of the full capabilities of `SHERLOCK` (Dévora-Pajares et al., 2024), which is described in Section 2.3, Francisco J. Pozuelos and Martín Dévora-Pajares initiated the Hidden Gems project. The early stages of the survey focused on systems with a known TOI, and it was later extended to all known transiting planetary systems orbiting low-mass stars. Indeed, in Section 1.2.3 and Section 1.4 I showed that stars with masses below 0.6 $M_{\odot}$ offer a unique opportunity to find small transiting planets with radii below $4R_{\oplus}$ thanks to the large planet-to-star surface ratios. Statistical population studies demonstrate that Earth- to Neptune-sized planets exist twice as frequently around low-mass stars than solar analogs (e.g. Mulders et al., 2015a), and are commonly part of multi-planetary systems (Latham et al., 2011). The presence of at least one confirmed planet in a system then increases the probability that convincing low S/N signals are produced by real planets. Transiting planets also offer the geometric advantage of already having a favorable orbital inclination to discover extra transiting planets. We limit our target list to K- and M-dwarf stars with $T_{eff} < 5300$K within 50 pc, corresponding to 190 planets in 107 unique systems[1]. Our dynamical strategy relies on three steps: (1) perform the transit search with `SHERLOCK` on the available TESS sectors; (2) update the input data if new sectors become available to increase the S/N of putative signals, giving access to longer periods and smaller planets as well; (3) periodically include newly discovered transiting systems in the target list.

The Hidden Gems project led to the low S/N detection of a candidate with a period of 1.76 days in the TOI-237 system. TOI-237 b was published in Waalkes et al. (2021), and given its period of 5.43 days, this new candidate was close to a 3:1 mean-motion resonance. This constituted a strong argument in favor of its validity. The existence of the transit was later confirmed with an extensive filler program on TS and more follow-up observations with the SSO telescopes. The detection of a second candidate in the TOI-4336 A system was published in the discovery paper of TOI-4336 A b (Timmermans et al., 2024). I quickly launched a follow-up campaign with ground-based observatories to confirm its existence, and the transit was first confirmed on March 2, 2024.

[1]Data from NASA Exoplanet Archive, August 13 2024, https://exoplanetarchive.ipac.caltech.edu/

The second paper I am leading for this PhD thesis is presenting the confirmation of TOI-4336 A c and TOI-237 c in the context of the Hidden Gems project. Francisco J. Pozuelos and Martín Dévora-Pajares performed the `SHERLOCK` search and alerted me of the existence of TOI-237 c in 2021. I coordinated the follow-up campaign, scheduled the observations on TS and SSO, and performed the reduction of the data as well as the photometric extraction. I also contacted Jose Almenara to provide us with the transit light curves of TOI-237 b obtained with ExTrA that were available to the TFOP WG community and not used in the discovery paper. TOI-4336 A c found by Martín Dévora-Pajares as we collaborated on the validation of the first planet of the system. Given that there were not many transit opportunities, I decided to enlist the help of the LCO facilities in addition to SSO, and I liaised with Karen Collins and Khalid Barkaoui for the follow-up campaign. Unfortunately, the transit was too shallow to attempt a detection with TS. Khalid Barkaoui provided me with the reduced LCO images, and I performed the photometric extraction of both the SSO and LCO data. Francisco J. Pozuelos supervised me for the global analysis and model comparison for both systems. Bárbara Rojas-Ayala provided an updated stellar characterization of TOI-237 through advanced synthetic spectral fitting methods. Francisco J. Pozuelos is currently working on a dynamical analysis of the TOI-237 system to evaluate its stability and potential TTVs. Daniel Sebastian will discuss the prospects for a mass measurement of these planets. Finally, Elsa Ducrot will contribute a discussion on the atmospheric characterization prospects for both system. The paper is a work in progress and will be submitted in Astronomy & Astrophysics in the coming months.

5.2 Search for additional candidates

The search for additional candidates of the Hidden Gems targets is performed with the custom pipeline `SHERLOCK`. It is a publicly available Python package that allows to search for transiting planetary signals in the light curves of space-based missions. With this, we aim to scour the data to retrieve any potentially missed planet candidates by allowing a lower detection threshold than the TESS pipelines.

I refer to Section 2.3 for a full description of the seven modules of `SHERLOCK`. However, they can be summarized as follows: `SHERLOCK` automatically downloads the light curves at the desired cadence from the Mikulski Archive for Space Telescopes thanks to the `Lightkurve` package (Lightkurve Collaboration et al., 2018). It then uses the `wōtan` package (Hippke et al., 2019) to detrend the light curves with a bi-weight filter and a user-specified number of window sizes. Each detrended light curve is then searched in an iterative way for periodic signals using the `Transit Least Squares` algorithm (Hippke & Heller, 2019). A transit-like signal is elected if the S/N value is above a threshold, usually set to 5. In that case, the signal is recorded as potential candidate then masked to perform a new search. The search ends as no more viable candidates are found or if the number of iterations, called *runs*, reaches a number specified by the user. The planet candidates found during the search then go through a vetting module. It runs a suite of diagnostic tests to identify any possible false positive scenario. Next, the candidate is statistically validated following a procedure based on the `Triceratops` package (Giacalone et al., 2021). Finally, the fitting module uses the nested sampling algorithm of `Allesfitter` to retrieve the system parameters (Günther & Daylan, 2019, 2021). Observation plans can then be automatically created for any ground-based observatory using the newly calculated ephemeris of the candidate.

5.2.1 TOI-237

TOI-237 was observed in three TESS sectors with 2-min cadence: Sector 2, Sector 29, and Sector 69, it is shown in Figure 5.1. We initially performed the search only on Sector 2 which was the only one available at the time. As Sectors 29 and 69 became available, we repeated the search each time including a new sector to improve the S/N of the candidate signals. For all the analyses, we limited our search to a maximum number of 5 runs and used 10 different windows the produce the detrended light curves. We selected a threshold of 5 for the S/N to ensure to detect shallow signals. `SHERLOCK` proposes the option to use a sliding Savitzky-Golay filter (SG, Savitzky & Golay, 1964) which smooths the light curve before the bi-weight filter is applied. This is useful to enhance possible shallow signals, as was demonstrated in Delrez et al. (2022). This filter reduces the local white noise at the cost of correlating adjacent flux measurements by decreasing the global standard deviation of the curve. By doing so, local artifacts might be occasionally confused with transit shapes. We initially used this pre-detrending step in the search of Sector 2. After inspecting the results, we did not notice any significant variability warranting the use of this filter, and decided to remove it for the subsequent analyses including Sectors 29 and 69.

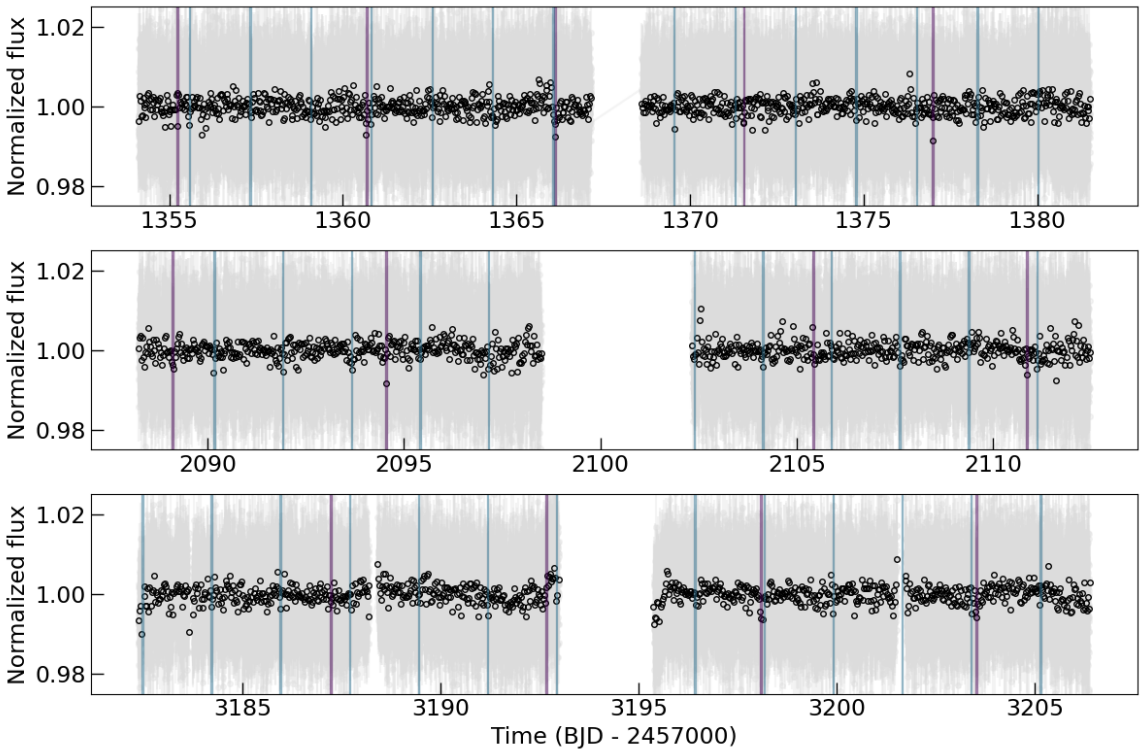

Figure 5.1: TESS 2-min cadence photometry of the TOI-237 system (Sectors 2, 29, 69). The transits of TOI-237 b and c are highlighted in purple and blue, respectively.

In the initial search of Sector 2, we identified the TOI 237 b 5.43 days signal in all the detrended light curves of the first run. The signal was elected with a maximum S/N of 18 and a signal detection efficiency (SDE, Hippke & Heller, 2019) of 15. The SDE is a metric used to assess whether a periodic signal is significant enough to be detected among random noise fluctuations. The SDE differs from the S/N that evaluates the strength of a signal compared to the noise in any setting (periodic or not). Indeed, the SDE computation is based on the strength of the signal specifically in a periodogram. A second signal of 1.74 days was also spotted in half of the detrended light curves, with a maximum S/N of 12 and

an SDE of 5.9. We note that these S/N values are higher than one would expect because the SG filter enhances the signals. The period ratio of the known planet b and the planet candidate is given by $\frac{P_b}{P_{cand}} \approx 3.1$, which is close enough to a 3:1 mean motion resonance. The vetting of this signal did not show any odd/even effects or significant secondary events. Furthermore, possible centroids shifts and a source offset were discarded, whilst the optical ghost check was passed. After passing succesfully the vetting stage, a Bayesian fit provided the transit parameters of the candidate. Unfortunately, the ephemeris uncertainties were high enough to substantially reduce the chances of a positive detection. However, the short period and transit depth of ~ 3 ppt of the candidate encouraged us to launch an exploratory filler program on the TRAPPIST-South telescope. With such an expected depth, a small 0.6m telescope is well-suited to the task.

We carried out the same `SHERLOCK` search by combining Sectors 2 and 29 as soon as it became available. To our surprise, the 1.74-day candidate was the signal found in all the detrended light curves of the first run. It appeared to be the strongest signal in the data with an S/N of 11, and an SDE of 11. We note it as TIC 305048087.02. The signal of TOI-237 b was found in the second run with an S/N of 16 and an SDE of 13 in 8 out of the 10 detrended light curves. The signal of TIC 305048087.02 passed the vetting stage again, and we then performed the newly implemented statistical validation procedure. The resulting null Nearby False Positive Probability (NFPP) showed no hints of possible contamination from nearby sources, as expected since the target star is the only one in the TESS apertures. However, the False Positive Probability (FPP), with FPP= 0.89, was high enough to question the validity of the candidate. Given this value, the candidate cannot be classified as validated or likely planet, and falls within the ambiguous region of the NFPP-FPP plane (Giacalone et al., 2021). Given the shallowness of the transit, we expected such a result. Adding Sector 29 in the Bayesian fit improved significantly the precision on the ephemeris ($\sim$ 10 minutes of uncertainty). After matching two possible events already observed in the TS data to this candidate, we directed our search towards the expected transit nights only. The ground-based observing campaign is described in Section 5.4.

Finally, the last analysis including Sector 69 gave similar results: we confirmed that both signals were still present in the TESS data. TOI-237 b was found in the first run on 9 out of 10 detrended light curves (S/N= 8.9, SDE= 22), and TIC 305048087.02 was identified in the second run in all of them (S/N= 7.9, SDE= 25). The elected signal for the candidate is given in Figure 5.2.

5.2.2 TOI-4336 A

TOI-4336 A was observed by TESS in Sectors 11, 38, and 64 with short cadence, as shown in Figure 5.3. The search for additional candidate was initially performed in the context of the discovery of TOI-4336 A b (Timmermans et al., 2024). I refer to Section 5.2 of the paper for a detailed description of the search parameters. The signal of TOI-4336 A b was recovered in the first run of the analysis with a S/N of 18.70. The second candidate, denoted as TIC 166184428.02 was found in four out of the ten detrended light curves of the second run with a period of 7.59 days. The S/N was close to the set threshold with a value of 5.35, and the periodic signal of 1.2 ppt passed the vetting tests.

5.3 Stellar characterisation

The stellar characterization of TOI-237 is derived from publicly available astrometric, photometric, and spectral data, employing advanced synthetic spectral fitting techniques to determine its fundamental parameters: effective temperature (T_{eff}), metallicity ([M/H]), surface

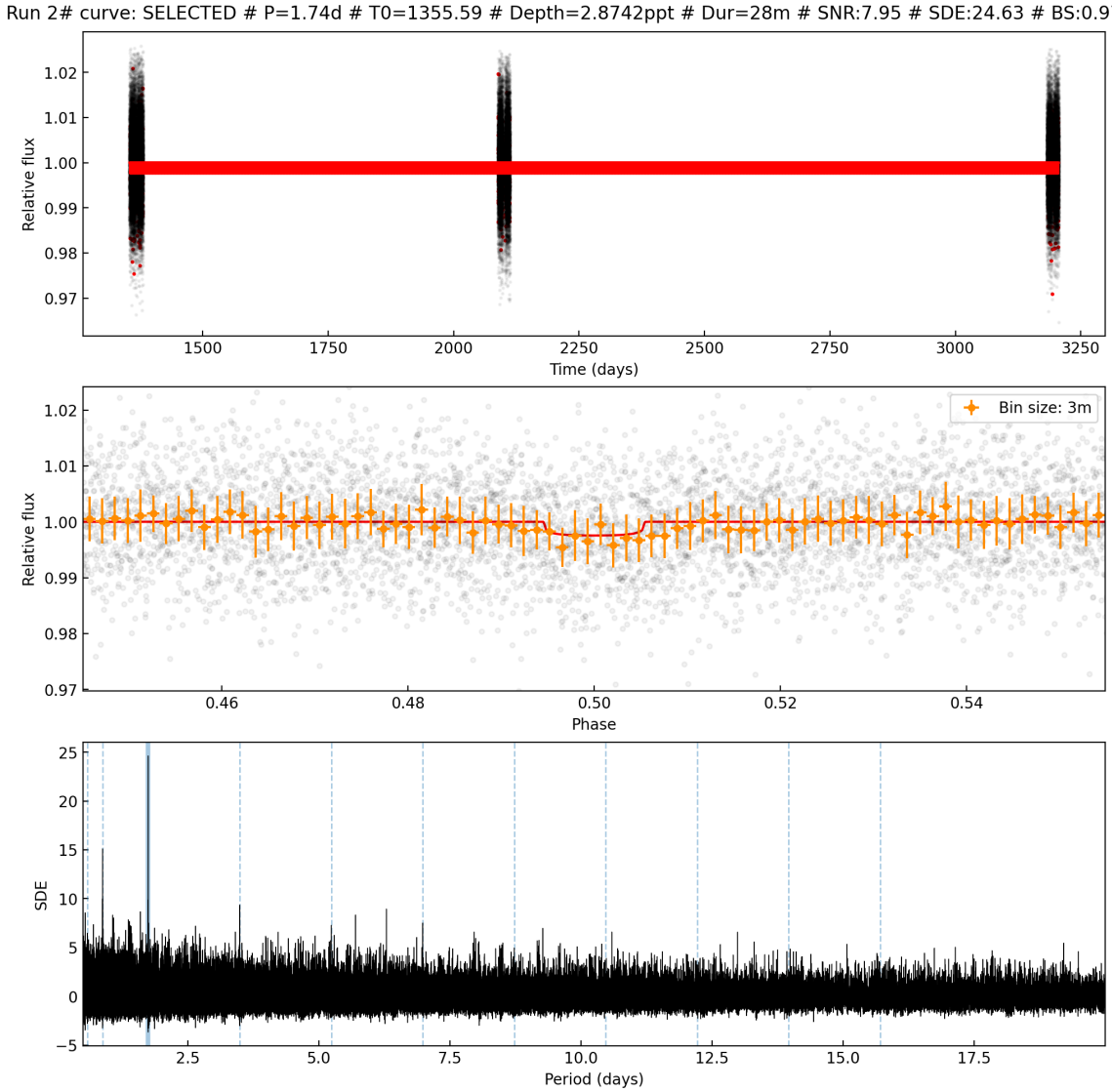

Figure 5.2: Elected signal for TIC 305048087.02 (TOI-237 c) in the SHERLOCK analysis of Sectors 2, 29, and 69. The top plot represents the TESS light curves overplotted with a theoretical model as the solid red line, based on the TLS results. The middle plot shows the phase folded light curve, the model is plotted as the solid red line. The bottom plot shows the TLS periodogram, with the period as a function of the SDE. The signal corresponding to TIC 305048087.02 is highlighted in blue, and the harmonics are given as blue dashed lines.

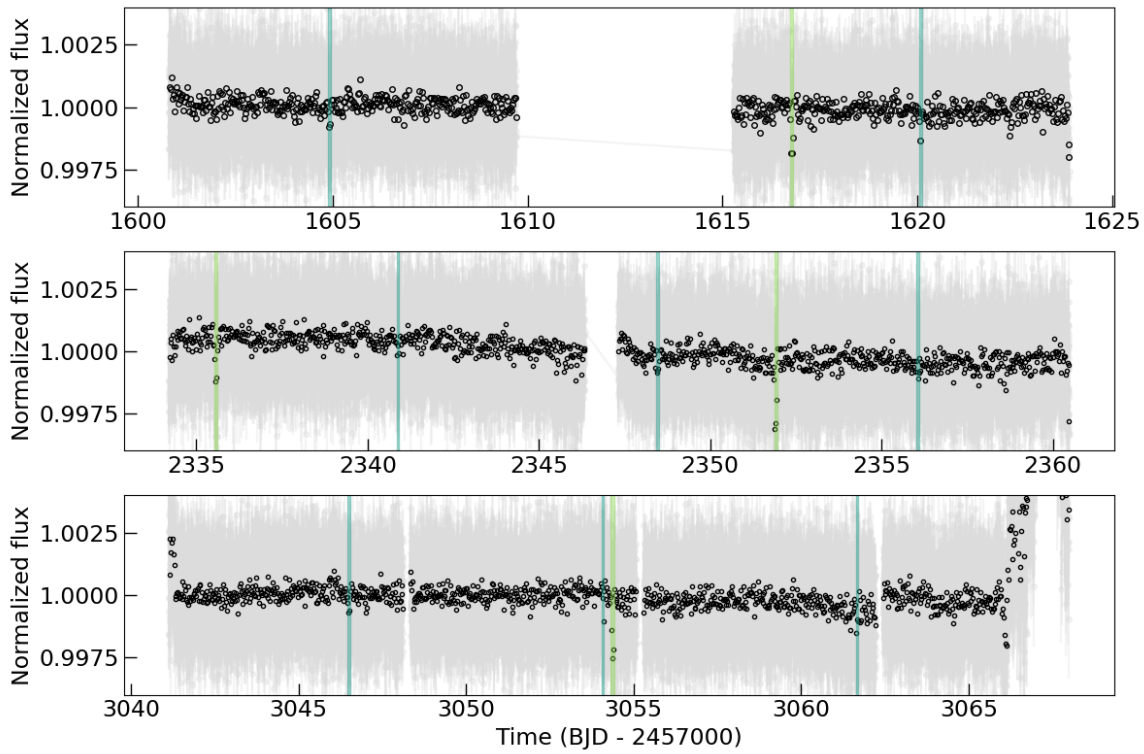

Figure 5.3: TESS 2-min cadence photometry obtained using the custom apertures presented in Timmermans et al. (2024) of the TOI-4336 A system (Sectors 11, 38, 64). The transits of TOI-4336 A b and c are highlighted in green and teal, respectively.

gravity (log g), and radius. This principle of this technique was first introduced in Stassun & Torres (2016). It relies on the measurement of the bolometric flux F_{bol} of a star based on the fitting of the spectral energy distribution (SED), given by broadband photometry spanning a large wavelength range, to stellar models. From this, the parallax allows to obtain the bolometric luminosity L_{bol}. The stellar radius can also be obtained from F_{bol} and T_{eff}, and the mass can then be calculated using the empirical relationship from Mann et al. (2019). Our methodology, which will be detailed in Rojas-Ayala et al. (in prep), differs from traditional SED fitting approaches for planet-hosting stars by incorporating four distinct synthetic spectral grids, as described below. We did not perform a similar analysis for TOI-4336 A as it was done very recently in Timmermans et al. (2024).

The photometric data for TOI-237 were sourced from the Two Micron All-Sky Survey (2MASS) and AllWISE catalogs (Cutri et al., 2003, 2021). Specifically, the 2MASS J, H, and K_s band photometry, along with the AllWISE W1 and W2 band photometry, were utilized to constrain the star's SED in the near and mid-infrared regions. Additionally, the Gaia Data Release 3 (DR3, Gaia Collaboration et al., 2023) provided a precise parallax measurement for TOI-237, which is critical for accurately estimating the star's size, along with its Gaia XP spectrum. The Gaia XP spectra are absolute flux-calibrated, low-resolution (R $\sim$ 30-100) spectra, represented by a set of Hermite functions that approximate the continuous spectrum obtained from the BP and RP photometers (Carrasco et al., 2021; Montegriffo et al., 2023; De Angeli et al., 2023). In our analysis, instead of using the full Gaia XP spectrum for TOI-237, we utilized the `GaiaXPy`[2] package to reconstruct the spectra specifically for the RP photometer. This approach was chosen to avoid the low S/N issues at the blue end

[2]DOI v2.1.2: 10.5281/zenodo.11617977 https://gaia-dpci.github.io/GaiaXPy-website/

of the BP spectrum, which overlaps with the CaH feature characteristic of M dwarfs (see Figure 3 of Carrasco et al., 2021). For the fitting process, we focused on the 0.63-0.76 µm region of the RP spectrum. This spectral range was selected because it includes strong CaH and TiO absorption bands, which are particularly sensitive to metallicity (e.g., metallicity classes by Lépine et al., 2007). Additionally, this choice helps to avoid potential artifacts at longer wavelengths that may arise from the spectrum reconstruction process using Hermite functions. These data sets were selected for their reliability, completeness, and relevance to the spectral characteristics of M dwarfs.

To derive the stellar parameters, we utilized the `species` Python toolkit (Stolker et al., 2020), which facilitates the fitting of observed stellar data to a grid of synthetic spectra using Bayesian inference with nested sampling. Given that TOI-237 is an M dwarf, we employed all suitable publicly available synthetic spectral grids that cover the M dwarf regime:

- BT-SETTL AGSS (Allard, 2014): These models offer a comprehensive treatment of dust formation and opacity in cool atmospheres, making them particularly suitable for M dwarfs. They utilize the solar abundances from (Asplund et al., 2009).
- BT-SETTL CIFIST (Allard, 2014): Similar to the AGSS models but updated with solar abundances from (Caffau et al., 2011).
- PHOENIX-ACES (Husser et al., 2013): A widely used model grid that includes detailed molecular line lists and enhanced opacity handling.
- SPHINX (Iyer et al., 2023): A more recent model grid specifically designed for low-mass stars and brown dwarfs, with a focus on molecular opacity.

The astrometric, photometric, and spectral data described above were fitted against these model grids to estimate the effective temperature, metallicity, surface gravity, and radius of TOI-237. From these parameters, the star's mass and luminosity were subsequently derived using the estimated surface gravity, radius, and effective temperature using fundamental relations. The fitting process using the `species` toolkit was performed with priors that could be defined as either normal distributions or boundaries for uniform or log-uniform priors. To minimize degeneracies in the fitting, we employed the $BP - RP$ color and absolute K_s relationships from Mann et al. (2015), applying a small correction to the BP and RP magnitudes, for the effective temperature and stellar radius priors, respectively. For the stellar mass prior, we used the absolute K_s relationship and its corresponding error from Mann et al. (2019). The Gaia DR3 parallax and its associated error were incorporated as a normal prior, while a boundary condition was set for the interstellar medium extinction (A_v). We then derived posterior probability distributions and Bayesian evidence for each of the synthetic spectral grids using the `UltraNest`[3] package (Buchner, 2021).

To ensure robust estimates of the stellar parameters of TOI-237, we employed Bayesian Model Averaging (BMA) across all the posterior probability distributions. BMA is a statistical technique that enhances predictions and provides reliable uncertainty estimates when fitting data to different synthetic spectral grids. Since multiple synthetic grids can explain the observational data with varying degrees of likelihood due to their differing physical assumptions, BMA allows us to simultaneously consider all four synthetic spectral grids described above. Each grid contributes to the final prediction, weighted by its relative evidence, which indicates how well the grid fits the data compared to the others. Our approach differs from other BMA-based SED fitting techniques, such as ARIADNE (Vines & Jenkins, 2022), by including both spectral data (Gaia XP spectra) and photometric data, and by utilizing grids

[3]Available at https://johannesbuchner.github.io/UltraNest/

specifically tailored for the M dwarf regime, such as BT-Settl AGSS, BT-SETTL CIFIST, and SPHINX, which are not available in ARIADNE. The BMA results for TOI-237 are presented in Table 5.1.

Table 5.1: Stellar characterization of TOI-237.

Parameters	**Values**
Luminosity $L_\star(L_\odot)$	0.0041 ± 0.0003
Radius $R_\star$ $(R_\odot)$	$0.2056^{0.0047}_{0.0067}$
Mass $M_\star$ $(M_\odot)$	$0.1698^{0.0385}_{0.0350}$
Surface gravity log $g_\star$ (cgs)	$5.0494^{0.0865}_{0.0923}$
Effective temperature T_{eff} (K)	3226^{47}_{48}
Metallicity [Fe/H] (dex)	$-0.3443^{0.6245}_{0.3964}$
Parallax ϖ(mas)	$26.1213^{0.0346}_{0.0438}$

5.4 Ground-based photometric observations

The photometric campaigns that led to the confirmation of the transits of TOI-237 c and TOI-4336 A c were conducted between the TRAPPIST, SPECULOOS and LCO facilities. We also obtained photometric observations of TOI-237 b with TRAPPIST, SPECULOOS and ExTrA to get new estimates of the system parameters.

5.4.1 TOI-237 b and c

The TRAPPIST-South telescope, described in Section 2.2.1, was used to confirm the existence of TOI-237 c by performing an informed search. It was done over a full observing season of TOI-237 on the basis of the observation plans provided by `SHERLOCK`. This was part of the filler program of the Exo-TRAPPIST project dedicated to the observation of Hidden Gems candidates, totalling 43 nights and over 175 hours of observation of TOI-237. The observations were all obtained in the $I+z$ filter to maximize the S/N with exposure times of 120 s, they are summarized in Table 5.2. The data reduction and analysis were performed using a dedicated pipeline designed with the `prose` package (Garcia et al., 2021, 2022). The nights were processed independently, for each of them a set of comparison stars and an optimal aperture were selected to reduce the white noise in the light curve. To evaluate whether the planet would be recovered in our observations, we computed the phase coverage as for periods between 0 and 8 days with intervals of 0.001 days, it is shown in Figure 5.4. The percentage of phase coverage represents how much of the orbit at a certain orbital period is explored by our observations. We find that we reach a phase coverage of ∼80% at a period of P=5.15 days, and ∼98% for P=1.74 days. We have thus sampled efficiently the phases of potential inner planets to TOI-237 b. In doing so, we recover the transit signal of TOI-237 c at the predicted ephemeris and do not find any hints of additional transit signals by eye.

We used the SSO telescopes to observe transits of TOI-237 b and c over two observing seasons. The facilities are described in Section 2.2.2. Photometric observations were obtained with five different filters accross the visible and NIR wavelength range, they are summarized in Table 5.2. The data reduction and photometric extraction was done with the same custom pipeline used for the TRAPPIST-South data, built with the `prose` package.

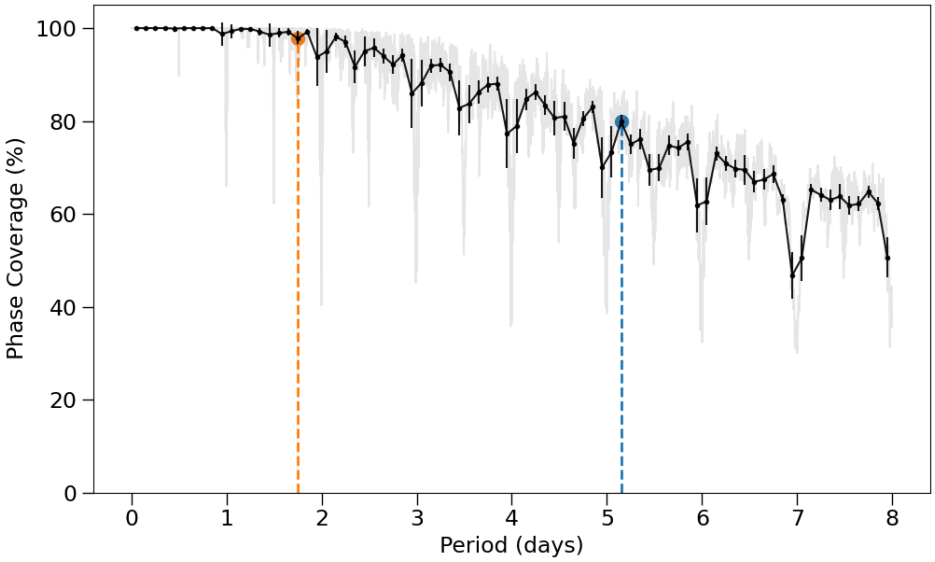

Figure 5.4: Phase coverage from the observations of TOI-237 obtained with TRAPPIST-South. The light gray line represents the percentage of phase covered for each orbital period from 0.001 days to 8 days with steps of 0.001 days. The black line shows the phase coverage for periods binned by 2.4 hours. The dashed orange line corresponds to P=1.74 days, the period of TOI-237 c, at which we find a coverage of ∼98%. The blue line corresponds to P=5.15 days at which a coverage of ∼80% is reached.

Finally, because we are part of TFOP WG, we noticed that a fellow team had obtained transits of TOI-237 b in 2021 and 2022 and invited them to join our effort. ExTrA (Exoplanets in Transits and their Atmospheres, Bonfils et al., 2015) is a low-resolution near-infrared (0.85 to 1.55 μm) multi-object spectrograph that allows high-precision spectro-photometry. It is fed by three 60-cm telescopes, and is located at La Silla Observatory in Chile. Six transits of TOI-237 b were observed using one or two of the ExTrA telescopes, they are detailed in Table 5.2. We used 8″ diameter aperture fibers, and the low-resolution mode (R∼20) of the spectrograph. Five fibers are positioned in the focal plane of each telescope to select light from the target and four comparison stars. The resulting ExTrA data were analyzed using custom data reduction software.

5.4.2 TOI-4336 A c

Two full transits of TOI-4336 A c were observed with the 1m-class telescope LCO-CTIO (Brown et al., 2013) at Cerro Tololo Interamerican Observatory in Chile. The telescope is equipped with 4096×4096 SINISTRO cameras with a pixel scale of 0.389″ per pixel, resulting a FOV of 26′×26′. We also obtained a full transit of TOI-4336 A c with the 2m-class telescope LCO-HAL at Haleakala Observatory in Hawaii. It is equipped with with the MuSCAT3 multiband imager (Narita et al., 2020). The transit was carried out simultaneously with the *Sloan-g'*, *-r'*, *-i'* and *Pan-STARRS-zs* filters. All the follow-up observations are described in Table 5.3. The science data were calibrated with the standard `BANZAI` (McCully et al., 2018) pipeline. The photometric extraction was performed using our custom `prose` pipeline.

Finally, we obtained one transit of TOI-4336 A c with SSO in the *Sloan-r'* filter simultaneously on two telescopes. The details of the observations are given in Table 5.3. The data reduction and photometric extraction was done with our custom pipeline similarly to TOI-237 b and c.

Table 5.2: Summary of the ground-based follow-up observations obtained for the TOI-237 system. [a] The light curve is too noisy and was not included in the global analysis. [b] The observation is affected by bad weather and was not included in the global analysis.

Observatory	Filter	Date	Coverage	Exposure (s)	FWHM (″)	Aperture (″)	Images
Planet b							
ExTrA (T2)	*1.21µm*	2021 Jul 03	Full	60	1.48	4.00	134
ExTrA (T2)	*1.21µm*	2021 Aug 20	Full	60	1.32	4.00	129
ExTrA (T3)	*1.21µm*	2021 Aug 20	Full	60	1.25	4.00	129
ExTrA (T2)	*1.21µm*	2021 Oct 19	Full	60	1.64	4.00	203
ExTrA (T3)	*1.21µm*	2021 Oct 19	Full	60	1.45	4.00	203
ExTrA (T2)	*1.21µm*	2021 Oct 30	Full	60	1.63	4.00	216
TS	*I+z*	2021 Oct 30	Full	120	2.63	4.87	153
TS	*I+z*	2021 Dec 07	Full	120	2.66	4.53	92
TS	*I+z*	2022 Sep 21	Full	120	2.42	4.48	184
ExTrA (T2)	*1.21µm*	2022 Oct 02	Full	60	1.30	4.00	150
TS	*I+z*	2022 Oct 02	Full	120	3.60	5.77	103
SSO/Europa	*Sloan-g'*	2022 Oct 13	Egress	150	1.46	1.61	185
SSO/Callisto	*zYJ*	2022 Oct 13	Egress[a]	7	2.02	1.21	4012
SSO/Io	*I+z*	2022 Oct 13	Egress	13	1.82	3.36	1308
SSO/Io	*I+z*	2022 Nov 02	Full	13	1.77	2.84	757
TS	*I+z*	2022 Nov 09	Full	120	2.91	3.93	123
ExTrA (T2)	*1.21µm*	2022 Nov 09	Full	60	1.28	4.00	150
Planet c							
TS	*I+z*	2021 Oct 29	Full	120	2.50	3.90	90
TS	*I+z*	2021 Nov 05	Full	120	2.71	5.34	75
TS	*I+z*	2021 Nov 19	Full	120	2.62	4.33	83
TS	*I+z*	2021 Nov 26	Full	120	3.17	5.20	110
TS	*I+z*	2021 Dec 03	Full	120	2.83	4.79	109
TS	*I+z*	2021 Dec 17	Egress[b]	120	3.02	4.47	78
TS	*I+z*	2022 May 14	Full	120	1.37	3.75	80
TS	*I+z*	2022 Jun 11	Full	120	2.87	3.88	137
TS	*I+z*	2022 Aug 25	Full	120	1.93	3.09	141
TS	*I+z*	2022 Sep 01	Full	120	2.33	3.72	146
TS	*I+z*	2022 Sep 15	Full	120	2.25	3.60	215
TS	*I+z*	2022 Sep 22	Full	120	2.17	4.01	134
TS	*I+z*	2022 Sep 29	Full	120	2.24	4.15	158
SSO/Europa	*Sloan-g'*	2022,Oct 13	Full	150	1.46	1.61	185
SSO/Callisto	*zYJ*	2022 Oct 13	Full[a]	7	2.02	1.21	4012
SSO/Io	*I+z*	2022 Oct 13	Full	13	1.82	3.36	1308
TS	*I+z*	2022 Oct 13	Full[b]	120	3.11	4.98	188
SSO/Europa	*Sloan-r'*	2022 Oct 20	Full	120	1.27	2.67	110
SSO/Io	*I+z*	2022 Oct 20	Full	16	1.51	3.55	530
TS	*I+z*	2022 Oct 20	Full	120	2.42	4.47	105
SSO/Io	*I+z*	2022 Oct 27	Full	16	1.67	3.09	369
TS	*I+z*	2022 Oct 27	Full	120	2.62	4.19	122
SSO/Io	*I+z*	2022 Nov 10	Full	13	1.23	2.59	473

Table 5.3: Summary of the ground-based follow-up observations obtained for the TOI-4336 A system.

Observatory	Filter	Date	Coverage	Exp. (s)	FWHM (″)	Aperture (″)	Images
Planet c							
LCO-CTIO	*Sloan-i'*	2024 Mar 02	Full	22	1.74	2.34	262
SSO/Io	*Sloan-r'*	2024 Apr 09	Full	10	1.70	2.72	1041
SSO/Callisto	*Sloan-r'*	2024 Apr 09	Full	10	1.00	3.26	1251
LCO-CTIO	*Sloan-i'*	2024 Apr 09	Full	22	1.32	3.42	263
MuSCAT3	*Sloan-g'*	2024 Jun 01	Full	144	3.02	3.08	71
MuSCAT3	*Sloan-r'*	2024 Jun 01	Full	17	2.67	3.08	480
MuSCAT3	*Sloan-i'*	2024 Jun 01	Full	12	2.84	3.08	611
MuSCAT3	*PanSTARRS-zs*	2024 Jun 01	Full	10	2.59	2.46	804

5.5 Global photometric analysis

We performed a global analysis of the all the available photometric data of both systems using `Allesfitter` (Günther & Daylan, 2019, 2021), a Python-based inference package. This includes all the data published in Waalkes et al. (2021) and Timmermans et al. (2024). By doing so, our aim is to provide stronger constraints on the estimations of the physical parameters of the systems thanks to the combination of all the available observational information. `Allesfitter` allows to build transit models using the `ellc` package (Maxted, 2016), while including the modeling of astrophysical noise sources such as flares, spots, and variability. Correlated noise can be accounted for using splines, or Gaussian Processes (GPs) (e.g. Rasmussen & Williams, 2006) implemented with the `celerite` package (Foreman-Mackey et al., 2017; Foreman-Mackey, 2018). To perform model comparisons, we used the nested sampling algorithm implemented by the `Dynesty` package (Speagle, 2020) in `Allesfitter`. This sampling method allows to compute the Bayesian evidence for each model, we then calculate the Bayes Factor to determine whether a model is statistically favored over the others (Kass & Raftery, 1995).

The data sets are separated according to their exposure times, filters and instruments. Given the large gap in the TRAPPIST-South data between the transit of TOI-237 b obtained in 2019 and the rest, we treated them as separate instruments. Because we include all the available photometry in our analysis, we chose wide uniform priors on the fitted planetary parameters (the radius ratio $R_p/R_\star$, the scale parameter $(R_p+R_\star)/a$, the cosine of the orbital inclination cos$i$, the epoch T_0, and the orbital period P). The prior distributions used in the modeling of the TOI-237 and TOI-4336 A systems can be found in Table 5.4 and Table 5.5, respectively. The derived parameters appearing in the Tables are: the radius of the planet R_p, the semi-major axis a, the orbital inclination i, the total transit duration T_{1-4}, the equilibrium temperature T_{eq} defined with an albedo of 0.3, the transit depth δ corresponding to the minimum of the stellar flux, and the impact parameter b.

The photometric observations span a range of different filters. We obtained the quadratic limb darkening coefficients u_1, u_2 from Claret et al. (2012) and Claret (2018) for the ground-based data and TESS, respectively, except for the ExTrA 1.2 μm and *Sloan-zs* filters for which we used the `PyLDTK` package (Parviainen & Aigrain, 2015) based on the PHOENIX model atmospheres (Husser et al., 2013). We converted the u_1, u_2 into the q_1, q_2 parametrisation presented in Kipping (2013), as required by `Allesfitter`. We opted for normal priors on these values for our models, they are given in Table A.1 and Table A.2.

In the case of the TOI-4336 A system, we include a free dilution factor with a wide uniform

prior for TESS where both TOI-4336 A and B are included in the aperture to account for possible blended faint additional stars. The dilution parameter is defined in `Allesfitter` as $D_0 = \frac{1-F_{source}}{(F_{source}+F_{blend})}$, with F_{source} the flux of the target star and F_{blend} the total flux of the blended sources. In the case of the MuSCAT3 data, the defocusing of the observations produced a slight blending of the wings of the two stars' PSFs. We include a smaller dilution factor to account for this effect. The dilution factors obtained for the global analysis of TOI-4336 A b and c are given in Table 5.7.

Finally, we use GPs with a *Matérn 3/2* kernel to model stellar variability and any correlated noise. In the first instance, we place wide uniform priors on the GP hyperparameters (σ, the amplitude scale, and ρ, the length scale). We then use the fitted hyperparameters of the first analysis as priors for the subsequent analyses to reduce the computational time for the different models. A flaring event is present in the simultaneous light curves of TOI-4336 A c obtained on June 1, 2024 with MuSCAT3. This initially caused the GP to overfit the data, as shown in Section A.2.3 for the *Sloan-i'* filter. Modeling the flare is beyond the scope of this work, we opted to simply mask it out.

For this modeling procedure, we used the option available in `Allesfitter` to use a prior on the stellar density. This prior is calculated from the stellar parameters given as input. At each step of the sampling, a stellar density is computed following $\rho_\star \approx \frac{3\pi}{GP^2}(\frac{a}{R_\star})^3$ and compared to the prior. If the computed value does not match with the prior, the fit is penalized. This method is particularly beneficial for small planets and low S/N data because the stellar density is often better constrained from the stellar characterization than from the transit light curves (Günther & Daylan, 2021).

5.5.1 Model comparison

For both systems, we performed an initial analysis with a 1-planet circular fit. We then tested 2-planet fits with a combination of circular and eccentric orbits: (1) both planets have circular orbits (we note it 2p-1c2c for convenience), (2) planet b is circular and planet c is eccentric (2p-1c2e), (3) planet b is eccentric and planet c is circular (2p-1e2c), and (4) both planets are eccentric (2p-1e2e). An eccentric orbit is parametrized in `Allesfitter` by $f_c = \sqrt{e}\cos\omega$ and $f_s = \sqrt{e}\sin\omega$, with e the eccentricity and ω the argument of periastron. For all eccentric fits, we chose wide uniform priors $\mathcal{U}$(-1, 1) for f_c and f_s. We computed the Bayes Factor $\Delta lnZ = lnZ - lnZ_0$ by comparing the model evidences given by lnZ to the one of the null hypothesis given by lnZ_0. The null hypothesis represents the simplest model capable of explaining the data, and we chose it to be the 1-planet circular fit in the analysis of both systems. Kass & Raftery (1995) gives $\Delta log(Z) > 3$ as the limit for strong evidence of one model. We also note that a Bayes factor indicating evidence in favor of one model is primarily suggestive. In our case, observational constraints on the architecture of the system could also be obtained from RV measurements as they are sensitive to the eccentricity and orbital angles. However, for this study we did not have access to such measurements, thus we relied on the model comparison approach to determine if the orbits appear eccentric. The results are illustrated as bar plots in Figure 5.5.

For the TOI-237 system, we find that all 2-planet scenarios are very strongly statistically favored ($\Delta lnZ > 85$). Comparing their Bayesian evidences assuming circular and eccentric orbits, the model including eccentric orbits for both planets is the most likely. Although, compared to the other 2-planet models, 2p-1e2e is not strongly favored against 2p-1c2c and 2p-1c2e with Bayes factors of 1 and 2, respectively. We note that the 2p-1e2c model presents the smallest evidence and is thus ruled out. The eccentricities and arguments of periastron found for each scenario are given in Table 5.6. All models are consistent with a zero eccentricity at the 1σ level. We do not consider this to be a significant detection of eccentricity. To comply with the basic principle of model comparison, i.e. the simplest model able to explain

the data should be favored, we select the 2-planet circular fit as the most likely outcome. The fitted and derived parameters of the preferred model are given in Table 5.4, and the phase folded light curves and associated models are shown in Figure 5.6.

Similarly, the 2-planet fits are also strongly statistically favored compared to the null hypothesis in the case of the TOI-4336 A system, with $\Delta lnZ > 220$. The models combining circular and eccentric orbits are statistically indistinguishable from each other with a Bayes factor of 0.06. The 2-planet circular fit, with circular orbits for TOI-4336 A b and TOI-4336 A c, is strongly favored in this model comparison analysis with a $\Delta lnZ = 3.6$ compared to the eccentric one. We give the phase folded light curves and individual model in Figure 5.7, as well as the fitted and derived parameters in Table 5.5.

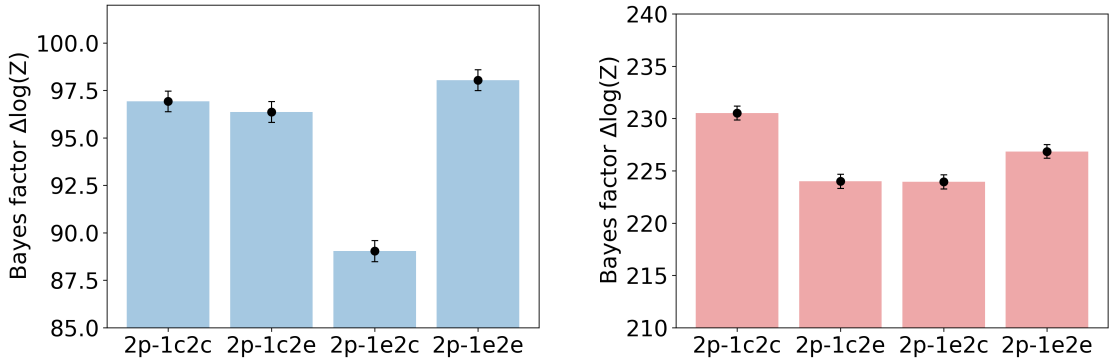

Figure 5.5: Bar plots representing the Bayes factor of the tested models. The blue plot corresponds to the model comparison for the TOI-237 system, and the red plot to the one of the TOI-4336 A system. The null hypothesis is taken as a one-planet circular fit, the other models are two-planet fits: two circular orbits (2p-1c2c), planet b circular and planet c eccentric (2p-1c2e), the inverse (2p-1e2c), and two eccentric orbits (2p-1e2e).

Table 5.4: Properties of TOI-237 system (see Section 5.5).

Parameters	**Values**		**Priors**	
	Planet b	*Planet c*	*Planet b*	*Planet c*
$R_p/R_\star$	$0.0606^{+0.0010}_{-0.0011}$	$0.0537^{+0.0010}_{-0.0011}$	$\mathcal{U}(0.01, 0.1)$	$\mathcal{U}(0.01, 0.1)$
$(R_\star + R_p)/a$	$0.02992^{+0.00078}_{-0.00058}$	$0.0537^{+0.0010}_{-0.0011}$	$\mathcal{U}(0.01, 0.05)$	$\mathcal{U}(0.01, 0.08)$
cos$i$	$0.0028^{+0.0057}_{-0.0091}$	0.01266 ± 0.00086	$\mathcal{U}(0.00, 0.04)$	$\mathcal{U}(0.00, 0.04)$
T_0 (BJD-TDB$_{2450000}$)	$8697.72077^{+0.00046}_{-0.00042}$	$9540.35063^{+0.00021}_{-0.00022}$	$\mathcal{U}(8697.70, 8697.74)$	$\mathcal{U}(9540.32, 9540.38)$
P (days)	$5.4361392^{+0.0000028}_{-0.0000029}$	$1.74486136^{+0.0000011}_{-0.00000086}$	$\mathcal{U}(5.4, 5.5)$	$\mathcal{U}(1.7, 1.8)$
R_p ($R_\oplus$)	1.394 ± 0.047	1.234 ± 0.043	-	-
a (au)	0.0347 ± 0.0013	0.01626 ± 0.00049	-	-
i (deg)	$89.84^{+0.52}_{-0.33}$	89.274 ± 0.050	-	-
T_{1-4} (hours)	1.215 ± 0.014	0.8308 ± 0.0084	-	-
T_{eq} (K)	349 ± 12	$510. \pm 16$	-	-
δ (ppt)	$4.18^{+0.6}_{-0.06}$	$3.19^{+0.05}_{-0.04}$	-	-
b	$0.10^{+0.20}_{-0.32}$	0.210 ± 0.014	-	-

5.6 Work in progress

As mentioned in the introduction, this work is currently in progress and will be submitted for publication in the coming months. In this Section, I give an overview of the sections still

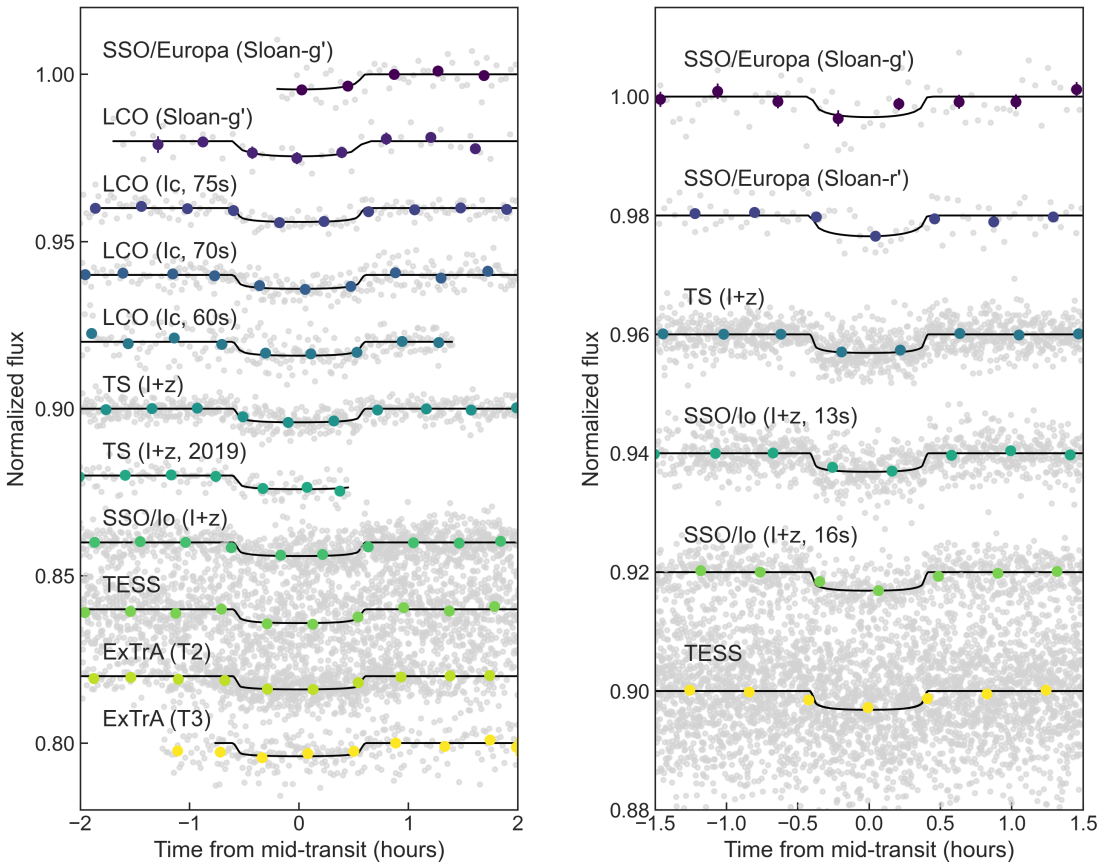

Figure 5.6: Phase folded transits of TOI-237 b (left) and TOI-237 c (right). The transit models are obtained with `Allesfitter`.

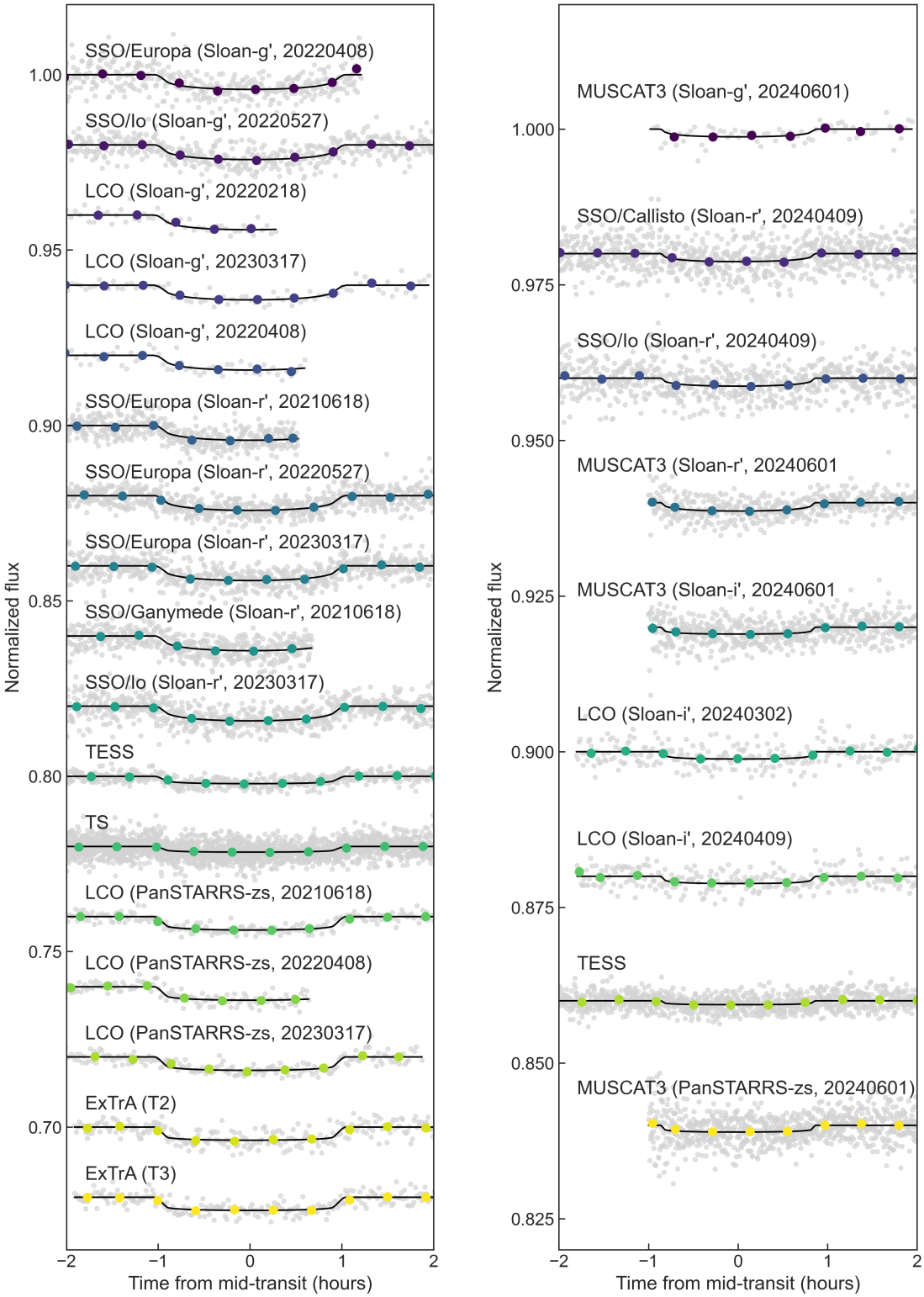

Figure 5.7: Phase folded transits of TOI-4336 A b (left) and TOI-4336 A c (right). The transit models are obtained with `Allesfitter`.

Table 5.5: Properties of TOI-4336 A system (see Section 5.5).

Parameters	**Values**		**Priors**	
	Planet b	*Planet c*	*Planet b*	*Planet c*
$R_p/R_\star$	0.05929 ± 0.0010	0.0337 ± 0.0014	$\mathcal{U}(0.01, 0.1)$	$\mathcal{U}(0.01, 0.1)$
$(R_\star + R_p)/a$	$0.01879^{+0.00062}_{-0.00055}$	$0.03084^{+0.00068}_{-0.00077}$	$\mathcal{U}(0.01, 0.05)$	$\mathcal{U}(0.01, 0.08)$
cos$i$	0.0087 ± 0.0012	$0.0052^{+0.0034}_{-0.0030}$	$\mathcal{U}(0.00, 0.04)$	$\mathcal{U}(0.00, 0.04)$
T_0 (BJD-TDB$_{2450000}$)	9335.57276 ± 0.00045	$9333.2933^{+0.0011}_{-0.0012}$	$\mathcal{U}(9335.54, 9335.60)$	$\mathcal{U}(9333.26, 9333.32)$
P (days)	16.336351 ± 0.000017	$7.587266^{+0.000011}_{-0.000013}$	$\mathcal{U}(16.00, 16.50)$	$\mathcal{U}(7.55, 7.62)$
R_p (R$_\oplus$)	2.122 ± 0.074	1.205 ± 0.063	-	-
a (au)	0.0859 ± 0.0037	$0.0512^{+0.0020}_{-0.0019}$	-	-
i (deg)	89.500 ± 0.067	$89.70^{+0.17}_{-0.20}$	-	-
T_{1-4} (hours)	2.077 ± 0.017	$1.760^{+0.031}_{-0.061}$	-	-
T_{eq} (K)	284.2 ± 7.8	368.3 ± 9.5	-	-
δ (ppt)	$4.02^{+0.09}_{-0.07}$	$1.36^{+0.04}_{-0.03}$	-	-
b	$0.492^{+0.049}_{-0.052}$	$0.18^{+0.11}_{-0.10}$	-	-

Table 5.6: Eccentricities e and arguments of periastron ω obtained in the model comparison for the 2-planet fits of the TOI-237 system (see Section 5.5).

Model	**Parameter**	
	e	ω (deg)
2p-1c2e (TOI-237 c)	$0.101^{+0.206}_{-0.075}$	$198.83^{+137.46}_{-133.46}$
2p-1e2c (TOI-237 b)	$0.082^{+0.162}_{-0.060}$	$180.58^{+124.59}_{-126.85}$
2p-1e2e (TOI-237 b)	$0.095^{+0.179}_{-0.070}$	$175.37^{+70.07}_{-113.21}$
2p-1e2e (TOI-237 c)	$0.088^{+0.176}_{-0.066}$	$188.90^{+121.89}_{-127.48}$

to be completed.

5.6.1 Planet validation

From ground-based observations and in the absence of a mass measurement, there are two ways one can reduce substantially the probability of a false positive: evaluating the chromaticity of the transit, and checking for odd/even discrepancies. In the case of TOI-4336 A, a publication presenting the masses of both planets of the system is planned simultaneously with ours. This publication is led by the team of François Bouchy at the University of Geneva, Switzerland. This paper will unequivocally prove TOI-4336 A c is in fact a planet, and for that reason, we will refer to that work for the validation aspect.

In the case of the TOI-237 system, we perform a new global analysis with two planets with circular orbits including a possible chromatic effect. To account for potential variations of the transit depths, we include a free dilution parameter for each ground-based observation sampled uniformly between -1 and 1, following the method used in Pozuelos et al. (2023). We fix the dilution parameter of TESS to 0 for TOI-237 because the large amount of transits present in the three sectors provide the best estimation of the depth. Given the noise present in the only light curve available in the *Sloan-g'* band, we obtained new observations on August 8, 2024, simultaneously on two SSO telescopes to increase the S/N. Unfortunately, that night corresponded to a double transit of TOI-237 b and TOI-237 c, making the chromaticity check difficult. However, we are still currently assessing whether the other light curves obtained for both planets in the *Sloan-g'* band are sufficient to constrain the transit depth. If not, we

Table 5.7: Dilution parameters obtained in the global analysis of the TOI-4336 A system (see Section 5.5).

Parameters	**Values**	**Priors**
Dilution TESS	$0.474^{+0.025}_{-0.026}$	$\mathcal{U}$(-1,1)
Dilution TS	0.591 ± 0.084	$\mathcal{U}$(-1,1)
Dilution MuSCAT3 (*Sloan-g'*)	$-0.20^{+0.16}_{-0.13}$	$\mathcal{U}$(-0.4,0.4)
Dilution MuSCAT3 (*Sloan-r'*)	$-0.22^{+0.14}_{-0.11}$	$\mathcal{U}$(-0.4,0.4)
Dilution MuSCAT3 (*Sloan-i'*)	$0.17^{+0.14}_{-0.16}$	$\mathcal{U}$(-0.4,0.4)
Dilution MuSCAT3 (*PanSTARRS-zs*)	$-0.22^{+0.14}_{-0.11}$	$\mathcal{U}$(-0.4,0.4)

will request new observations to perform a robust chromaticity check.

In the TESS data, our `SHERLOCK` analysis did not reveal any odd/even difference in the transit depths. However, data obtained with 1m-class telescopes provide a much higher precision on the depth. Given the period of 1.74 days, transits are visible from Chile every four transits. Since we conducted our follow-up efforts from the TS and SSO facilities, all the transits we obtained were even. The SAINT-Ex facility, part of the SPECULOOS network, is the only one where odd transits are observable with an elevation above 30 degrees. We requested an observation on August 11, 2024, which was unfortunately cancelled due to high humidity at the observing site. SAINT-Ex is currently down due to technical difficulties. As soon as it is back on sky, we will attempt to get the odd transit we are missing to perform a robust odd/even check.

5.6.2 Dynamical analysis

Given the period ratio of 3.1 in the TOI-237 system, we can expect some mild gravitational interactions between the planets. We will perform a dynamical analysis to study the stability of the system, evaluate the expected TTVs and the mass measurement prospects with this method.

5.6.3 Discussion

The `forecaster` package (Chen & Kipping, 2017) provides a probabilistic estimation of the planetary mass from the posterior distribution of the planetary radius. With a radius of $1.23 \pm 0.04 R_\oplus$ for TOI-237 c, we estimate the mass to be $1.905^{+1.333}_{-0.588} M_\oplus$. Similarly, for TOI-4336 A c, we estimate a mass of $1.768^{+1.238}_{-0.571} M_\oplus$ from its radius of $1.21 \pm 0.06 R_\oplus$. This results in radial velocity semi-amplitudes of 2.86 m/s and 0.80 m/s, respectively. This poses quite a challenge for the available spectrographs. Measuring the mass of TOI-4336 A c is possible on ESPRESSO thanks to its brightness Vmag= 13.6. It has been done last year and is the subject of an upcoming publication. We plan to evaluate the feasibility of a mass measurement of TOI-237 c with ESPRESSO and NIRPS.

Following Kempton et al. (2018), we computed the equilibrium temperature for zero albedo and full day-night heat redistribution, and used it to calculate the TSM for both planets. We found values of 70 for TOI-237 c and 60 for TOI-4336 A c. These are well above the threshold recommended for atmospheric characterisation of 10 for planets with radii below $1.5 R_\oplus$ (referred to as *terrestrial* planets in Kempton et al., 2018). In fact, TOI-237 c and TOI-4336 A c have two of the highest TSM values for transiting planets in that category, as shown in Figure 5.8. The prospects of atmospheric characterisation will further

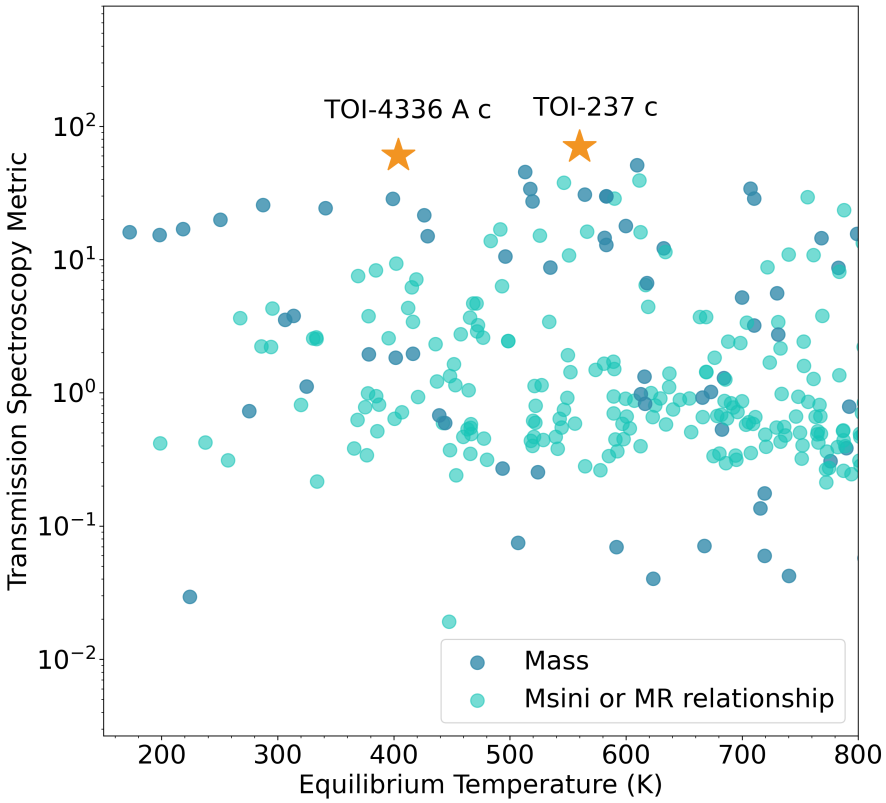

Figure 5.8: Transmission Spectroscopy Metric as a function of equilibrium temperature for known transiting exoplanets with radii below 1.5 $R_\oplus$ (data obtained from the NASA Exoplanet Archive, accessed on September 7, 2024). The values were computed using the expressions found in Kempton et al. (2018). We highlight the planets with a mass measurement in dark blue, and the ones with a minimal mass or mass obtained from a mass-radius relationship in light blue. TOI-237 c and TOI-4336 A c are marked by the yellow stars.

be discussed on the basis of synthetic JWST transmission spectra obtained with `Pandexo`[4] (Batalha et al., 2017).

[4]Available at https://exoctk.stsci.edu/pandexo/

Chapter 6

MANGOs

6.1 Introduction

Back in 2022, the TESS vetting team was releasing dozens of planetary candidates each time a new sector became available. In particular, the TESS Faint Star Search (Kunimoto et al., 2022) revealed a surprising number of giant planet candidates orbiting low-mass stars. George Dransfield brought my attention to this intriguing type of planet, and our discussion inspired the MANGOs (M dwarfs Accompanied by close-iN Giant Orbiters) project. By combining the observing capabilities of TRAPPIST and SPECULOOS, we decided to dedicate an entire program to the validation of giant planets orbiting low-mass stars. However, we quickly realised that by doing so, we would inevitably encounter false positives that are still highly scientifically valuable: transiting brown dwarfs (BDs) and M-dwarf (MD) binaries. Seizing this opportunity, we decided to include these systems in our systematic search. The science goals of the MANGOs project are then threefold:

- **Hot/warm Jupiters**: at the time of writing, there are only $\sim$ 20 systems that can be considered equivalent to hot Jupiters orbiting low-mass stars, i.e. close-in giant planets. As explained in Section 1.5, their existence challenges what astronomers know of giant planet formation. Overall, creating such massive planets in the protoplanetary disks of low-mass stars is a difficult task given the amount of material available. With the MANGOs project, we aim to increase the number of characterized close-in giants orbiting low-mass stars to create a statistically significant sample. The goal is to allow the study of this population as a whole to find patterns that would point towards specific formation and evolution pathways.

- **Transiting BDs**: BDs are sub-stellar objects with sizes similar to giant planets and masses between $\sim$ 13 and 80 M_{Jup} (Chabrier et al., 2000; Chabrier, 2003). They are the bridge between stars and planets, thought to form in the same way of stars but lacking the required mass to start hydrogen burning in their core. Because of this, they are very cool objects ($T_{eff} < 2800K$) and produce achromatic transit depths accross the visible and NIR wavelength range. Although, they can easily be distinguished from gas giants by using the RV technique as their large masses produce much higher semi-amplitudes. Only $\sim$40 transiting BDs have been confirmed around main-sequence stars (Henderson et al., 2024b), with only a few transiting low-mass stars (e.g. Jackman et al., 2019; Maldonado et al., 2023; Henderson et al., 2024a). This number is much lower than what is expected from the hot Jupiter or low-mass eclipsing binary populations, it is known as the BD desert (Grether & Lineweaver, 2006). The existence of this desert is still poorly understood, although it is likely due to the formations mechanisms of such systems. Similarly to close-in giants, populating the sparse parameter space of the BD

desert with characterized systems will shed light on the physical processes creating it.

- **M-dwarf binaries**: as mentioned in Section 1.2.3, the planetary parameters inferred from a transit light curve can only be as precise as the stellar parameters used in the analysis. Because the quantities are intrinsically linked, the uncertainties from the stellar characterization directly propagate to the measurements of the planetary parameters. Studies show that there is a discrepancy between predicted and observed values of stellar radius for low-mass stars (e.g. Ribas, 2006; Spada et al., 2013). Indeed, evolutionary models seem to systematically underestimate the stellar radius, and the leading explanation resides in the high magnetic activity of such systems (e.g. Demory et al., 2009; Morales et al., 2010). The observational determination of the stellar radii and masses of low-mass stars is then important to refine the stellar models. Interferometry can be used for isolated stars, and double-lined low-mass eclipsing binaries also allow a direct measurement of these parameters by combining transit photometry and spectroscopic observations. With the MANGOs project, we aim to increase the number of known double-lined eclipsing binaries to improve stellar models of low-mass stars, and ultimately increase the precision on the parameters for planets orbiting such stars.

This large-scale project is made possible thanks to the 50% of observing time of the TRAPPIST telescopes dedicated to exoplanets, and the 20% of observing time of the SPECULOOS telescopes allocated to annex programs. The latter is handled by the Working Group 6 (WG6) of the consortium led by Amaury Triaud. The MANGOs core team is composed of members of the WG6: George Dransfield, Elsa Ducrot, Khalid Barkaoui, and myself. George Dransfield and I are the co-PIs of the project, and as such we are coordinating the work of the team. I am also in charge of keeping the target list up to date, and the monthly selection of candidates to observe. During the first year of the project, the large data analysis and reporting workload was equally split between the members of the team. This task is now mostly handled by Khalid Barkaoui. Finally, I am active in the scheduling of the transit observations for the SPECULOOS and TRAPPIST facilities.

I describe the MANGOs target list and strategy in Section 6.2, and the work that has been done by the MANGOs team to obtain RV measurements for a select number of targets in Section 6.3.

6.2 The MANGOs program

6.2.1 Target list

As the definition of a hot Jupiter is unclear for low-mass stars, we defined arbitrary limits for the MANGOs target list. Based on the TOIs list, we selected candidates with radii larger than 7 $R_\oplus$ and orbital periods below 7 days, orbiting stars with effective temperatures below 4000 K to include stars up to M0. The full target list is shown against the population of known transiting planets in Figure 6.1. The initial target list included 103 planet candidates, and has since grew to 165 with the following TOI releases. In consultation with the SPECULOOS PIs, we have decided to stop the systematic addition of new MANGOs candidates with each release, and select them on a case by case basis instead. This decision is motivated by the large observing time allocated to the MANGOs program compared to others. Finalising the target list will allow to bring the project to an end in the coming years.

6.2.2 Observing Strategy

Because MANGOs targets are initially TOIs, we follow a similar observing strategy as for all TESS follow-up candidates:

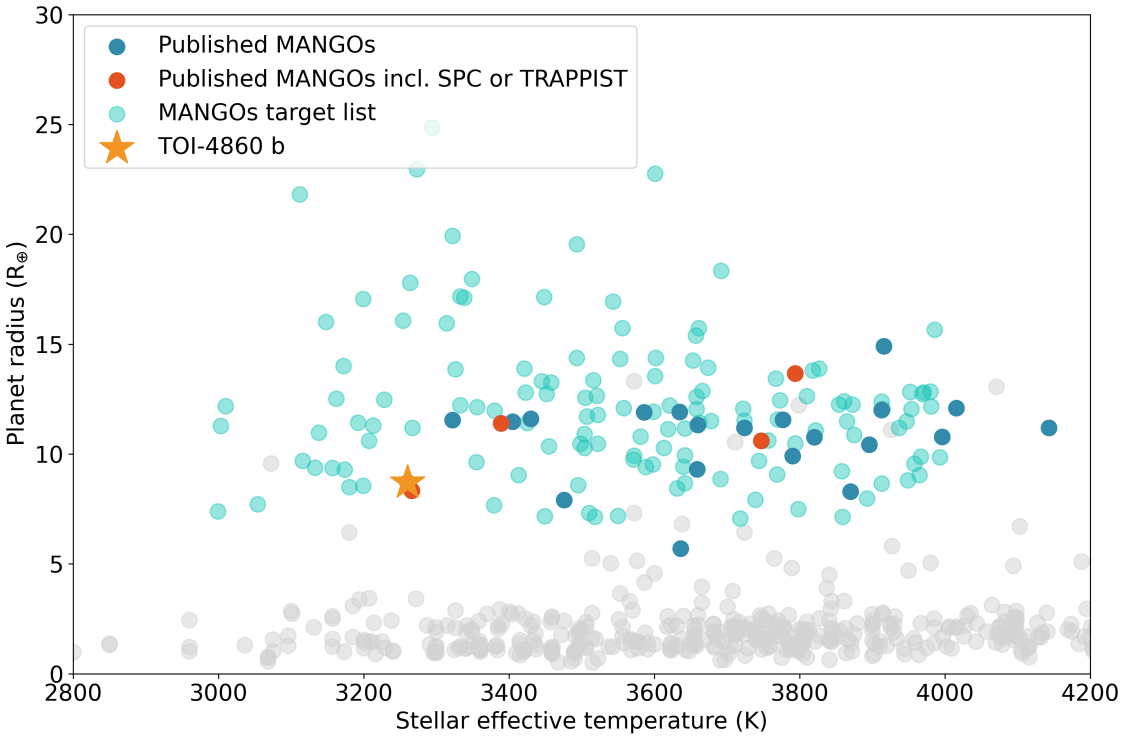

Figure 6.1: Planetary radius as a function of stellar effective temperature for all known transiting planets. The MANGOs targets are highlighted in light blue, the ones that are published not including data from the MANGOs program are in dark blue, and the ones that do are highlighted in red. The discovery of TOI-4860 b is the first MANGOs publication, and it is marked by the yellow star. The rest of the known planets are shown in light gray, the data is obtained from the NASA Exoplanet Archive, accessed on September 7, 2024.

- Confirm the transit is on target with TRAPPIST in the *I+z* filter, or *Exo* filter for the faintest stars. This also allows to evaluate the transit shape and depth from a ground-based facility.
- Perform a chromaticity check with SPECULOOS. It should be simultaneous in *Sloan-g'* and *Sloan-z'* in the case of southern targets, thanks to the four telescopes of SSO. If the star is bright enough, it can also be done simultaneously between TRAPPIST-North and SPECULOOS-North, and in some cases SAINT-Ex.
- Obtain an optical or NIR spectrum of the target star through our colleagues of the Working Group 3 of SPECULOOS. It is dedicated to the stellar characterization of the core program targets, as well as TESS follow-up targets.

Thanks to the two networks of the TRAPPIST and SPECULOOS telescopes, we are able to gather quickly a large number of observations. The biggest strength of our program lies in the possibility of obtaining simultaneous chromaticity checks. In addition, for a short period of time, the SPIRIT infrared camera was installed on one of the SPECULOOS telescopes. For a full description of the instrument, I refer to Pedersen et al. (2024). It allowed to obtain transits and occultations in the NIR with its custom made *zYJ* filter (0.81 to 1.33 μm, e.g. Triaud et al., 2023). Unfortunately, due to a technical issue, the camera is currently under repair.

The observations are managed through a Google sheet, shown in Appendix Figure A.2.

The targets have a given priority labeled as "A" for active candidates, "B" for false positives (i.e. blended eclipsing binaries, nearby eclipsing binaries, or nearby planetary candidates), "C" for published systems, and "D" for validated systems either by the MANGOs team or TFOP WG but not published yet. There, we keep track of all the successful observations in each filter. We also note if we observe any occultations, if we notice spot crossings that would manifest in the form of a deformation of the transit shape, or any chromatic behavior.

Each month, up to twelve nights (of about eight hours) of observations can be used for the MANGOs project. This is roughly equivalent to the validation of four to five targets. For the monthly selection, I use the `SPOCK`[1] (SPECULOOS Observatories sChedule maKer) package (Sebastian et al., 2021) to check which targets are observable (see Figure 6.2 for an example for the upcoming months of September to December 2024). In parallel, I examine the list of active candidates and select the most interesting ones by ranking them with the following criteria: the smallest host star, highest equilibrium temperature, and brightest magnitude in J. The active candidates are shown in the form of a plot in Figure 6.3. The selected targets are then discussed within the MANGOs team, and scheduled once they are approved.

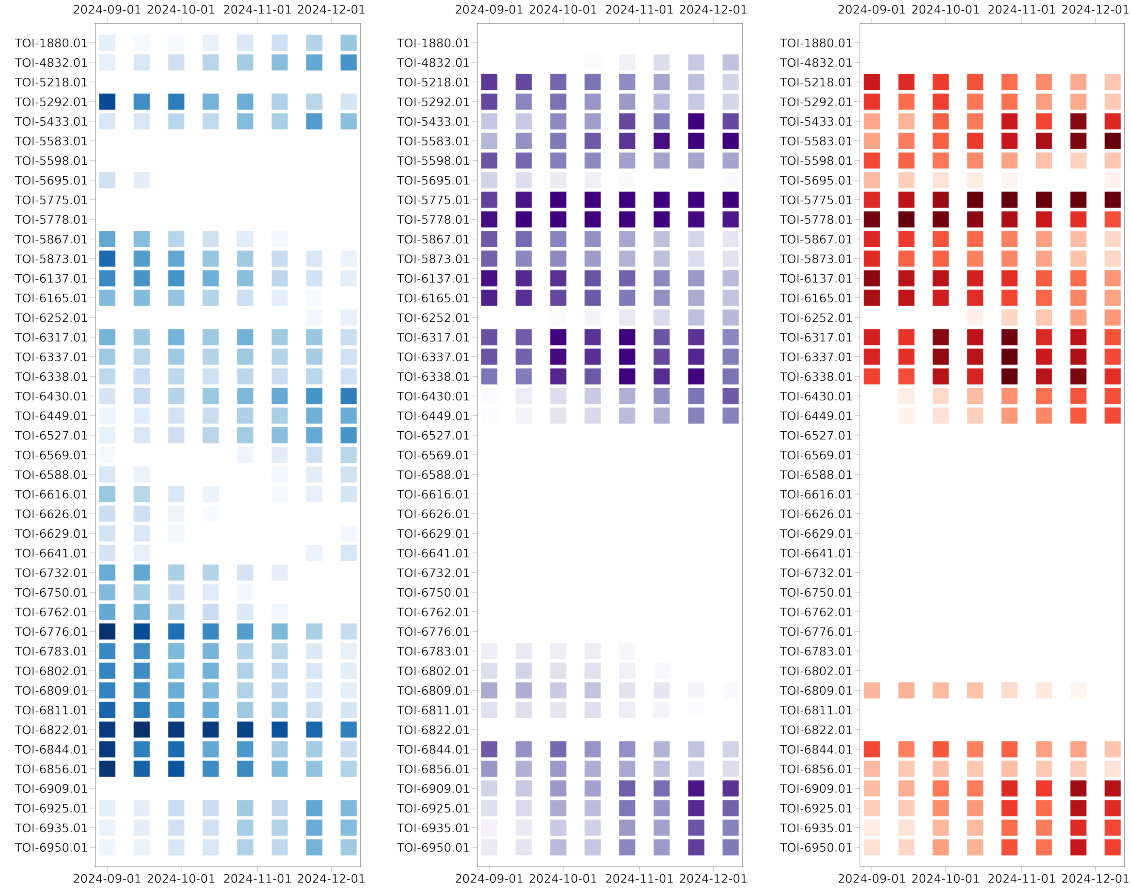

Figure 6.2: Visibility plots for the MANGOs target for the period September 1, 2024, to December 1, 2024. Each panel represents an observatory: on the left is the SPECULOOS Southern Observatory (in blue), in the middle is shown the SPECULOOS Northern Observatory (in purple), and the right shows the visibility from the SAINT-Ex telescope (in red). The color gradient indicates the visibility of the target, from a full night of visibility being the darkest, to not visible at all being in white.

[1]Available at https://github.com/educrot/SPOCK

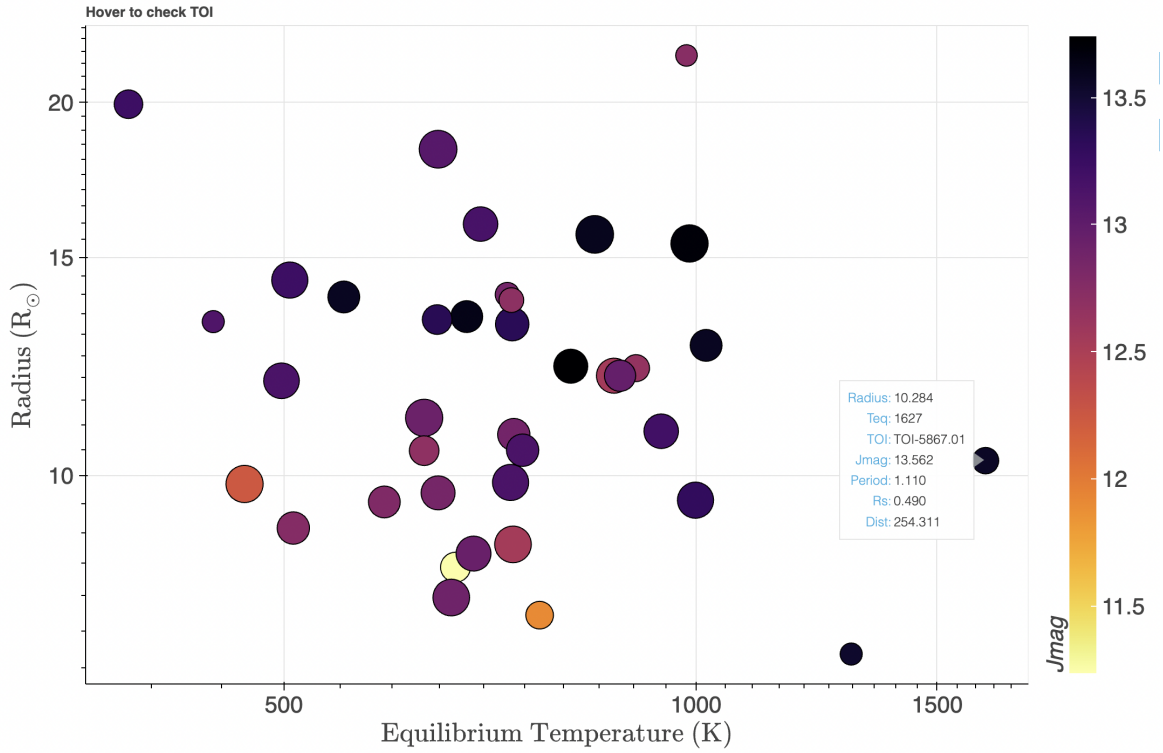

Figure 6.3: Planetary radius as a function of equilibrium temperature for all active candidates of the MANGOs target list. This plot is used in its interactive form by the MANGOs team to visualize the full list while still accessing all the system parameters. The color code indicates the magnitudes of the host stars in the J-band. The size of the markers are relative to the host star size.

6.2.3 Current status

Of the full MANGOs target list, 105 targets have been observed at least once, corresponding to more than 550 observations in total. Since the start of the program in early 2022, over 700 hours and nearly 1400 hours of telescope time has been dedicated to MANGOs targets for the TRAPPIST and SPECULOOS facilities, respectively.

Our program allowed the validation of 40 targets with observations in at least three filters, and the ruling out of 10 blended eclipsing binary systems. Figure 6.4 shows the current disposition of the targets: planet candidates, false positives, confirmed BD and MD binaries, published planets, and planets in the process of being published. Eighty-four are still candidates, and of those 45 are currently validated. They will require RV measurements to confirm their planetary nature (see Section 6.3).

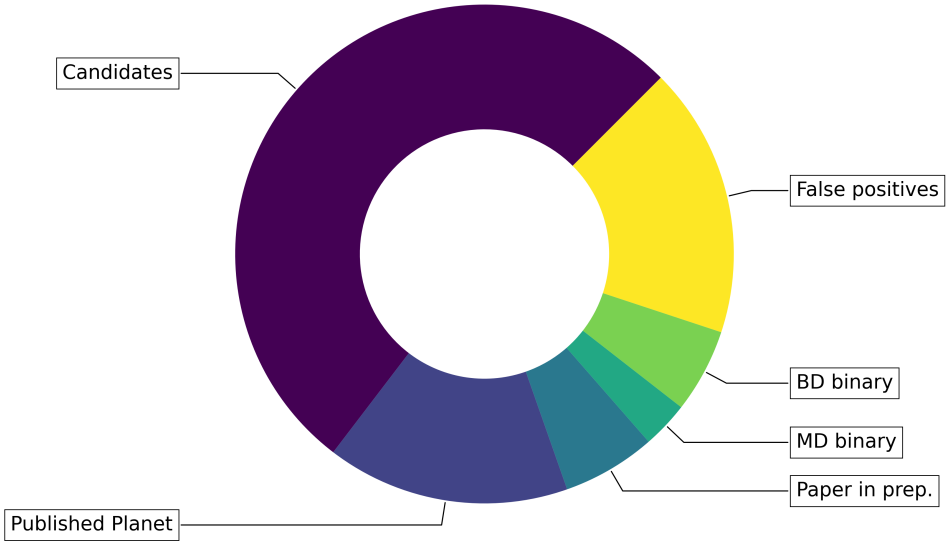

Figure 6.4: Pie chart representing the current dispositions of the MANGOs targets. About 52% of the targets are still candidates, 22% are either published planets or are the object of a publication currently in preparation, 18% are false positives, and the BD and MD binaries represent 5 and 3%, respectively.

6.2.4 MANGOs publications

Because giant planets orbiting low-mass stars are part of such an interesting niche and are easily detected, there are multiple research teams working on their validation and confirmation. Thanks to TFOP WG, we are able to discuss any publication effort with the other teams that are also part of it, and collaborate by sharing our respective data. This allowed us to participate in the discovery papers of TOI-4201 b and TOI-5344 b (Hartman et al., 2023), TOI-3235 b (Hobson et al., 2023), and TOI-762 b (Hartman et al., 2024). Other papers are currently in preparation, such as the discovery of TOI-6894 b (Bryant et al., submitted), and the one of TOI-2379 b and TOI-2384 b (Bryant et al., accepted at *Monthly Notices of the Royal Astronomical Society*).

The first publication of a giant orbiter around a low-mass star of the MANGOs team is the confirmation of TOI-4860 b (Triaud et al., 2023). It is a $0.76 \pm 0.02 R_{Jup}$ planet, with a mass of

$0.67 \pm 0.14 M_{Jup}$, orbiting a 0.34 $M_\odot$ star every 1.52 days. Because we needed to coordinate publications with a competing team, we published this planet as a Letter in the journal *Monthly Notices of the Royal Astronomical Society: Letters*. Given these circumstances, we did not have the time to publish the paper presenting the project prior to this.

The second paper in the MANGOs series is led by George Dransfield. It will present the MANGOs project by detailing its science goals, the observing strategy, and target list. To demonstrate our methods, we will present the validation of seven candidates, spanning all three flavors of MANGOs: (1) TOI-234 b, TOI-4666 b, and TOI-3288 b as statistically validated planets; (2) TOI-734 B, TOI-2415 B, and TOI-5278 B as BD binaries; (3) TOI-2208 B as an MD binary.

6.3 Mass measurements with ESPRESSO

The statistical validation of MANGOs targets allows us to determine that the candidate has a consistent transit depth between the bluer filters and the redder ones. However, this does not guarantee that the candidate is in fact a planet. As mentioned in Section 6.1, transiting BDs can show a similar behavior. Only by constraining the masses can we unmistakably identify the true nature of the candidate, as planets have masses $<13 M_{Jup}$ and BDs between $\sim 13 M_{Jup}$ and $\sim 80 M_{Jup}$.

Constraining the mass of giants orbiting low-mass stars is absolutely crucial to trace their formation histories. The bulk density can be compared against interior structure models to infer an approximation of the mass of the core (e.g. Kagetani et al., 2023; Ulmer-Moll et al., 2023). In addition, combining the transit and RV measurements, we can estimate the planetary metallicity from the bulk density through a mass-metallicity relationship (Thorngren et al., 2016). The mass also gives access to the atmospheric scale height, which is a necessary parameter to interpret any subsequent atmospheric study on these planets.

For the MANGOs project, we do not currently have a privileged access to RV facilities. This led us to apply for observing time on the Very Large Telescope where the ESPRESSO spectrograph is mounted. We proposed a first program to measure the mass of MANGOs targets during the P112 period (P112.25ZF, PI: George Dransfield, dPI: Mathilde Timmermans) that was accepted as a filler program. Unfortunately, only four spectra of four different targets were obtained over the dedicated period. With this, we could not fulfill our science goals. This motivated the second accepted program (P114.27JF, PI: Mathilde Timmermans, dPI: Khalid Barkaoui) for which the data will soon be acquired during P114.

For this ESPRESSO program, we selected twelve targets that were statistically validated with ground-based facilities. Among those, we chose the brightest ones that would be within reach of ESPRESSO. The targets are given in Table 6.1 with their estimated parameters. The mass is estimated using the Chen & Kipping mass-radius relationship (Chen & Kipping, 2017), and the RV semi-amplitude K is calculated following Equation 1.26, assuming a circular orbit. We obtained the RV precision using the ESPRESSO ETC[2], and selected the following observing conditions: a fraction of lunar illumination up to 90%, a turbulence category of 85% (seeing below 1.3″) to facilitate the scheduling, precipitable water vapor lower than 30 mm, the presence of thin cirrus accepted, and a maximal airmass of 1.5. Given the faintness of the targets, the detector mode used is Single UT, high spectral/RV resolution, 2×1 binning, and slow readout. For each, we selected the exposure time that maximizes the S/N while minimizing the number of spectra to request for a 10σ mass measurement, with a value between 600 and 1800 seconds. We set a minimum of 5 data points in order to sample effectively the phase and constrain the eccentricity.

[2] https://www.eso.org/observing/etc/bin/gen/form?INS.NAME=ESPRESSO+INS.MODE=spectro

Table 6.1: Estimated parameters for the accepted ESO proposals on ESPRESSO of P112 and P114.

Target	**Mass ($M_\oplus$)**	**K (m/s)**	**RV precision (m/s)**	**Exp. time (s)**	**S/N**	**10σ detection**	**Request P112**	**Request P114**
TOI-734.01	100.73	162.49	53.53	1800	1.12	10.86	10	7
TOI-2205.01	131.46	119.24	28.97	600	2.07	5.90	5	5
TOI-2208.01	104.76	212.89	37.62	1200	1.05	3.12	5	5
TOI-2341.01	55.60	123.09	9.97	600	6.24	0.65	5	5
TOI-3288.01	103.49	100.10	9.29	600	6.46	0.86	5	5
TOI-4201.01	98.71	57.99	10.48	600	5.72	3.26	5	-
TOI-4666.01	110.50	84.90	11.76	600	5.10	1.92	5	4
TOI-4858.01	101.15	120.47	33.61	1200	1.44	7.78	7	7
TOI-5007.01	79.75	83.62	11.71	600	5.12	1.96	5	4
TOI-5694.01	176.17	149.60	23.82	600	2.52	2.53	5	-
TOI-5695.01	64.32	130.97	36.66	1800	1.63	7.83	9	6
TOI-5916.01	83.58	102.28	22.44	900	2.67	4.81	6	6

Four spectra were obtained in the initial program, the resulting RV precisions and S/N obtained from the automatic reduction pipeline are given in Table 6.2. The seeing was poor (close to 2″) for the observations of TOI-4858.01 and TOI-734.01. Overall, the S/N is larger than predicted for all four targets. Although the RV precision seems similar than predicted for TOI-4666.01 and TOI-5007.01, but more than a factor of 2 worse for TOI-4858.01, and more than a factor of 2 better for TOI-734.01. A first analysis of the ESPRESSO spectrum of TOI-734.01 revealed it to be a double-lined eclipsing binary. This makes it a rare find as it is currently the lowest mass of its kind.

Table 6.2: Summary of the ESPRESSO spectra obtained for the program P112.25ZF.

Target	**Date**	**RV precision (m/s)**	**S/N**
TOI-4666.01	Dec. 17, 2023	14.09	6.59
TOI-4858.01	Jan. 23, 2024	73.36	2.71
TOI-734.01	Jan. 29, 2024	19.55	2.73
TOI-5007.01	Feb. 23, 2024	14.85	6.55

The second program aims to complete the first one, and allow us to reach our science goals of measuring the masses of these targets. Two targets were removed from the list: TOI-4201 b was published, and TOI-5694.01 was confirmed to be a blended eclipsing binary. In this case, we adjusted the number of spectra we requested based on the results of the first program, they are given in Table 6.1. The data collection of P114 will start on October 1, 2024.

Chapter 7

Conclusion

I began this thesis by an introduction on our place in the Universe. Considering the hundreds of billion stars in our Galaxy, the emergence of life on Earth naturally raises important questions. These have shaped the field of Exoplanetology and define the broad context of this thesis: (1) understanding how exoplanetary systems form and evolve, and (2) searching for life beyond the solar system. These two guiding principles have directed this PhD research, which focused on two sub-populations of planets orbiting red dwarf stars: sub-Neptunes and close-in giants.

Sub-Neptunes and super-Earths are believed to share a common formation pathway. However, the existence of the radius valley for solar-type stars points to distinct evolutionary steps for these planets. For low-mass stars, some studies suggest a density valley rather than a radius valley, while others argue there is a continuity in the composition and volatile content. The biggest limitation to the interpretation of such population studies resides in the small statistics. The current number of well-characterized super-Earths and sub-Neptunes, those with precise radius and mass measurements, is still too limited. Additionally, atmospheric characterization is critical to remove model degeneracies related to planetary composition and internal structure. Finally, the atmospheres of super-Earths and sub-Neptunes are also key in the search for biosignatures, with planets within the habitable zone of their host stars being of particular interest.

Giant planets orbiting low-mass stars challenge formation theories. Thanks to the TESS mission, the number of detected planets has more than doubled in the last four years. Still, the sample remains small with only about 20 planets confirmed. Most of them appear to be orbiting close to their host star, making them the equivalent of hot Jupiters. Considering similar formation mechanisms, studies have shown that in-situ formation is impossible for low-mass stars, which suggests that a migration mechanism is responsible for the existence of close-in giants. By determining their atmospheric composition, it is possible to trace the formation history of these planets. To identify trends within this population and better understand the mechanisms at play, a statistically significant sample of well-characterized planets is needed.

During this PhD, I worked towards increasing the number of sub-Neptunes and close-in giants orbiting low-mass stars amenable for a thorough characterization. I was involved in a wide range of projects on both the detection and characterization aspects.

First, throughout this PhD, I was involved in the photometric follow-up of TESS candidates with the TRAPPIST and SPECULOOS ground-based facilities. The goal of this endeavor is to identify false positives and statistically validate the planetary nature of TOIs. For TRAPPIST and SPECULOOS, it roughly totals to 500 TOI observations per year, all telescopes combined. They are handled by the Exo-TRAPPIST team and the WG6 of SPECULOOS, both of which I am a part of. Being active in all the tasks related to the

validation of planetary candidates, I scheduled observations, took care of the data analysis, and reported the results to TFOP. This way, I contributed to the statistical validation of hundreds of TOIs, and co-authored 38 publications related to the discovery of new planets. Additionally, I contributed to the development of `prose`[1] to facilitate the processing of such a large amount of images. I collaborated with Lionel Garcia, its main developer, to design methods specifically useful for the photometric follow-up of TESS candidates. They are available to the community in the form of an annex package called `verse`[2].

Of the candidates I followed-up on, I led the publication of the validation of TOI-4336 A b. It is a 2.1±0.1 $R_\oplus$ sub-Neptune planet at the inner edge of the habitable zone, with a period of 16.3 days. The host star is a M3.5 star in a nearby triple M-dwarf system. TOI-4336 A b is currently one of the best temperate sub-Neptunes for atmospheric characterization. I am also leading the atmospheric reconnaissance program of this planet with HST/WFC3 (mid-cycle 29, P16875). Due to technical difficulties with HST, the data acquisition is still ongoing. The outcome of this program will give the first insights into the composition of the upper atmosphere of TOI-4336 A b. In the absence of aerosols and high altitude clouds, we expect to find the signature of H_2O/CH_4 at 1.4μm in the transmission spectrum.

The Hidden Gems project searches for additional candidates in known transiting systems orbiting low-mass stars. Using the `SHERLOCK`[3] pipeline, the TESS data are examined to find low S/N periodic signals. I am leading the publication of the first discoveries of the project: TOI-237 c and TOI-4336 A c. These two super-Earths have radii of 1.23 ± 0.04 and 1.21 ± 0.06 $R_\oplus$, respectively. They are both on inner orbits compared to the first planets discovered in the systems, with periods of 1.7 days for TOI-237 c, and 7.6 days for TOI-4336 A c. Notably, to confirm the existence of TOI-237 c, we conducted an extensive follow-up campaign in the form of a filler program on TRAPPIST-South. The global analyses of the photometric data show that both these planets are ideal candidates for transmission spectroscopy. The paper is currently being written, and will be submitted in the coming months.

Finally, I have been leading the MANGOs project with George Dransfield since its early days in 2022. This large observing program on TRAPPIST and SPECULOOS targets close-in giants orbiting low-mass stars. The science goals are based on the statistical validation of giant planets, but also include identifying any transiting brown dwarf and M-dwarf binary. In a little over two years, our observations allowed to validate 40 planets, and ruling out 10 systems as blended eclipsing binaries. About half of the target list remains to be fully validated. To go further into the characterization of MANGOs targets, we have obtained time on ESPRESSO for the upcoming P114 period to obtain a mass measurement for 10 of our validated candidates (P114.27JF).

Some of the projects undertaken during this thesis are still unfinished or are only beginning. I am very happy to be able to continue my journey in research with a postdoc position at the University of Birmingham. Following the order of the summary above, here are a few things I will keep in mind for the coming year:

- TESS may have already scanned most of the sky, the extended missions still allow to discover new planet candidates. There are still plenty to observe and validate using the high-precision photometric measurements of the TRAPPIST and SPECULOOS facilities.

- In the coming months, I am hoping to update the `verse` package to the latest additions of `prose` for an even more efficient data analysis procedure.

[1] https://github.com/lgrcia/prose
[2] https://github.com/mathtimm/verse
[3] https://github.com/franpoz/SHERLOCK

- A mass measurement of both planets of the TOI-4336 A system will soon be published. HST is now in Reduced Gyro Mode, but I am hopeful to still be able to obtain the last transits due for the program on the atmospheric exploration of planet b. The early results suggest a non-flat spectrum, which is very exciting. Most of the sub-Neptunes published so far have displayed flat spectra due to the opacity of a cloud layer. In this case, combining the mass measurement and the transmission spectra, we will have a first look at the content of the upper atmosphere in water vapor and methane. Such results would be very encouraging for the upcoming JWST Cycle 3 program (GO 4711, PI: Renyu Hu) targeting TOI-4336 A b as a temperate water world candidate.

- The Hidden Gems project has already yielded the detection of additional planets in two of the systems analyzed. As the project is only beginning, we expect to find more candidates as the project progresses. The publication of TOI-4336 A c and TOI-237 c will be my very first task following this PhD. Given the high scientific value of these planets, their publication is paramount to obtain time on JWST for a characterization of their atmosphere and search for biosignatures.

- I will continue to lead the MANGOs project with George Dransfield. It is very dear to me, we have worked hard to set it up and bring it to where it is today. It has already led to the publication of one very high-impact paper with the discovery of TOI-4860 b, and allowed us to be a part of the discovery of four other close-in giants. The upcoming ESPRESSO data will allow me to directly work on the mass determination of planet candidates. I have not had the opportunity to do it so far, and I am very much looking forward to it.

To conclude, I believe this PhD thesis has achieved the goal of finding new exciting planetary systems orbiting red dwarf stars, both in the sub-Neptune and close-in giant regimes. Their upcoming mass and atmospheric characterization will contribute to increasing the number of well-characterized planets for these sub-populations. Overall, in two decades, the growing technological capabilities has allowed the detection of nearly 6000 exoplanets. With the addition of upcoming facilities such as PLATO (Rauer et al., 2016), this number will likely grow spectacularly in the coming years. On the aspect of characterization, the Ariel mission (Tinetti et al., 2016) and the ELT (Neichel et al., 2018) notably promise exciting results with an in-depth study of a large number of planets so far unexplored. The field of Exoplanetology is young, and as new technology is developed, we will push the boundaries of observational and theoretical advances.

Appendix

A.1 `verse` reports

TESS follow-up

TOI-4860.01

2022 03 27 · TRAPPIST-South · Exo

NIGHT

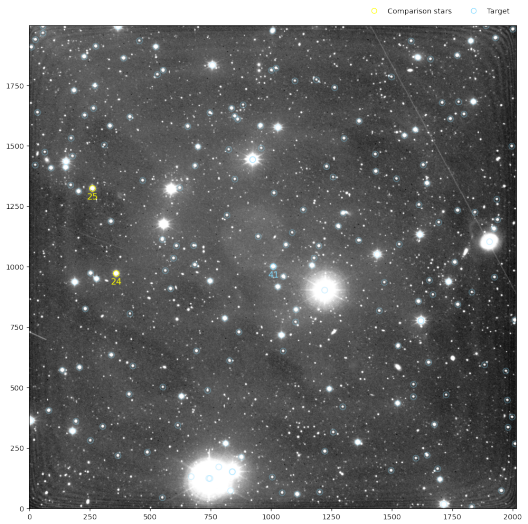

TIC id	335590096
Time	02:47 - 07:44 [4h57]
RA - DEC	183.56458 -13.17481
Images	136
GAIA id	3571038605366263424
Mean std · fwhm (epsf)	2.00 · 4.71 pixels
Fwhm (target)	3.28 pixels · 2.10 arcsec
Optimum aperture	6.15 pixels · 3.94 arcsec
Telescope	TRAPPIST-South
Filter	Exo
Exposure	120.0 s

PSF

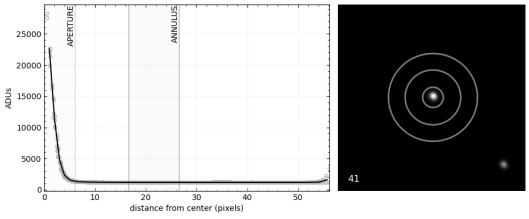

LIGHTCURVE

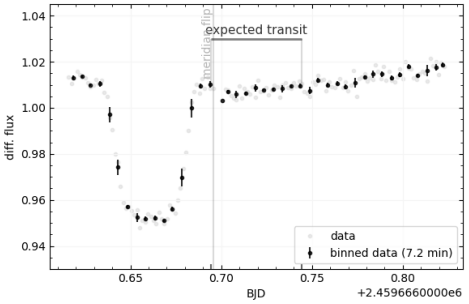

RAW

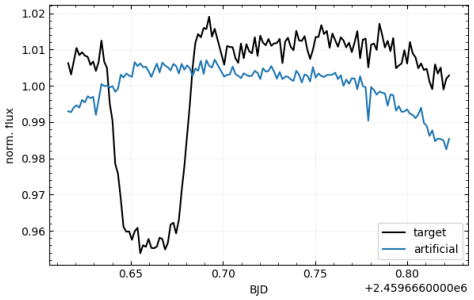

SYSTEMATICS (scaled to diff. flux)

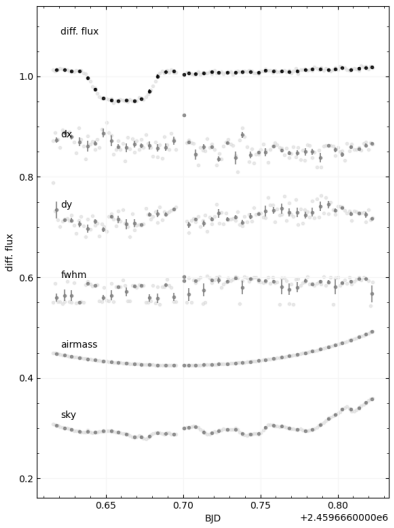

COMPARISON STARS

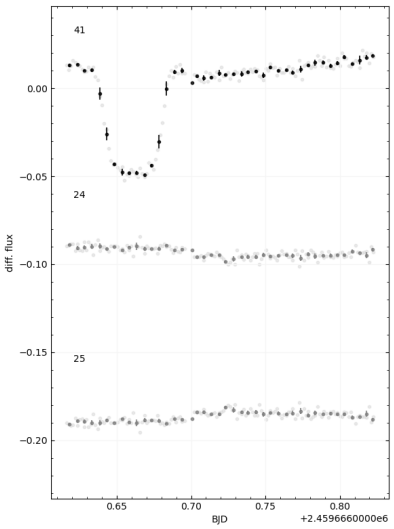

TRANSIT MODEL

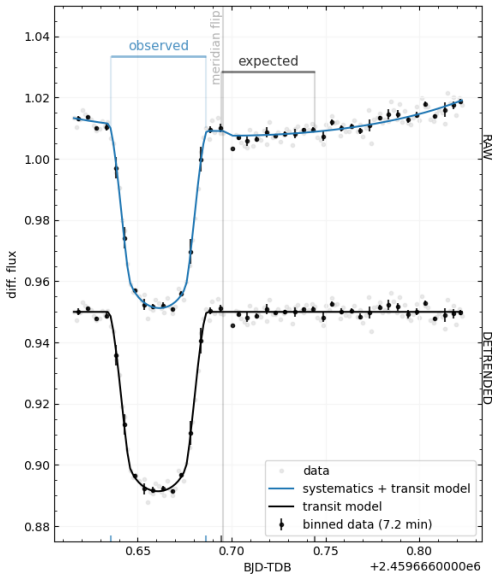

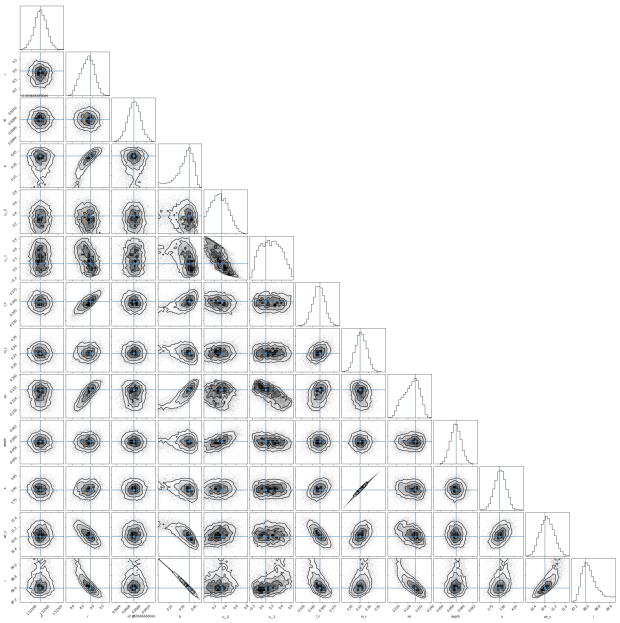

MODEL PARAMETERS

Parameters	Model	TESS
u1	0.2936±0.156	-
u2	0.2845±0.3067	-
R*	0.3546±0.0084$R_\odot$	0.3500±0.0100$R_\odot$
M*	0.3358±0.0184$M_\odot$	0.3376±0.0205$M_\odot$
P	1.523±0.0001d	1.5230±0.0001d
Rp	8.7596±0.3305$R_\oplus$	8.9948±0.4850$R_\oplus$
Tc	2459666.6608±0.0001	2459666.7193±0.0167
b	0.3277±0.109	-
Duration	73.37 min	71.76±9.36 min
$(Rp/R^*)^2$	58.9e-3±1.0e-3	58.06e-3±0.10e-3
Apparent depth (min. flux)	5.86e-02	-
a/R*	10.9189±0.2617	-
i	88.269±0.5972	-
SNR	149.44	-
RMS per bin (5.0 min)	1.59e-03	-

ADDITIONAL NOTES

Summary: Mathilde Timmermans/TRAPPIST-South observed a full on 20220327 in Exo and detected an 84 min (5.9σ) early 59 ppt event using an uncontaminated 3.9" target aperture.

- Aperture radius = 3.9"
- Typical FWHM = 2.1"
- Predicted Tc = 9666.7193
- Measured Tc = 9666.6608
- Transit depth on target = 59 ppt.
- Duration of the transit : 73 min
- Precision reached = 1.6ppt/5min.
- Meridian flip at 9666.6955
- Detrending parameters : airmass, flip
- Comments in TTF before the observation: QLP S36 PC: found in faint-star QLP search; Confirm event on target and/or check field for NEBs within 2.5' using a red (rp, R, ip, I, z) filter.

TESS follow-up

TOI-2354.01

2021 04 12 · Trappist-South · z

NIGHT

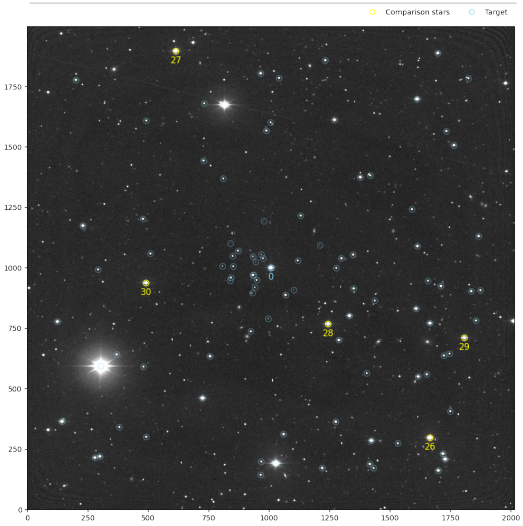

TIC id	219766989
Time	03:50 - 08:18 [4h28]
RA · DEC	192.32171 -21.333
Images	319
GAIA id	3502630870240466560
Mean std · fwhm (epsf)	1.23 · 2.91 pixels
Fwhmx · fwhmy (target)	3.15 · 3.04 pixels
Optimum aperture	6.04 pixels
Telescope	Trappist-South
Filter	z
Exposure	40.0 s

PSF

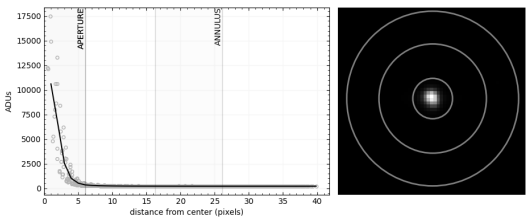

LIGHTCURVE

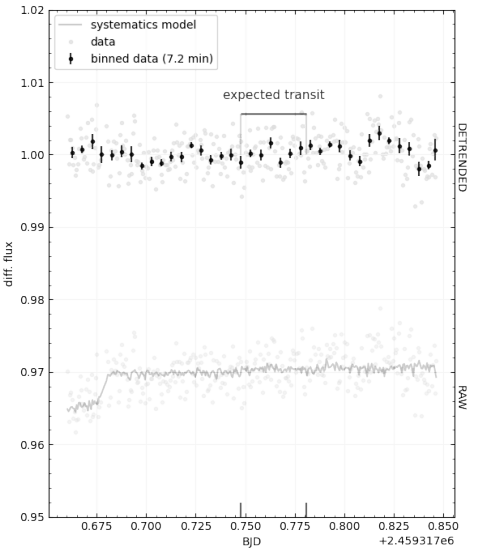

RAW

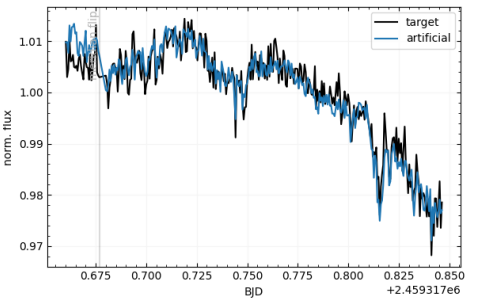

SYSTEMATICS

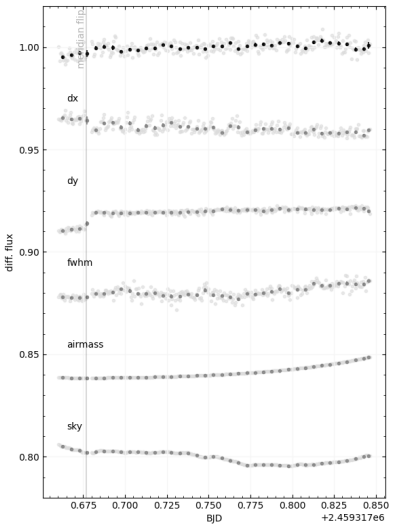

COMPARISON STARS

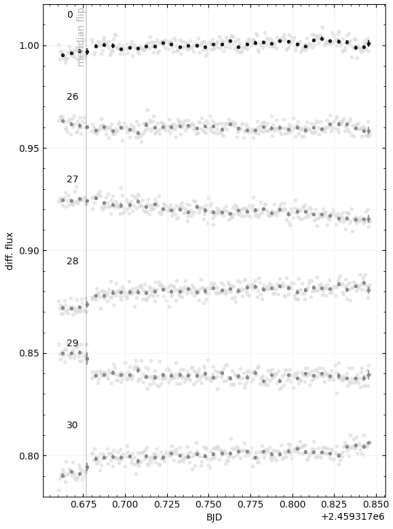

Near eclipsing binary diagnostic

RADIUS

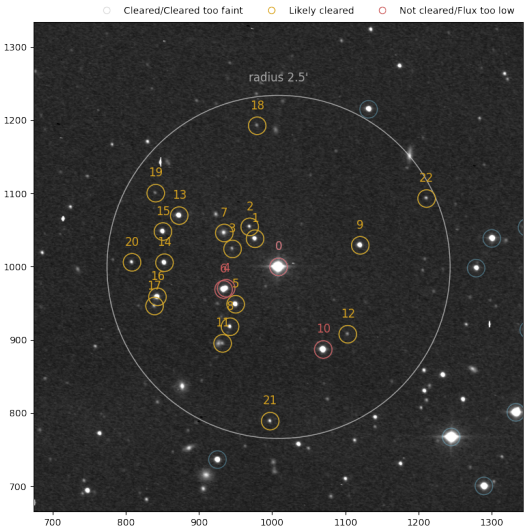

SUMMARY

Cleared	Likely Cleared	Cleared too faint	Not cleared	Flux too low
0	19	0	4	0

DMAG vs RMS

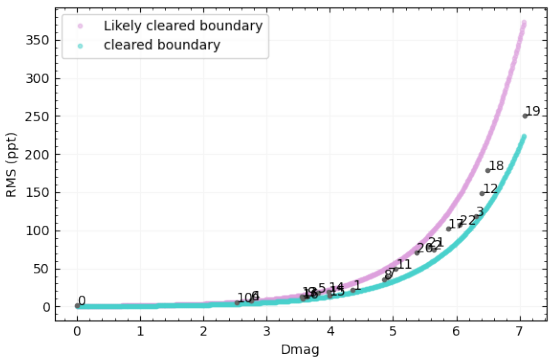

LIGHT CURVES (ONLY SUSPECTS))

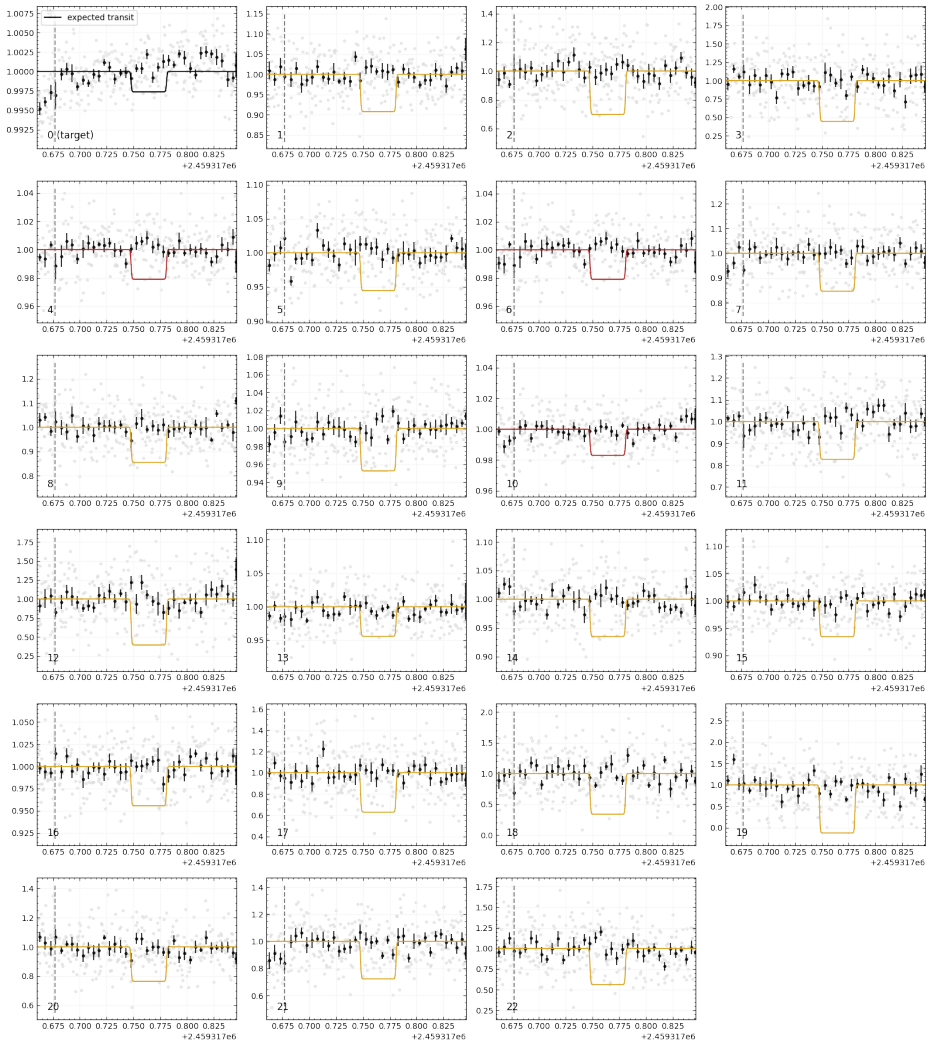

ADDITIONAL NOTES

Goal of the observation: full transit in a red filter to check for the return of the transit at the revised ephemeris.

- TOI-2354.01 has been observed with the TRAPPIST-South 0.6m telescope on the night of UTC 20210412 in the z' filter with an exposure time of 40s (e-174/i+142 min; -4.2/+3.4 sigma).
- The transit is not detected on the target star which is labeled 0 on the stack image, the predicted depth is of about 2.64 ppt. The precision reached is 0.9 ppt/5 min.
- The expected mid-transit timing is 2459317.7644 BJD-TDB.
- The target star light curve has been detrended for dx and dy.
- Five stars are used for comparison, all of them flat and of similar brightness as the target.
- A meridian flip took place at 2459317.6768 BJD-TDB.
- We performed an NEB check following a procedure similar to AstroImageJ. Out of the 23 Gaia stars: none are cleared, 19 likely cleared and 4 not cleared. There are no obvious NEBs.
- Weather conditions were stable throughout the observation and the moon was at 1% at 158°.
- Comments in TTF before the observation: QLP S10 VPC?: [P=0.51117] a/R 1.85; CTOI Marco Montalto; TG Tan observed a full (Tc -3.0/+5.7 hrs) on 20210324 in Rc and probably detected an on-target 246 min (1.8 sigma) late 5 ppt (2xdeep) event in an uncontaminated 8.5" aperture. [P=0.5112946] The TRAPPIST-N team observed a full on 20210402 in zp and tentatively detected a 30 min late 2.7 ppt event on target. Georgia Mraz analyzed a full on 20210329 in 1m0 ip. Inconclusive due to strong scattered light from moon (100% @ 20degrees) and low exposure level. Results were inconclusive. The next observation should be a high precision (<1.0 ppt/5 min) full transit in a red (r', R, i', I, z) filter to check for the return of the transit at the revised ephemeris. Multi-band observations preferred.
- Updated comments in TTF since the observation: QLP S10 VPC?: [P=0.51117] a/R 1.85; CTOI Marco Montalto; TG Tan observed a full (Tc -3.0/+5.7 hrs) on 20210324 in Rc and probably detected an on-target 246 min (1.8 sigma) late 5 ppt (2xdeep) event in an uncontaminated 8.5" aperture. [P=0.5112946] The TRAPPIST-N team observed a full on 20210402 in zp and tentatively detected a 30 min late 2.7 ppt event on target. Georgia Mraz analyzed a full on 20210329 in 1m0 ip. Inconclusive due to strong scattered light from moon (100% @ 20degrees) and low exposure level. Rick Schwarz analyzed a nominal full of a 6 late ephemeris on 20210422 in 1m0 ip and possibly detected a 114 min (total of 9) late 3 ppt ingress in an uncontaminated 3.9" target aperture. [P=0.5113499] TG Tan observed a gapped full on 20210603 in Rc and maybe detected an on-target 5.5hr (7.5 sigma!) late 5ppt (2x deep) event in a 9.2" uncontaminated aperture. The predicted event fell in the gap so an on-time event cannot be ruled out. This ephemeris is already 6.6 hours late, so the total is 0.5 days late, or 1 orbital period. [P=0.51117] The next observation should be a high precision (<1.0 ppt/5 min) full transit in a red (r', R, i', I, z) filter to check for the return of the transit at the original ephemeris. Multi-band observations preferred.

Conclusions: we observed TOI-2354.01 on 2021.04.12 with the z' filter (e-174/i+142 min; -4.2/+3.4 sigma), and no transit was detected. The field was searched for NEBs, there are no obvious NEBs and most stars are likely cleared.

A.2 Hidden Gems

A.2.1 Limb darkening coefficients obtained for the TOI-237 system

Table A.1: Limb darkening coefficients obtained in the global analysis of the TOI-237 system (see section 5.5).

Parameters	Values	Priors	Source
Limb darkening $q_{1,TESS}$	0.413 ± 0.042	$\mathcal{N}(0.398,\, 0.050^2)$	Fitted
Limb darkening $q_{2,TESS}$	0.122 ± 0.042	$\mathcal{N}(0.121,\, 0.050^2)$	Fitted
Limb darkening $q_{1,I+z}$	$0.294^{+0.040}_{-0.043}$	$\mathcal{N}(0.316,\, 0.050^2)$	Fitted
Limb darkening $q_{2,I+z}$	$0.183^{+0.041}_{-0.045}$	$\mathcal{N}(0.184,\, 0.050^2)$	Fitted
Limb darkening $q_{1,Sloan-g'}$	0.685 ± 0.046	$\mathcal{N}(0.686,\, 0.050^2)$	Fitted
Limb darkening $q_{2,Sloan-g'}$	0.289 ± 0.046	$\mathcal{N}(0.289,\, 0.050^2)$	Fitted
Limb darkening $q_{1,Ic}$	0.377 ± 0.043	$\mathcal{N}(0.376,\, 0.050^2)$	Fitted
Limb darkening $q_{2,Ic}$	0.176 ± 0.042	$\mathcal{N}(0.173,\, 0.050^2)$	Fitted
Limb darkening $q_{1,ExTrA}$	0.121 ± 0.045	$\mathcal{N}(0.121,\, 0.050^2)$	Fitted
Limb darkening $q_{2,ExTrA}$	0.275 ± 0.046	$\mathcal{N}(0.278,\, 0.050^2)$	Fitted
Limb darkening $q_{1,Sloan-r'}$	0.677 ± 0.044	$\mathcal{N}(0.670,\, 0.050^2)$	Fitted
Limb darkening $q_{2,Sloan-r'}$	$0.339^{+0.043}_{-0.046}$	$\mathcal{N}(0.324,\, 0.050^2)$	Fitted
Limb darkening $u_{1,TESS}$	0.157 ± 0.053	-	Derived
Limb darkening $u_{2,TESS}$	0.485 ± 0.064	-	Derived
Limb darkening $u_{1,I+z}$	$0.197^{+0.046}_{-0.049}$	-	Derived
Limb darkening $u_{2,I+z}$	0.342 ± 0.056	-	Derived
Limb darkening $u_{1,Sloan-g'}$	0.478 ± 0.078	-	Derived
Limb darkening $u_{2,Sloan-g'}$	0.349 ± 0.076	-	Derived
Limb darkening $u_{1,Ic}$	0.215 ± 0.053	-	Derived
Limb darkening $u_{2,Ic}$	0.396 ± 0.060	-	Derived
Limb darkening $u_{1,ExTrA}$	0.188 ± 0.048	-	Derived
Limb darkening $u_{2,ExTrA}$	$0.152^{+0.048}_{-0.045}$	-	Derived
Limb darkening $u_{1,Sloan-r'}$	0.556 ± 0.077	-	Derived
Limb darkening $u_{2,Sloan-r'}$	$0.264^{+0.079}_{-0.072}$	-	Derived

A.2.2 Limb darkening coefficients obtained for the TOI-4336 A system

A.2.3 Impact of the flaring event in the MuSCAT3 light curves

A.3 MANGOs

Table A.2: Limb darkening coefficients obtained in the global analysis of the TOI-4336 A system (see section 5.5).

Parameters	**Values**	**Priors**	**Source**
Limb darkening $q_{1,TESS}$	$0.384^{+0.037}_{-0.035}$	$\mathcal{N}(0.376,\ 0.050^2)$	Fitted
Limb darkening $q_{2,TESS}$	0.106 ± 0.036	$\mathcal{N}(,0.125,\ 0.050^2)$	Fitted
Limb darkening $q_{1,Sloan-g'}$	$0.647^{+0.032}_{-0.034}$	$\mathcal{N}(0.686,\ 0.050^2)$	Fitted
Limb darkening $q_{2,Sloan-g'}$	0.294 ± 0.038	$\mathcal{N}(0.289,\ 0.050^2)$	Fitted
Limb darkening $q_{1,Sloan-z'}$	0.291 ± 0.032	$\mathcal{N}(0.282,\ 0.050^2)$	Fitted
Limb darkening $q_{2,Sloan-z'}$	$0.136^{+0.024}_{-0.028}$	$\mathcal{N}(0.153,\ 0.050^2)$	Fitted
Limb darkening $q_{1,ExTrA}$	$0.142^{+0.034}_{-0.027}$	$\mathcal{N}(0.110,\ 0.050^2)$	Fitted
Limb darkening $q_{2,ExTrA}$	$0.242^{+0.030}_{-0.035}$	$\mathcal{N}(0.280,\ 0.050^2)$	Fitted
Limb darkening $q_{1,Sloan-r'}$	0.682 ± 0.037	$\mathcal{N}(0.687,\ 0.050^2)$	Fitted
Limb darkening $q_{2,Sloan-r'}$	$0.320^{+0.029}_{-0.032}$	$\mathcal{N}(0.403,\ 0.050^2)$	Fitted
Limb darkening $q_{1,Sloan-i'}$	0.397 ± 0.037	$\mathcal{N}(0.206,\ 0.050^2)$	Fitted
Limb darkening $q_{2,Sloan-i'}$	$0.154^{+0.024}_{-0.031}$	$\mathcal{N}(0.332,\ 0.050^2)$	Fitted
Limb darkening $q_{1,PanSTARSS-zs}$	0.235 ± 0.036	$\mathcal{N}(0.247,\ 0.050^2)$	Fitted
Limb darkening $q_{2,PanSTARSS-zs}$	0.282 ± 0.037	$\mathcal{N}(0.278,\ 0.050^2)$	Fitted
Limb darkening $u_{1,TESS}$	0.131 ± 0.045	-	Derived
Limb darkening $u_{2,TESS}$	0.488 ± 0.052	-	Derived
Limb darkening $u_{1,Sloan-g'}$	0.471 ± 0.061	-	Derived
Limb darkening $u_{2,Sloan-g'}$	0.331 ± 0.065	-	Derived
Limb darkening $u_{1,Sloan-z'}$	$0.146^{+0.027}_{-0.030}$	-	Derived
Limb darkening $u_{2,Sloan-z'}$	$0.392^{+0.040}_{-0.036}$	-	Derived
Limb darkening $u_{1,ExTrA}$	0.181 ± 0.031	-	Derived
Limb darkening $u_{2,ExTrA}$	$0.195^{+0.037}_{-0.031}$	-	Derived
Limb darkening $u_{1,Sloan-r'}$	$0.528^{+0.056}_{-0.060}$	-	Derived
Limb darkening $u_{2,Sloan-r'}$	$0.297^{+0.052}_{-0.047}$	-	Derived
Limb darkening $u_{1,Sloan-i'}$	$0.193^{+0.032}_{-0.041}$	-	Derived
Limb darkening $u_{2,Sloan-i'}$	$0.436^{+0.045}_{-0.037}$	-	Derived
Limb darkening $u_{1,PanSTARSS-zs}$	$0.272^{+0.041}_{-0.039}$	-	Derived
Limb darkening $u_{2,PanSTARSS-zs}$	0.210 ± 0.042	-	Derived

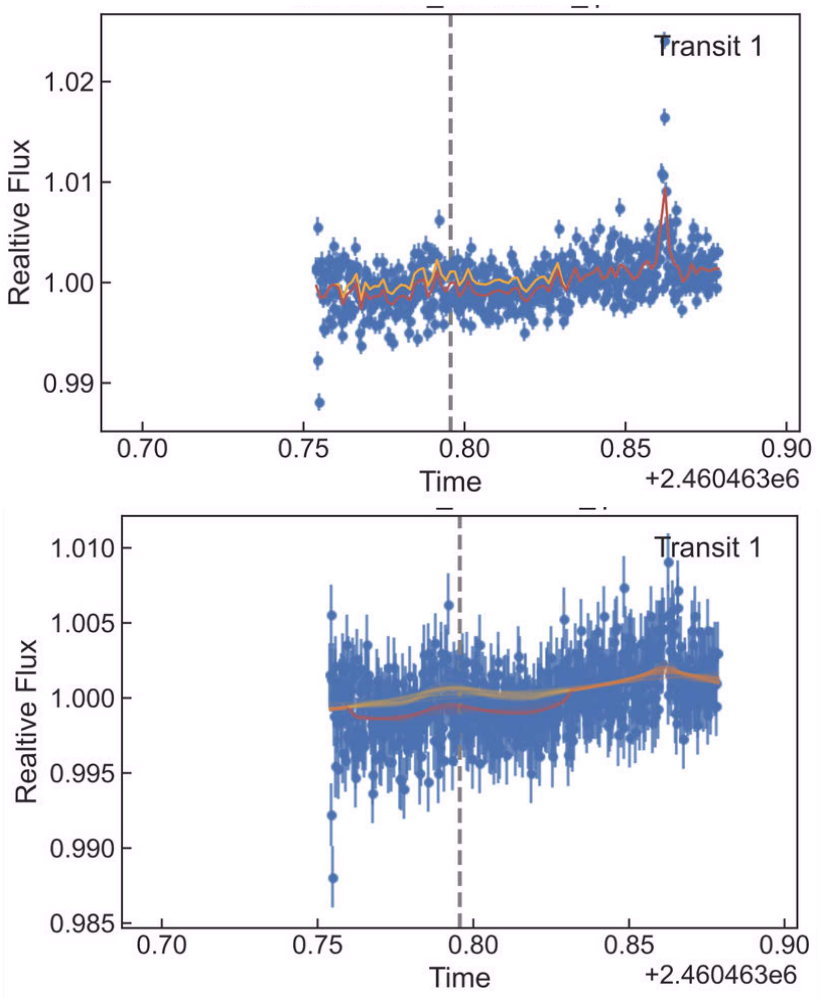

Figure A.1: Comparison between the best fit models including the flaring event and masking it for the TOI-4336 A c observation with MuSCAT3 in the *Sloan-i'* filter.

	TOI	Priority	gp	rp	ip	zp	I+z	Exo	zYJ	Secondary	Needs	SPOT?	Achromatic ?	Paper	Comments
37	TOI-4506.01	D	1	0	0	1	1	0	1	zYJ, rp, ip					Low-mass EB, MANGOS II
38	TOI-457.01	A	0	0	0	0	0	0	0						1 arcsec neighbor
39	TOI-4587.01	C	0	0	0	0	0	0	0						Kepler-1624 b
40	TOI-4622.01	B	0	0	0	0	0	0	0						FA ? Never could find the transit
41	TOI-4666.01	D	2	2	1	2	2	0	2	I+z, zYJ, i'					MANGOS II, NIRPS GTO
42	TOI-468.01	C	0	0	0	0	0	0	0					narvard.edu/abs/2015AJ....1	HATS-6 b
43	TOI-472.01	B	0	0	0	0	0	0	0						BEB
44	TOI-4728.01	D	1	1	1	0	0	0	1						
45	TOI-4817.01	B	0	0	0	0	1	1	0						NEB
46	TOI-4832.01	A	0	0	0	0	1	0	0						
47	TOI-4858.01	D	1	2	1	4	1	0	1						
48	TOI-4860.01	C	1	1	1	2	1	1	1	zp, zYJ				tps://arxiv.org/abs/2308.014	MANGOS I
49	TOI-4988.01	A	0	0	0	0	1	0	0						
50	TOI-4991.01	D	2	2	0	0	1	1	2	zp					
51	TOI-5007.01	D	1	0	1	1	3	0	0						
52	TOI-5010.01	D	1	2	0	1	1	0	0						
53	TOI-5023.01	D	1	1	1	1	0	0	0						
54	TOI-5041.01	B	2	2	2	1	0	1	0						BEB
55	TOI-507.01	D	1	0	1	1	0	0	0						In prep. by Hannu
56	TOI-5090.01	C	0	0	0	0	0	0	0					tps://arxiv.org/abs/1706.030	BD-MD binary
57	TOI-5102.01	B	0	0	0	0	3	0	0						BEB
58	TOI-5139.01	D	0	0	0	0	0	0	0						Validated by TFOP
59	TOI-519.01	C	0	0	0	0	0	0	0					rvard.edu/abs/2021A%26A..	Known HJ
60	TOI-5199.01	B	0	0	0	0	0	0	0						NEB
61	TOI-5205.01	C	1	2	0	0	1	0	0					narvard.edu/abs/2023AJ....1	Known HJ
62	TOI-5218.01	C	0	0	0	0	0	0	0					tps://arxiv.org/abs/2408.1469	
63	TOI-5245.01	B	1	0	0	1	0	0	0						BEB
64	TOI-5268.01	D	0	0	0	0	0	0	0						Validation in prep Emma Esparza-Bo
65	TOI-5278.01	D	1	1	0	2	1	0	0						MANGOS II

Figure A.2: Google sheet used to manage the MANGOs observations.

List of publications

⋆ E. M. Bryant, et al. incl. **M. Timmermans** "TOI-2379 b and TOI-2384 b: two super-Jupiter mass planets transiting low-mass host stars", *Monthly Notices of the Royal Astronomical Society*, vol. 533, no. 4, pp. 3893–3906, October 2024. https://doi.org/10.1093/mnras/stae2034

⋆ M. Dévora-Pajares, F. J. Pozuelos, A. Thuillier, **M. Timmermans**, et al., "The SHERLOCK pipeline: new exoplanet candidates in the WASP-16, HAT-P-27, HAT-P-26, and TOI-2411 systems", *Monthly Notices of the Royal Astronomical Society*, vol. 532, no. 4, pp. 4752-4773, August 2024. https://doi.org/10.1093/mnras/stae1740

⋆ M. Ghachoui, B. V. Rackham, M. Dévora-Pajares, J. Chouqar, **M. Timmermans**, et al. "TESS discovery of two super-Earths orbiting the M-dwarf stars TOI-6002 and TOI-5713 near the radius valley", *Astronomy and Astrophysics*, accepted, August 2024. https://doi.org/10.48550/arXiv.2408.00709

⋆ P. P. Pedersen, et al. incl. **M. Timmermans**, "Infrared photometry with InGaAs detectors: first light with SPECULOOS", *Society of Photo-Optical Instrumentation Engineers (SPIE) Conference Series*, Vol. 13096, Ground-based and Airborne Instrumentation for Astronomy X, 130963X, July 2024. https://doi.org/10.1117/12.3018320.

⋆ **M. Timmermans** et al., "TOI-4336 A b: A temperate sub-Neptune ripe for atmospheric characterization in a nearby triple M-dwarf system", *Astronomy and Astrophysics*, vol. 687, Art. no. A48, July 2024. https://doi.org/10.1051/0004-6361/202347981.

⋆ J. D. Hartman, et al. incl. **M. Timmermans**, "TOI 762 A b and TIC 46432937 b: Two Giant Planets Transiting M Dwarf Stars", *The Astronomical Journal*, accepted, July 2024. https://doi.org/10.48550/arXiv.2407.07187

⋆ M. Gillon, et al. incl. **M. Timmermans**, "Detection of an Earth-sized exoplanet orbiting the nearby ultracool dwarf star SPECULOOS-3", *Nature Astronomy*, vol. 8, pp. 865-878, July 2024 https://doi.org/10.1038/s41550-024-02271-2

⋆ J. Schulte, et al. incl. **M. Timmermans**, "Migration and Evolution of giant ExoPlanets (MEEP). I. Nine Newly Confirmed Hot Jupiters from the TESS Mission", *The Astronomical Journal*, vol. 168, no. 1, Art. no. 32, July 2024 https://doi.org/10.3847/1538-3881/ad4a57

⋆ A. Fortier, et al. incl. **M. Timmermans**, "CHEOPS in-flight performance. A comprehensive look at the first 3.5 yr of operations", *Astronomy & Astrophysics*, vol. 687, Art. no.

A302, July 2024 https://doi.org/10.1051/0004-6361/202348576

⋆ P. C. Thao, et al. incl. **M. Timmermans**, "TESS Hunt for Young and Maturing Exoplanets (THYME). X. A Two-planet System in the 210 Myr MELANGE-5 Association", *The Astronomical Journal*, vol. 168, no. 1, Art. no. 41, July 2024 https://doi.org/10.3847/1538-3881/ad4993

⋆ S. Dholakia, et al. incl. **M. Timmermans**, "Gliese 12 b, a temperate Earth-sized planet at 12 parsecs discovered with TESS and CHEOPS", *Monthly Notices of the Royal Astronomical Society*, vol. 531, no. 1, pp.1276-1293, June 2024 https://doi.org/10.1093/mnras/stae1152

⋆ Y. Hori, et al. incl. **M. Timmermans**, "The Discovery and Follow-up of Four Transiting Short-period Sub-Neptunes Orbiting M Dwarfs", *The Astronomical Journal*, vol. 167, no. 6, Art. no. 289, July 2024 https://doi.org/10.3847/1538-3881/ad4115

⋆ K. Barkaoui, et al. incl. **M. Timmermans**, "An extended low-density atmosphere around the Jupiter-sized planet WASP-193 b", *Nature Astronomy*, vol. 8, pp. 909-919, July 2024 https://doi.org/10.1038/s41550-024-02259-y

⋆ B. J. Hord, et al. incl. **M. Timmermans**, "Identification of the Top TESS Objects of Interest for Atmospheric Characterization of Transiting Exoplanets with JWST", *The Astronomical Journal*, vol. 167, no. 5, Art. no. 233, May 2024 https://doi.org/10.3847/1538-3881/ad3068

⋆ M. I. Jones, et al. incl. **M. Timmermans**, "A long-period transiting substellar companion in the super-Jupiters to brown dwarfs mass regime and a prototypical warm-Jupiter detected by TESS", *Astronomy & Astrophysics*, vol. 683, Art. no. A192, March 2024 https://doi.org/10.1051/0004-6361/202348147

⋆ H. Parviainen, et al. incl. **M. Timmermans**, "TOI-2266 b: A keystone super-Earth at the edge of the M dwarf radius valley", *Astronomy & Astrophysics*, vol. 683, Art. no. A170, March 2024 https://doi.org/10.1051/0004-6361/202347431

⋆ J. M. Almenara, X. Bonfils, T. Guillot, **M. Timmermans**, et al. "Evidence for transit-timing variations of the 11 Myr exoplanet TOI-1227 b", *Astronomy & Astrophysics*, vol. 683, Art. no. A96, March 2024 https://doi.org/10.1051/0004-6361/202348492

⋆ B. A. Henderson, et al. incl. **M. Timmermans**, "NGTS-28Ab: a short period transiting brown dwarf", *Monthly Notices of the Royal Astronomical Society*, vol. 530, no. 1, pp.318-339, February 2024 https://doi.org/10.1093/mnras/stae508

⋆ F. Rescigno, et al. incl. **M. Timmermans**, "A hot mini-Neptune and a temperate, highly eccentric sub-Saturn around the bright K-dwarf TOI-2134", *Monthly Notices of the Royal Astronomical Society*, vol. 527, no. 1, pp.5385-5407, January 2024 https://doi.org/10.1093/mnras/stad3255

⋆ G. Dransfield, **M. Timmermans**, et al. "A 1.55 $R_\oplus$ habitable-zone planet hosted by TOI-715, an M4 star near the ecliptic South Pole", *Monthly Notices of the Royal Astronomical Society*, vol. 527, no. 1, pp.35-52, January 2024 https://doi.org/10.1093/mnras/stad1439

⋆ M. Rice, et al. incl. **M. Timmermans**, "Evidence for Low-level Dynamical Excitation in Near-resonant Exoplanet Systems", *The Astronomical Journal*, vol. 166, no. 6, Art. no. 266, November 2023 https://doi.org/10.3847/1538-3881/ad09de

⋆ A. H. M. J. Triaud, G. Dransfield, T. Kagetani, **M. Timmermans**, et al. "An M dwarf accompanied by a close-in giant orbiter with SPECULOOS", *Monthly Notices of the Royal Astronomical Society: Letters*, vol. 525, no. 1, pp.L98–L104, October 2023 https://doi.org/10.1093/mnrasl/slad097

⋆ T. Gan, et al. incl. **M. Timmermans**, "A Massive Hot Jupiter Orbiting a Metal-rich Early M Star Discovered in the TESS Full-frame Images", *The Astronomical Journal*, vol. 166, no. 4, Art. no. 165, October 2023 https://doi.org/10.3847/1538-3881/acf56d

⋆ J. Hartman, et al. incl. **M. Timmermans**, "TOI 4201 b and TOI 5344 b: Discovery of Two Transiting Giant Planets around M-dwarf Stars and Revised Parameters for Three Others", *The Astronomical Journal*, vol. 166, no. 4, Art. no. 163, October 2023 https://doi.org/10.3847/1538-3881/acf56e

⋆ K. Barkaoui, **M. Timmermans**, et al. "TOI-2084 b and TOI-4184 b: Two new sub-Neptunes around M dwarf stars", *Astronomy & Astrophysics*, vol. 677, Art. no. A38, September 2023 https://doi.org/10.1051/0004-6361/202346838

⋆ M. Ghachoui, et al. incl. **M. Timmermans**, "TESS discovery of a super-Earth orbiting the M-dwarf star TOI-1680", *Astronomy & Astrophysics*, vol. 677, Art. no. A31, September 2023 https://doi.org/10.1051/0004-6361/202347040

⋆ P. Mistry, et al. incl. **M. Timmermans**, "VaTEST. II. Statistical Validation of 11 TESS-detected Exoplanets Orbiting K-type Stars", *The Astronomical Journal*, vol. 166, no. 1, Art. no. 9, June 2023 https://doi.org/10.3847/1538-3881/acd548

⋆ G. Morello, et al. incl. **M. Timmermans**, "TOI-1442 b and TOI-2445 b: Two potentially rocky ultra-short period planets around M dwarfs", *Astronomy & Astrophysics*, vol. 673, Art. no. A32, May 2023 https://doi.org/10.1051/0004-6361/202243592

⋆ F. J. Pozuelos, **M. Timmermans**, et al. "A super-Earth and a mini-Neptune near the 2:1 MMR straddling the radius valley around the nearby mid-M dwarf TOI-2096", *Astronomy & Astrophysics*, vol. 672, Art. no. A70, April 2023 https://doi.org/10.1051/0004-6361/202245440

⋆ S. W. Yee, et al. incl. **M. Timmermans**, "The TESS Grand Unified Hot Jupiter Survey. II. Twenty New Giant Planets", *The Astrophysical Journal Supplement Series*, vol. 265, no. 1, Art. no. 1, March 2023 https://doi.org/10.3847/1538-4365/aca286

⋆ M. J. Hobson, et al. incl. **M. Timmermans**, "TOI-3235 b: A Transiting Giant Planet around an M4 Dwarf Star", *The Astrophysical Journal Letters,*, vol. 946, no. 1, Art. no. L4, March 2023 https://doi.org/10.3847/2041-8213/acbd9a

⋆ P. P. Perdersen, et al. incl. **M. Timmermans**, "Precise near-infrared photometry, accounting for precipitable water vapour at SPECULOOS Southern Observatory", *Monthly Notices of the Royal Astronomical Society*, vol. 518, no. 2, pp.2661–2670, January 2023

https://doi.org/10.1093/mnras/stac3154

⋆ L. Delrez, et al. incl. **M. Timmermans**, "Two temperate super-Earths transiting a nearby late-type M dwarf", *Astronomy & Astrophysics*, vol. 667, Art. no. A59, November 2022 https://doi.org/10.1051/0004-6361/202244041

⋆ T. Gan, et al. incl. **M. Timmermans**, "TESS discovery of a sub-Neptune orbiting a mid-M dwarf TOI-2136", *Monthly Notices of the Royal Astronomical Society*, vol. 514, no. 3, pp.4120–4139, August 2022 https://doi.org/10.1093/mnras/stac1448

⋆ C. A. Murray, et al. incl. **M. Timmermans**, "A study of flares in the ultra-cool regime from SPECULOOS-South", *Monthly Notices of the Royal Astronomical Society*, vol. 513, no. 2, pp.2615–2634, June 2022 https://doi.org/10.1093/mnras/stac1078

⋆ L. J. Garcia, **M. Timmermans**, et al. "PROSE: a PYTHON framework for modular astronomical images processing", *Monthly Notices of the Royal Astronomical Society*, vol. 509, no. 4, pp.4817–4828, February 2022 https://doi.org/10.1093/mnras/stac3113

⋆ N. Schanche, et al. incl. **M. Timmermans**, "TOI-2257 b: A highly eccentric long-period sub-Neptune transiting a nearby M dwarf", *Astronomy & Astrophysics*, vol. 657, Art. no. A45, January 2022 https://doi.org/10.1051/0004-6361/202142280

⋆ R. D. Wells, et al. incl. **M. Timmermans**, "A large sub-Neptune transiting the thick-disk M4 V TOI-2406", *Astronomy & Astrophysics*, vol. 653, Art. no. A97, September 2021 https://doi.org/10.1051/0004-6361/202141277

⋆ J. Dong, et al. incl. **M. Timmermans**, "Warm Jupiters in TESS Full-frame Images: A Catalog and Observed Eccentricity Distribution for Year 1", *The Astrophysical Journal Supplement Series*, vol. 255, no. 1, Art. no. 6, June 2021 https://doi.org/10.3847/1538-4365/abf73c

Bibliography

Abe, Y., Abe-Ouchi, A., Sleep, N. H., & Zahnle, K. J. 2011, Astrobiology, 11, 443

Agol, E., Dorn, C., Grimm, S. L., et al. 2021, PSJ, 2, 1

Agol, E. & Fabrycky, D. C. 2018, in Handbook of Exoplanets, ed. H. J. Deeg & J. A. Belmonte, 7

Al-Refaie, A. F., Changeat, Q., Waldmann, I. P., & Tinetti, G. 2021, ApJ, 917, 37

Allard, F. 2014, in IAU Symposium, Vol. 299, Exploring the Formation and Evolution of Planetary Systems, ed. M. Booth, B. C. Matthews, & J. R. Graham, 271–272

Almenara, J. M., Bonfils, X., Forveille, T., et al. 2022, A&A, 667, L11

Almenara, J. M., Bonfils, X., Guillot, T., et al. 2024, A&A, 683, A96

Artigau, É., Bouchy, F., Doyon, R., et al. 2024, arXiv e-prints, arXiv:2406.08304

Asplund, M., Grevesse, N., Sauval, A. J., & Scott, P. 2009, ARA&A, 47, 481

Astropy Collaboration, Robitaille, T. P., Tollerud, E. J., et al. 2013, A&A, 558, A33

Auvergne, M., Bodin, P., Boisnard, L., et al. 2009, A&A, 506, 411

Bachelet, E., Specht, D., Penny, M., et al. 2022, A&A, 664, A136

Bakos, G., Noyes, R. W., Kovács, G., et al. 2004, PASP, 116, 266

Barclay, T., Pepper, J., & Quintana, E. V. 2018, ApJS, 239, 2

Barkaoui, K., Burdanov, A., Hellier, C., et al. 2019, AJ, 157, 43

Barkaoui, K., Timmermans, M., Soubkiou, A., et al. 2023, A&A, 677, A38

Batalha, N. E., Mandell, A., Pontoppidan, K., et al. 2017, PASP, 129, 064501

Benneke, B. & Seager, S. 2012, ApJ, 753, 100

Benneke, B., Wong, I., Piaulet, C., et al. 2019, ApJL, 887, L14

Bennett, D. P., Sumi, T., Bond, I. A., et al. 2012, ApJ, 757, 119

Benz, W., Broeg, C., Fortier, A., et al. 2021, Experimental Astronomy, 51, 109

Berta, Z. K., Charbonneau, D., Désert, J.-M., et al. 2012, ApJ, 747, 35

Bézard, B., Charnay, B., & Blain, D. 2022, Nature Astronomy, 6, 537

Bonfanti, A., Brady, M., Wilson, T. G., et al. 2024, A&A, 682, A66

Bonfils, X., Almenara, J. M., Jocou, L., et al. 2015, in Society of Photo-Optical Instrumentation Engineers (SPIE) Conference Series, Vol. 9605, Techniques and Instrumentation for Detection of Exoplanets VII, 96051L

Borucki, W. J., Koch, D. G., Basri, G., et al. 2011, ApJ, 736, 19

Boss, A. P. 1997, Science, 276, 1836

Brande, J., Crossfield, I. J. M., Kreidberg, L., et al. 2022, AJ, 164, 197

Brandl, B. R., Agócs, T., Aitink-Kroes, G., et al. 2016, in Society of Photo-Optical Instrumentation Engineers (SPIE) Conference Series, Vol. 9908, Ground-based and Airborne Instrumentation for Astronomy VI, ed. C. J. Evans, L. Simard, & H. Takami, 990820

Broeg, C., Fernández, M., & Neuhäuser, R. 2005, Astronomische Nachrichten, 326, 134

Brown, T. M., Baliber, N., Bianco, F. B., et al. 2013, Publications of the Astronomical Society of the Pacific, 125, 1031

Bryant, E. M., Bayliss, D., & Van Eylen, V. 2023, MNRAS, 521, 3663

Buchner, J. 2021, The Journal of Open Source Software, 6, 3001

Burdanov, A., Delrez, L., Gillon, M., & Jehin, E. 2018, in Handbook of Exoplanets, ed. H. J. Deeg & J. A. Belmonte, 130

Burn, R., Mordasini, C., Mishra, L., et al. 2024, Nature Astronomy, 8, 463

Burn, R., Schlecker, M., Mordasini, C., et al. 2021, A&A, 656, A72

Butler, R. P., Marcy, G. W., Vogt, S. S., & Apps, K. 1998, PASP, 110, 1389

Butler, R. P., Marcy, G. W., Williams, E., Hauser, H., & Shirts, P. 1997, ApJL, 474, L115

Cadieux, C., Plotnykov, M., Doyon, R., et al. 2024, ApJL, 960, L3

Caffau, E., Ludwig, H. G., Steffen, M., Freytag, B., & Bonifacio, P. 2011, Sol. Phys., 268, 255

Carrasco, J. M., Weiler, M., Jordi, C., et al. 2021, A&A, 652, A86

Chabrier, G. 2003, PASP, 115, 763

Chabrier, G., Baraffe, I., Allard, F., & Hauschildt, P. 2000, ApJ, 542, 464

Chachan, Y., Knutson, H. A., Lothringer, J., & Blake, G. A. 2023, ApJ, 943, 112

Charbonneau, D., Brown, T. M., Latham, D. W., & Mayor, M. 2000, ApJL, 529, L45

Charbonneau, D., Brown, T. M., Noyes, R. W., & Gilliland, R. L. 2002, ApJ, 568, 377

Chauvin, G., Lagrange, A. M., Dumas, C., et al. 2005, A&A, 438, L25

Chen, J. & Kipping, D. 2017, ApJ, 834, 17

Clampin, M., Sirianni, M., Hartig, G. F., et al. 2002, Experimental Astronomy, 14, 107

Claret, A. 2018, A&A, 618, A20

Claret, A., Hauschildt, P. H., & Witte, S. 2012, A&A, 546, A14

Cloutier, R. & Menou, K. 2020, AJ, 159, 211

Cockell, C. S., Bush, T., Bryce, C., et al. 2016, Astrobiology, 16, 89

Collier Cameron, A., Ford, E. B., Shahaf, S., et al. 2021, MNRAS, 505, 1699

Collins, K. A., Kielkopf, J. F., Stassun, K. G., & Hessman, F. V. 2017, AJ, 153, 77

Cridland, A. J., van Dishoeck, E. F., Alessi, M., & Pudritz, R. E. 2019, A&A, 632, A63

Currie, T., Fukagawa, M., Thalmann, C., Matsumura, S., & Plavchan, P. 2012, ApJL, 755, L34

Cutri, R. M., Skrutskie, M. F., van Dyk, S., et al. 2003, VizieR Online Data Catalog: 2MASS All-Sky Catalog of Point Sources (Cutri+ 2003), VizieR On-line Data Catalog: II/246. Originally published in: 2003yCat.2246....0C

Cutri, R. M., Wright, E. L., Conrow, T., et al. 2021, VizieR Online Data Catalog: AllWISE Data Release (Cutri+ 2013), VizieR On-line Data Catalog: II/328. Originally published in: IPAC/Caltech (2013)

Dawson, R. I. & Johnson, J. A. 2018, ARA&A, 56, 175

De Angeli, F., Weiler, M., Montegriffo, P., et al. 2023, A&A, 674, A2

de Beurs, Z. L., Vanderburg, A., Shallue, C. J., et al. 2022, AJ, 164, 49

Delrez, L., Gillon, M., Queloz, D., et al. 2018, in Society of Photo-Optical Instrumentation Engineers (SPIE) Conference Series, Vol. 10700, Ground-based and Airborne Telescopes VII, ed. H. K. Marshall & J. Spyromilio, 107001I

Delrez, L., Murray, C. A., Pozuelos, F. J., et al. 2022, A&A, 667, A59

Delrez, L., Santerne, A., Almenara, J. M., et al. 2016, MNRAS, 458, 4025

Demory, B.-O., Gillon, M., de Wit, J., et al. 2016, Nature, 532, 207

Demory, B. O., Pozuelos, F. J., Gómez Maqueo Chew, Y., et al. 2020, A&A, 642, A49

Demory, B. O., Ségransan, D., Forveille, T., et al. 2009, A&A, 505, 205

Dévora-Pajares, M., Pozuelos, F. J., Thuillier, A., et al. 2024, MNRAS[[arXiv]2407.14602]

Díaz, R. F., Almenara, J. M., Santerne, A., et al. 2014, MNRAS, 441, 983

Donati, J.-F., Kouach, D., Lacombe, M., et al. 2018, in Handbook of Exoplanets, ed. H. J. Deeg & J. A. Belmonte, 107

Dransfield, G., Timmermans, M., Triaud, A. H. M. J., et al. 2024, MNRAS, 527, 35

Dressel, L. 2022, in WFC3 Instrument Handbook for Cycle 30 v. 14, Vol. 14, 14

Dressing, C. D. & Charbonneau, D. 2015, ApJ, 807, 45

Duane, S., Kennedy, A. D., Pendleton, B. J., & Roweth, D. 1987, Physics Letters B, 195, 216

Dumusque, X. 2018, A&A, 620, A47

Edwards, B. & Changeat, Q. 2024, ApJL, 962, L30

Fairman, C., Wakeford, H. R., & MacDonald, R. J. 2024, AJ, 167, 240

Fischer, D. A. & Valenti, J. 2005, ApJ, 622, 1102

Foreman-Mackey, D. 2016, The Journal of Open Source Software, 1, 24

Foreman-Mackey, D. 2018, Research Notes of the American Astronomical Society, 2, 31

Foreman-Mackey, D., Agol, E., Ambikasaran, S., & Angus, R. 2017, celerite: Scalable 1D Gaussian Processes in C++, Python, and Julia, Astrophysics Source Code Library, record ascl:1709.008

Foreman-Mackey, D., Hogg, D. W., Lang, D., & Goodman, J. 2013, PASP, 125, 306

Foreman-Mackey, D., Luger, R., Agol, E., et al. 2021, arXiv e-prints, arXiv:2105.01994

Fraine, J., Deming, D., Benneke, B., et al. 2014, Nature, 513, 526

Fressin, F., Torres, G., Charbonneau, D., et al. 2013, ApJ, 766, 81

Fulton, B. J., Petigura, E. A., Howard, A. W., et al. 2017, AJ, 154, 109

Gaia Collaboration, Vallenari, A., Brown, A. G. A., et al. 2023, A&A, 674, A1

Gan, T., Wang, S. X., Wang, S., et al. 2023, AJ, 165, 17

Garcia, L. J., Timmermans, M., Pozuelos, F. J., et al. 2021, prose: FITS images processing pipeline, Astrophysics Source Code Library, record ascl:2111.006

Garcia, L. J., Timmermans, M., Pozuelos, F. J., et al. 2022, MNRAS, 509, 4817

Gardner, J. P., Mather, J. C., Clampin, M., et al. 2006, Space Sci. Rev., 123, 485

Gaudi, B. S. 2010, in Exoplanets, ed. S. Seager, 79–110

Gelman, A., Carlin, J., Stern, H., et al. 2013, Bayesian data analysis, third edition, 1–646

Gelman, A. & Rubin, D. B. 1992, Statistical Science, 7, 457

Ghachoui, M., Soubkiou, A., Wells, R. D., et al. 2023, A&A, 677, A31

Giacalone, S., Dressing, C. D., Jensen, E. L. N., et al. 2021, AJ, 161, 24

Gillon, M. 2018, Nature Astronomy, 2, 344

Gillon, M., Jehin, E., Fumel, A., Magain, P., & Queloz, D. 2013, in European Physical Journal Web of Conferences, Vol. 47, European Physical Journal Web of Conferences, 03001

Gillon, M., Jehin, E., Lederer, S. M., et al. 2016, Nature, 533, 221

Gillon, M., Jehin, E., Magain, P., et al. 2011, EPJ Web of Conferences, 11, 06002

Gillon, M., Pedersen, P. P., Rackham, B. V., et al. 2024, Nature Astronomy

Gillon, M., Triaud, A. H. M. J., Demory, B.-O., et al. 2017, Nature, 542, 456

Gillon, M., Triaud, A. H. M. J., Fortney, J. J., et al. 2012, A&A, 542, A4

Ginzburg, S., Schlichting, H. E., & Sari, R. 2018, MNRAS, 476, 759

Gomes da Silva, J., Bensabat, A., Monteiro, T., & Santos, N. C. 2022, A&A, 668, A174

Goodman, J. & Weare, J. 2010, Communications in Applied Mathematics and Computational Science, 5, 65

Gregory, P. C. 2005, Bayesian Logical Data Analysis for the Physical Sciences: A Comparative Approach with 'Mathematica' Support

Greklek-McKeon, M., Knutson, H. A., Vissapragada, S., et al. 2023, AJ, 165, 48

Grether, D. & Lineweaver, C. H. 2006, ApJ, 640, 1051

Grimm, S. L., Demory, B.-O., Gillon, M., et al. 2018, A&A, 613, A68

Guenther, E. W., Díaz, R. F., Gazzano, J. C., et al. 2012, A&A, 537, A136

Guerrero, N. M., Seager, S., Huang, C. X., et al. 2021, ApJS, 254, 39

Günther, M. N. & Daylan, T. 2019, Allesfitter: Flexible Star and Exoplanet Inference From Photometry and Radial Velocity, Astrophysics Source Code Library

Günther, M. N. & Daylan, T. 2021, ApJS, 254, 13

Gupta, A. & Schlichting, H. E. 2019, MNRAS, 487, 24

Han, C., Bond, I. A., Udalski, A., et al. 2024, A&A, 687, A241

Hartman, J. & Bakos, G. 2016, Astronomy and Computing, 17, 1

Hartman, J. D., Bakos, G. Á., Csubry, Z., et al. 2023, AJ, 166, 163

Hartman, J. D., Bayliss, D., Brahm, R., et al. 2024, arXiv e-prints, arXiv:2407.07187

Hastings, W. K. 1970, Biometrika, 57, 97

Haswell, C. A. 2010, Transiting Exoplanets

Haynes, K., Mandell, A. M., Madhusudhan, N., Deming, D., & Knutson, H. 2015, ApJ, 806, 146

Henderson, B. A., Casewell, S. L., Goad, M. R., et al. 2024a, MNRAS, 530, 318

Henderson, B. A., Casewell, S. L., Jordán, A., et al. 2024b, MNRAS, 533, 2823

Henry, G. W., Marcy, G. W., Butler, R. P., & Vogt, S. S. 2000, ApJL, 529, L41

Hippke, M., David, T. J., Mulders, G. D., & Heller, R. 2019, AJ, 158, 143

Hippke, M. & Heller, R. 2019, A&A, 623, A39

Hobbs, R., Shorttle, O., & Madhusudhan, N. 2022, MNRAS, 516, 1032

Hobson, M. J., Jordán, A., Bryant, E. M., et al. 2023, ApJL, 946, L4

Hoffman, M. D. & Gelman, A. 2014, JMLR, 15, 1593

Howard, A. W., Marcy, G. W., Bryson, S. T., et al. 2012, ApJS, 201, 15

Howell, S. B., Sobeck, C., Haas, M., et al. 2014, PASP, 126, 398

Huang, C. X., Vanderburg, A., Pál, A., et al. 2020a, Research Notes of the American Astronomical Society, 4, 204

Huang, C. X., Vanderburg, A., Pál, A., et al. 2020b, Research Notes of the American Astronomical Society, 4, 206

Husser, T. O., Wende-von Berg, S., Dreizler, S., et al. 2013, A&A, 553, A6

Ida, S. & Lin, D. N. C. 2005, ApJ, 626, 1045

Iyer, A. R., Line, M. R., Muirhead, P. S., Fortney, J. J., & Gharib-Nezhad, E. 2023, ApJ, 944, 41

Jackman, J. A. G., Wheatley, P. J., Bayliss, D., et al. 2019, MNRAS, 489, 5146

Jehin, E., Gillon, M., Queloz, D., et al. 2018, The Messenger, 174, 2

Jehin, E., Gillon, M., Queloz, D., et al. 2011, The Messenger, 145, 2

Jenkins, J. M. 2020, Kepler Data Processing Handbook: Overview of the Science Operations Center, id. 2, Kepler Science Document KSCI-19081-003, id. 2. Edited by Jon M. Jenkins.

Jenkins, J. M., Twicken, J. D., McCauliff, S., et al. 2016, in Society of Photo-Optical Instrumentation Engineers (SPIE) Conference Series, Vol. 9913, Software and Cyberinfrastructure for Astronomy IV, ed. G. Chiozzi & J. C. Guzman, 99133E

Johnson, S. A., Penny, M., Gaudi, B. S., et al. 2020, AJ, 160, 123

Kagetani, T., Narita, N., Kimura, T., et al. 2023, PASJ, 75, 713

Kaltenegger, L. 2017, ARA&A, 55, 433

Kaltenegger, L. & Sasselov, D. 2011, ApJL, 736, L25

Kaltenegger, L. & Traub, W. A. 2009, ApJ, 698, 519

Kass, R. E. & Raftery, A. E. 1995, Journal of the American Statistical Association, 90, 773

Kasting, J. F., Kopparapu, R., Ramirez, R. M., & Harman, C. E. 2014, Proceedings of the National Academy of Science, 111, 12641

Kempton, E. M. R., Bean, J. L., Louie, D. R., et al. 2018, PASP, 130, 114401

Kempton, E. M. R., Lupu, R., Owusu-Asare, A., Slough, P., & Cale, B. 2017, PASP, 129, 044402

Kempton, E. M. R., Zhang, M., Bean, J. L., et al. 2023, Nature, 620, 67

Keppler, M., Benisty, M., Müller, A., et al. 2018, A&A, 617, A44

Kim, S.-L., Lee, C.-U., Park, B.-G., et al. 2016, Journal of Korean Astronomical Society, 49, 37

Kipping, D. M. 2013, MNRAS, 435, 2152

Knutson, H. A., Benneke, B., Deming, D., & Homeier, D. 2014a, Nature, 505, 66

Knutson, H. A., Dragomir, D., Kreidberg, L., et al. 2014b, ApJ, 794, 155

Knutson, H. A., Madhusudhan, N., Cowan, N. B., et al. 2011, ApJ, 735, 27

Koch, D. G., Borucki, W. J., Basri, G., et al. 2010, ApJL, 713, L79

Kopparapu, R. K., Ramirez, R., Kasting, J. F., et al. 2013, ApJ, 765, 131

Kopparapu, R. k., Wolf, E. T., Arney, G., et al. 2017, ApJ, 845, 5

Kovács, G., Zucker, S., & Mazeh, T. 2002, A&A, 391, 369

Kreidberg, L. 2018, in Handbook of Exoplanets, ed. H. J. Deeg & J. A. Belmonte, 100

Kreidberg, L., Bean, J. L., Désert, J.-M., et al. 2014, Nature, 505, 69

Kreidberg, L., Line, M. R., Parmentier, V., et al. 2018, AJ, 156, 17

Kuchner, M. J. 2003, ApJL, 596, L105

Kunimoto, M., Daylan, T., Guerrero, N., et al. 2022, ApJS, 259, 33

Latham, D. W., Rowe, J. F., Quinn, S. N., et al. 2011, ApJL, 732, L24

Laughlin, G., Bodenheimer, P., & Adams, F. C. 2004, ApJL, 612, L73

Laureijs, R., Amiaux, J., Arduini, S., et al. 2011, arXiv e-prints, arXiv:1110.3193

Léger, A., Selsis, F., Sotin, C., et al. 2004, Icarus, 169, 499

Lépine, S., Rich, R. M., & Shara, M. M. 2007, ApJ, 669, 1235

Libby-Roberts, J. E., Berta-Thompson, Z. K., Désert, J.-M., et al. 2020, AJ, 159, 57

Libby-Roberts, J. E., Schutte, M., Hebb, L., et al. 2023, AJ, 165, 249

Lightkurve Collaboration, Cardoso, J. V. d. M., Hedges, C., et al. 2018, Lightkurve: Kepler and TESS time series analysis in Python, Astrophysics Source Code Library, record ascl:1812.013

Line, M. R., Stevenson, K. B., Bean, J., et al. 2016, AJ, 152, 203

Louie, D. R., Deming, D., Albert, L., et al. 2018, PASP, 130, 044401

Lovelock, J. E. 1965, Nature, 207, 568

Lovis, C. & Fischer, D. 2010, in Exoplanets, ed. S. Seager, 27–53

Luque, R. & Pallé, E. 2022, Science, 377, 1211

Madhusudhan, N., Bitsch, B., Johansen, A., & Eriksson, L. 2017, MNRAS, 469, 4102

Madhusudhan, N., Piette, A. A. A., & Constantinou, S. 2021, ApJ, 918, 1

Madhusudhan, N., Sarkar, S., Constantinou, S., et al. 2023, ApJL, 956, L13

Maldonado, J., Petralia, A., Mantovan, G., et al. 2023, A&A, 674, A132

Mandel, K. & Agol, E. 2002, ApJL, 580, L171

Mann, A. W., Dupuy, T., Kraus, A. L., et al. 2019, ApJ, 871, 63

Mann, A. W., Feiden, G. A., Gaidos, E., Boyajian, T., & von Braun, K. 2015, ApJ, 804, 64

Marcy, G., Butler, R. P., Fischer, D., et al. 2005, Progress of Theoretical Physics Supplement, 158, 24

Marcy, G. W., Weiss, L. M., Petigura, E. A., et al. 2014, Proceedings of the National Academy of Science, 111, 12655

Margulis, L. & Lovelock, J. E. 1974, Icarus, 21, 471

Marois, C., Macintosh, B., Barman, T., et al. 2008, Science, 322, 1348

Maxted, P. F. L. 2016, A&A, 591, A111

Mayor, M., Marmier, M., Lovis, C., et al. 2011, arXiv e-prints, arXiv:1109.2497

Mayor, M., Pepe, F., Queloz, D., et al. 2003, The Messenger, 114, 20

Mayor, M. & Queloz, D. 1995, Nature, 378, 355

McCormac, J., Pollacco, D., Skillen, I., et al. 2013, PASP, 125, 548

McCully, C., Volgenau, N. H., Harbeck, D.-R., et al. 2018, in Society of Photo-Optical Instrumentation Engineers (SPIE) Conference Series, Vol. 10707, Software and Cyberinfrastructure for Astronomy V, ed. J. C. Guzman & J. Ibsen, 107070K

Meadows, V. S. 2008, in Exoplanets, ed. J. W. Mason, 259

Ment, K. & Charbonneau, D. 2023, AJ, 165, 265

Mikal-Evans, T., Madhusudhan, N., Dittmann, J., et al. 2023, AJ, 165, 84

Mikal-Evans, T., Sing, D. K., Barstow, J. K., et al. 2022, Nature Astronomy, 6, 471

Mollière, P., Wardenier, J. P., van Boekel, R., et al. 2019, A&A, 627, A67

Montegriffo, P., De Angeli, F., Andrae, R., et al. 2023, A&A, 674, A3

Morales, J. C., Gallardo, J., Ribas, I., et al. 2010, ApJ, 718, 502

Mordasini, C., van Boekel, R., Mollière, P., Henning, T., & Benneke, B. 2016, ApJ, 832, 41

Morton, T. D. 2012, ApJ, 761, 6

Mulders, G. D., Pascucci, I., & Apai, D. 2015a, ApJ, 798, 112

Mulders, G. D., Pascucci, I., & Apai, D. 2015b, ApJ, 814, 130

Murray, C. D. & Correia, A. C. M. 2010, in Exoplanets, ed. S. Seager, 15–23

Narita, N., Fukui, A., Yamamuro, T., et al. 2020, in Society of Photo-Optical Instrumentation Engineers (SPIE) Conference Series, Vol. 11447, Ground-based and Airborne Instrumentation for Astronomy VIII, 114475K

Neichel, B., Mouillet, D., Gendron, E., et al. 2018, in SF2A-2018: Proceedings of the Annual meeting of the French Society of Astronomy and Astrophysics, ed. P. Di Matteo, F. Billebaud, F. Herpin, N. Lagarde, J. B. Marquette, A. Robin, & O. Venot, Di

Nettelmann, N., Fortney, J. J., Kramm, U., & Redmer, R. 2011, ApJ, 733, 2

Nikolov, N., Sing, D. K., Gibson, N. P., et al. 2016, ApJ, 832, 191

Nutzman, P. & Charbonneau, D. 2008, PASP, 120, 317

Öberg, K. I., Murray-Clay, R., & Bergin, E. A. 2011, ApJL, 743, L16

Oshagh, M., Santos, N. C., Boisse, I., et al. 2013, A&A, 556, A19

Owen, J. E. & Wu, Y. 2013, ApJ, 775, 105

Owen, J. E. & Wu, Y. 2017, ApJ, 847, 29

Parc, L., Bouchy, F., Venturini, J., Dorn, C., & Helled, R. 2024, arXiv e-prints, arXiv:2406.04311

Parker, E. N. 1955, ApJ, 121, 491

Parviainen, H. 2018, in Handbook of Exoplanets, ed. H. J. Deeg & J. A. Belmonte, 149

Parviainen, H. & Aigrain, S. 2015, MNRAS, 453, 3821

Pedersen, P. P., Queloz, D., Garcia, L., et al. 2024, in Society of Photo-Optical Instrumentation Engineers (SPIE) Conference Series, Vol. 13096, Ground-based and Airborne Instrumentation for Astronomy X, 130963X

Pepe, F., Cristiani, S., Rebolo, R., et al. 2021, A&A, 645, A96

Pepe, F., Molaro, P., Cristiani, S., et al. 2014, Astronomische Nachrichten, 335, 8

Perryman, M. 2018, The Exoplanet Handbook

Pinhas, A., Rackham, B. V., Madhusudhan, N., & Apai, D. 2018, MNRAS, 480, 5314

Pollacco, D. L., Skillen, I., Collier Cameron, A., et al. 2006, PASP, 118, 1407

Pozuelos, F. J., Suárez, J. C., de Elía, G. C., et al. 2020, A&A, 641, A23

Pozuelos, F. J., Timmermans, M., Rackham, B. V., et al. 2023, A&A, 672, A70

Rajpurohit, A. S., Allard, F., Teixeira, G. D. C., et al. 2018, A&A, 610, A19

Ramirez, R. M. & Kaltenegger, L. 2017, ApJL, 837, L4

Ramírez, V., Cridland, A. J., & Mollière, P. 2020, A&A, 641, A87

Rasmussen, C. E. & Williams, C. K. I. 2006, Gaussian Processes for Machine Learning

Rauer, H., Aerts, C., Cabrera, J., & PLATO Team. 2016, Astronomische Nachrichten, 337, 961

Redfield, S., Batalha, N., Benneke, B., et al. 2024, arXiv e-prints, arXiv:2404.02932

Rein, H. & Liu, S. F. 2012, A&A, 537, A128

Reiners, A., Zechmeister, M., Caballero, J. A., et al. 2018, A&A, 612, A49

Rektsini, N. E. & Batista, V. 2024, arXiv e-prints, arXiv:2407.06689

Rektsini, N. E., Batista, V., Ranc, C., et al. 2024, AJ, 167, 145

Ribas, I. 2006, Ap&SS, 304, 89

Ricker, G. R., Winn, J. N., Vanderspek, R., et al. 2014, in Society of Photo-Optical Instrumentation Engineers (SPIE) Conference Series, Vol. 9143, Space Telescopes and Instrumentation 2014: Optical, Infrared, and Millimeter Wave, 914320

Rigby, F. E. & Madhusudhan, N. 2024, MNRAS, 529, 409

Rocchetto, M., Waldmann, I. P., Venot, O., Lagage, P. O., & Tinetti, G. 2016, ApJ, 833, 120

Rogers, J. G., Schlichting, H. E., & Owen, J. E. 2023, ApJL, 947, L19

Rogers, L. A. & Seager, S. 2010, ApJ, 712, 974

Roy, P.-A., Benneke, B., Piaulet, C., et al. 2023, ApJL, 954, L52

Rustamkulov, Z., Sing, D. K., Mukherjee, S., et al. 2023, Nature, 614, 659

Salvatier, J., Wiecki, T. V., & Fonnesbeck, C. 2016, PyMC3: Python probabilistic programming framework, Astrophysics Source Code Library, record ascl:1610.016

Sanchis-Ojeda, R., Rappaport, S., Pallè, E., et al. 2015, ApJ, 812, 112

Savitzky, A. & Golay, M. J. E. 1964, Analytical Chemistry, 36, 1627

Schanche, N., Pozuelos, F. J., Günther, M. N., et al. 2022, A&A, 657, A45

Schlecker, M., Burn, R., Sabotta, S., et al. 2022, A&A, 664, A180

Schwieterman, E. W., Kiang, N. Y., Parenteau, M. N., et al. 2018, Astrobiology, 18, 663

Seager, S., Deming, D., & Valenti, J. A. 2009, in Astrophysics and Space Science Proceedings, Vol. 10, Astrophysics in the Next Decade, 123

Seager, S. & Mallén-Ornelas, G. 2003, ApJ, 585, 1038

Seager, S. & Sasselov, D. D. 2000, ApJ, 537, 916

Sebastian, D., Gillon, M., Ducrot, E., et al. 2021, A&A, 645, A100

Seifahrt, A., Bean, J. L., Stürmer, J., et al. 2020, in Society of Photo-Optical Instrumentation Engineers (SPIE) Conference Series, Vol. 11447, Ground-based and Airborne Instrumentation for Astronomy VIII, ed. C. J. Evans, J. J. Bryant, & K. Motohara, 114471F

Skaf, N., Bieger, M. F., Edwards, B., et al. 2020, AJ, 160, 109

Skilling, J. 2004, in American Institute of Physics Conference Series, Vol. 735, Bayesian Inference and Maximum Entropy Methods in Science and Engineering: 24th International Workshop on Bayesian Inference and Maximum Entropy Methods in Science and Engineering, ed. R. Fischer, R. Preuss, & U. V. Toussaint (AIP), 395–405

Spada, F., Demarque, P., Kim, Y. C., & Sills, A. 2013, ApJ, 776, 87

Speagle, J. S. 2020, MNRAS, 493, 3132

Spruit, H. C. 1976, Sol. Phys., 50, 269

Stassun, K. G., Oelkers, R. J., Paegert, M., et al. 2019, AJ, 158, 138

Stassun, K. G. & Torres, G. 2016, AJ, 152, 180

Stevenson, K. B., Désert, J.-M., Line, M. R., et al. 2014, Science, 346, 838

Stolker, T., Quanz, S. P., Todorov, K. O., et al. 2020, A&A, 635, A182

Sullivan, P. W., Winn, J. N., Berta-Thompson, Z. K., et al. 2015, ApJ, 809, 77

Thorngren, D. P., Fortney, J. J., Murray-Clay, R. A., & Lopez, E. D. 2016, ApJ, 831, 64

Timmermans, M., Dransfield, G., Gillon, M., et al. 2024, A&A, 687, A48

Tinetti, G., Drossart, P., Eccleston, P., et al. 2016, in Society of Photo-Optical Instrumentation Engineers (SPIE) Conference Series, Vol. 9904, Space Telescopes and Instrumentation 2016: Optical, Infrared, and Millimeter Wave, ed. H. A. MacEwen, G. G. Fazio, M. Lystrup, N. Batalha, N. Siegler, & E. C. Tong, 99041X

Tonry, J. & Davis, M. 1979, AJ, 84, 1511

Torres, G., Fressin, F., Batalha, N. M., et al. 2011, ApJ, 727, 24

Traub, W. A. & Oppenheimer, B. R. 2010, in Exoplanets, ed. S. Seager, 111–156

Triaud, A. H. M. J., Dransfield, G., Kagetani, T., et al. 2023, MNRAS, 525, L98

Triaud, A. H. M. J., Neveu-VanMalle, M., Lendl, M., et al. 2017, MNRAS, 467, 1714

Trotta, R. 2008, Contemporary Physics, 49, 71

Tsiaras, A., Rocchetto, M., Waldmann, I. P., et al. 2016a, ApJ, 820, 99

Tsiaras, A., Waldmann, I. P., Rocchetto, M., et al. 2016b, ApJ, 832, 202

Tsiaras, A., Waldmann, I. P., Tinetti, G., Tennyson, J., & Yurchenko, S. N. 2019, Nature Astronomy, 3, 1086

Tsiaras, A., Waldmann, I. P., Zingales, T., et al. 2018, AJ, 155, 156

Turrini, D., Schisano, E., Fonte, S., et al. 2021, ApJ, 909, 40

Twicken, J. D., Catanzarite, J. H., Clarke, B. D., et al. 2018, PASP, 130, 064502

Twicken, J. D., Jenkins, J. M., Seader, S. E., et al. 2016, AJ, 152, 158

Udalski, A., Szymanski, M., Kaluzny, J., Kubiak, M., & Mateo, M. 1992, Acta Astron., 42, 253

Udry, S., Mayor, M., Naef, D., et al. 2000, A&A, 356, 590

Ulmer-Moll, S., Osborn, H. P., Tuson, A., et al. 2023, A&A, 674, A43

Van Eylen, V., Astudillo-Defru, N., Bonfils, X., et al. 2021, MNRAS, 507, 2154

Venturini, J., Guilera, O. M., Haldemann, J., Ronco, M. P., & Mordasini, C. 2020, A&A, 643, L1

Venturini, J., Ronco, M. P., Guilera, O. M., et al. 2024, A&A, 686, L9

Vines, J. I. & Jenkins, J. S. 2022, MNRAS, 513, 2719

Waalkes, W. C., Berta-Thompson, Z. K., Collins, K. A., et al. 2021, AJ, 161, 13

Wells, R. D., Rackham, B. V., Schanche, N., et al. 2021, A&A, 653, A97

Wheatley, P. J., West, R. G., Goad, M. R., et al. 2018, MNRAS, 475, 4476

Wildi, F., Blind, N., Reshetov, V., et al. 2017, in Society of Photo-Optical Instrumentation Engineers (SPIE) Conference Series, Vol. 10400, Techniques and Instrumentation for Detection of Exoplanets VIII, ed. S. Shaklan, 1040018

Winn, J. N. 2010, in Exoplanets, ed. S. Seager, 55–77

Winters, J. G., Henry, T. J., Lurie, J. C., et al. 2015, AJ, 149, 5

Wogan, N. F., Batalha, N. E., Zahnle, K. J., et al. 2024, ApJL, 963, L7

Wolszczan, A. & Frail, D. A. 1992, Nature, 355, 145

Wright, J. T., Marcy, G. W., Howard, A. W., et al. 2012, ApJ, 753, 160

Zeng, L., Jacobsen, S. B., Sasselov, D. D., et al. 2019, Proceedings of the National Academy of Science, 116, 9723

Zhang, J., Kempton, E. M. R., & Rauscher, E. 2017, ApJ, 851, 84